博士論文

Stiffness condition assessment of bridge lateral resisting systems with unscented Kalman filter using seismic acceleration response measurements

(地震応答計測を利用したアンセンテッドカルマンフィルタによる
橋梁の水平方向復元力特性同定)

クレリ ミュゲ

KULELI MUGE

Abstract

Stiffness assessment of bridges under seismic excitation is of great importance especially in earthquake-prone countries. The identification reveals dynamic characteristics and allows condition assessment. Seismic response measurements from small and frequent earthquakes (e.g. aftershocks) and analysis of these records may reveal deficiencies in stiffness which may be due to large main shocks or poor construction quality. If condition is assessed, corresponding measures can be taken to prevent failure/undesired response during future big earthquakes. Using seismic response measurements from large earthquakes, both residual stiffness and hysteresis response can be theoretically identified, which would provide substantial information on the behavior of the element. Hysteresis response can provide the total energy dissipation of the element and hence enable the engineer to assess occurred damage. Decisions towards closure or repair may be made more rapidly in the aftermath. However, ground motion and response records of bridges during earthquakes are often not available, except for some signature bridges; even if data is available, the identification techniques have limitations.

Current structural identification methods have several problems in terms of application to real bridges. These methods can be grouped in two general categories, namely, a) Frequency Domain Methods and b) Time Domain Methods. While the frequency domain methods provide modal parameters, the conversion from the modal to the physical domain is difficult as the conversion usually requires empirical knowledge. In addition, most modal identification methods assume linear behaviors of structures; the structural performance including the nonlinear characteristics, such as hysteresis responses, is difficult to evaluate. On the other hand, typical time domain methods of data assimilation methods, such as Extended Kalman Filter (EKF) and Unscented Kalman Filter (UKF) can directly provide physical parameter estimations of nonlinear dynamic systems. The stiffness parameters are included in the state vector; the parameters are estimated as a part of the augmented state vector. UKF, which has been shown to be superior to EKF because UKF can deal with up to the second

order of nonlinearity, however, has never been validated using laboratory or in-situ measurements.

Common problem which prevents application of data assimilation methods to full-scale bridges is the lack of robustness and the data. UKF requires initial process and measurement noise covariance matrices to be known a-priori and keeps both matrices constant over time. If these matrices are not known, UKF performs sub-optimal or even diverges. In addition, UKF is also sensitive to initial state vector assignments. These problems become severe in particular when the size of the state vector is large. Thus, in order to practically apply UKF to structural identification, estimation methods addressing these robustness issues are needed. Furthermore, seismic response monitoring has been limited to some signature bridges where sensor networks are readily available. The number of channels is also limited. Seismic response data to be utilized in the data assimilation methods is rare.

This thesis first prepares seismic response measurement data to be utilized in the stiffness condition assessment of full-scale bridges and proposes the use of the Robbins-Monro stochastic approximation scheme with UKF (UKF-RM) for the stiffness estimation problems to address the robustness issues. The performance of the proposed algorithm is then examined through simulations and measured records. Lastly, the UKF-RM is extended to hysteresis loop estimation of structural elements under nonlinear motion.

To study the applicability and robustness of data assimilation techniques, the availability of seismic response data is essential. The large-scale laboratory test on an RC concrete pier and in-situ measurement of earthquake responses, which provide data sets the proposed algorithm is investigated with, are first explained. The shake table test on an RC pier conducted at the E-Defense facility provides detailed dynamic motion records during a variety of ground excitations. The pier is equipped with numerous accelerometers, displacement sensors, and load-cells; input and output records are all available together with data to validate the structural identification results. Movies and detailed description of the pier during the excitation are also available; stiffness identification results can be interpreted with these detailed infor-

mation. The in-situ measurement, on the other hand, was made possible with the recent advance in the wireless sensor technologies. Wireless sensor nodes with low cost, weeks-long battery life, and seismometer-class high quality sensors made the detailed seismic response measurements on ordinary bridges possible. Using the wireless sensors, shortly after April 2016 Kumamoto Earthquake, a 60 m span steel box girder bridge was instrumented. The bridge sits on rubber bearings. Over a period of two weeks, 61 seismic response records had been obtained. Records were obtained on pier, abutment, and corresponding girder locations. These records provide input and output information of the rubber bearing system.

Consequently, the use of the Robbins-Monro stochastic approximation scheme with UKF (UKF-RM) has been proposed and numerically investigated. Through simulations UKF-RM scheme is shown to significantly improve the robustness of the filter when compared to conventional UKF. The performance is investigated in detail through simulations considering changes in initial process, measurement, and error covariance matrices, initial state vector, measurement noise, and UKF-RM parameter α. The sensitivities of the UKF-RM approach to the changes are shown low. In addition, since UKF-RM adapts noise covariance during estimation, its convergence rate is fast. The change in stiffness during nonlinear responses is traceable with UKF-RM.

The method has been further validated using laboratory experiments on a reinforced concrete bridge column with response measurements from small and large earthquakes. Experimental validation of the proposed algorithm is presented using measurement records from shake-table laboratory tests of linear and nonlinear response levels. In both cases, UKF-RM proved to be faster in convergence than the conventional UKF. The proposed method is capable of tracing the stiffness change of nonlinear behavior. This application is the first example of a stiffness condition identification of a 1:1 scale bridge lateral resisting system component, an RC pier, using UKF-RM.

The method is then validated using the in-situ measurement seismic response data. The stiffness condition of the rubber bearings has been investigated with the proposed

UKF- RM method. The stiffness coefficients of the bearings on the pier and on the abutment have been successfully obtained considering multi-support excitation. The identified stiffness coefficients are shown consistent with factory testing results.

Lastly, hysteresis response identification only using acceleration measurements are proposed by employing the UKF-RM approach together with numerical integration of the acceleration records. As the nonlinear model, non-degrading conventional Bouc-Wen model is employed; the hysteresis is estimated by identifying the augmented state vector including the non-linear parameters. First, the observability analysis was performed. To make the system observable even when only one response observation in addition to the ground motion is available, the reduction of the Bouc-Wen model is shown necessary. The model is reduced considering the practical conditions of the target structure. Then, the algorithm performance to identify the parameters of the reduced model and the hysteresis loop was investigated numerically. UKF-RM results in more robust and stable parameter estimations than the conventional UKF. The effect of neglecting residual displacement due to the high-pass filtering associate with the acceleration integration is investigated; the effect of residual displacement on total energy dissipation is shown small. Except for the energy dissipated by the residual displacement, the hysteresis response obtained with UKF-RM using double-integrated acceleration as observation contains the hysteresis cycles where most of the energy from the input excitation is dissipated by the RC pier. Finally, hysteresis response identification with Bouc-Wen model using only acceleration measurements with UKF-RM algorithm was validated using measurement from the shake table test. The hysteresis estimated from the acceleration signals is shown consistent with the hysteresis directly measured using displacement sensor and load-cells.

Acknowledgments

First and foremost, I would like to express my sincere gratitude to my advisor, Dr. Tomonori Nagayama, for his guidance on my research. His indefatigable attitude towards academic truth committed to excellence deeply influenced me. His patient attitude towards his students committed to openness and transparency always encouraged me. Without his support, both in my academic and non-academic life, this dissertation would have simply not been possible.

I sincerely appreciate the efforts of my committee members Dr. Takeshi Ishihara, Dr. Tsuyoshi Ichimura, Dr. Yoshiaki Okui and Dr. Di Su for their valuable feedback and advice on every step of this dissertation and shaping the story line like puzzle pieces.

Dr. Makato Suzuki, and his research team for their immense effort to realize the prototype wireless sensor which has been used for seismic response measurement on a full scale bridge in this thesis. Without their support and help, the measurement would have not been possible.

Valuable advice from Mr. Yasuyuki Nakamura at Sumitomo Riko is sincerely appreciated during the preparation of this dissertation.

I would like to thank all of the Bridge & Structure laboratory research group members. Dr. Tsukasa Mizutani, Dr. Di Su, Dr. Zhao Byou and Haoqi Wang for providing their valuable comments during my presentation in the group meeting. The support from Dr. Zhao Byou is deeply appreciated in my both academic and non-academic life since I arrived Japan. Without his cherished accompany and friendship the life would be much harder during the PhD. I would like to extend my gratitude one of the former members of our group, Yasutaka Narazaki, for helping me regarding daily issues in Japan and also for sharing his experience and knowledge on especially the E-Defense experiment. Without his support, the progress of this thesis would have been much slower.

I sincerely appreciate the support from Prof. Yozo Fujino and his kind understanding of my academic endeavors. Discussions with him has always been informative and

enlightening.

I would like to extend my gratitude to my former professors who taught me before and has a part in my decision towards become an academician. To Dr. Barlas Ozden Caglayan, who advised me during my Bachelor and Master theses. Discussions with him has always been stimulating. His support in my academic and non-academic life is indispensable. To Dr. Hasan Boduroglu and Dr. Billie F. Spencer Jr., who introduced and taught me structural dynamics, which became the focus of my academic life. Without the solid foundation provided by them this thesis would have not been possible. To Dr. Zeki Hasgur for introducing me to earthquake engineering during my undergraduate studies. His support on my academic quests is deeply appreciated.

This study could not have been conducted without the generous scholarship granted by Japanese Ministry of Education, Culture, Sports, Science and Technology (MEXT). This work was partially supported by Council for Science, Technology and Innovation, "Cross-ministerial Strategic Innovation Promotion Program (SIP), Infrastructure Maintenance, Renovation, and Management". (funding agency: JST). These supports are gratefully appreciated.

I'm sincerely appreciative of the support of my friends in Turkey throughout mu life. I'm thankful to them for listening my complaints, sharing stimulating ideas and dreams and making me laugh when I most needed. I would like to extend my gratitude to Dr. Ohnishi Akiko and Dr. Aykut Pamuk for providing motivation and support during the course of my dissertation. Without their involvement in my life, the tough times during my studies would have been much harder.

Finally and most importantly, I would like to thank my parents, my brother and sister, and my grandparents for their love, support, and understanding, not only in the course of my Ph.D. studies, but throughout my entire life. I'm indebted to them for providing me a loving, stimulating and democratic environment while I was growing up. I'm very thankful for their support on my education throughout my life. This dissertation is dedicated to my family.

To my family

Contents

List of Figures

List of Tables

Chapter 1

Introduction

Civil infrastructure is often referred "lifeline systems" which consist of power and water supply facilities, transportation structures, and telecommunication lines. Among lifeline systems, bridges are vital links which provide accessibility to society. Thus, bridges are expected to continue service during and after natural disasters such as earthquakes. Hence performance evaluation and maintenance of bridges hold importance so that serviceability conditions are met in times of extreme events.

Maintenance of civil infrastructure in practice has been a long-sought problem, yet an unresolved issue. Although there are methodologies proposed by many researchers there are problems preventing maintenance to be realized in a practice effectively. The fundamental problem is the difficulties encountered during the decision-making process, which requires condition assessment of an existing structure. Here, the "condition" term refers to the physical state of characteristic structural parameters such as mass, stiffness, damping. If the current status of structural parameters can be identified, the degree of change in condition can be assessed by comparison to the structure's initial design. Consequently, decisions towards maintenance can be taken in a quantitative manner.

Structural condition assessment for civil infrastructure, however, often not straightforward. From a general point of, first and foremost reason is the abundance of infrastructure in especially industrialized countries. For example, there are more than 150.000 bridges (>15 m) in Japan [4] and monitoring all structures is not practical.

Thus, some representative regular bridges, important links on highway bridges and signature bridges can be selected for condition assessment.

Secondly, condition assessment can be achieved by estimating structural parameters with system identification using measured response data. However, lifelines such as bridges are usually large structures with many elements are in complex interaction with each other. In laboratory conditions, exciting a full-scale bridge with its all components (i.e. foundation) is also not practical. In order to achieve successful identification on existing bridges, dense and quality measurements are needed which are usually not available except some signature bridges especially in the case of seismic events. Thus, sensors without the need for external power which are capable of measurements with a low average noise level for a sufficient time are needed to allow system identification in practice.

Furthermore, Japan is a highly earthquake-prone country and thus both small and big earthquakes occur very often. However, by instrumenting the selected bridges with proper sensors, with a careful consideration of measurement planning, advantage can be taken from the natural hazards which provide full-scale experiment chance.

On the other hand, selection of the feature to be extracted from the gathered data should be determined before measurement. Stiffness is usually considered as the most desired feature type among structural parameters since it directly relates to the remaining capacity of the element, especially when seismic excitation is considered. Usually, accelerometers are the most practical sensor type to carry out measurements in practice because often measuring displacement or force is not possible. Thus, the feasibility of identifying stiffness with only acceleration measurements should be investigated.

Furthermore, exploiting target features of dynamic systems successfully does not only depend on the input/output couple, but also the system description [5]. System description includes the structure, algorithm, and uncertainties in the model. For example, the selected algorithm should be capable of handling possible nonlinear behavior when seismic induced vibration is considered. Moreover, often environmental conditions or model errors are not known a-priori in the case of structural dynamics

applications in the real world. Thus, algorithms should also be adapt themselves to various noise and model errors in practical applications. Moreover, algorithms should achieve convergence fast because earthquake excitation exert energy to systems in a short amount of time where stiffness change occurs.

Thus, collaborative thinking from structural health monitoring and system identification fields is a beneficial approach to the parameter estimation problem when dealing with stiffness identification of the lateral resisting components of bridges under seismic loads.

1.1 Summary Review of Condition Assessment Methods

System identification techniques are either carried out in frequency (and modal) or time domains. Although existing literature [6, 7] mostly focuses on the modal and frequency domain based techniques, there are several problems with these approaches need addressing to improve system identification applications in practice.

One of the problems is that data (e.g. acceleration, strain, etc.) is recorded in the time domain and when converting it to frequency or further to modal domain there may be information loss. Information loss when converting time to the frequency domain is small when the system is linear [8]. However, in reality, civil structures usually exhibit nonlinear behavior, especially under earthquake excitation. Secondly, frequency and modal domain methods provide an indirect estimation of parameters such as mode shapes which are in fact functions of physical parameters, i.e. stiffness. Although such methods have been previously successfully applied to practical cases in civil engineering they are usually limited to signature bridges [9].

Moreover, when frequency domain methods are adopted, conversion of estimation from frequency to physical domain is needed to obtain stiffness. However, this conversion process often requires empirical information and is prone to errors. On the other hand, modal and frequency information is considered as global structural

parameters so that local phenomenon such as stiffness change of an element cannot be observed with such methods. The lower frequencies are usually associated with global modes and not sensitive to changes in the properties of structural elements in the large systems such as civil infrastructure.

On the other hand, time-domain methods eliminate the need for conversion between domains, because the measured data is in the same domain with the estimation algorithm. Methods such as Least-squares based time domain methods were successfully applied to significant bridges in practice under earthquake excitation [10]. However, such methods are also limited to the linear response. Furthermore, data assimilation methods such as Kalman filters allow integration of model and measurement and direct physical parameter estimation. In addition, Kalman filter [11] is known to be robust to noise contaminated data under the assumption both process and measurement noise are known a-priori.

However, parameter identification problems are often nonlinear. For example, the joint state and parameter estimation problem itself is nonlinear even though the system is linear. Thus, various extensions of Kalman filter has been developed, namely extended Kalman filter (EKF) and unscented Kalman filter (UKF) which are capable of handling different levels of nonlinearity in the system. However, studies which dealt with direct physical parameter estimation methods in structural system identification literature considered using simulated response and added artificial noise with a limited attempt of practical application.

For instance, structural system identification using Extended Kalman filter (EKF) were studied with simulated data and known damage scenarios [12, 13, 14, 15, 16]. However, structural identification on a realistic structure using EKF has not been attempted until 2008 [17]. Similarly, although many studies demonstrated advantages of the use of UKF in structural engineering related problems considering high nonlinearity [18, 19, 20], structural identification on a realistic structure using UKF has not been attempted yet.

In addition, structural system identification inevitably deals with highly nonlinear systems. In structures non-linear response is mainly due to energy dissipation in

joints [21], structural elements such as reinforced concrete columns [22, 23], and also mounted damping devices [24] which are usually characterized by hysteresis response. The studies addressed UKF use in structural identification [18, 19, 20] often employs Bouc-Wen model [25, 26] which is one of the most well-studied hysteresis models. However, aforementioned studies explored the capabilities of UKF by implementing known damage scenarios and using simulated data. Thus, experimental verification of such a parametric identification tool yet remains an open area.

Recent studies in the literature which consider the application of data assimilation methods to nonlinear structural parameter identification on realistic structures is as follows. A scaled three-bent bridge was excited by one-directional earthquake input on a shake-table in [17]. First, an FEM model was calibrated based on the experiment results which was later used in extended Kalman filter as state transition matrix. Elemental residual stiffness values of each bent were estimated using EKF.

In another study using simulated response measurements [19] structural parameters of a 3DOF system which consists of a Bouc-Wen element in the first DOF were estimated using GPS displacement for the first DOF observation and acceleration measurements for the other two DOFs' observations. Later in [27], systems including Bouc-Wen elements were further investigated from the observability and identifiability point of view as Bouc-Wen element consists of many parameters.

Recently, [28] proposed a method for online Bayesian model assessment for UKF. However, process noise parameters are assumed as known which is not a real condition when practical structures are considered. Verification examples were presented with simulations and then a laboratory experiment on a test apparatus which was designed to simulate a 2DOF non-conservative dissipative joint element as presented in [29].

1.2 Motivation and Objectives

There are many proposed system identification methods for stiffness condition assessment of bridges, both in frequency and time domains. However, application of such methods has been limited to some signature bridges where sensor networks are

readily available in practice. In addition, frequency domain methods are limited to linear response and direct physical parameter estimation is not possible. On the other hand, data assimilation methods, which are capable of handling non-linear motion, have never been used to estimate stiffness condition of a full-scale civil infrastructure.

The common problem for system identification methods is that their application to the real world is still limited, especially when the seismic response is considered. There are two main reasons for this limitation. First is the lack of adequate response measurements from full-scale structures during earthquakes. Second is the lack of robust algorithms which can adapt themselves to unknown initial conditions and noise, especially for highly nonlinear and time-variant systems.

First motivation of this study is; by taking advantage of the seismic hazards in Japan, studying the feasibility of seismic response measurement on a full-scale bridge using only wireless accelerometers. Bridge structures are usually large and complex systems which require dense sensor arrays to achieve system identification. Thus, considering only accelerometer measurements is important as they are the most economically viable option for application of system identification methods to the real world. Moreover, using obtained accelerometer measurements, the feasibility of obtaining stiffness condition change should be investigated.

Secondly, although under small excitation the structure is in the linear range, as both parameters and states are unknown in the system, estimation problem becomes inherently nonlinear. In addition, when structures excited with large enough earthquakes they exhibit nonlinear behavior in terms of damage, such as cracking, yielding. Implementation of a robust algorithm which can deal with high nonlinearity in the system under unknown initial conditions and various noise is needed. Although many algorithms were proposed, their performance investigation has been done using various different models and input/output couples. Using publicly available data from 1:1 scale structural experiments, verification of the performance of the proposed methods both under small and large earthquake excitation is needed.

Thirdly, in earthquake-prone countries, i.e Japan, both small and big earthquakes occur very often. After verification of the proposed algorithm through laboratory

experiments, the validation of the adopted stiffness parameter estimation algorithm and its performance using responses of full-scale bridges under both small and big earthquakes should be studied.

Small earthquakes can be grouped in two categories:

1. Single events, usually having small return period

2. After- and fore-shocks which occur in abundant numbers after and before large earthquakes.

Small earthquakes can be used to estimate the stiffness condition of lateral resisting systems especially in earthquake-prone countries such as Japan. Although they only induce linear response the benefits may have two folds. First is, if the bridge only experienced small earthquake however stiffness estimation of a structural element deviates from the design assumption it may be an indicator of some deficiencies (e.g. manufacturing/construction faults, etc.) which may be present of the bridge starting from the construction. Using response measurement from frequent small earthquakes the current stiffness condition of the element can be assessed. If the estimation indicates any deficiency, corresponding measures can be taken to prevent failure/undesired response during big earthquakes. Secondly, large seismic events are usually followed by many smaller aftershocks. Using such ground excitation and response measurements on the full-scale bridge, information on the post-seismic stiffness capacity of the lateral resisting systems can be obtained which would help making decisions towards inspection, maintenance in the aftermath.

Lastly, although estimated linear stiffness, either initial or residual, provides valuable information on the structure's behavior, under large seismic excitation damage is related to the energy dissipation of the elements. Thus, to have a complete understanding of the stiffness change hysteresis loops needs to be identified. Consequently, capabilities of the proposed system identification algorithm also need to be investigated under extreme seismic events using input and output response acceleration measurements.

The objectives of this thesis are as follows. 1) Preparation of seismic response measurement data to be utilized in the stiffness condition assessment of full-scale bridges 2) Proposal of a robust stiffness condition estimation algorithm 3) Verification and validation of the proposed algorithm through full-scale laboratory experiments and field measurements using only accelerometers 4) Extension of the proposed algorithm to hysteresis loop estimation of structural elements non-linear motion.

1.3 Outline of Thesis

This research focuses on the realization of a system identification method on full-scale bridge or bridge components by implementing an adaptive rule with Unscented Kalman Filter. Specifically, stiffness condition assessment has been performed for two different lateral resisting systems, namely; a reinforced concrete (RC) bridge column and elastomeric rubber bearings under several levels of input excitation.

Chapter 2 provides information on the response measurements which are used to verify and investigate the performance of the proposed stiffness estimation algorithm. First, the test set up of a 3D shake-table test for a full-scale RC bridge pier is reviewed. Then, measured input and response data and behavior of the test specimen during different shaking levels are explained. Moreover, a displacement estimation methodology and its verification studies are presented. In the second section of this chapter, a field measurement partially conducted by the author on two full-scale bridges, description of test bridges and seismic monitoring system are provided. Moreover, characteristics of the measured data with prototype wireless accelerometers investigated in detail in terms of time-history, response spectra. Lastly, displacement trajectories and bearing behavior characteristics are presented.

Chapter 3 first describes the theoretical background on the conventional UKF. Then, the use of the Robbins-Monro stochastic approximation scheme with UKF (UKF-RM) has been proposed to address robustness issues by adapting noise covariances. Lastly, a simulation of an SDOF dynamic system considering a linear model has been simulated. Performance of conventional UKF and UKF-RM methods is

compared with an ideal case in which the noise covariances are manually fine-tuned.

Chapter 4 using a linear SDOF model, the performance of UKF-RM and conventional UKF is further investigated considering their sensitivity to change in initial state vector selection (model error), initial process noise covariance, initial measurement noise covariance with various levels of measurement noise, initial error noise covariance and selection of Robbins-Monro parameters, α_Q, and α_R.

Chapter 5 describes experimental verification of the implemented algorithm. In the first section, the shake-table test was used and validation has been confirmed under both small and large earthquake response. Trackability and convergence rate, estimation results in three different response ranges, namely; initial, nonlinear and residual, are discussed based on the findings from the experiment. In the second section, the applicability of the proposed system identification algorithm on a full-scale bridge is shown by experimental verification using data obtained after Kumamoto earthquake.

Chapter 6 first presents the theory for a hysteretic model. Observability analysis and model reduction procedure are explained. Next, the applicability of the proposed algorithm to a highly nonlinear SDOF system which consists of a Bouc-Wen element is shown. Verification of the estimated parameters using only acceleration measurements and simulated response data has been presented. Furthermore, using the nonlinear SDOF model, the performance of UKF-RM is further investigated considering their sensitivity to change in initial state vector selection (model error), initial process noise covariance, initial measurement noise covariance with various levels of measurement noise, initial error noise covariance and selection of Robbins-Monro parameters, α_Q and α_R. Moreover, experimental verification of the hysteresis parameter estimation is described. Using a shake-table laboratory test data on a single reinforced-concrete bridge pier the application of the proposed method to a full-scale structural element in laboratory conditions has been confirmed by identification of the hysteresis parameters with an SDOF system.

Chapter 2

Measurement

In this chapter, two experiments on lateral resisting system components of bridges and collected seismic response data are explained in detail. Obtained data sets are later used to assess stiffness condition of various bridge lateral resisting systems in the subsequent chapters of this thesis.

First, a laboratory experiment which was conducted on a full-scale reinforced concrete (RC) bridge pier in a shake-table facility is presented. Data set consists seismic response data measured with various types of instruments deployed as dense arrays on RC pier under both small and large excitation levels. Both measured data and the experiment report is open to public [1] which made validation of the proposed stiffness estimation methodology and investigation of its performance on a realistic bridge component possible.

Secondly, a field experiment on a full-scale single span bridge which was conducted by the author is explained in terms of the structural properties of the target bridge, instrumentation and collected seismic response data from aftershocks of a large earthquake. Considering the fact that real-world seismic response measurements had been mostly limited to long-span bridges, gathered high-quality data holds importance as it allows validation of the proposed parameter estimation algorithm on a full-scale bridge using a sensor array that is practical and cost-effective.

2.1 Laboratory Experiment

The performance of the proposed stiffness condition assessment method is first investigated using data obtained from a full-scale bridge pier shake table experiment, conducted in E-Defense facility, provided by National Research Institute for Earth Science and Disaster Prevention [1]. E-Defense shake-table facility was constructed after 1995 Kobe Earthquake to provide open access benchmark experiment data on real scale structures (so that data does not include scaling effects which are inherent in small-scale specimens) to scientific community and thus pave the way to better understanding of structures' behavior and collapse mechanisms before another large and devastating earthquake occurs [30]. With this purpose, a series of tests were conducted on real scale reinforced concrete bridge piers which were designed based on both before and after 1995 Kobe Earthquake seismic design criteria to understand the collapse mechanisms. In this section specifications of one part of this experiment and obtained data will be presented. Using various level of ground motions the bridge pier excited with small and large inputs and detailed response measurements were recorded using a dense array of various kinds of sensors including accelerometers, velocimeters, displacement and strain gauges, and load cells. Design details of the RC pier, sensor array and recorded measurements are presented as follows.

2.1.1 Description of Test Bridge Pier

Component test outlined in this section was conducted on a RC bridge pier which was designed based on 1964 Japanese bridge design code [31]. The RC pier behaves as a typical flexural failure dominant column. The set of specimen tests were called C1-1 experiments [1]. C1-1 column design was based on working stress design under an equivalent static lateral load and were representative of columns constructed in 1970s in Japan. The column was mounted on the shake table with its deck and weights to represent the inertia force from the superstructure (Fig. 2-1). The test configuration also consists a steel catch frame to prevent the column collapsing in case it experiences excessive damage (Fig. 2-2). Arrangement of reinforcement in C1-1

Figure 2-1: C1-1 Experiment setup on E-Defense shake table [1]

column cross section is given in Fig. (2-3). Design conditions, including cross-section dimensions, weights and material properties, are given in Table (2.1).

The girder was not designed to obey strength and stiffness of a real deck but to provide support to the mass blocks on top which represented the superstructure inertia effect. Girders were connected to the bent cap with fix bearings where they were connected to the end supports with movable bearings. Fig (2-4) depicts the bearings conditions of the test specimen. The friction bearings (sliders) on both sides of the fixed bearing on the column end were designed so that the rotation of the decks around their own axis was prevented. Sliders on the end supports were designed to prevent the deck rotation more than 10 degrees. More detailed explanations on the support conditions and their experience can be found in [1, 30]. The design basis of the support conditions were to avoid interference of the torsional rigidity of the deck on the displacement of the pier.

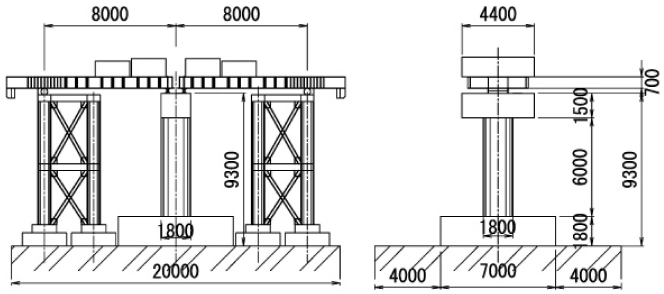

(a) Support System

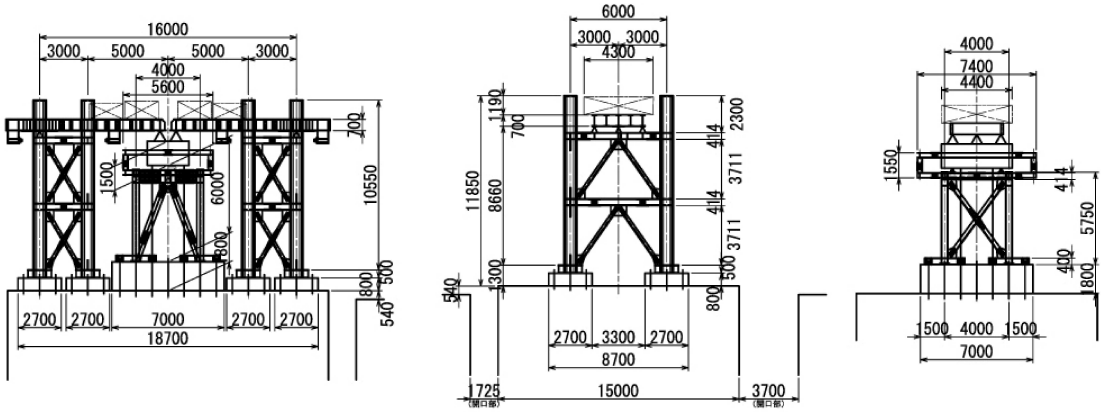

(b) Support and Catch Systems

Figure 2-2: C1-1 Experiment support and catch system [2]

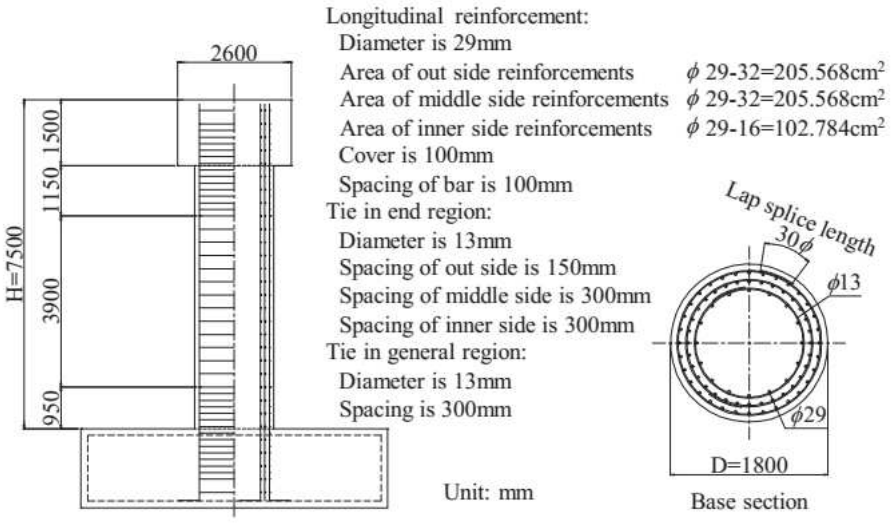

Figure 2-3: C1-1 column - Arrangement of reinforcements in cross section [1]

Table 2.1: C1-1 column - Summary of design conditions (modified from [1])

Item			Value
Pier Height, H			$7.5m$
Section shape of pier			Circular
Diameter of cross section, D			$1.8m$
Reaction Force (dead load), R_D			$2080kN$
Weight	Superstructure	Longitudinal, W_U^{LG}	$2960kN$
		Transverse, W_U^{TR}	$2080kN$
Weight	Pier, W_P		$794.5kN$
Material strength	Concrete, σ_{ck}		$27N/mm^2$
	Yield strength of reinforcement, σ_{sy}		$345N/mm^2$
Modulus of elasticity	Concrete, E_c		$2.65x10^4N/mm^2$
	Reinforcement, E_s		$2.0x10^5N/mm^2$

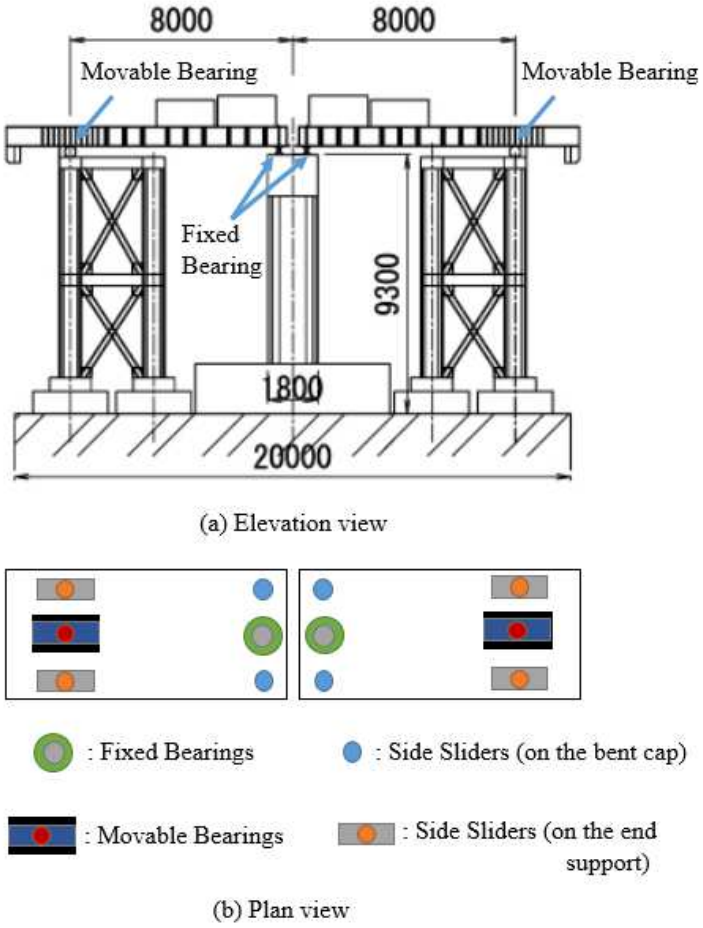

Figure 2-4: C1-1 column - Bearing conditions (modified from [1])

2.1.2 Description of Monitoring System

In total, 191 channels of acceleration, 32 channels of load, 256 channels of strain, 116 channels of displacement and 18 channels of velocity measurements were obtained at various locations on the shaking table, the pier and the superstructure. From which the acceleration measurements on the shake-table and column-top locations were used in this study to investigate the performance of the proposed parameter estimation algorithm. In addition, displacement measurements on top of the bent cap were used to investigate the accuracy of displacement estimation scheme from corresponding acceleration measurements by double-integration. Above mentioned displacement estimation scheme will be explained in the next section in detail.

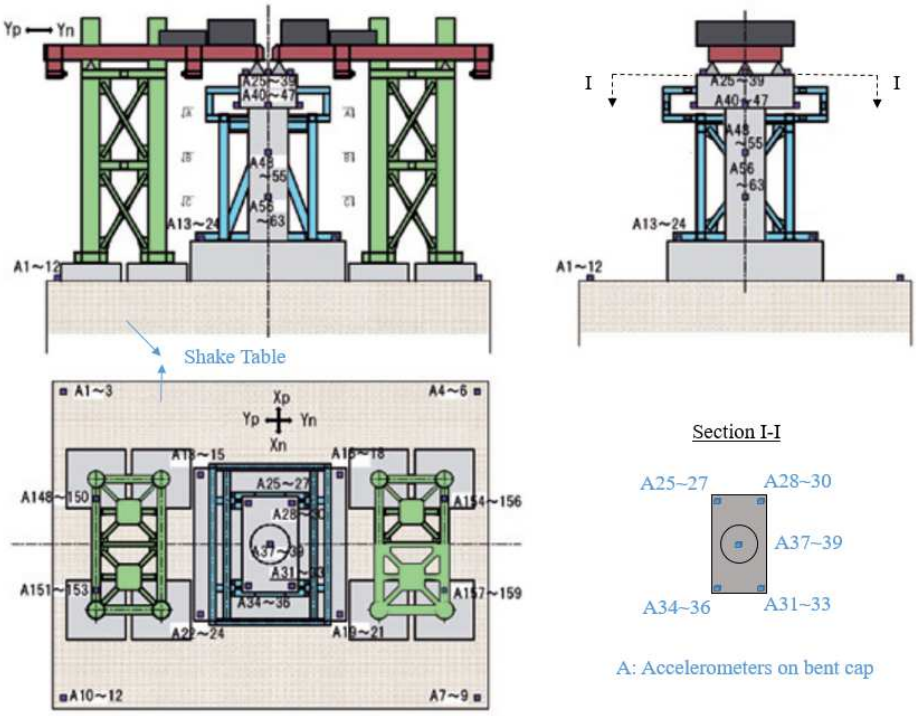

Figure 2-5: C1-1 column - Accelerometer measurement locations on the shake table and bent cap (modified [1])

Fig. (2-5) shows the a summary of the accelerometer locations. All accelerometers are TA-25E-10-1 (wired) from the manufacturer Tokyo KEIKI. Accelerometers on shake-table, A1-12, are used as input to the system after averaging in each direction in the subsequent sections in this study. Output acceleration response measurements

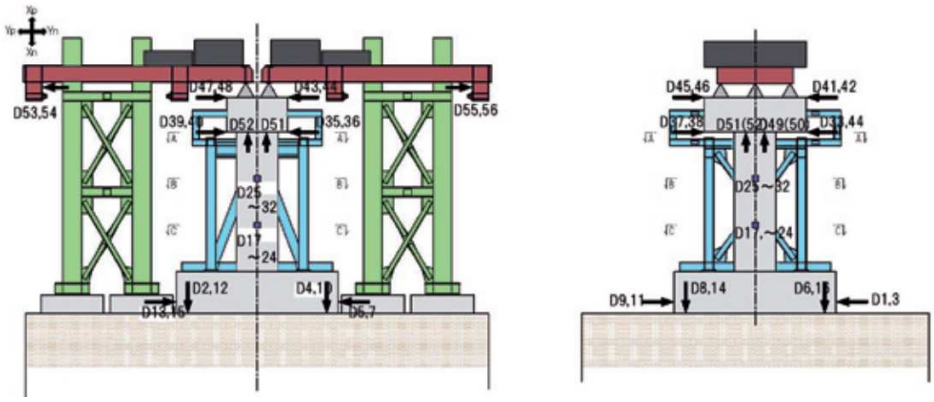

Figure 2-6: C1-1 column - Displacement measurement locations on the bent cap [1]

at the column top locations, A25-33, are treated as the only measurements available during laboratory validation of the proposed stiffness estimation methodology. In this study, the accelerometer measurements from the nodes A1-12 and A25-36 are averaged in each direction to obtain input and observation accelerations, respectively.

In addition, displacement measurements (Fig. 2-6) on the bent cap (D33-48) which correspond to accelerometer locations are also available. The displacement measurements were collected by DP-2000DS wired displacement transducers from the manufacturer Tokyo Sokki which has a range of $\pm 1000mm$. In this study, the displacement measurements from the nodes D33-48 are first corrected based on the information provided in the experiment report [1] and then averaged in each direction.

Lastly, P05-4226 type load cells from Kyowa Electronic Instruments Co., Ltd. were used to measure force under earthquake excitation. There are 32 load cells in total and their locations are depicted in Fig. (2-7). The capacity of load cells are $250kN$ in transverse (X and Y) and $400kN$ in vertical (Z) directions. In this study, the force measurements from all load cells are summed to find the force in the later parts of this thesis.

2.1.3 Input and Measured Response Data

Excitation types consist of random excitations, pulse excitations and earthquake excitations measured at Takatori station during the Kobe earthquake in 1995. Random

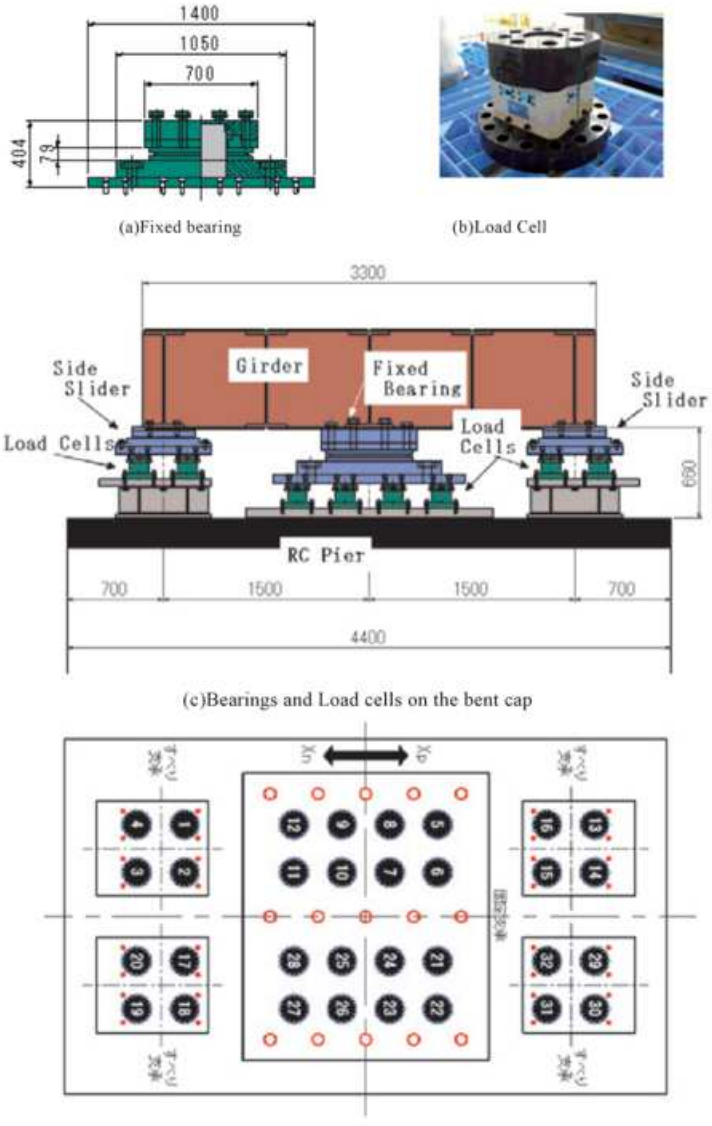

Figure 2-7: C1-1 column - Loadcell locations on the bent cap (modified [1])

excitations were applied in order to identify the dynamic characteristics of the whole system including both the test structure and the shaking table. The Takatori excitation was exerted on the RC column with various magnification factors.

Table 2.2: Example excitation data sets used in C1-1 experiment

ID	Excitation type	Excitation level
2007-1206-009-1M	Pulse(XYZ)	100gal
2007-1206-010-1M	Takatori	10%
2007-1206-011-1M	Pulse(XYZ)	100gal
2007-1206-012-1M	Takatori	20%
2007-1206-013-1M	Pulse(XYZ)	100gal
2007-1206-014-1M	Pulse(XYZ)	100gal
2007-1206-015-1M	Takatori	20%
2007-1206-016-1M	Pulse(XYZ)	100gal
2007-1212-006-1M	Takatori(Modified)	30%
2007-1213-003-1M	Pulse(XYZ)	100gal
2007-1213-004-1M	Takatori(Modified)	100%
2007-1213-013-1M	Pulse(XYZ)	100gal
2007-1213-014-1M	Takatori(Modified)	100%
2007-1213-015-1M	Pulse(XYZ)	100gal

Table 2.3: Publicly available data sets from the excitation used in C1-1 experiment

ID	Excitation type	Excitation level
2007-1212-006-1M	Takatori(Modified)	30%
2007-1213-004-1M	Takatori(Modified)	100%
2007-1213-014-1M	Takatori(Modified)	100%

In some cases, the input signals to the shaking table system were modified to eliminate the effect of the test structure on the dynamic behavior of the shaking table. 14 datasets presented in Table 2.2 show example excitation during experiment. It should be noted that the amplitude of the original Takatori excitation was reduced to 80% of its original level at the beginning of the experiment considering the interaction between structures and the ground generally observed in real structures. The magnification factors listed in the Table 2.2 are applied to this scaled down Takatori excitation. Between the magnified Takatori excitations, the structural properties of

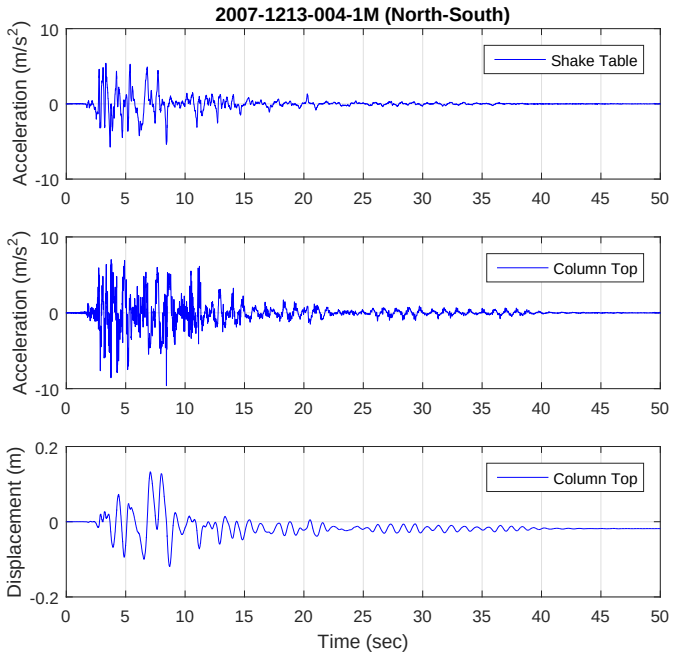

Figure 2-8: Measured shake table input and column top response for 2007-1213-004-1M (North-South direction)

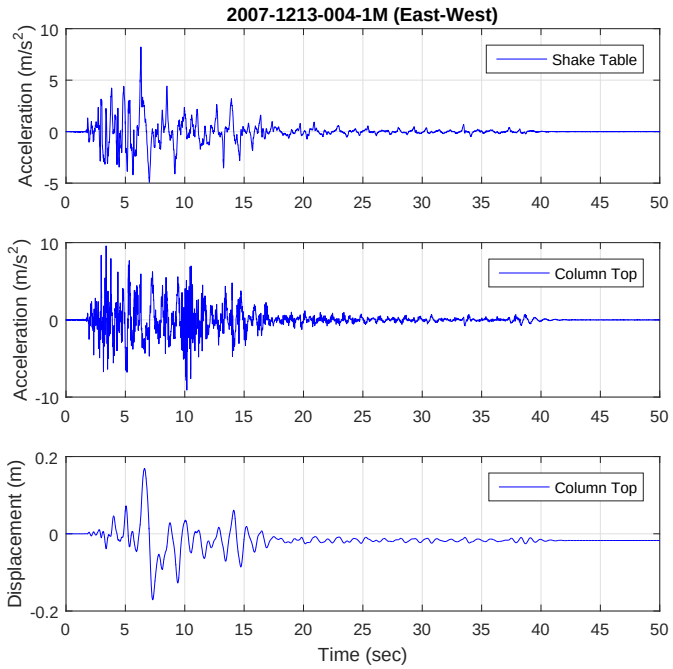

Figure 2-9: Measured shake table input and column top response for 2007-1213-004-1M (East-West direction)

the RC column were tested by $10Hz$ sinusoidal excitations. Among the representative excitation data, publicly available ones which are presented in Table 2.3 are used for the validation of the proposed method in this study. Publicly available data allow performance investigation of the parameter estimation algorithm both in linear and nonlinear response ranges which will be explained in future chapters in detail. Example acceleration time-history for $2007-1213-004-1M$ input are depicted in Figures (2-8) and (2-9) for North-South and East-West directions, respectively.

To understand the ground motion, some characteristics need to be defined. One of the ground motion charateristics is peak ground value of one of the three time histories namely; acceleration, velocity and displacement. Peak ground acceleration (PGA) is one of the most widely used parameter. PGA is $5.78m/s^2$ and $8.22m/s^2$ for the $2007-1213-004-1M$ input in North-South and East-West directions, respectively. PGAs for the remaining inputs can be easily calculated based on the magnification factors. However, only PGA (or PGV) is not solely sufficient to represent the characteristic of the ground motion. The frequency content and also the duration need to be examined [32]. In E-Defense experiment only one input was used to excite the RC pier with different magnification factors, thus the dominant frequency range and duration is same for all earthquake inputs. However, it is beneficial to give the duration definition which is used in this study as one of the criteria to judge the convergence rate performance of the parameter estimation algorithm in the successive chapters.

There are many duration definitions in literature, however current duration definitions can be grouped into four categories [33]. These are; bracketed duration, uniform duration, significant duration and structural response duration. Summary of studies which proposed a definition for duration can be found in [32]. In this study significant duration has been chosen to define the duration of the earthquake, in which the energy transmission from input to the structure is identified.

Significant duration is the time interval in which a portion of the energy is accumulated. The integral of the squared ground motion acceleration or velocity can be chosen as the representative of the energy. When acceleration is used the integral is related to the Arias Intensity [34] which is given by the equation below:

$$I_A = \pi/2g \int_0^T a^2(t)dt \tag{2.1}$$

where, g is the acceleration of gravity, $a(t)$ is the acceleration time history, and T represents the complete duration of $a(t)$.

Then, the accumulated energy over time is tracked by the Husid plot [35] where it is normalized value for I_A. Two intervals which are commonly accepted in literature are the intervals between $5-95\%$ and $5-75\%$ of I_A [33, 36]. In this study $5-95\%$ of I_A is adopted for the significant duration definition. Fig. (2-10) depicts the input shake table acceleration for 2007-1213-004-1M (North-South direction) and it's corresponding Husid plot. In this figure, the first and second vertical red lines represent the beginning, D_{a5}, and end ,D_{a95}, of the significant duration which are equal to $2.855sec$ and $12.81sec$, respectively.

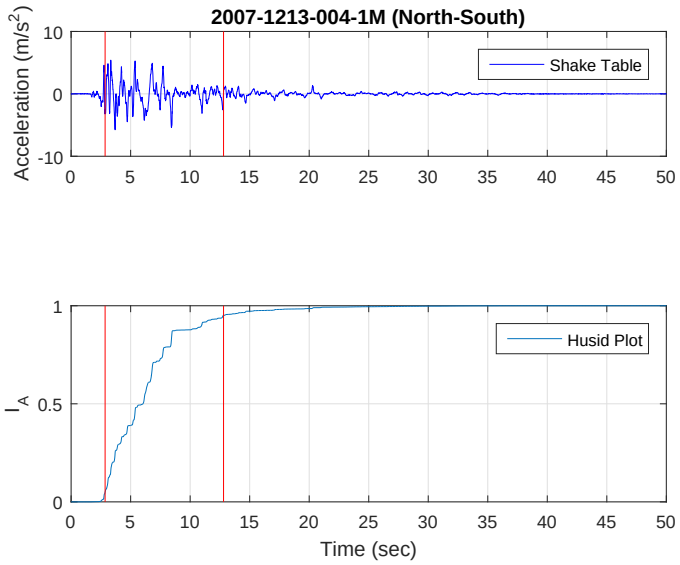

Figure 2-10: Evaluation of significant duration for 2007-1213-004-1M (North-South direction)

2.1.4 Displacement estimation from acceleration measurement

Displacement measurement is often more expensive than acceleration measurements and is not always feasible due to a lack of reference point. In addition, simultaneous

response data from many nodes is easier with accelerometers when compared to other kinds of sensors, such as displacement transducers. Thus, displacement estimation using acceleration has been an interest. Moreover, in terms of system identification displacement measurement is often preferred as it closely relates to structural parameters such as stiffness.

While many researchers suggested effective yet complicated solutions to this problem, simple and effective methods are also readily available to obtain displacement from acceleration measurements by double-integration. The current consensus on this approach in structural dynamics area usually adopts only a high-pass filter (either in time or frequency domain) and then double integrates the acceleration to obtain displacement. However, preparation of data with appropriate pre-processing steps prior to filtering, selection of cut-off frequency and application of the filter to the data are also important parameters which needs attention. In engineering seismology area, references such as ([37],[38]) present necessary steps for pre-processing targeting both low and high frequency noise inherent in any kind of measurement. These suggestions will be reviewed in this chapter briefly and then displacement estimation results will be validated by comparison with the measured displacements during E-Defense test.

In any case, measured data will be contaminated by noise. The causes of these noise in the records is not only from one source but often from multiple sources. For example, analog to digital conversion [39], inherent analog or digital sensor noise, environmental noise, DC offset, effect of resolution (sampling rate) and unknown initial conditions can be listed as some the error sources. Although basic understanding of each source is necessary, quantification of errors is not considered realistic. However, effects of noise are very distinct on the data and often reveals itself as distortion of the obtained parameter. For instance, both integration and differentiation alters the frequency characteristics of the data due to information loss. Integration causes low-frequency noise accumulation while differentiation causes high-frequency noise accumulation. However, for specific engineering applications appropriate pre-processing steps can be applied to obtain the information which is needed, such as displacement from acceleration or vice versa with some limitations.

The suggestions given by references [37],[38] are followed to understand the source of the errors which cause erroneous displacement estimation due to integration. In order to avoid distortion of obtained displacement history, several pre-processing steps such as analysis of the noise levels, selection of cut-off frequency and selection filtering procedure/order are briefly discussed.

Removal of nonstandard noise

One of the examples to nonstandard noise is given in [37], spurious spikes which may be present in the data and can be identified by calculating the differentiation of acceleration (jerk). Once they are identified, it is recommended to remove these spikes with the mean of the acceleration measurement.

Second type of non-standard noise is the baseline shifts which may be present in the measurement. Such shifts in acceleration can be identified from the velocity and once identified, the baseline correction can be applied to acceleration data.

Selection of cut-off frequency

The key issue is to select the the cut-off frequency for the high-pass filter which ensures an appropriate signal-to-noise ratio for the rest of the data. Three suggestions for the criteria to decide a cut-off frequency were given by [37] as follows:

- Comparison of Fourier amplitude spectrum of the record with the instrument noise or a portion of the data before the earthquake for digital records so that the frequency where a ratio of 3 for signal-to-noise ratio can be identified.

- Second criteria is based on a seismological theory where the decay in long-period portion of FAS is assumed to obey to the line provided by f^2. Because except the residual displacement, the long-period motion of earthquake is pulse-like and hence the FAS will be finite at zero. This assumption in fact similar to structures which are excited by ground motion which will be shown later in this chapter.

- Lastly, the visual inspection of calculated displacement and velocity and judging whether there are any unreasonable portion is present.

Choice of high-pass (low-cut) filtering technique

Either in frequency or in time-domain, the choice of filter domain should not be present in the filtered signal as long as the frequency response of filters are same. In addition, although there may be minor differences in filter types such as Bessel, Butterworth or any other, these should not result in drastic changes between the filtered signals as long as the adopted filter is applied correctly.

More importantly, whether a filter is applied in a causal or acausal way is more important. Causal filters are known to cause phase shifts where acausal filter results in zero phase shift. The way to achieve an acausal filter applying the filter from start to end, and then applying it reverse in the opposite direction starting from the end in time domain. However, in order a filter to act as acausal the beginning and ends of the data must be added with zero points so that the filter can start acting before the actual data starts. This addition of zero values is called zero-padding and the length of the pads required before and after the data depends on the filter order and the cut-off frequency. The total duration of the zero-pad, T_{zpad}, is given by [40]

$$T_{zpad} = 1.5n/f_c \tag{2.2}$$

where is n is the filter order of Butterworth filter and f_c is the filter cut-off frequency. Half of this duration is added to the front and remaining half is added to the back of the data. Another issue when applying zero pads is to avoid abrupt changes in data when passing to zero values. This can be achieved either applying zeros starting from the first zero crossing or tapering. Further examples and details of the results of causal and acausal filters can be further found in [37]. Selection of filter order can be done by fitting a line to the velocity which is obtained by integration of the unfiltered and unprocessed acceleration.

Example displacement estimation procedure

Fourier amplitude spectra for $2007-1213-004-1M$ (North-South direction) is depicted in Fig. (2-11). Due to the lack of noise study for the measurement sensor, or an undisturbed potion of the recorded data, the cut-off frequency selection is first made by judging the FAS plot of the record. In the figure, the red line shows the f^2 line. The decay of the acceleration in the long-period portion is actually slightly faster (slope is steeper) than the f^2 line and it continues to decay until $0.16Hz$. Thus, $0.2Hz$ is selected for the cut-off frequency.

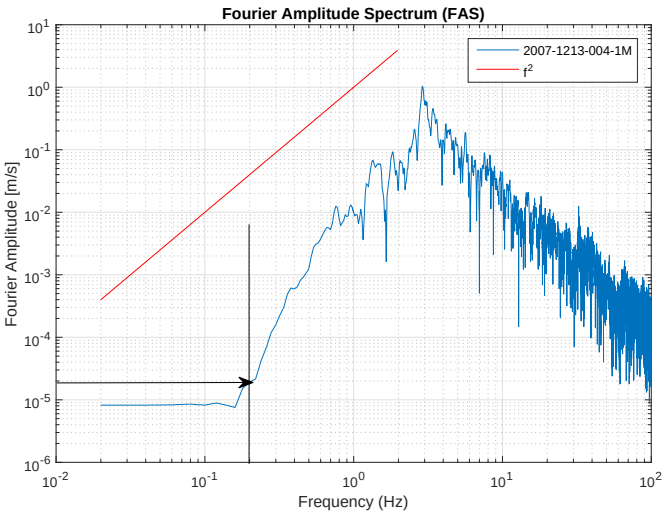

Figure 2-11: Fourier amplitude spectra for 2007-1213-004-1M (North-South direction)

Judging from Fig. (2-12), velocity obtained by integration of the unprocessed and unfiltered acceleration does not exhibit a trend except a slight linear trend. Thus, filter order, n, is chosen equal to 2.

Then following the procedures explained above, displacement estimation from double-integration of acceleration is obtained. Comparison between the estimated displacement and the measured displacement is depicted in Fig. (2-13). The figure shows good match between the peak displacements until the residual displacement occurs. However, wave forms and magnitude of displacement also matches after the residual displacement. Due to the application of high-pass filter recovery of residual displacement is not possible. However, for the purposed of this study the elimination

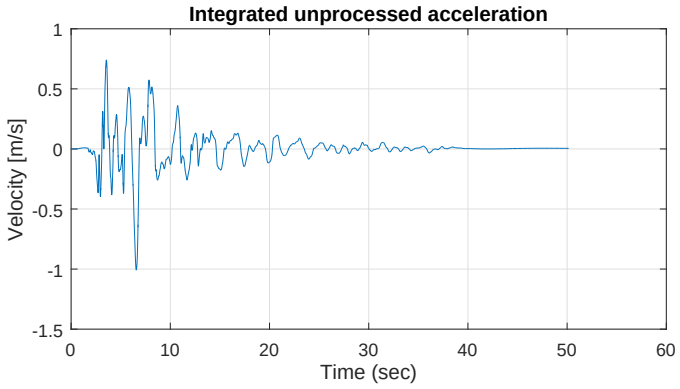

Figure 2-12: Velocity estimation with unprocessed acceleration from 2007-1213-004-1M (North-South direction)

of the residual displacement is considered acceptable.

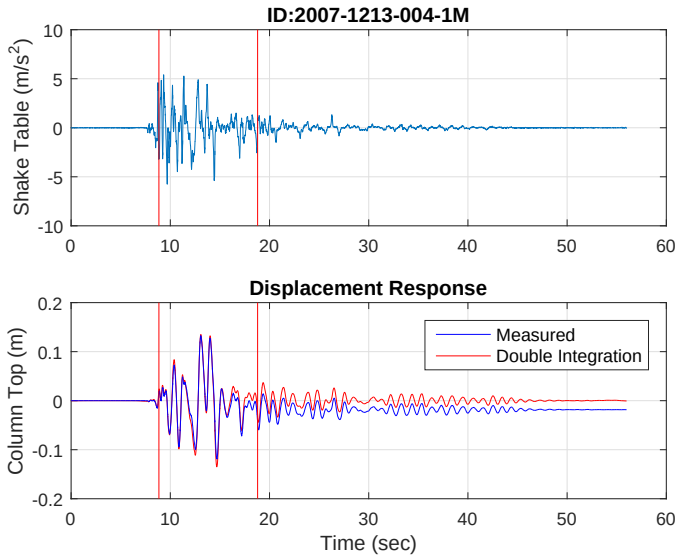

Figure 2-13: Displacement Estimation and measured displacement comparison for 2007-1213-004-1M (North-South direction)

2.2 Field Measurement

In this section in-situ seismic response measurement on two bridges which were partially conducted by the author is explained in detail.

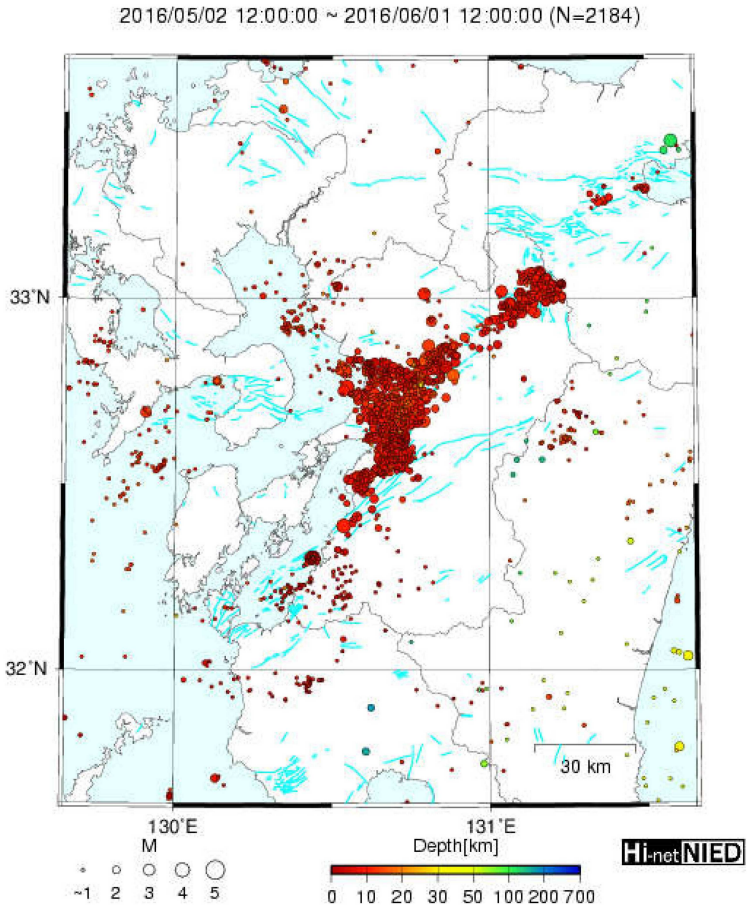

Figure 2-14: 2016 Kumamoto earthquake sequence aftershocks between 2016.05.02 – 2016.06.01 [http://www.hinet.bosai.go.jp/]

Table 2.4: List of Recorded Aftershocks from Kumamoto Earthquake in chronological order

Num	Date - Time	M^a	Dist.$(km)^b$	PGA Tra.$(gal)^c$	PGA Lon.$(gal)^d$
1	2016.05.01-13:45:00	3.0	10	9.9	6.71
2	2016.05.01-23:23:00	3.9	34	4.35	4.56
3	2016.05.01-23:27:47	3.4	30	2.05	2.07
4	2016.05.01-23:32:25	2.4	8	1.09	1.22
5	2016.05.02-00:39:20	1.9	6	1.3	0.58
6	2016.05.02-15:06:04	2.8	11	1.88	1.39
7	2016.05.02-15:35:00	4.1	34	3.64	4.29
8	2016.05.02-19:58:52	3.3	8	5.54	6.71
9	2016.05.03-06:05:00	3.8	13	18.6	28
10	2016.05.03-19:59:10	1.9	7	0.63	0.6
11	2016.05.03-23:24:02	3.1	19	1.07	1.3
12	2016.05.04-02:34:25	2.6	7	3.59	4.32
13	2016.05.04-03:27:53	2.8	7	5.67	6.14
14	2016.05.04-07:52:00	4.0	28	4.24	4.88
15	2016.05.04-08:44:27	2.7	4	7.94	7.9
16	2016.05.04-08:48:15	2.8	13	1.55	1.46
17	2016.05.04-14:11:00	3.3	28	1.05	0.87
18	2016.05.04-15:55:25	2.3	4	2.85	2.28
19	2016.05.04-16:22:00	3.4	26	1.37	1.29
20	2016.05.04-17:16:52	3.8	14	9.67	15.4
21	2016.05.04-19:20:00	4.0	10	11.1	19
22	2016.05.04-22:24:00	3.5	28	2.15	1.87
23	2016.05.05-04:21:21	2.3	9	1.33	0.94
24	2016.05.05-04:58:34	2.4	8	1.44	1.22
25	2016.05.05-10:31:00	4.6	41	10.5	9.86
26	2016.05.05-10:40:00	4.9	39	7.87	7.91

^{a}: Magnitude, ^{b}: Distance to measurement site, ^{c} and ^{d}: Peak ground acceleration in transverse and longitudinal directions of the bridge, respectively

Table 2.5: List of Recorded Aftershocks from Kumamoto Earthquake in chronological order (cont.)

Num	Date - Time	M^a	Dist.$(km)^b$	PGA Tra.$(gal)^c$	PGA Lon.$(gal)^d$
27	2016.05.05-11:55:51	2.5	12	4.82	1.86
28	2016.05.05-17:13:00	3.3	19	1.91	2.87
29	2016.05.06-02:03:20	3.2	17	2.19	2.38
30	2016.05.06-07:27:32	3.5	9	6.97	4.32
31	2016.05.06-13:09:41	3.0	20	2.41	1.62
32	2016.05.06-15:50:58	2.3	10	1.56	0.81
33	2016.05.06-16:18:44	3.8	27	5.39	5.88
34	2016.05.06-18:21:33	3.5	19	3.54	4.12
35	2016.05.07-16:35:59	2.6	6	12.6	4.23
36	2016.05.07-17:23:34	2.1	10	0.76	0.81
37	2016.05.07-18:03:01	1.3	8	0.75	0.59
38	2016.05.07-22:46:13	2.8	16	1.19	1.46
39	2016.05.07-23:10:47	3.3	16	1.37	1.86
40	2016.05.08-01:05:10	1.9	7	1.05	0.92
41	2016.05.08-13:00:23	3.6	12	4.02	5.23
42	2016.05.08-17:56:05	2.0	10	1.23	1.04
43	2016.05.08-18:06:50	3.0	7	3.77	2.56
44	2016.05.08-21:50:04	2.6	5	2.98	1.32
45	2016.05.09-01:39:09	2.9	17	0.93	0.92
46	2016.05.09-05:00:00	3.6	25	6.12	3.5
47	2016.05.09-05:36:10	3.3	9	9.69	6.57
48	2016.05.09-05:49:24	2.4	6	5.3	2.27
49	2016.05.09-07:10:44	1.8	6	1.87	0.94
50	2016.05.09-14:36:00	3.4	21	2.48	2.51
51	2016.05.09-20:55:00	3.5	7	6.79	4.62
52	2016.05.10-13:41:00	3.3	22	1.79	1.14
53	2016.05.10-14:40:00	3.0	22	0.91	1
54	2016.05.11-15:52:50	2.6	8	1.88	1.28
55	2016.05.12-03:41:01	2.8	10	2.44	3.21
56	2016.05.12-05:38:50	3.6	19	4.33	2.86
57	2016.05.12-17:04:00	4.1	20	25.4	24.1
58	2016.05.13-01:03:00	4.1	18	34.8	17.6
59	2016.05.13-13:05:00	2.8	23	1.21	1.05
60	2016.05.13-17:16:31	2.7	6	5.45	3.89
61	2016.05.14-00:04:00	3.1	25	1.08	0.95

[a]: Magnitude, [b]: Distance to measurement site, [c] and [d]: Peak ground acceleration in transverse and longitudinal directions of the bridge, respectively

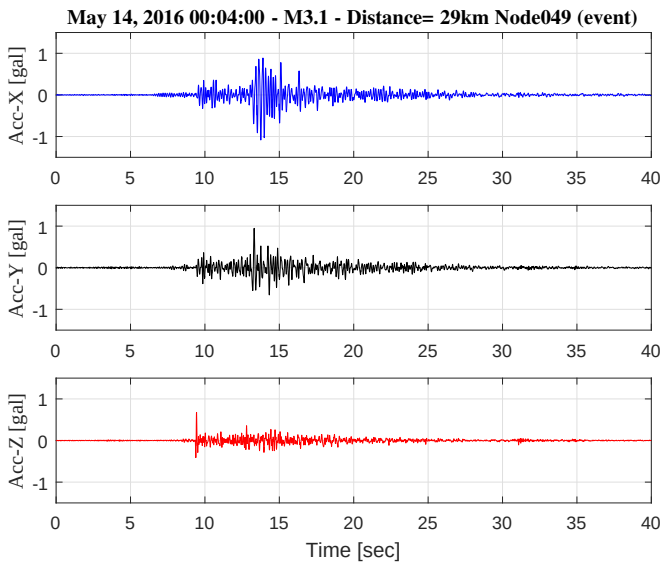

Figure 2-15: Representative waveform from measurement at the ground node (Node049)

Currently seismic response measurements have been limited to either to long-span bridges and/or bridges at dedicated test beds with a limited number of input excitation and response sensors. However, with the advent of stand-alone wireless systems without the need of external power source and communication lines, such measurements and investigations are recently made possible.

The sequence of 2016 Kumamoto earthquakes started with two strong fore-shocks, at 2016.04.14, 21:26:00 with a M6.5 and 2016.04.15, 00:03:00 with a M6.4, followed by a devastating M7.3 main-shock at 2016.04.16, 01:25:00 and thousands of aftershocks (Fig. 2-14). Taking advantage of the large earthquake occurrence, shortly after 2016 Kumamoto earthquakes, wireless sensor arrays were deployed on two target bridges in the area. Seismic response measurements on ground, pier, bearing, and superstructure nodes were all recorded from 61 aftershocks in a synchronous manner and examined in detail.

List of recorded earthquakes are presented in Tables (2.4) and (2.5). Representative waveform from the last recorded earthquake which occurred on 2016.05.14 at $00:04:00$ are depicted in Fig. (2-15). In the following sections details of the target test bridges, properties of wireless sensor arrays and characteristics of gathered data

are described and presented.

2.2.1 Description of Test Bridges

One of the target bridges, located in Kumamoto, Japan is a 59-meter span steel box-girder bridge, which forms the western end of a long viaduct. It is a road bridge carrying two lanes of traffic which was opened to traffic in 2013. The west end of the target span rests on an abutment and the east end is supported by a concrete pier. The girders on the consecutive spans are steel I-girder configuration. During visual inspection no obvious damage to the target bridge was observed. The bearing stoppers on the east end of the consecutive span showed deformation in transverse direction (Fig. 2-16) which was possibly due to the strong fore- and main-shocks. Evidence of friction was also found on the surface of bearing plates.

Figure 2-16: Deformation of the bearing stopper of the consecutive span

Second target road bridge consists of a rigid frame pre-stressed concrete (PC) box-girder and is supported by reinforced concrete piers. The construction of the bridge was completed in March 2015. The east end of the bridge rest on an abutment. During visual inspection large relative displacement at the joint between the abutment end and PC-box girder of the target span (Fig. 2-17) was found. Large cracks in the longitudinal direction of the bridge at the abutment joint were observed, which suggests large soil-structure interaction forces occurred between the back-fill soil, abutment, and the superstructure during the main events.

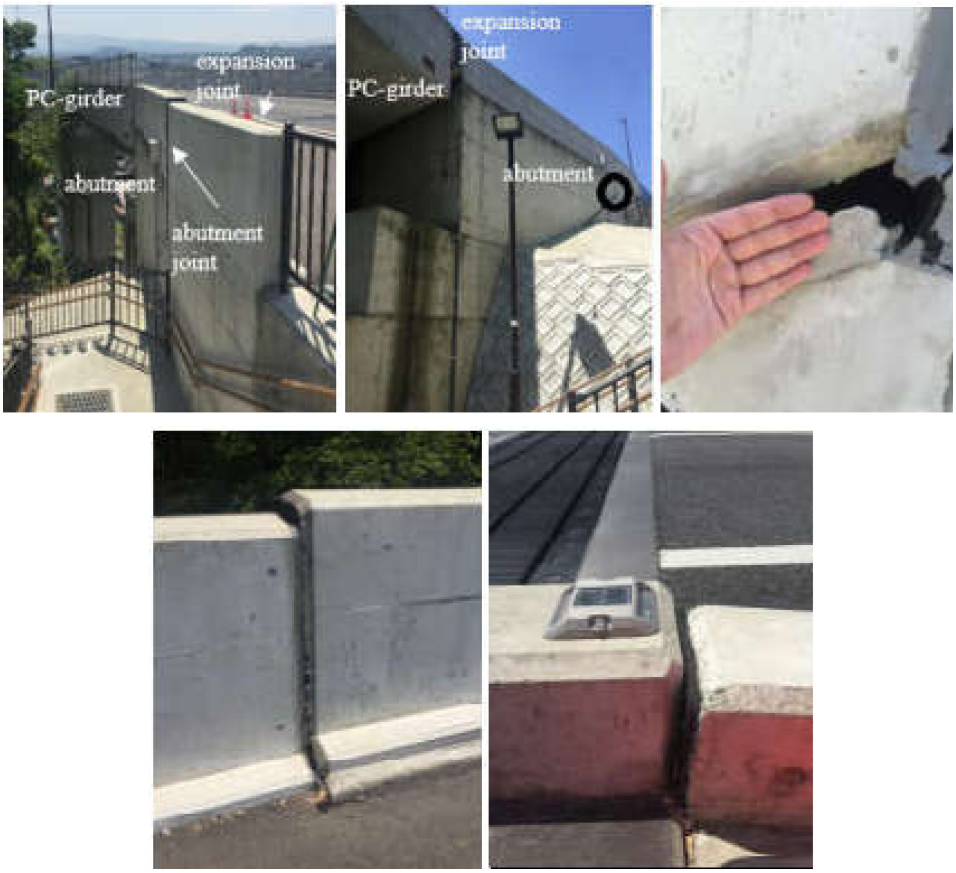

Figure 2-17: Side view of abutment and observed crack at the abutment joint of the PC-box girder bridge

2.2.2 Description of Seismic Monitoring System

Epson M-A351 [41] prototype wireless sensors have been developed and deployed on the above mentioned two target road bridges in Kumamoto for 16 days to capture seismic responses during aftershocks of the main event. The wireless sensors powered by D-cell batteries synchronize with each other through multi-hop communication and continuously record the acceleration in three directions at a sampling frequency of 100Hz. The continuous measurement last more than two weeks on the batteries. Average noise level is specified as $0.5\mu g/\sqrt{Hz}$ and single-hop communication distance of the prototype is about 20-30m [42, 43]. The collected data was saved in the SD card on each node. The stand-alone wireless system without the need of external power source or communication lines made it possible to establish this seismic monitoring

system with a large number of measurement nodes in the earthquake hit area in a short time after the main shock. In total more than 20 nodes were installed.

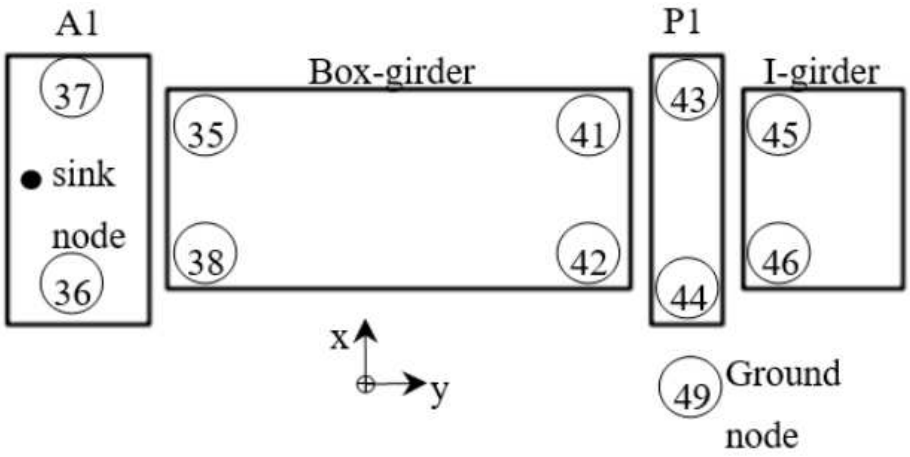

Figure 2-18: Sensor installation plan for steel box girder bridge

Sensors were deployed on abutment, girder-ends, pier caps, and ground at the bottom of the pier at the steel box girder bridge. Note that, not only box-girder side but also the girder ends on the I-girder side, where I-girders meet with the box-girders, were also equipped with sensors. The sensor locations and the numbering are presented in Figure (2-18). A1 denotes the abutment, and P1 denotes the pier. An example of sensor installation on the steel I-girder and next to one of the bearings on the pier at the measurement site is depicted on Figure (2-19). Epson M-A351 wireless sensors are depicted in Figure (2-20)

Two spans on the east end of the PC-box girder bridge were selected as the target and ten nodes were installed on the deck with 10-20m intervals including the sink node. Furthermore, three sensors were installed on the ground near abutment, at mid-elevation and at the bottom of the pier as depicted on the sensor installation plan. Sensor installation plan and an example of sensor installation at the pier bottom on measurement site are depicted in Figure (2-21).

Data collection from PC-box girder bridge nodes were only successful on four nodes about ten hours. The sensors were installed on the road side near the wall (Figure 2-21); antenna inside the water-proof casing was set close to the wall confining the RF

(a) Node 42

(b) Node 44

Figure 2-19: Sensor installation example (a) on the girder and (b) next to the bearing

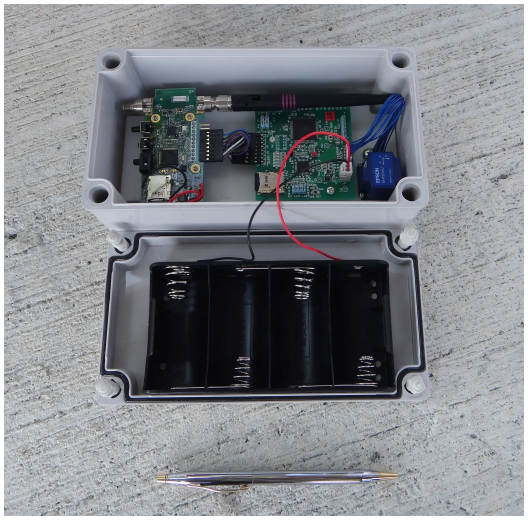

(a) Sensor prototype

(b) Installation on site

Figure 2-20: Epson M-A351 wireless sensor (a)prototype and (b) on site

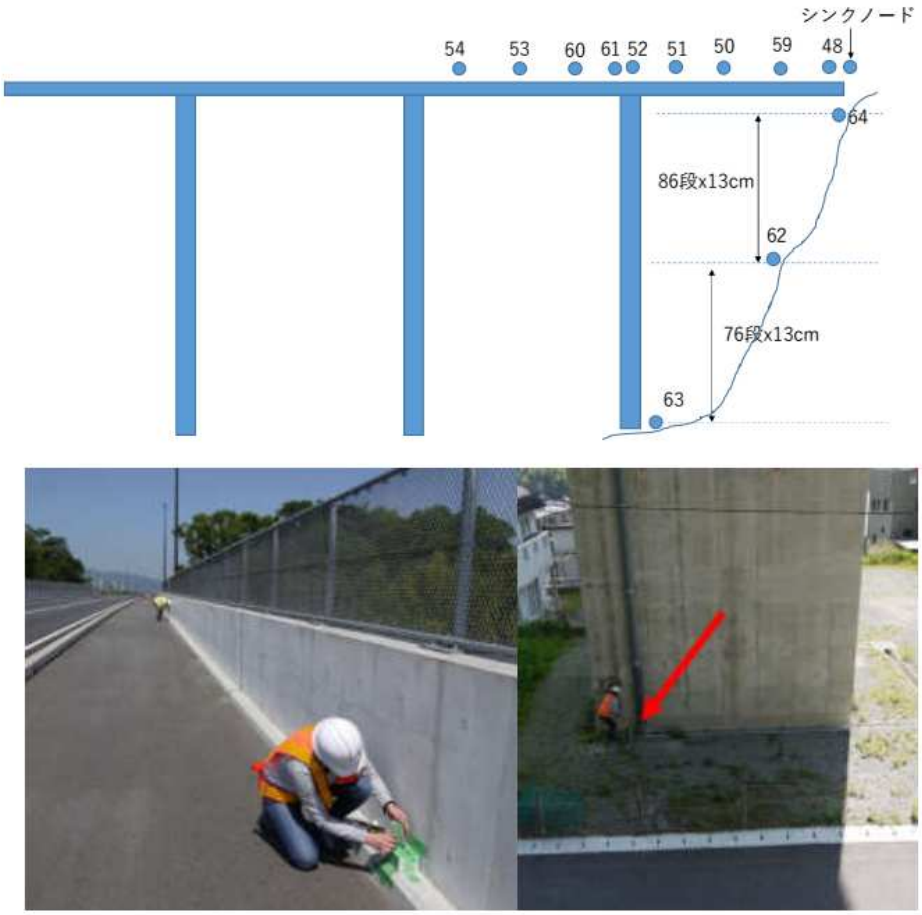

Figure 2-21: Sensor installation plan for PC box girder bridge

wave propagation fields, which is considered a partial reason behind the low success rate at this bridge. Thus, in this study only the records collected from steel box girder bridge are presented.

2.2.3 Measured Seismic Response Data

During the 16-days measurement period, 61 aftershocks occurred with a maximum magnitude of 4.9 according to Japanese Meteorological Agency (JMA) and National Research Institute for Earth Science and Disaster Resilience (NIED) databases. The response of the steel box girder bridge from all events were successfully captured.

In Table 2.5, magnitude, distance of the epicenter to the bridge site, and PGA in the transverse and longitudinal directions of the bridge were given. Figure 2-

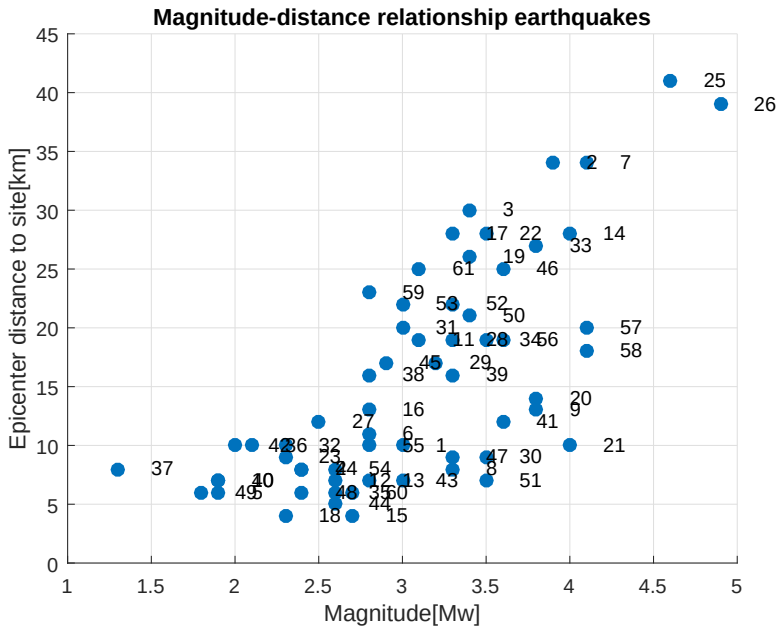

Figure 2-22: Magnitude and distance relationship of recorded earthquakes at the ground node

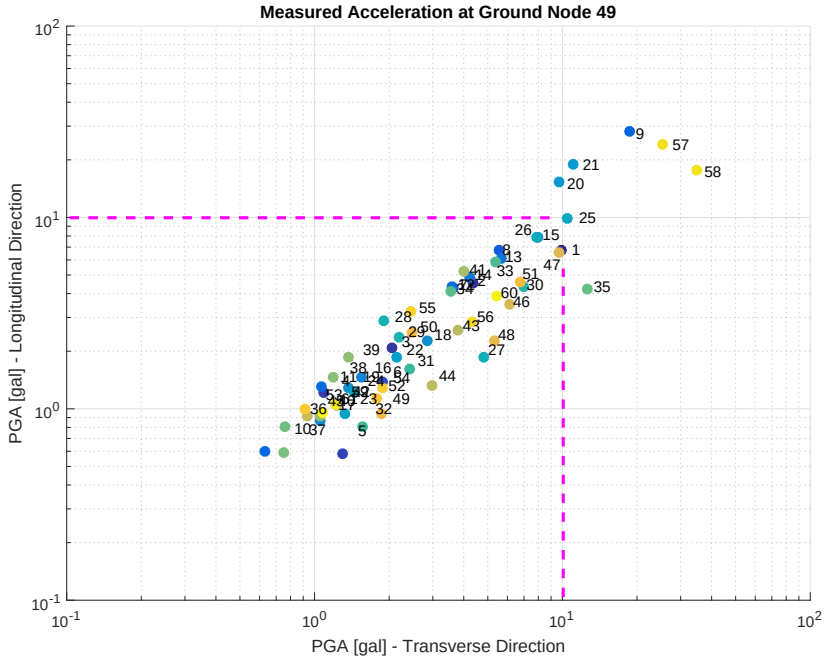

Figure 2-23: PGA measured at the Ground Node 049 (near the bottom of the pier)

22 depicts the magnitude - distance relationship of the recorded seismic motions at the ground node of the target bridge. The event with the largest magnitude was a Mw 4.9 earthquake with an epicenter distance of 39 km to bridge site. The farthest earthquake epicenter was 41 km with a magnitude of Mw 4.6.

Fig. (2-23) shows the the relationship between the measured PGA at the ground node near the bottom of the pier in the transverse and longitudinal directions.

Acceleration Time History

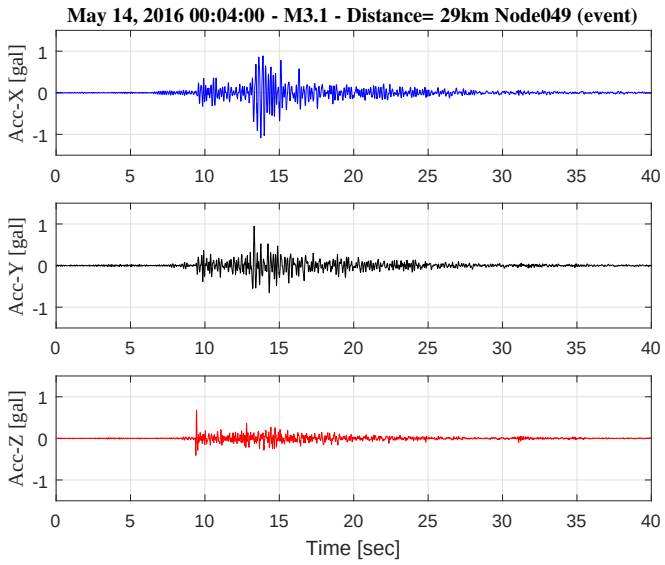

Figure 2-24: Representative waveform from measurement at the ground node (Node049)

Event data was extracted based on the occurrence times on JMA and NIED databases presented in the Appendix. The epicenter locations of the recorded events are in 40 km range from the target site. Figure (2-24) shows a representative waveform of the smallest events which were recorded at the ground node of steel box girder bridge. Even though the seismic excitation level is very low, the prototype sensors have a high sensitivity and are able to capture the responses.

Moreover, in the vertical direction the beginning of each event is inspected to validate the synchronization between nodes. Figure (2-25) shows the recorded responses

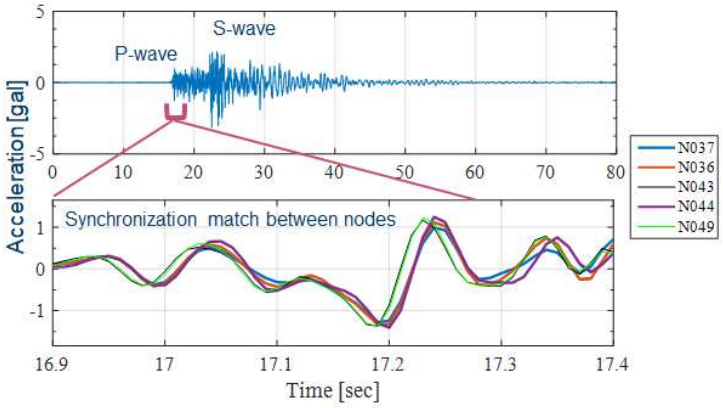

Figure 2-25: Synchronization between ground, pier and abutment nodes

at the beginning of an event in vertical direction. All nodes are found synchronized in a satisfactory manner. However, the synchronization error for one node is found 0.01 second (one sample) due to unexpected loss of one sample in the SD card saving process. For the purposes of this study the synchronization error is considered negligible.

Response Spectra of the Records

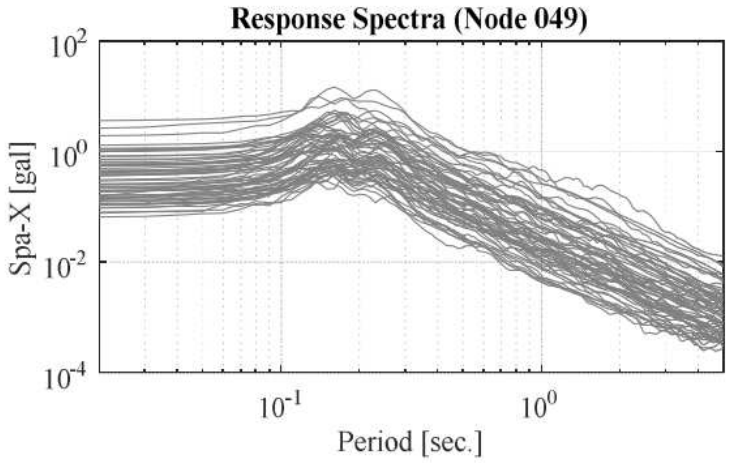

Figure 2-26: Response Spectra of ground node – Transverse direction

The response spectra in the transverse direction is calculated for the ground node

(Node 049) and presented in Figure (2-26). The peak horizontal acceleration ranges between 34.8 – 0.6 gal. and 27.9 – 0.6 gal. in transverse (X) and longitudinal (Y) directions of the target bridge. The peak vertical acceleration ranges between 14.8 – 0.2 gal. (see Tables (2.4) and (2.5)). Detailed inspection of the loading conditions based on response spectra will be given in section 4 in relation with the displacement response analysis of the bearings.

Displacement Estimation

Displacement estimation using acceleration is important because displacement measurement is not always feasible due to the lack of reference point and often more expensive than acceleration measurements. While many researchers suggested effective yet complicated solutions to this problem, simple and effective methods are not readily available. The suggestions given by references ([37],[38]) are followed to understand the source of the errors, which in turn cause erroneous displacement estimation due to integration, and to remove them with several pre-processing steps such as analysis of the noise levels, selection of cut-off frequency, and filtering procedure/order, tapering, and zero-padding.

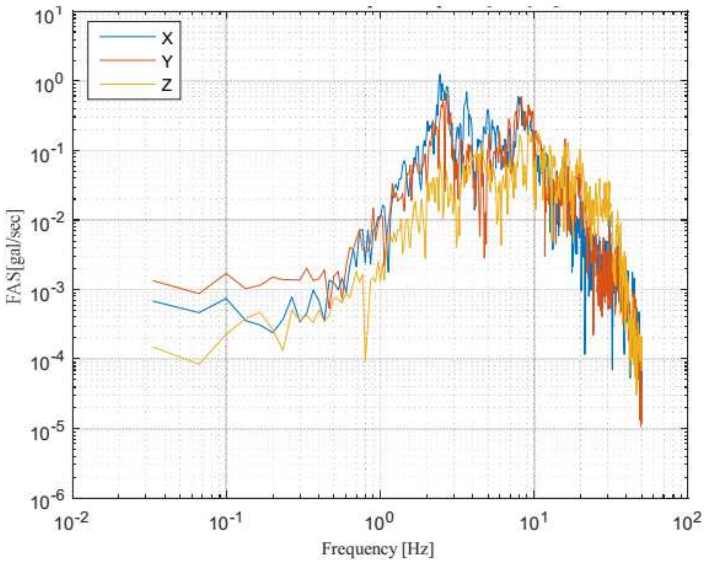

Figure 2-27: Frequency amplitude spectra of the response of the bearing on Node 46 during EQ9

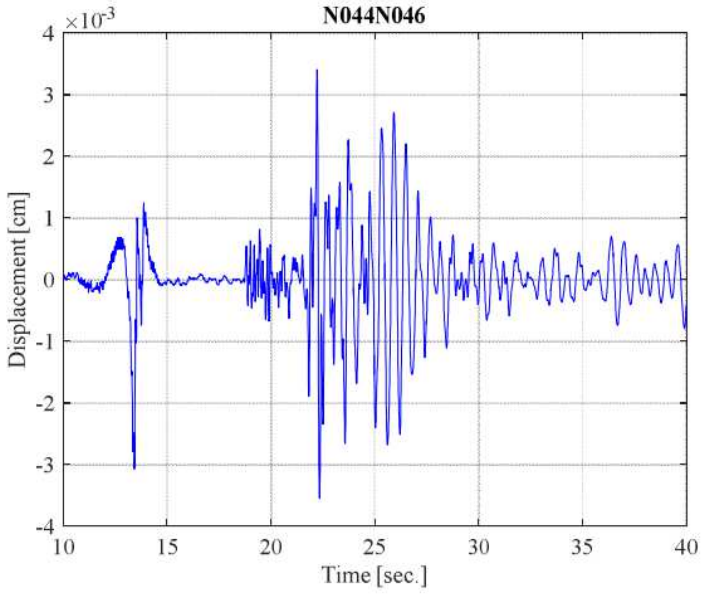

Figure 2-28: Relative displacement of a bearing under earthquake loads in horizontal direction

In order to eliminate the low-frequency noise and to obtain a realistic displacement estimation, first, cut-off frequency of the high-pass filter needs to be determined. Through examination of the descending trends of Fourier amplitude spectra (Figure 2-27) for each response record on bearings in low-frequency range it is obtained as 0.2-0.5 Hz. To achieve a signal-to-noise ratio of three for each earthquake is the reason for obtaining different cut-off frequencies. For instance, when a low amplitude signal is examined, to obtain a signal-to-noise ratio of three is possible with a selection of a high cut-off frequency such as 0.5 Hz, or vice versa. By examining the estimated displacements and to be consistent among all recorded response, the cut-off is chosen as 0.5 Hz for high-pass filter for each recorded seismic response.

In addition, zero-padding was applied to avoid the errors due to unknown initial conditions of velocity and displacement and thus tapering was applied both ends of the data to ensure the smooth transition from data to the zero-padded regions before filtering the records. Acceleration data was filtered (Butterworth IIR filter) in time domain twice, i.e. once in one direction and then in the reverse direction, to achieve zero-phase. Figure (2-28) shows a representative estimated displacement

time-history for a bearing under earthquake 6 in vertical direction. Here, between 10-15 sec. the displacement waveform presents some irregularity. This is due to the fact that some of the earthquake responses contaminated by vehicular load disturbance. Since the vehicular response cut-off frequency is different (0.2 Hz) from the seismic response cut-off, when high-pass filtered with a cut-off of (0.5 Hz), distortions in the displacement estimation occurs as an overshoot where there is a vehicular disturbance in the response data. The time frames of the vehicle disturbances within seismic response are determined and removed from the data before calculating displacements of the bearings.

In addition, the largest vehicular response in transverse, longitudinal, and vertical directions are found 0.8, 0.25 and 0.06 mm, respectively. Because the corresponding maximum displacements under seismic loads are 2, 1, and 0.04 mm, the horizontal behavior of the bearing during relatively large aftershocks is larger than the bearing motion due to vehicular passages. The bearing motion during aftershocks are thus studied.

Bearing Behavior

Bearing motions are obtained by subtracting the pier/abutment motion from the girder-end motion and by using the above mentioned method. Bearing behavior under some of the representative earthquakes are discussed in this section.

Based on the bearing displacement response, the demand from EQ57 and 58 in transverse direction is more dominant than the longitudinal direction. Displacement trajectories are presented in Figure (2-29). The node numbers of the bearings are presented on top of each figure and the locations can be seen from Figure 2-18. The relative displacement of the bearings located on the I-girder span are about twice larger than the displacement of the bearings supported by pier on the box-girder span, which are similar to the behavior of the bearings on the abutment.

Moreover, EQ58 has the largest PGA in the transverse direction (Tables (2.4) and (2.5)) of the viaduct and the PGA is about twice larger than the PGA in the longitudinal direction. On the other hand, although EQ57 has the second largest

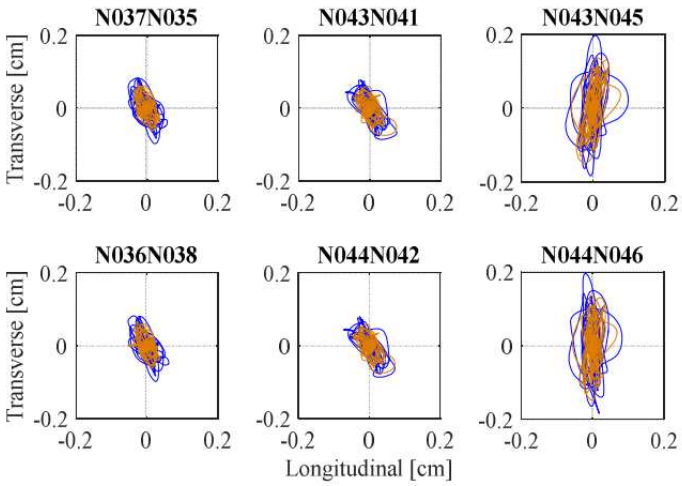

Figure 2-29: Bearing relative displacements under EQ57 (blue lines) and EQ58 (orange lines)

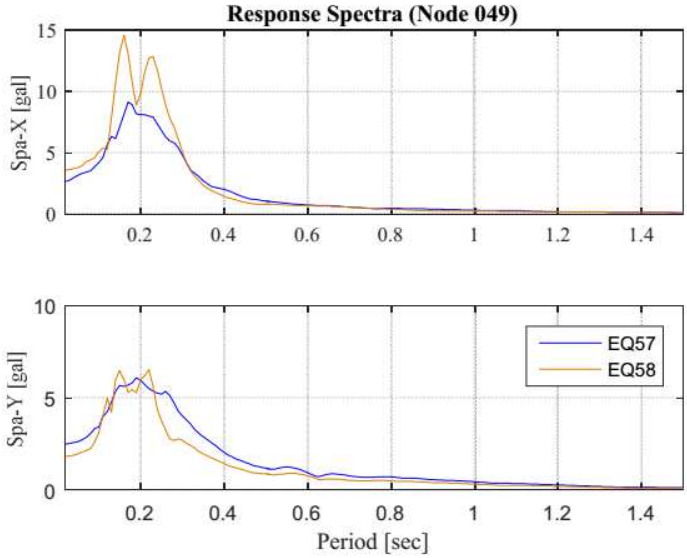

Figure 2-30: Response spectra on Node 049 for EQ57 (blue lines) and EQ58 (orange lines)

PGA (25.4 gal) in transverse direction, the PGA in the longitudinal direction is also similar (24.1 gal.). When response spectra (Figure 2-30) on Node 49 is examined in the longitudinal direction, both earthquakes have similar demands over the 0.1-0.25 period range. On the contrary, EQ58 has about twice larger energy input to the system between 0.12 – 0.3 period range in the transverse direction.

Chapter 3

Theory and Method Verification

Data assimilation methods such as Kalman filters has capability to estimate unknown states and system parameters jointly as long as the system is observable. However, in structural dynamics area their capability has been mostly investigated using simulations and not illustrated on a problem of practical significance. One of the important reason for this limitation is that data assimilation methods require full knowledge of the system noise statistics in order to achieve successful estimates. However, noise statistics of a system is unknown a-priori. In addition, for practical parameter estimation under seismic loads there are also other important goals to achieve in order to be successful. This is mainly due to the variation of each seismic input. First of all, robustness against initial conditions is of significance because for instance after a large earthquake the current condition of the structure is not known, so is the initial state vector which is needed for the algorithms. In this perspective, the more robust the algorithm, against unknowns, the more reliable the results of the estimation.

Secondly, seismic input transfers most of its energy to the system in a limited amount of time. This time period is known as "significant duration" and it is usually at the order of 2-8 seconds. Before and after this duration the observation (data) gathered from the system is mostly not informative so that the algorithm learn about the system and achieve an estimate. Moreover, significant duration is also a limited time for the algorithm to learn the information. Thus, in order to accomplish meaningful estimation under seismic loads algorithm should quickly converge and be able

to track the system behavior in a stable manner after the convergence. The convergence rate and track ability of the algorithm also depends on the unknown statistics, mainly the process noise covariance.

In this chapter, first a well studied nonlinear data assimilation method namely Unscented Kalman Filter (UKF) will be explained. In UKF, the initial process and measurement noise covariance always need to be fine tuned as they are kept constant over the estimation period. Unless the noise covariances are true, UKF cannot converge or provide a satisfactory estimation, especially for parameters. Consecutively, to overcome this drawback a stochastic approximation scheme, namely Robbins-Monro, has been adopted to optimize and update noise covariances during the estimation as suggested by [44]. Robbins-Monro scheme and its usage with UKF is explained in detail in Section 3.2. In the last section of this chapter, verification simulations are illustrated for UKF-RM with comparisons to UKF considering an ideal case. Here, an ideal case refers to the case where there is no measurement noise. In addition, process noise matrix, Q is found manually by trial and error method. Then two algorithms' performance is studied comparatively.

3.1 Unscented Kalman Filter (UKF)

With the use of the Unscented Transform in Kalman filter [45, 46], Unscented Kalman Filter (UKF) eliminates the need of linearization, and hence calculation of Jacobians, to find solutions for nonlinear parameter estimation problems. Although UKF is a considerably new filter compared to its counterpart such as Extended Kalman filter (EKF), it has been proven that UKF [47, 44] is superior based on the convergence performance, estimation accuracy especially when dealing with higher order nonlinear problems. Moreover, in structural dynamics the problems are often inevitably nonlinear when especially joint estimation of parameters and states is sought. Joint estimation problem is intrinsically nonlinear even though a linear model is considered due to its augmented state vector. UKF has also been proven to be highly capable when dealing with nonlinearities in the governing equations in structural dynamics

area when compared to its counterpart, EKF [18].

Such nonlinear problems are often the interest due to necessity in structural engineering. For example, using a softening SDOF system showed UKF's capability when dealing with highly nonlinear systems is better than EKF.

General UKF equations using scaled unscented transformations [48] are as follows.

$$x_a(k+1) = F(x_a(k)) + w(k) \tag{3.1}$$

where F: state transition function, x_a: augmented state vector and w: process noise with covariance Q and

$$z(k) = H(x_a(k)) + v(k) \tag{3.2}$$

where H: observation function, z: measurements and v: measurement noise with covariance R.

Initialize with:

$$\hat{x}_0 = E[x_0] \tag{3.3}$$

and

$$P_0 = E[(x_0 - \hat{x}_0)(x_0 - \hat{x}_0)^T] \tag{3.4}$$

For $k \in [1, ..., \infty]$

Calculate sigma points using unscented transform as:

$$\mathbf{X}_{k-1} = \begin{bmatrix} \hat{x}_{k-1} & \hat{x}_{k-1} + \gamma\sqrt{P_{k-1}} & \hat{x}_{k-1} - \gamma\sqrt{P_{k-1}} \end{bmatrix} \tag{3.5}$$

These sigma points are propagated through the nonlinear function $F(x_k)$

$$\mathbf{X}^i{}_{k|k-1} = \mathbf{F}[\mathbf{X}^i{}_{k-1}] \tag{3.6}$$

where $i = 0, ..., 2L$ and L is the dimension of the state vector x_a.

The set of the sample points ${\mathbf{X}^i}_{k|k-1}$ represents the predicted probability density $p(x_k|y_{1:k-1})$ where

$$p(x_k|y_{1:k-1}) = N(x_k; \hat{x}_{k|k}, P_{k|k}) \tag{3.7}$$

In Eq. (3.7), $N(x; m, P)$ represents a Gaussian density with argument x, mean m and covariance P.

After propagation of sigma points through function $F(x_k)$, the mean and covariance of the next state are approximated using a weighted sample mean and covariance of the posterior sigma points and the time update step is continued as follows:

$$\hat{x}_{k|k-1} = \sum_{i=0}^{2L} {W^{(m)}}_i {\mathbf{X}^i}_{k|k-1} \tag{3.8}$$

$$P_{k|k-1} = \sum_{i=0}^{2L} {W^{(c)}}_i [{\mathbf{X}^i}_{k|k-1} - \hat{x}_{k|k-1}][{\mathbf{X}^i}_{k|k-1} - \hat{x}_{k|k-1}]^T + \mathbf{Q}_{k-1} \tag{3.9}$$

where Q is the process noise covariance.

Consecutively the predicted measurements are obtained as propagating sigma points through measurement equation as follows:

$${\mathbf{Z}^i}_{k|k-1} = \mathbf{H}[{\mathbf{X}^i}_{k|k-1}] \tag{3.10}$$

$$\hat{z}_{k|k-1} = \sum_{i=0}^{2L} {W^{(m)}}_i {\mathbf{Z}^i}_{k|k-1} \tag{3.11}$$

Then the measurement update equations are as follows:

$$\hat{x}_{k|k} = \hat{x}_{k|k-1} + K_k(z_k - \hat{z}_{k|k-1}) \tag{3.12}$$

Here $e = (z_k - \hat{z}_{k|k-1})$ is called innovation which represents the difference between the actual measurements and the final estimation at the current time-step.

$$P_{k|k} = P_{k|k-1} - K_k {P_k}^{ZZ} {K_k}^T \tag{3.13}$$

where K_k is the Kalman gain and equal to

$$K_k = {P_k}^{XZ}({P_k}^{ZZ})^{-1} \tag{3.14}$$

$${P_k}^{ZZ} = \sum_{i=0}^{2L} {W^{(c)}}_i [{\mathbf{Z}^i}_{k|k-1} - \hat{z}_{k|k-1}][{\mathbf{Z}^i}_{k|k-1} - \hat{z}_{k|k-1}]^T + \mathbf{R}_k \tag{3.15}$$

$${P_k}^{XZ} = \sum_{i=0}^{2L} {W^{(c)}}_i [{\mathbf{X}^i}_{k|k-1} - \hat{x}_{k|k-1}][{\mathbf{Z}^i}_{k|k-1} - \hat{z}_{k|k-1}]^T \tag{3.16}$$

where $\mathbf{R}_k$ is the measurement noise covariance.

For a given dynamic system we usually do not know the parameter values accurately a-priori and they need to be determined to obtain the response. Such system parameters can be estimated when clean system states is known which is almost never the real case [44]. Thus the estimation problem at hand becomes a nonlinear estimation problem inherently where both states and parameters need to be estimated simultaneously even the system itself is linear. This is one of the reasons why UKF is chosen as the solution algorithm in this study.

Although UKF is a powerful tool for parameter estimation of nonlinear dynamic systems, it is a well known fact the performance of the filter is affected by the initial conditions provided to it such as process and measurement noise covariance matrices. If they are not provided correctly, the filter suffers from divergence, instability or false-true convergence [49]. On the other hand, for most of the dynamic systems in real world it is not possible to know these noise covariance a-priori. Thus, the application of UKF to real-world applications especially in structural dynamics is limited or non-existent.

Furthermore, for dynamic systems under such excitation as earthquakes the process itself is nonstationary and time variant, so as system response (measurement) is also nonstationary. Thus, in addition to the lack of knowledge on the initial conditions, the process and measurement noise are also not constant throughout the system which increases the uncertainty. Here Q and R matrices are covariance of the process

and measurement noise respectively and play an important role in the performance of UKF estimation. Especially Q play an important role in terms of rate of convergence and tractability of the estimation. Thus, in order to be able to use UKF in real-world problems a method that can adapt or approximate the noise covariance is needed. Examples which illustrate these problems will be numerically shown later in Chapter 4.

3.2 UKF with Robbins-Monro Scheme (UKF-RM)

Although adaptative linear Kalman filters have been studied in the literature extensively [50, 51, 52] and applied successfully to different dynamic problems, adaptive nonlinear Kalman filters are an open area. From a general proint of view, adaptive algorithms can be grouped in four categories, namely; Bayesian, maximum likelihood, correlation and covariance matching as described by [51]. Some example methods can be found in [53, 54, 55]

Current ad hoc approaches to make the filter convergent are limiting P from going to zero, add Q to increase P before calculating the gain, multiplying P by a factor to limit K which all have drawbacks and limitations [56].

In many fields such as aerospace engineering [57] adaptive Unscented Kalman filters have been a topic of recent interest. [44] summarized some options to approximate unknown process and measurement noise covariance matrices for nonlinear Kalman filters as follows:

- Constant diagonal noise covariance matrices obtained by trial and error

  In structural dynamics problems, this approach is widely adopted to define the noise covariance for the filter. The initial Q and R matrices are manually set by trial and error method and kept constant over time. Manual setting such values can be time-consuming and in fact does not always guarantee the optimal solution.

- Adaptation of noise estimation for Q. There are many ways to achieve adapta-

tion as explained in [58]. For example, Q can be defined as $Q = (\lambda_{RLS}^{-}1) * P$ where λ_{RLS} is the "forgetting factor" determined by the recursive least-squares algorithm. This way, past data is assigned approximate exponentially decaying weighting. Details of the approach can be found in [59]. Selecting a single value for adaptation of Q may cause problems as the ratio between the elements of Q are not known a-priori and not equal between every couple. For example let's assume the correct ratio is X, a scalar value, between the elements of a diagonal 2x2 Q matrix. If we start with a wrong value of the ratio between them, the correct value of the elements cannot be reached as the forgetting factor is always one value and both of the elements are multiplied with this same value.

- Adaptation of noise estimation for Q, R or both based on the Robbins-Monro stochastic approximation scheme [60] which can minimize the roots of functions through noisy observations in an iterative manner. Use of Robbins-Monro scheme to approximate noise estimations have been presented in [61] and its use in EKF has been explored by [62, 63]. Then, Wan and van der Merwe in [64] presented its use with UKF and discussed possible advantages. It allows update of Q and R based on the time-varying weighting calculated from the learned information during estimation.

Selection of these different approaches result in some advantages and disadvantages regarding the problems at hand and such investigations are still an area of open research [64]. On the other hand, adaptation of process and measurement noise estimations in Unscented Kalman Filter for nonlinear state and parameter estimation problems is necessary as explained in the previous section. Consequently, in this chapter the advantages of using an adaptation scheme for noise covariance determination in UKF, namely the Robbins-Monro method, has been explored and compared with the traditional method for structural dynamics problems via first simulations and then application to real-world problems.

Estimates of the noise covariance Q and R using Robbins-Monro stochastic approximation scheme can be formulated as follows [62],[61],[44].

$$Q_k = (1 - \alpha_Q) * (Q_{k-1}) + \alpha_Q * (K_k) * (z_k - z_k^-) * (z_k - z_k^-)^T * (K_k^T) \tag{3.17}$$

$$R_k = (1 - \alpha_R) * (R_{k-1}) + \alpha_R * (z_k - z_k^-) * (z_k - z_k^-)^T \tag{3.18}$$

where α: a small positive number, which is usually chosen at the order of 10^{-2},

K_k: Kalman Gain and $(z_k - z_k^-)$: innovation

After each time step, Q and R are calculated based on the latest estimation and fed back as the new noise covariance into the next estimation step.

Recently the above given Robbins-Monro scheme has been used in UKF application in varying fields such as; robotics [65], image processing [66], computer science [67].

3.3 Simulation Results for UKF and UKF-RM: Ideal Case

Using the E-Defense pier structural parameters, a SDOF system is defined. Mass is obtained from the E-Defense C1-1 experiment report [1]. The reaction force in the vertical direction measured by the load cells located on the pier cap is given equal to $2080kN$ (Table 2.1) from the dead load of the girder and added mass on top of the girder. In addition, the weight of the pier is given as $794.5kN$. Consequently, the mass is calculated as

$$m = (2080 + 794.5/2)/g = 252.5ton \tag{3.19}$$

where $g = 9.81m/s^2$ is the acceleration of gravity. Thus, half of the pier weight also contributes to the structure mass.

Design value for stiffness was also given as $k = 32506kN/m$ [1]. However, this value was used only to set an initial value for state vector by multiplying it by a

factor. In addition, $\zeta = 3\%$ viscous damping is assumed as $2-5\%$ viscous damping is considered a reasonable range for a single reinforced concrete column. Corresponding damping factor c is calculated based on mass and stiffness as $c = \zeta 2\sqrt{mk}$. For a SDOF system excited at its base with ground acceleration the governing equation of motion becomes:

$$m\ddot{x}(t) + c\dot{x}(t) + kx(t) = -m\ddot{x}_g(t) \tag{3.20}$$

where $x(t)$ is the displacement response and $\ddot{x}_g(t)$ is the ground motion acceleration.

SDOF system response is simulated with the above given structural parameters and using fourth order Runge-Kutta integration method to solve the governing equation. The input acceleration is the 100% Takatori (Modified) excitation.

Based on the above given governing equation the augmented state vector becomes

$$X_a = [x, \dot{x}, k, c]^T = [x_1, x_2, x_3, x_4]^T \tag{3.21}$$

with states $[x, \dot{x}, k, c]$ are to be estimated. Only mass is assumed as known in all following structural parameter estimation cases.

Based on Eq. (3.20) the state space equation is formulated as:

$$\dot{X}_a = f(X_a(t), u(t)) \tag{3.22}$$

where

$$f(\mathbf{X_a}(t), \mathbf{u}(t)) = \begin{bmatrix} x_2 \\ (-x_3 x_1 - x_4 x_2)/m + \ddot{x}_g \\ 0 \\ 0 \end{bmatrix} \tag{3.23}$$

In Equation (3.23) $u(t)$ is the input force and $u(t) = m\ \ddot{x}_g$

From simulated acceleration response, displacement response of the system is cal-

culated with double-integration as explained in Chapter 2.1.3. Displacement calculated from the acceleration response of the system is considered as the observation in the following parameter estimation algorithms. The reason why this displacement is used as observation in estimation algorithms is actually straight-forward. In a real-world measurement, often measuring velocity or especially displacement and force is not currently possible during a seismic event. Thus, obtaining stiffness condition of the target system with a practical tool using only acceleration measurements is needed so that it can be adopted widely in practice. Thus, the observation equation becomes:

$$y = \begin{bmatrix} x_1 \end{bmatrix} \tag{3.24}$$

The input acceleration, simulated displacement and calculated displacement from simulated acceleration response is presented in (Figure 3-1). From the top figure, it can be seen that max. PGA is about $5m/s^2$. The bottom figure shows that displacement response which is calculated from acceleration response with double integration matches well with the simulated displacement response. The vertical red lines correspond to the start and end of the $D5-95\%$ significant duration which contains $5-95\%$ of the total energy of the input.

In the following sections, using the above described system, performance comparison between the conventional UKF and UKF-RM are presented based on sensitivity to selection of different initial values. Namely, the definition of initial values for the elements of the process and measurement noise covariance Q and R, error noise covariance P, initial state vector X_0 and constants in Robbins-Monro α_Q and α_R are used as parameters to judge the performance of both algorithms and presented as follows.

For the purpose of a fair investigation between two methods, namely UKF and UKF-RM first, so-called optimum Q and R matrix covariance elements, which correspond to each state and measurement, respectively are found by conventional trial and error method. At this stage, only the common practice customs are used to determine

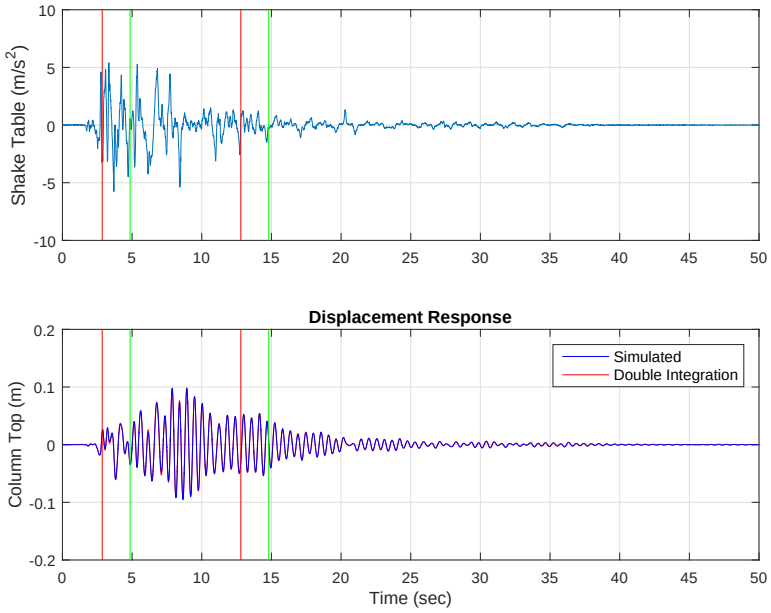

Figure 3-1: Input acceleration at the column bottom; Displacement response at the column top from simulation and double-integration of acceleration response

all the unknown initial filter parameters, e.g. Q ,and find a good estimation result with conventional UKF. Then, using same initial filter parameters estimation has been performed with UKF-RM. Finally, the results of two algorithm are compared.

Augmented state vector:

$$X_a = [x, \dot{x}, k, c]^T = [x_1, x_2, x_3, x_4]^T \tag{3.25}$$

As displacement and velocity starts from zero, the corresponding initial state vector values are assigned as zero. However, the current condition of stiffness and damping, hence, the initial values, is not known in practice. About a 20% difference from the true value is chosen for both because conventional UKF is also capable of handling such model error. Initial state vector is shown below.

$$X_0 = [0, 0, 0.8k, 0.8c]^T \tag{3.26}$$

Initial error covariance, by definition, is set to

$$P_0 = diag[0, 0, (k_{true} - X_0(3))^2, (c_{true} - X_0(4))^2] \tag{3.27}$$

Initially no measurement noise case is considered. Accordingly, R, measurement noise covariance is set to zero.

Using the SDOF system explained above and initial values, parameter estimation with UKF has been performed in which Q and R matrices are kept constant during the algorithm. Suitable Q values corresponding to each state vector element is searched, meaning the filter is manually tuned, until the convergence of the state estimations is obtained. The resultant Q matrix is shown below. Figures (3-2,3-3) shows the results of state and parameter estimations from UKF.

$$Q = diag[10^{-4}, 10^{-1}, 2 \times 10^5, 2 \times 10^2] \tag{3.28}$$

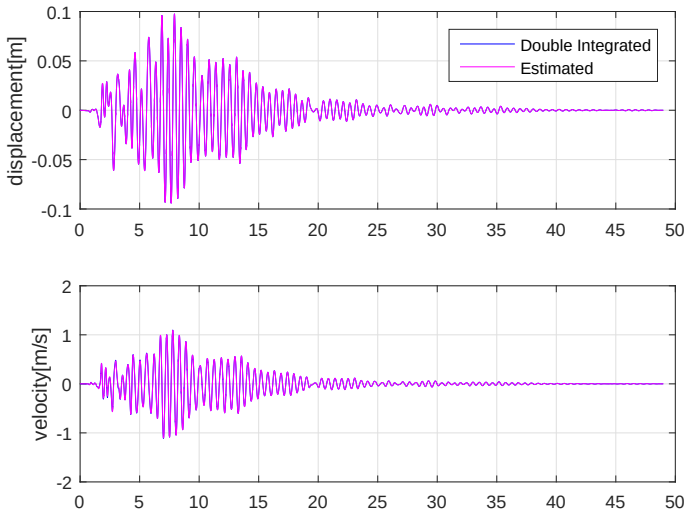

Figure 3-2: State estimation results for correct initial selection Q, R, P with UKF

Using same process noise covariance shown above, parameter estimation with UKF-RM algorithm has been performed. Figures (3-4,3-5) show the state and parameter estimation results, respectively. In UKF-RM extra parameters, α_Q and α_R, which do not exist in UKF, are both set to 1/30 without any further consideration at

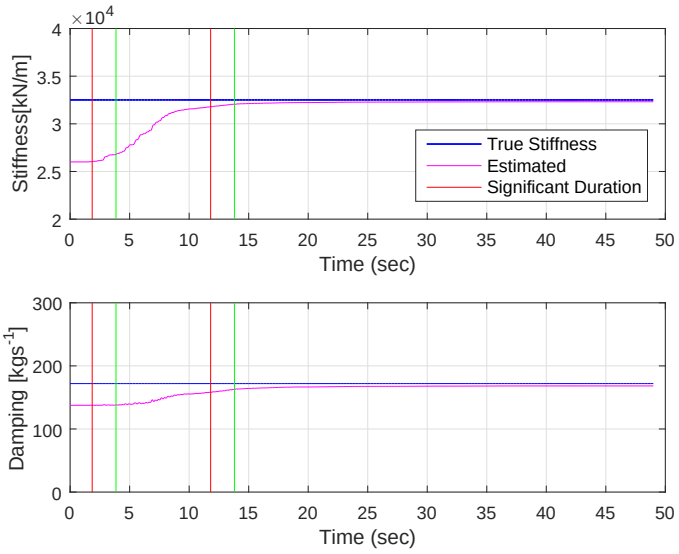

Figure 3-3: Parameter estimation results for correct initial selection Q, R, P with UKF

this stage. The sensitivity of the results to the selection of α values are later presented in Section 4.3

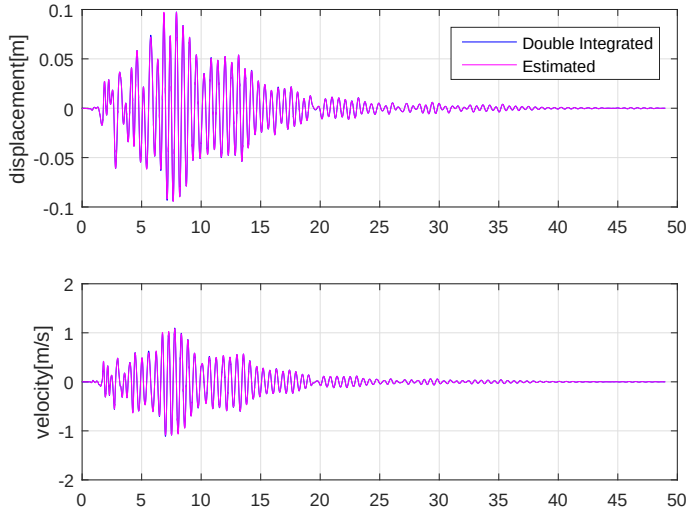

Figure 3-4: State estimation results for correct initial selection Q, R, P with $\alpha_Q = 1/30$ and $\alpha_R = 1/30$

From Figures (3-2,3-4), displacement and velocity response can be obtained with

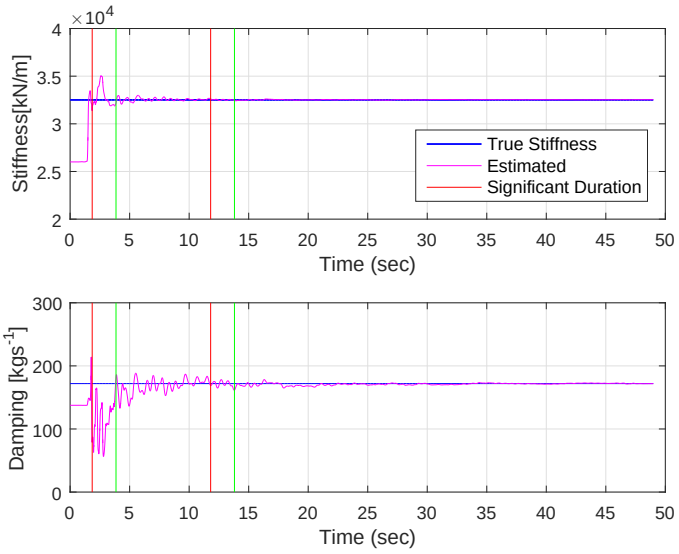

Figure 3-5: Parameter estimation results for correct initial selection Q, R, P with both $\alpha_Q = 1/30$ and $\alpha_R = 1/30$

both UKF and UKF-RM.

Furthermore, Figures (3-3) and (3-5) show that both methods can successfully estimate both stiffness and damping when the part of the data after the significant duration is considered.

However, in Figure (3-3), the stiffness estimation convergence does not occur until about 10 seconds from the beginning of the data. Considering the fact that the significant duration starts and end at 2.85 sec and 12.81 sec, the stiffness estimation during this important region could not achieved with UKF. However, with UKF-RM (Figure 3-3), the stiffness estimation convergence occur as soon as the significant duration begins and remains stable. Mean percentage error between the two vertical green lines (2 sec after the beginning and end of the significant duration) is 0.2% for stiffness estimation.

When damping estimations are compared, the UKF damping estimation is again slower than UKF-RM estimation inside the significant duration and remains stable. UKF-RM damping estimation convergence occur when the significant duration starts while with UKF convergence is achieved close to the end of significant duration. Mean percentage error of the damping estimation between the two vertical green lines is

2.1%.

It is a well known fact that the process noise covariance affects the tracking performance and the convergence rate in UKF [44]. Thus, with this simple example it is concluded that as UKF-RM can update the Q matrix during the estimation process. Its convergence rate and track-ability are superior over the conventional UKF in which Q is kept constant.

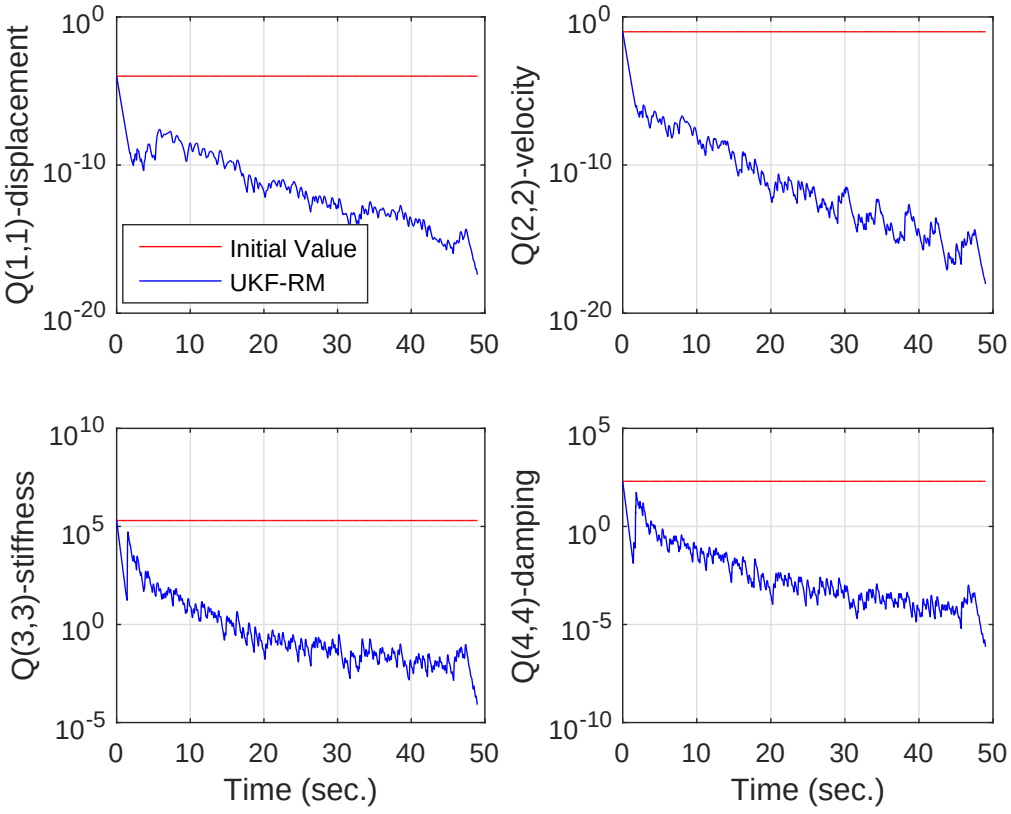

Figure 3-6: Change in elements of Q with $\alpha_Q = 1/30$ and $\alpha_R = 1/30$ for UKF-RM and UKF

Figures (3-6,3-7) displays the change in the elements of Q matrix and R, as the estimation propagates. Elements in Q and R evolves based on the learned new information from the filter UKF-RM while the conventional UKF keeps them constant.

Figure (3-8) displays the change in the elements of P matrix as the estimation propagates. As mentioned before P represents the error noise covariance in Kalman filter and it is the an evolving variable as estimation proceeds and it is common to

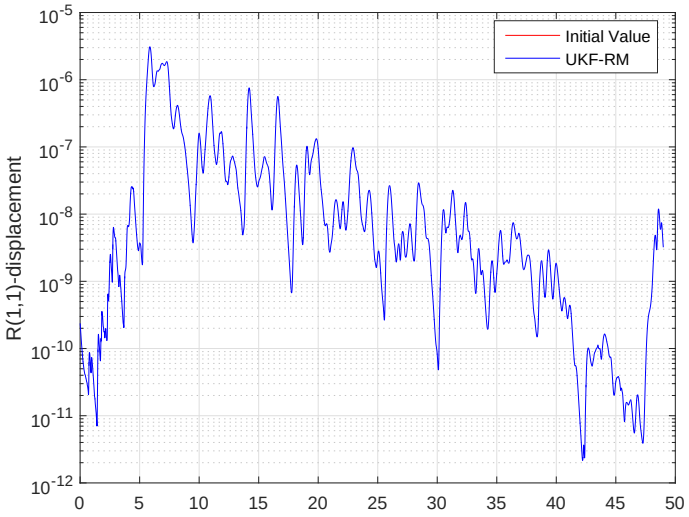

Figure 3-7: Change in elements of R with $\alpha_Q = 1/30$ and $\alpha_R = 1/30$ for UKF-RM and UKF

both conventional UKF and UKF-RM. However, it is the only evolving variable for UKF and thus, it can be seen as the only learning source of the filter.

When the trend of change in P matrix elements which correspond to stiffness and damping parameters is examined, it can be seen that they are getting larger in UKF with a very slow rate. This can be interpreted as the filter's evolution rate is also slow. In addition, it may be seen as an attempt to keep the filter stable and convergent by increasing P. On the other hand with UKF-RM same elements seems to get smaller with a much faster rate than UKF. This is due to better learning performance of UKF-RM as it updates not only P but also Q and R at each time step. In addition, it consists of a forgetting factor, α which helps the filter to forget the history and enforces learning from new information faster. These issues will be discussed more in detail in the following Section (4.1) with more insight given for physical meanings of these variables.

Comparison of two methods with the so-called "true" Q and R matrices in this section showed two important results. First is that the performance of convergence and track-ability of the parameter estimation algorithm is important, especially when the response under seismic excitation is of interest. Because response is divided into

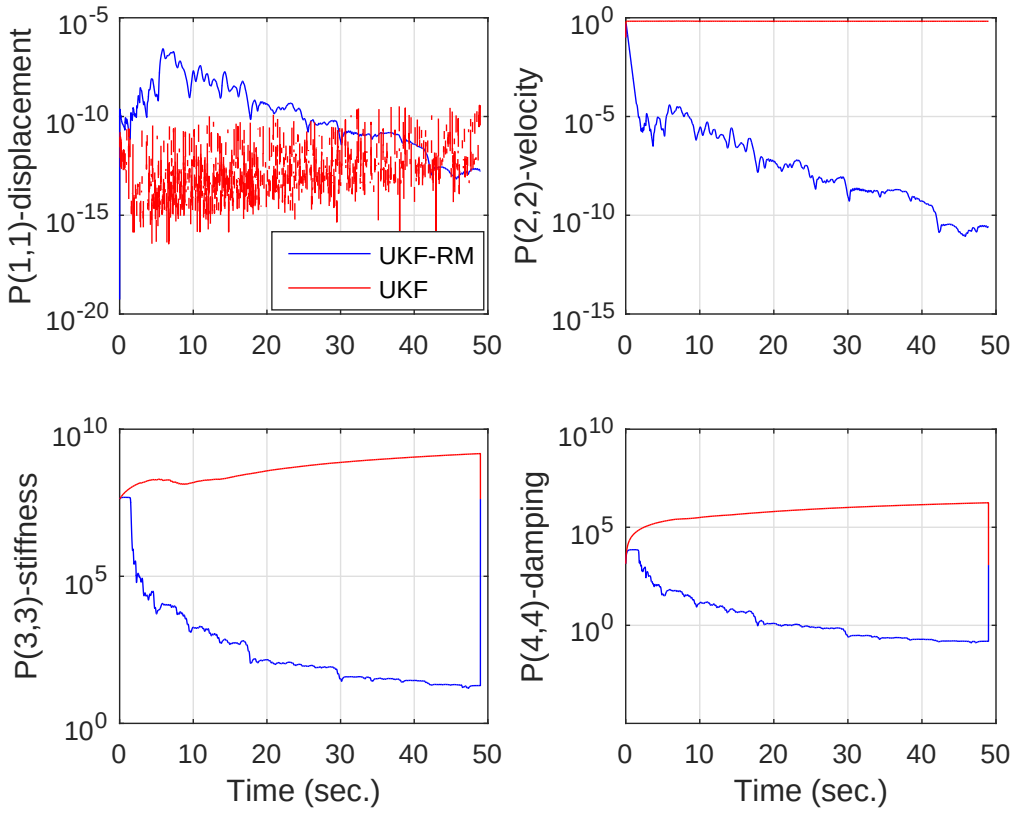

Figure 3-8: Change in elements of P with $\alpha_Q = 1/30$ and $\alpha_R = 1/30$ for UKF-RM and UKF

three regions based on the energy exerted on the structure, namely; before, during, and after significant duration. Before and after significant duration the response can be considered as linear response. For example, when only residual stiffness is of interest, UKF results showed that the filter has enough time to converge and thus convergence rate and track-ability may not be crucial performance targets of concern. However, when large earthquake response is of interest, the seismic energy is mostly dissipated by structural elements during significant duration. Thus, thus the convergence rate and tractability inside significant duration becomes significant.

Secondly, nonetheless, UKF needs manual fine tuning to achieve a successful estimation, which is not practical especially when seismic response is of concern. Thus, the performance of two estimation methods, the sensitivity of the estimation results to change in initial assumptions of the filters must be comparatively investigated.

These initial assumptions include; initial filter statistics, Q_0, R_0 and P_0; initial state vector, X_0 in both filters. Moreover, the sensitivity UKF-RM results to change in the scalar parameters α_Q and α_R should also be examined. To do so, the following sections will focus on the physical meanings of these parameters in the context of the filter. Simulations will be carried out to show the sensitivity of estimation results to the change in initial variables considering different response regions under seismic excitation.

Chapter 4

Simulation Results for Sensitivity Investigation with Linear Model

4.1 Sensitivity to initial filter statistics; Q_0, R_0 and P_0

Kalman filter requires filter statistics, P_0, Q_0 and R_0, to be known a-priori [50]. Currently, the widely accepted method in structural dynamics is tuning these statistics manually by trial and error method which is time-consuming and does not guarantee optimal solution. Although there are attempts for adaptive procedures, filter tuning does not have a commonly accepted procedure especially for the nonlinear variants of the Kalman filter such as Extended Kalman filter or Unscented Kalman Filter in structural dynamics area. In order to have an estimation method which can be applied in practical estimation problems related to structural dynamics, especially under earthquake loads, using candidate estimation algorithms the sensitivity of estimation results to initial selection of the filter statistics Q, R, P_0 should be investigated comparatively.

In Kalman Filter, the noise is assumed to be zero mean, and Gaussian. Consider the noise is additive. Q, process noise covariance, controls the evolution of the filter because it represents the uncertainty injected in the state equations providing. Thus,

it provides assistance to the filter to learn through measurements. If it is 0, filter does not learn any new information from the measurements [68, 56]. On the other hand, finding an analytical approximation for Q is almost impossible because it represents errors rising from many different sources, such as modeling errors, numerical errors, and computational errors. In addition, the ratio of its elements also holds importance during estimations.

P_0 and Q are closely related because they both contribute to the evolution of the filter. P_0 is especially effective during the transition from the initial transient response to the steady state response, which is controlled by both P and Q as the filter evolves.

One trick that is applied in the current conventional UKF method is to assign the initial P matrix, P_0, rather a large value than it should be, so that the filter is forced to converge quickly. However it is clear from above explanations that both P_0 and Q have significant roles in order to make a filter optimal. Selecting large P_0 values to enforce convergence may only be a quick fix, and can merely be a solution for practical applications when this complex interacting problem at hand.

R, measurement error covariance, may be the easiest noise statistics to deal with, as long as there is no measurement fault which requires special attention. In this study, measurement fault detection is not a focus. Thus R will be treated as measurement noise where the errors are assumed to be risen only from sources such as environment noise and inherent sensor noise. R is also zero mean, Gaussian noise and assumed to be additive similar to Q. Statistics of R can be determined from the measured data objectively, when there is no measurement fault. However, it will be treated as unknown in this section for the purpose of sensitivity investigation and for revealing the capabilities of the algorithms.

When searching for upper and lower bound for each initial filter parameter, the judging criteria is that the filter must be able to achieve a successful estimate of states from the beginning of the data, stiffness and damping from the beginning of the significant duration. The following suggestions on bounds is given based on this criteria.

4.1.1 Sensitivity to change in elements of Q:

Let's first consider the system in Section (3.3) and all other initial values are same as before except Q matrix. The elements of Q is changed one by one and convergence and stability of the filter is examined in both the "residual stiffness" and "significant duration" ranges of the response. Suggestions to choose Q are made accordingly.

The so called correct Q was found as Eq. (3.28):

$$Q = diag[10^{-4}, 10^{-1}, 2 \times 10^{5}, 2 \times 10^{2}] \tag{4.1}$$

in the previous section.

Starting with the element that corresponds to stiffness, $Q(3,3)$, first an upper bound value that results in convergent and stable state and parameter estimation has been searched. Usually when searching for such values it is common to increase/decrease the element value by a factor of 10. Thus with new Q matrix as

$$Q = diag[10^{-4}, 10^{-1}, 10^{6}, 2 \times 10^{2}] \tag{4.2}$$

estimation algorithm with UKF is run.

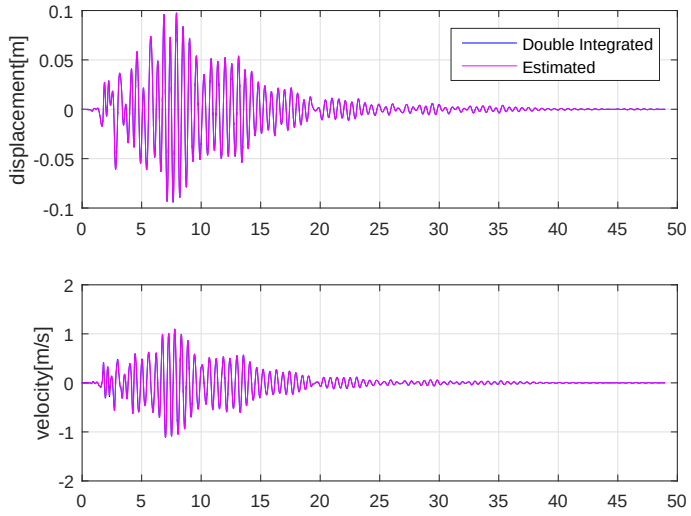

Figure 4-1: State estimation with UKF - $Q(3,3) = 10^{6}$

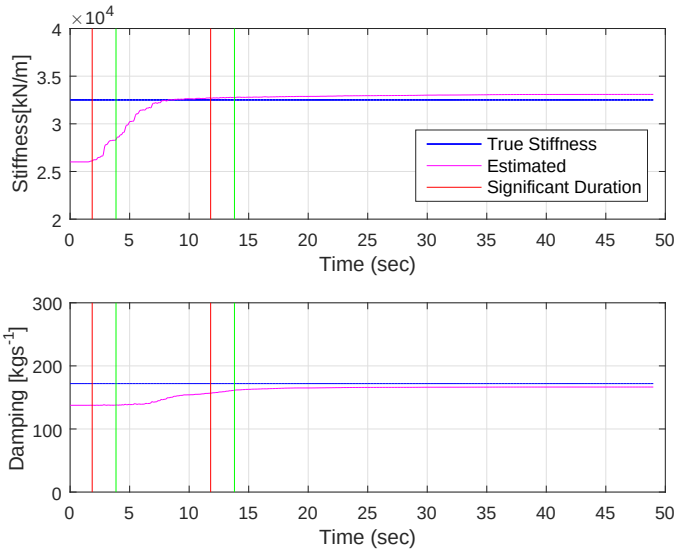

Figure 4-2: Parameter estimation with UKF - $Q(3,3) = 10^6$

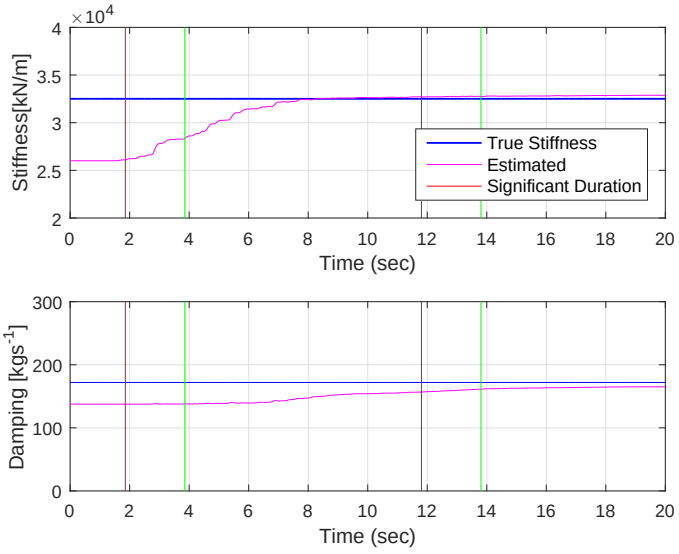

Figure 4-3: Parameter estimation with UKF - $Q(3,3) = 10^6$ (zoomed)

Figures (4-1,4-2) show the results of state and parameter estimations from UKF with $Q(3,3) = 10^6$. Although state estimations are correct, the stiffness estimation starts a small divergent behavior starting across the significant duration at about 9 sec. This is also displayed in the zoomed estimation results Figure (4-3). In addition, from the same figure it is observed that damping estimation convergence also slows

down. Although it stays stable after convergence, the full convergence to the true value could be achieved only after 20 sec.

Here there are two relevant information should be pointed out. First is the fact that this is a simulation example. Thus, the uncertainty is considered to be small, or controlled, when compared to a practical case and both algorithms strictly expected to perform good. However, even with a small change in one of the elements in Q, the corresponding parameter estimation results suffer.

Second point is, although the Q(4,4) was kept as the so-called true value as in previous section, the change in Q(3,3) had an negative effect on the estimation convergence of damping parameter. This is simply an evidence that the ratio of the elements of Q is as much as significant as the individual values itself. Small changes in the elements of Q which changes the ratio between the elements has a negative effect on the individual estimation results.

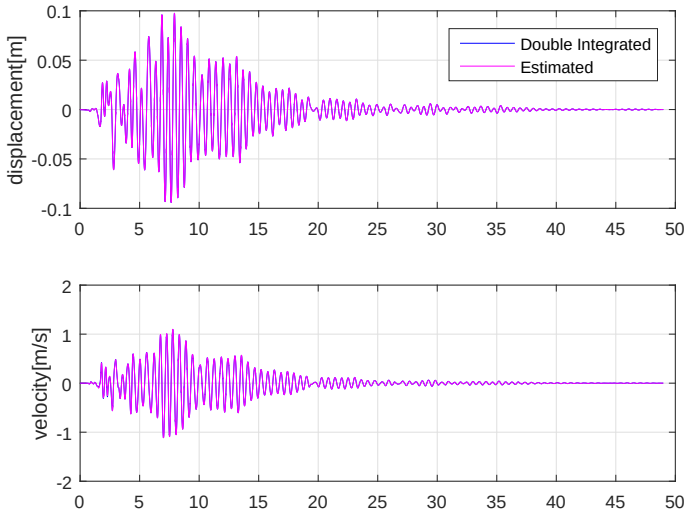

Figure 4-4: State estimation with UKF - $Q(3,3) = 10^7$

When $Q(3,3)$, is increased one more time by a factor of 10 as:

$$Q = diag[10^{-4}, 10^{-1}, 10^{7}, 2 \times 10^{2}] \tag{4.3}$$

The estimation results display the points made above more clear. Figures (4-4,4-

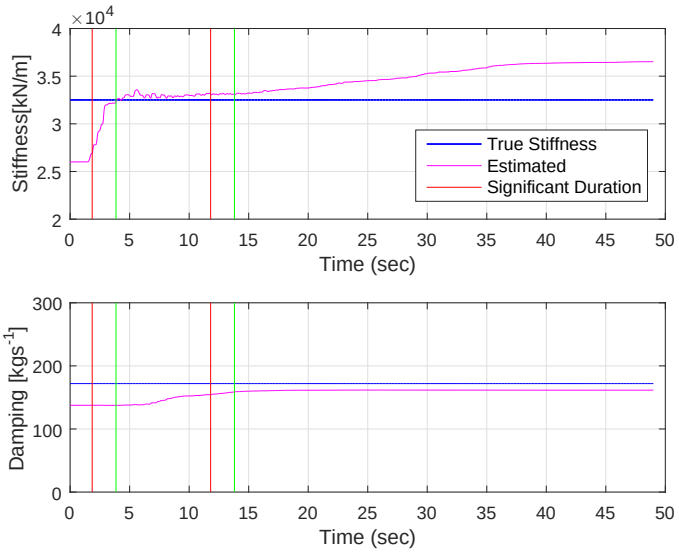

Figure 4-5: Parameter estimation with UKF - $Q(3,3) = 10^7$

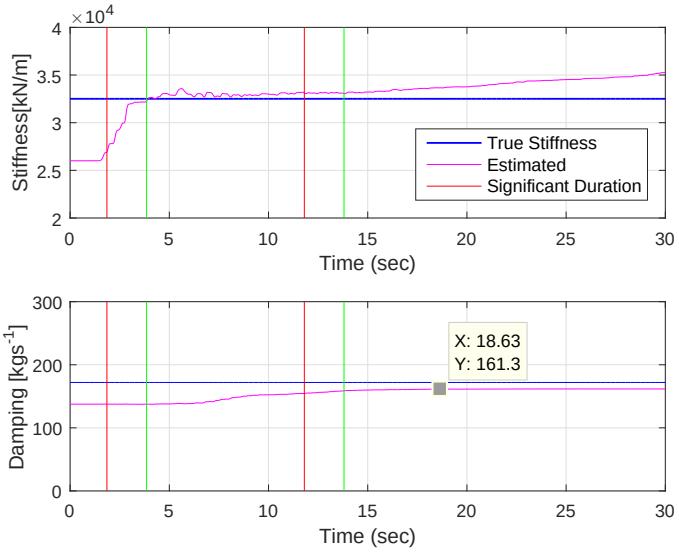

Figure 4-6: Parameter estimation with UKF - $Q(3,3) = 10^7$ (zoomed)

5) show the results of state and parameter estimations from UKF with $Q(3,3) = 10^7$. Although state estimations are correct, the weak performance of stiffness and damping estimations are more clear. Divergence occurs in stiffness estimation which starts inside the significant duration and becomes obvious at the later stages of the response. In fact, even the "residual stiffness" cannot be estimated. In addition, from Figure

(4-6) it is observed damping estimation convergence is even slower when compared to previous cases and eventually it converges to a smaller value than the true value.

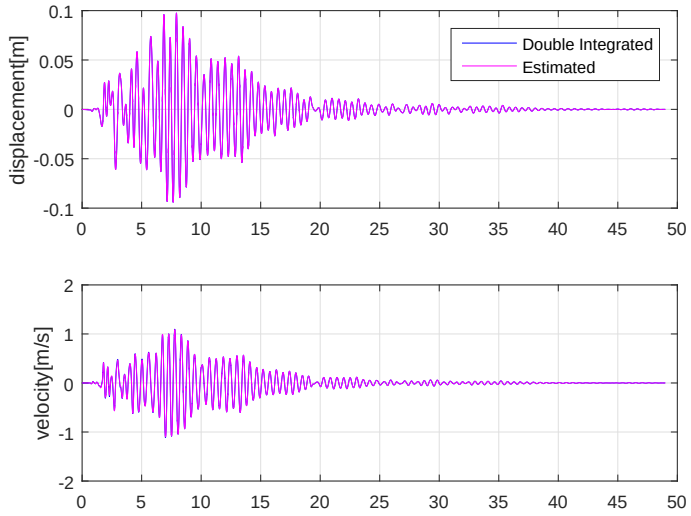

Figure 4-7: State estimation with UKF - $Q(3,3) = 10^5$

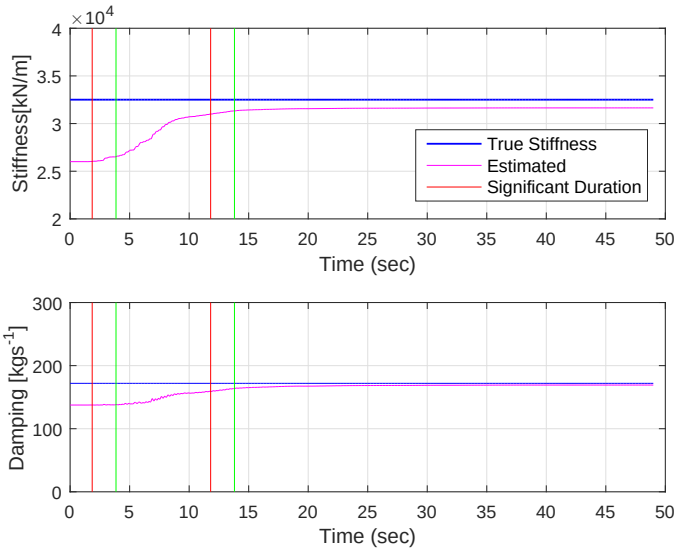

Figure 4-8: Parameter estimation with UKF - $Q(3,3) = 10^5$

Then $Q(3,3)$ is set to 10^5 to search for a lower bound value which results in a successful estimation of all states and parameters. Figures (4-7,4-8) shows the results

of state and parameter estimations from UKF with $Q(3,3) = 10^5$. Although state estimations are correct, stiffness estimation converges to a wrong (lower value) which means filter is unable to learn enough from the information provided to it to ensure a convergence. The only reason behind it is assigning a lower value to $Q(3,3)$, because the filter can estimate states and parameters correctly with Q equal to Eq. (3.28). Here it should be noted that the value of $Q(3,3)$ is lowered by only a factor two which shows UKF's extreme dependency to the correct assignment of noise statistics in order to be able to achieve a successful estimation. This is often referred as "fine tuning" in literature as Kalman Filter needs the exact noise statistics a-priori.

Another note is that estimation of parameters in a practical problem would not let the user to judge what is the correct final estimate. As the current condition is unknown, and in fact the target of the solution, by not using the exact correct noise statistics the results of the estimation may be misjudged or even may not be possible. This is one of the reasons why the sensitivity analysis is done using simulated data in a controlled environment.

Figure (4-9) displays the change in the elements of P matrix as the estimation propagates. As mentioned before P represents the error noise covariance in Kalman filter and it is the only evolving noise statistics in conventional UKF. Hence, it is the only learning source for the filter. When it is compared to Figure (3-8) P values in the case of failed estimation are close to the case (Section 3.3) where successful estimation is achieved. Thus, it can be concluded that there is no change in the evolution rate of the filter. Hence this the best conventional UKF can do and it can only handle small deviations from the true Q matrix.

Finally, $Q(3,3)$ is lowered one more time by a factor of 10 and set to 10^4 to study the UKF behavior. State estimations were successfully obtained. However, parameter estimations suffer from the performance of the filter as depicted in Figure (4-10). Stiffness estimation converges to a lower value which means filter performance depends very much on the initially assigned Q value because of the lack of adaptation. In addition, as the ratio of the elements of Q to each other is also important to ensure a good filter performance, when the ratio is disturbed by changing only one element

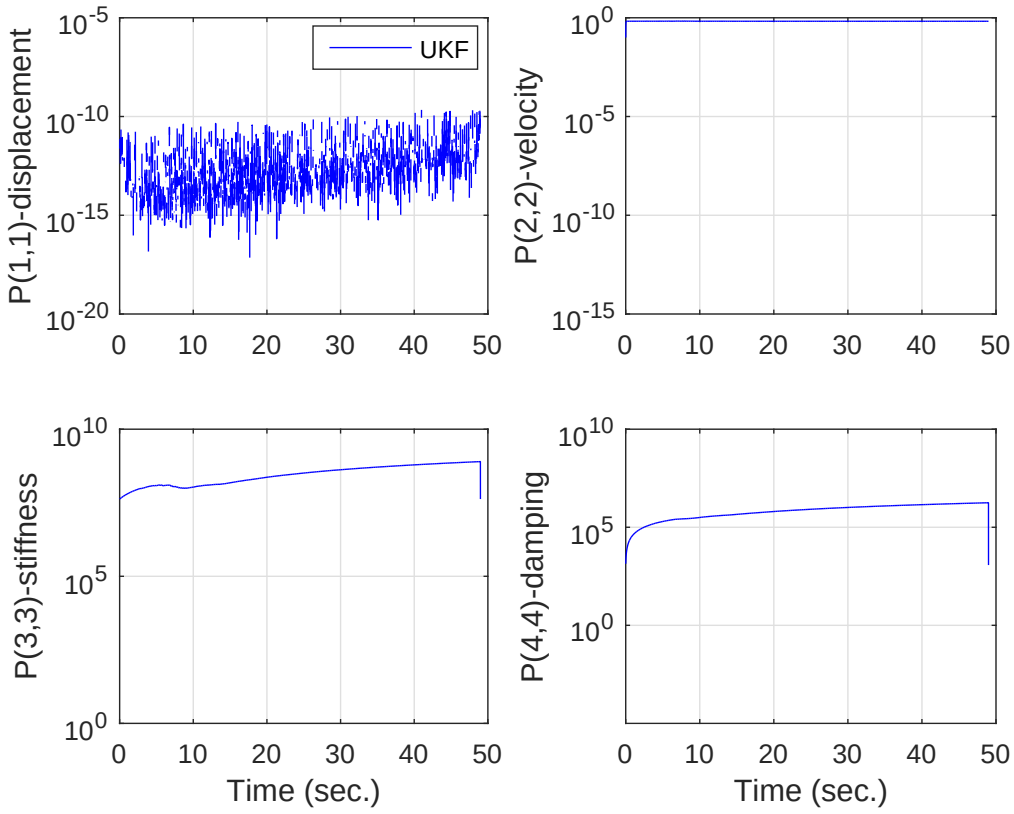

Figure 4-9: Change in P values with UKF - $Q(3,3) = 10^5$

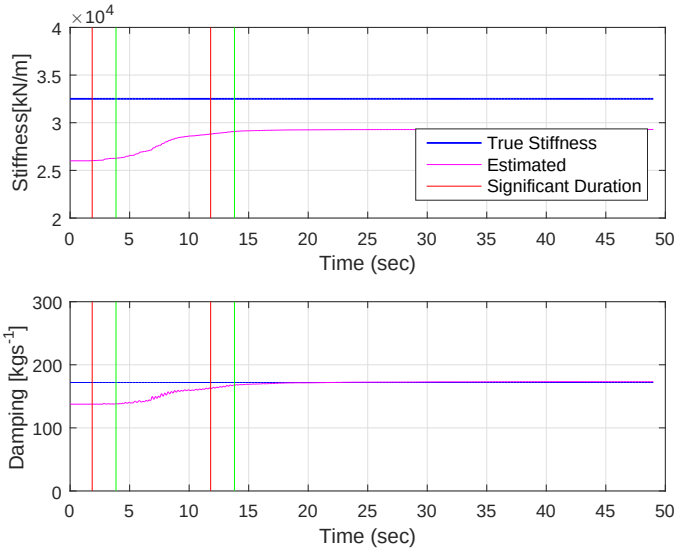

Figure 4-10: Parameter estimations with UKF - $Q(3,3) = 10^4$

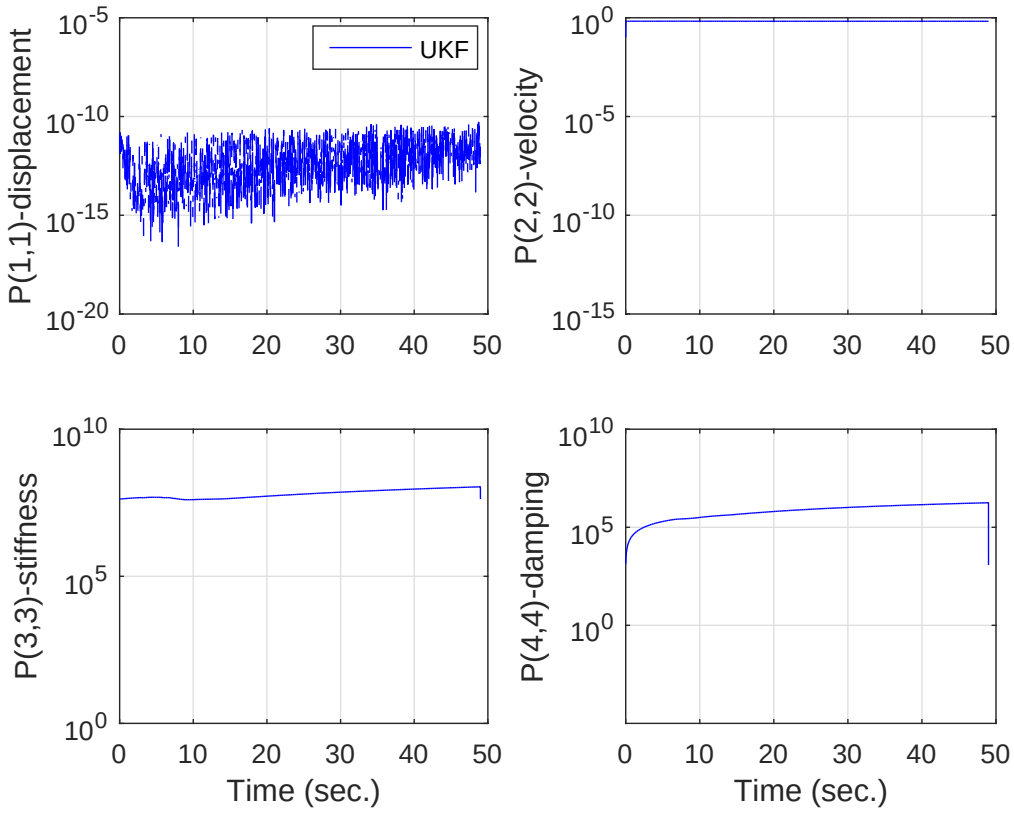

Figure 4-11: Change in P values with UKF - $Q(3,3) = 10^4$

of the matrix (corresponding to stiffness parameter) the second parameter, damping, also suffers from divergence.

The poor evolution ability of the filter is also evident from the rate of change in P element as depicted in Figure (4-11). As the assigned $Q(3,3)$ is small, $P(3,3)$ stays almost constant and equal to its initial value as the estimation proceeds. Hence, filter cannot learn new information as it becomes available.

When such lower and upper bounds is searched for UKF-RM with similar methodology above, it has been found that the range can be selected is much wider.

As for the lower bound, it seems there is none. As a representative, estimation results of states and parameters that correspond to $Q(3,3) = 10^{-20}$ are presented as follows. From Figure (4-12) that displacement and velocity response can be obtained successfully with UKF-RM even though $Q(3,3)$ has been intentionally set to a very

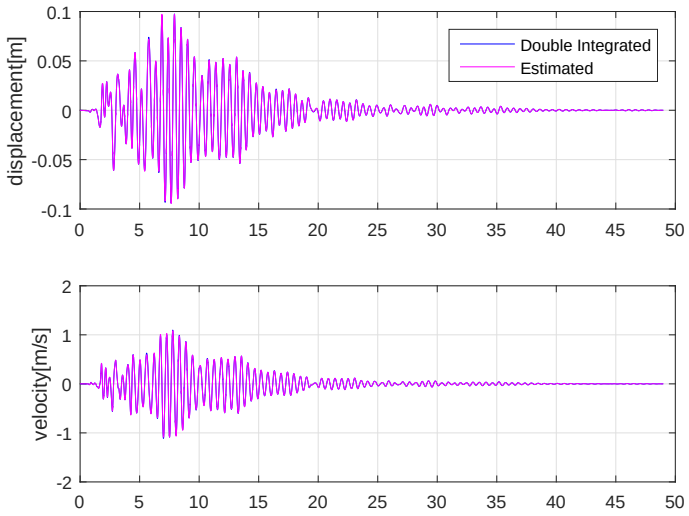

Figure 4-12: State estimation results with UKF-RM - $Q(3,3) = 10^{-20}$ and $\alpha_Q = 1/30$ and $\alpha_R = 1/30$

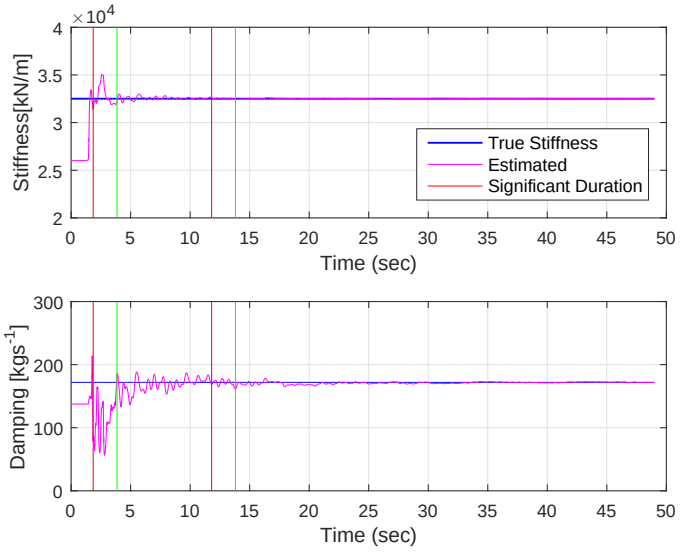

Figure 4-13: Parameter estimation results with UKF-RM - $Q(3,3) = 10^{-20}$ and $\alpha_Q = 1/30$ and $\alpha_R = 1/30$

small value. Figure (4-13) shows the parameter estimation results. We can clearly see that when the significant duration starts, the convergence is achieved for both stiffness and damping. The mean percentage error between the two vertical green lines is only 0.2% for stiffness estimation. When damping estimation is examined, although

the initial ripples in damping estimation seems larger than stiffness estimation, the percentage error of the mean between the vertical green lines is about 2.1%. It should be noted that when a merely smaller value was set in UKF, parameter estimation results was very much affected as evolution rate of the filter was very slow. The results obtained with UKF-RM proves that with Robbins-Monro stochastic scheme, Q can be updated and thus filter can reach to a successful parameter estimation even when a wrong initial Q is set.

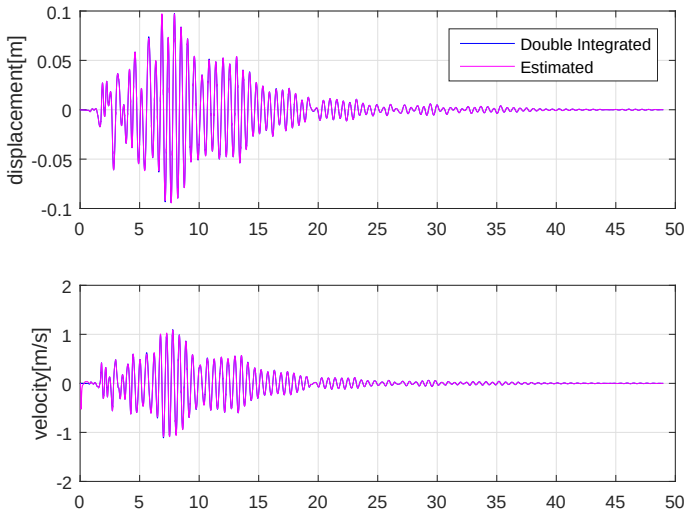

Figure 4-14: State estimation results with UKF-RM - $Q(3,3) = 10^{13}$ and $\alpha_Q = 1/30$ and $\alpha_R = 1/30$

As for the higher bound, $Q(3,3) = 10^{13}$ seems to be the value as filter results in divergence when $Q(3,3) = 1e14$. From Figure (4-14) that displacement and velocity response can be obtained successfully with UKF-RM even though $Q(3,3)$ has been intentionally set to a large value. Figure (4-15) shows the parameter estimation results. We can clearly see that 2 seconds after the significant duration the convergence is achieved for both stiffness and damping. In both stiffness and damping estimation although there is a small ripple right after the convergence the estimation is considered stable as the mean percentage error between the two vertical green lines (2 sec after the beginning and end of the significant duration) is less than 1%.

With the above investigation when $Q(3,3)$ is assigned a value with in the $[10^{-20}\ 10^{13}]$

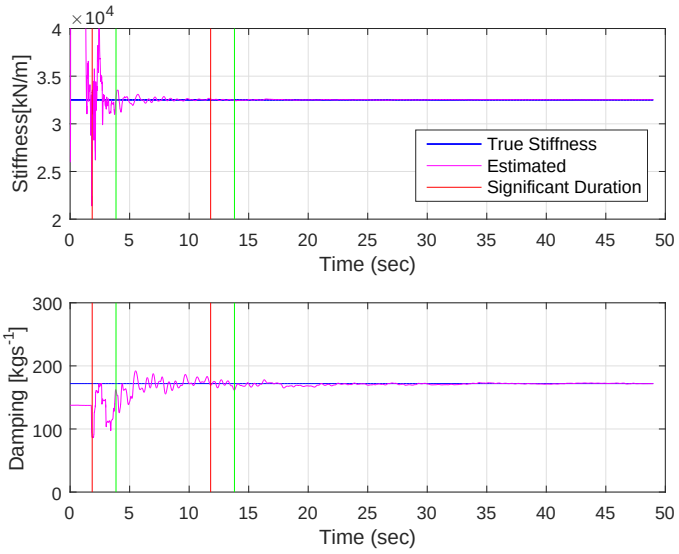

Figure 4-15: Parameter estimation results with UKF-RM - $Q(3,3) = 10^{13}$ and $\alpha_Q = 1/30$ and $\alpha_R = 1/30$

limits, the proposed method is able to reach stable and consistent successful state and parameter estimation results. Given limits for initial selection of an element in Q matrix is much wider and provides flexibility in the analysis. This conclusion hold true for both "residual stiffness" and the stiffness estimation inside the significant duration which corresponds to nonlinear behavior range for this case. Additionally the change in Q, R and P matrix elements for both both lower and upper bound of $Q(3,3)$ are presented as follows in Figures (4-16-4-21). From these figures it is evident that although the assigned Q value for stiffness is wrong, the filter adapts itself as the new information becomes available and does it in a quick manner as all estimation results in a satisfactory performance even inside the significant duration. Thus, the proposed method is promising especially to be applied in problems of practical significance. In the following chapter practical application of UKF-RM to a variety of practical problems will be studied.

Now let's look at the ratio of each Q element as the estimation evolves. Figure (4-22) presents the ratio of $Q(3,3)/Q(4,4)$ which represents the change of the ratio of Q elements that corresponds to stiffness parameter to Q elements that corresponds to damping parameter. Both parameter converges to their true values just around 5

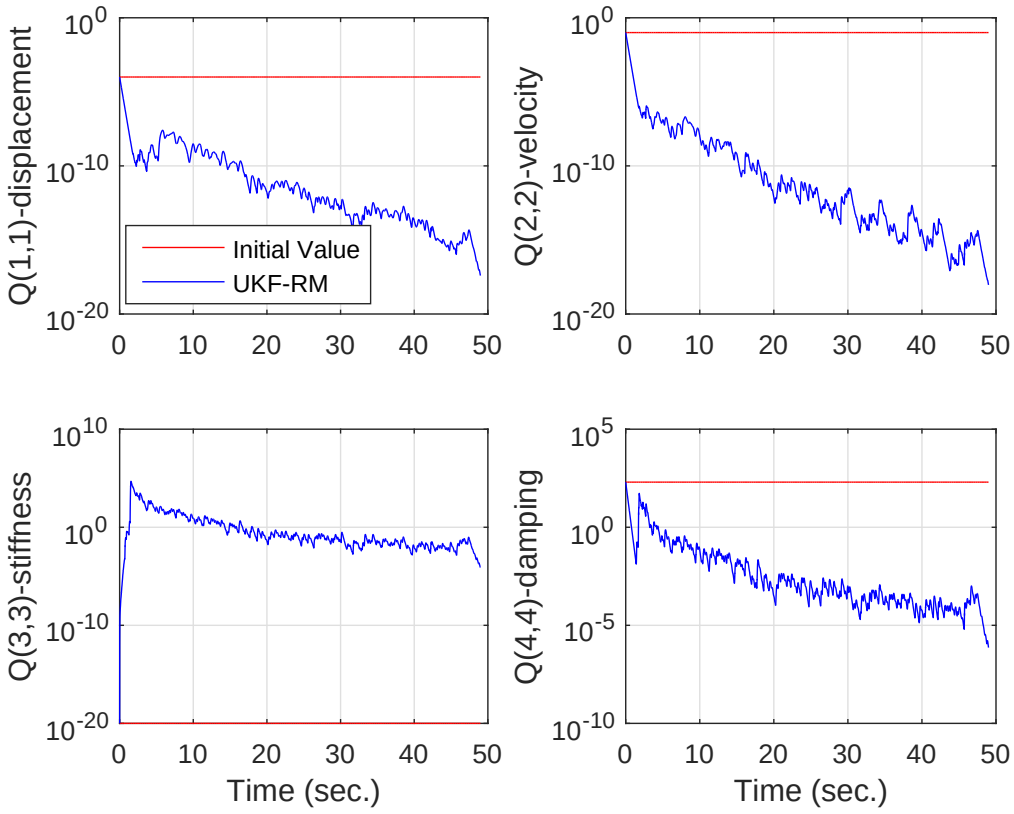

Figure 4-16: Change in Q values with UKF-RM - $Q(3,3) = 10^{-20}$ and $\alpha_Q = 1/30$ and $\alpha_R = 1/30$

seconds. Before this time, both $Q(3,3)$ and $Q(4,4)$ try to settle down as they try to achieve convergence, hence the ratio of these values is not constant. After 5 seconds, the ratio of change in Q elements becomes constant as convergence occurs for both parameters.

Furthermore, Figure (4-23) presents the ratio of $Q(3,3)/Q(1,1)$ which represents the change of the ratio of Q elements that corresponds to stiffness parameter to Q elements that corresponds to displacement state. Figure (4-24) presents the ratio of $Q(3,3)/Q(2,2)$ which represents the change of the ratio of Q elements that corresponds to stiffness parameter to Q elements that corresponds to velocity state.

Thus, the change in ratio between the elements of Q as the estimation evolves proves that UKF-RM is capable to update Q by scaling the noise covariance matrix by multiple factors and provides a robust estimation scheme.

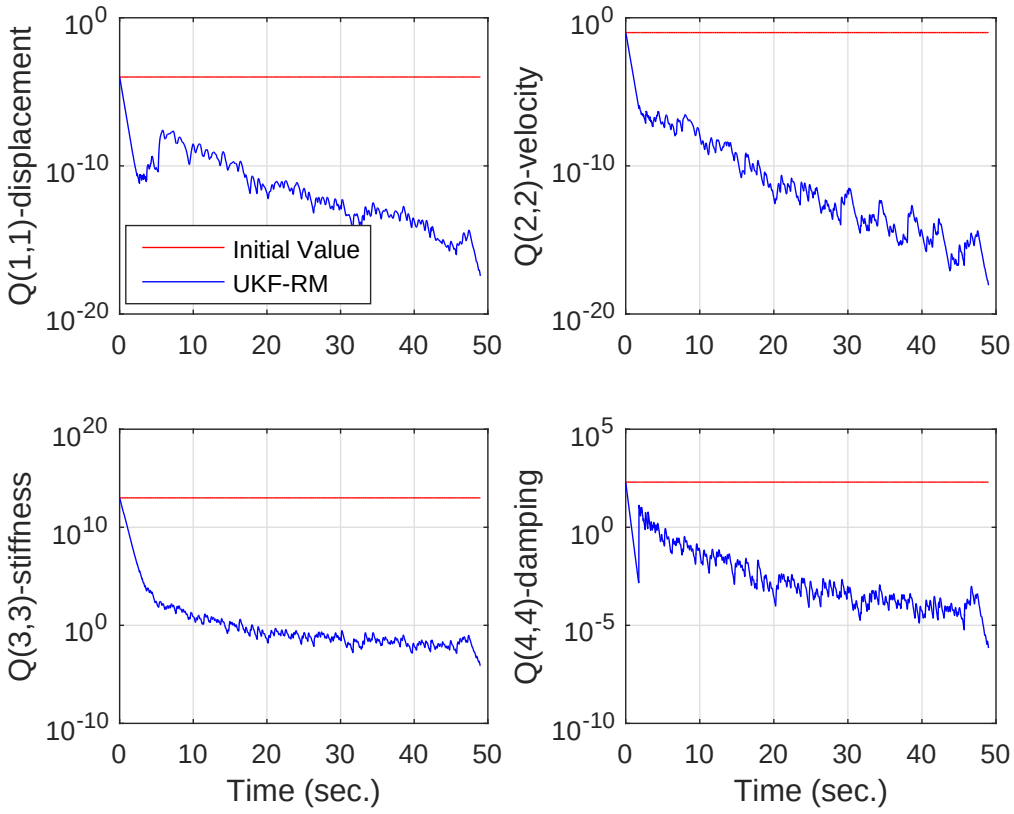

Figure 4-17: Change in Q values with UKF-RM - $Q(3,3) = 10^{13}$ and $\alpha_Q = 1/30$ and $\alpha_R = 1/30$

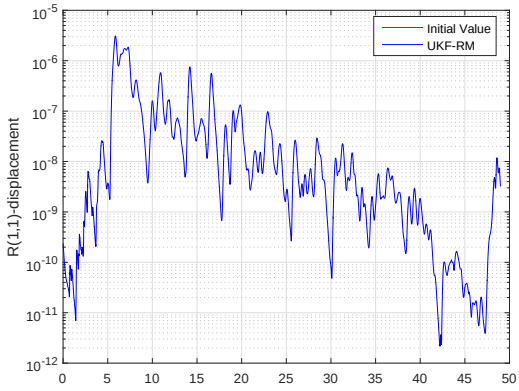

Figure 4-18: Change in R values with UKF-RM - $Q(3,3) = 10^{-20}$ and $\alpha_Q = 1/30$ and $\alpha_R = 1/30$

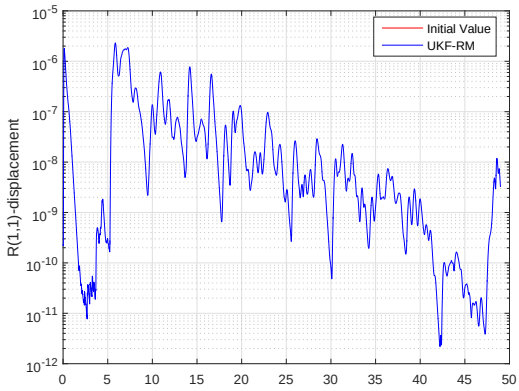

Figure 4-19: Change in R values with UKF-RM - $Q(3,3) = 10^{13}$ and $\alpha_Q = 1/30$ and $\alpha_R = 1/30$

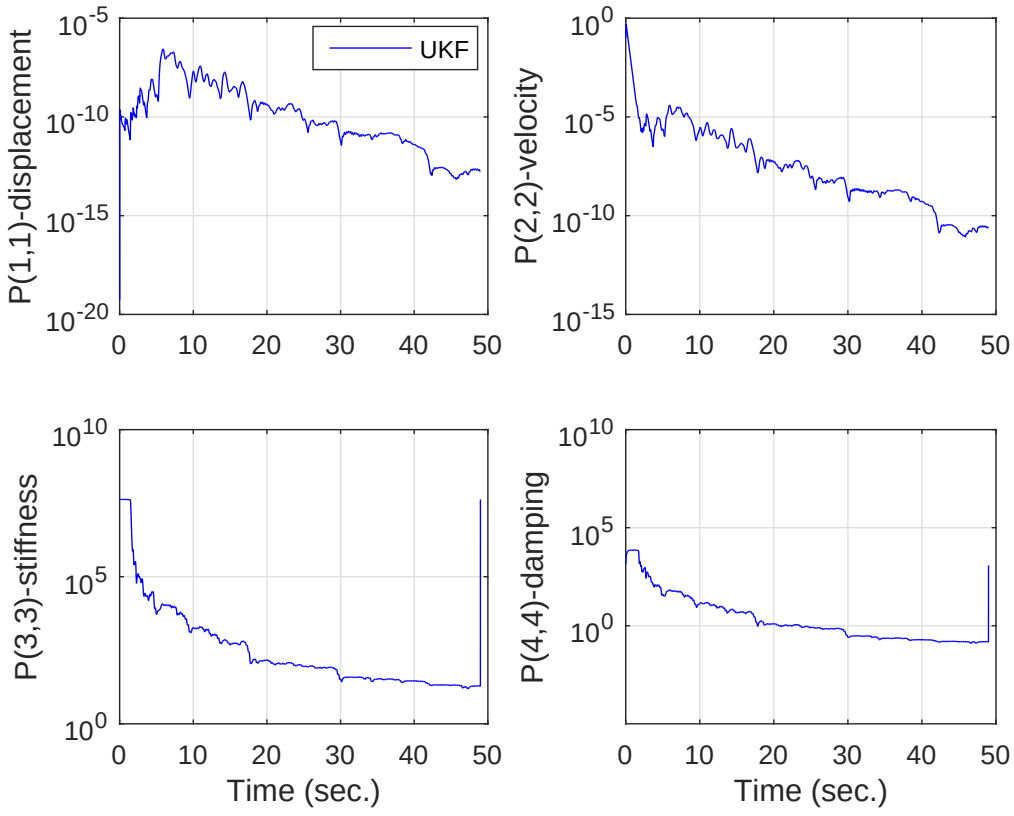

Figure 4-20: Change in P values with UKF-RM - $Q(3,3) = 10^{-20}$ and $\alpha_Q = 1/30$ and $\alpha_R = 1/30$

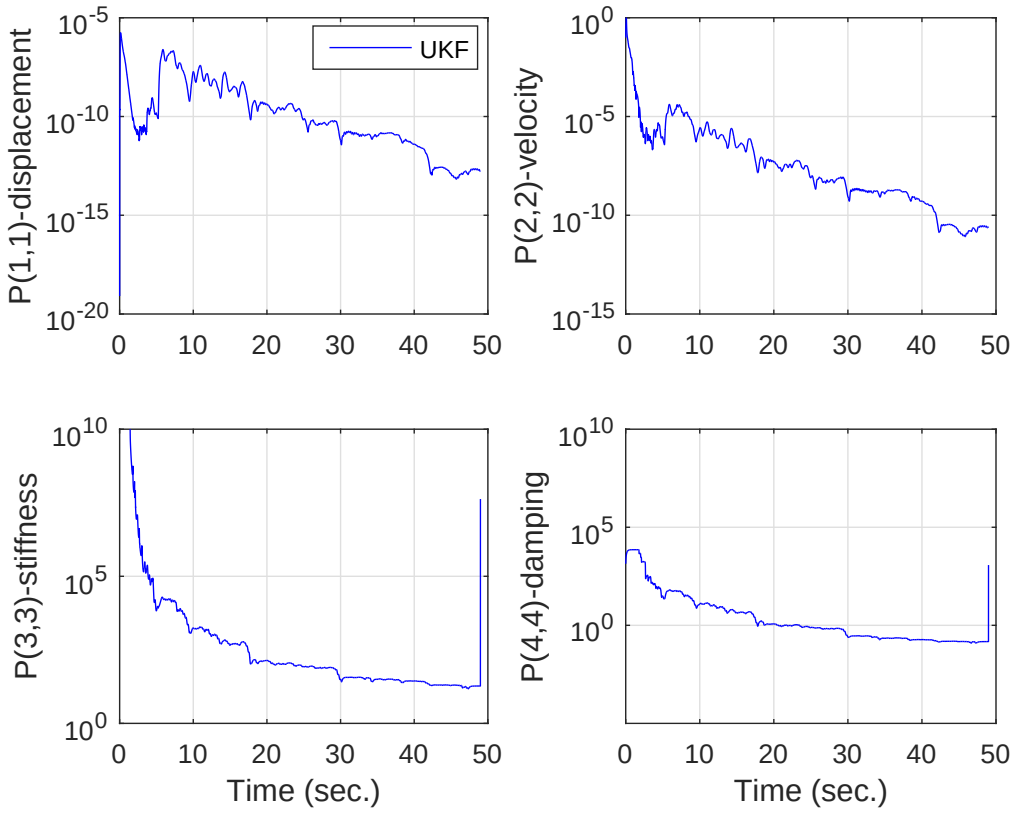

Figure 4-21: Change in P values with UKF-RM - $Q(3,3) = 10^{13}$ and $\alpha_Q = 1/30$ and $\alpha_R = 1/30$

In a similar manner, lower and upper bounds also searched for $Q(4,4)$ which relates to damping parameter. The lower and upper bounds for $Q(4,4)$ element in Q matrix are found as $[10^{-20}\ 10^{8}]$. The proposed method is able to reach stable and consistent successful state and parameter estimation results within the given limits of initial value for $Q(4,4)$. When $Q(4,4)$ is set to $10^{9}9$ the algorithm encounters a numerical failure and stops estimation. Thus $Q(4,4) = 10^{8}$ is selected as the upper bound. For the lower bound, as in the case for $Q(3,3)$ it seems like there is no limit also for $Q(4,4)$. Even when it is assigned as equal to 10^{-200} the estimation proceeds and results in successful state and parameter estimation. However, as setting such a low value for Q is not realistic the lower bound is limited to 10^{-20}. Results of state and parameter estimations are given in Figures (4-25) and (4-26) as representative when $Q(4,4) = 10^{8}$. Corresponding change in Q, R and P changes during estimation

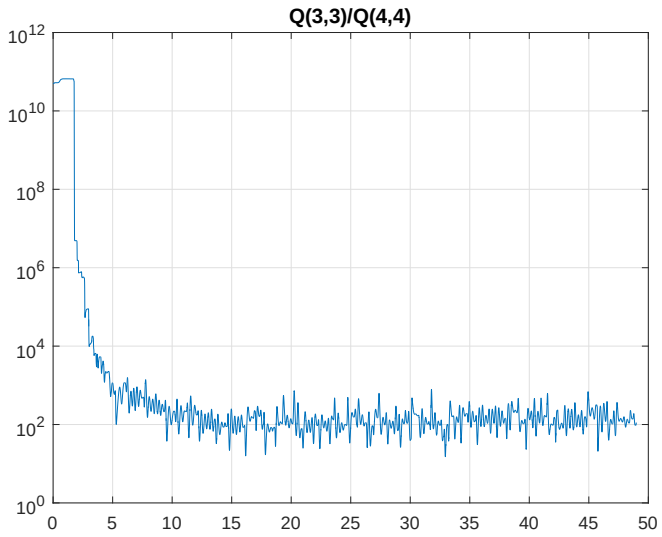

Figure 4-22: Ratio of $Q(3,3)/Q(4,4)$ with UKF-RM - $Q(3,3) = 1e13$ and $\alpha_Q = 1/30$ and $\alpha_R = 1/30$

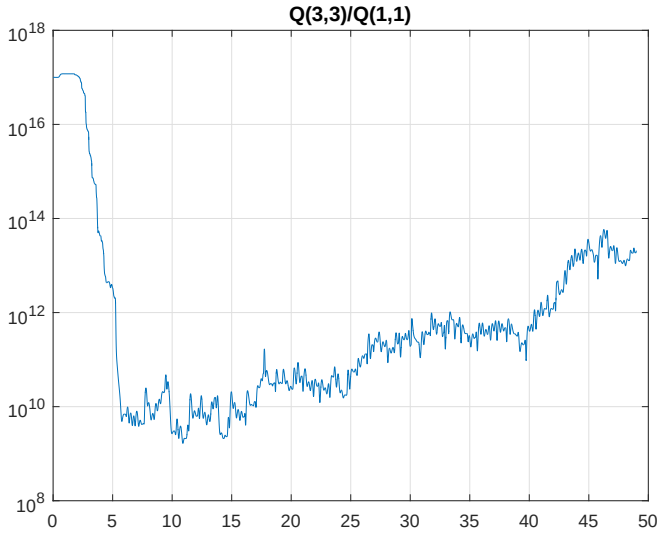

Figure 4-23: Ratio of $Q(3,3)/Q(1,1)$ with UKF-RM - $Q(3,3) = 1e13$ and $\alpha_Q = 1/30$ and $\alpha_R = 1/30$

are depicted in Figures ((4-27-4-29)).

Thus, it can be concluded that initial values of the elements in Q matrix which correspond to unknown parameters can be assigned in a flexible way when this problem setting is considered. As given before, the problem consists of 20% modeling

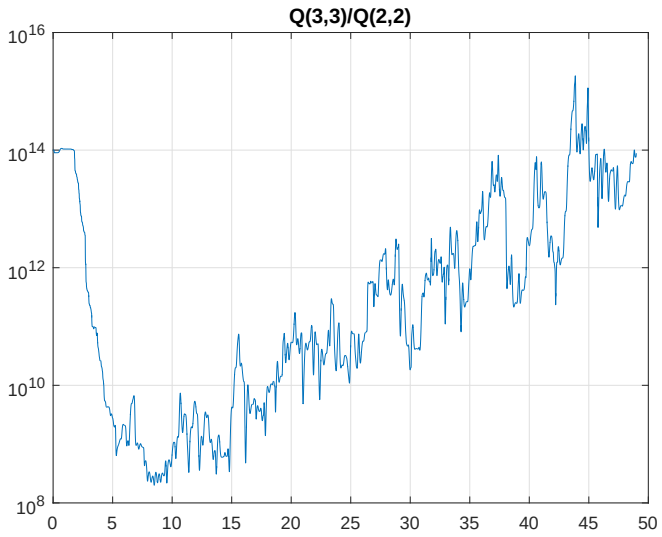

Figure 4-24: Ratio of $Q(3,3)/Q(2,2)$ with UKF-RM - $Q(3,3) = 1e13$ and $\alpha_Q = 1/30$ and $\alpha_R = 1/30$

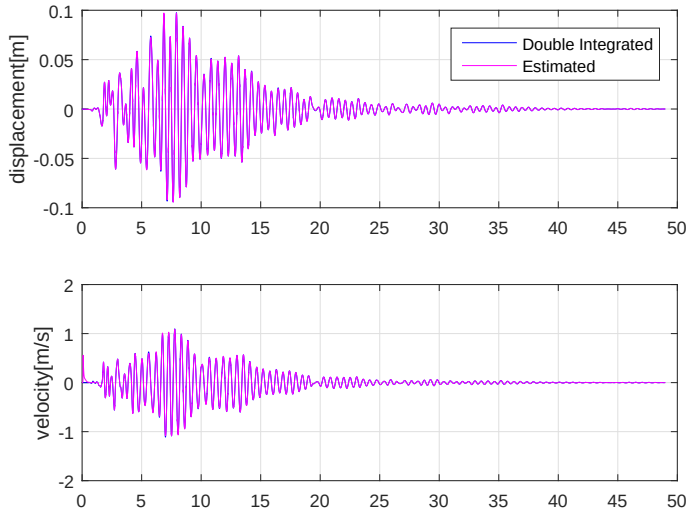

Figure 4-25: State estimation results with UKF-RM - $Q(4,4) = 10^8$ and $\alpha_Q = 1/30$ and $\alpha_R = 1/30$

error as initial parameter assumption and P_0 is given as in Eq. (3.27) and there is no measurement error. Although both states and parameters were successfully estimated regardless of the assigned initial values of $Q(3,3)$ and $Q(4,4)$, it should be carefully noted the simulations are in a controlled environment and in practice there is larger

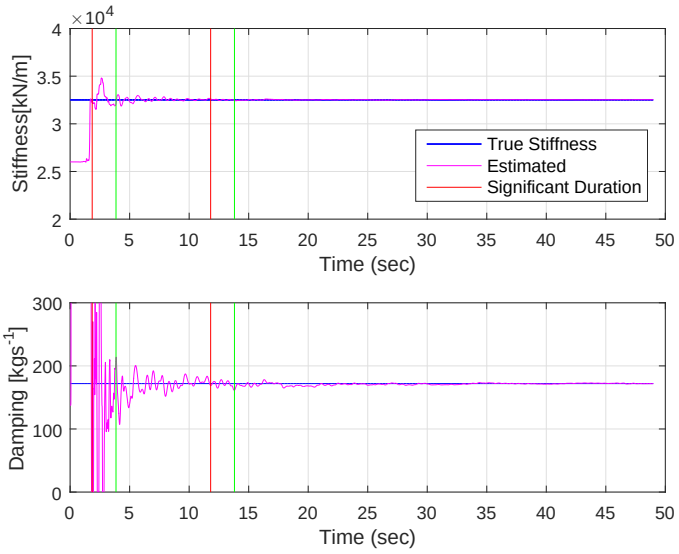

Figure 4-26: Parameter estimation results with UKF-RM - $Q(4,4) = 10^8$ and $\alpha_Q = 1/30$ and $\alpha_R = 1/30$

uncertainty. In theory, as Q becomes close to zero the evolution ability of the filter also decreases for conventional UKF. Although this drawback can be overcome using UKF-RM as shown with the above investigation, it is recommended to assign initial values of Q for parameters at the order (or higher) of the parameter value itself.

Following, sensitivity to change in elements of Q that correspond to states, $Q(1,1)$ and $Q(2,2)$ is investigated. First, let's consider $Q(1,1)$ which corresponds to the process noise covariance of displacement state. The lower and upper bounds for $Q(1,1)$ element in Q matrix are found as $[10^{-17}\ 10^{31}]$, which results in successful estimation of both states and parameters starting from the beginning of the significant duration. When $Q(1,1)$ is set to 10^{-18} the algorithm encounters a numerical failure and stops estimation. Thus $Q(1,1) = 10^{-17}$ is selected as the lower bound. Results of state and parameter estimations are given in Figures (4-30) and (4-31) when $Q(1,1) = 10^{-17}$. Moreover, when $Q(1,1)$ is set to 10^{32} or a larger value divergence occur in state estimations, namely in velocity. When $Q(1,1) = 1e31$ both states and parameters can be estimated successfully. Results of state and parameter estimations are given in Figures (4-32) and (4-33) when $Q(1,1) = 10^{31}$. However, successful damping and stiffness parameter estimations can only be achieved after the significant duration

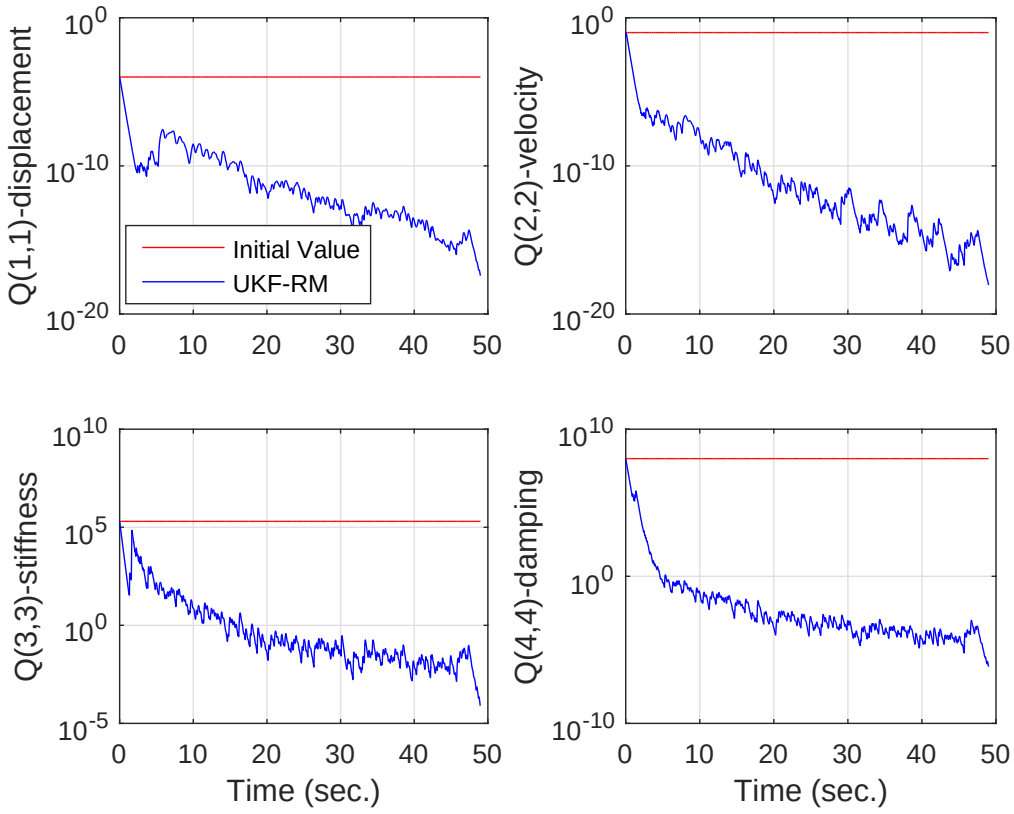

Figure 4-27: Change in Q values with UKF-RM - $Q(4,4) = 10^8$ and $\alpha_Q = 1/30$ and $\alpha_R = 1/30$

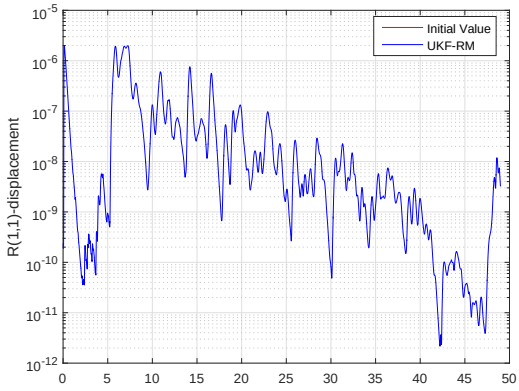

Figure 4-28: Change in R values with UKF-RM - $Q(4,4) = 10^8$ and $\alpha_Q = 1/30$ and $\alpha_R = 1/30$

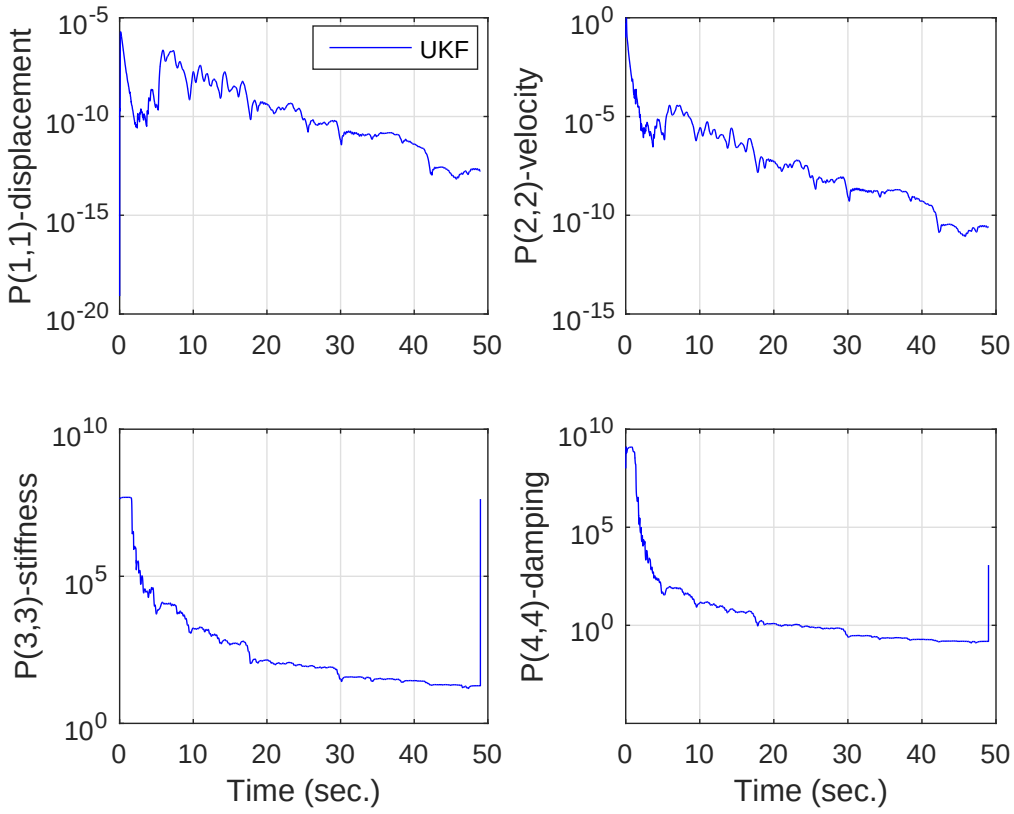

Figure 4-29: Change in P values with UKF-RM - $Q(4,4) = 10^8$ and $\alpha_Q = 1/30$ and $\alpha_R = 1/30$

ends. Thus, by lowering the upper bound gradually an acceptable upper bound for the criteria in consideration is found as 10^8. 2 seconds after the start of the significant duration, both stiffness and damping results in an estimation with an error less than 5% away from the true value. Results of state and parameter estimations are given in Figures (4-34) and (4-35) when $Q(1,1) = 10^8$.

Similarly, the lower and upper bounds for $Q(2,2)$ element (which corresponds to velocity) in Q matrix are found as $[10^{-20}\ 10^{12}]$, which results in successful estimation of both states and parameters starting from the beginning of the significant duration. For the lower bound, as in the case for $Q(3,3)$ it seems like there is no limit also for $Q(2,2)$. Even when it is assigned as equal to 10^{-200} the estimation proceeds and results in successful state and parameter estimation. However, as setting such a low value for Q is not realistic the lower bound is limited to 10^{-20}. Results of state and

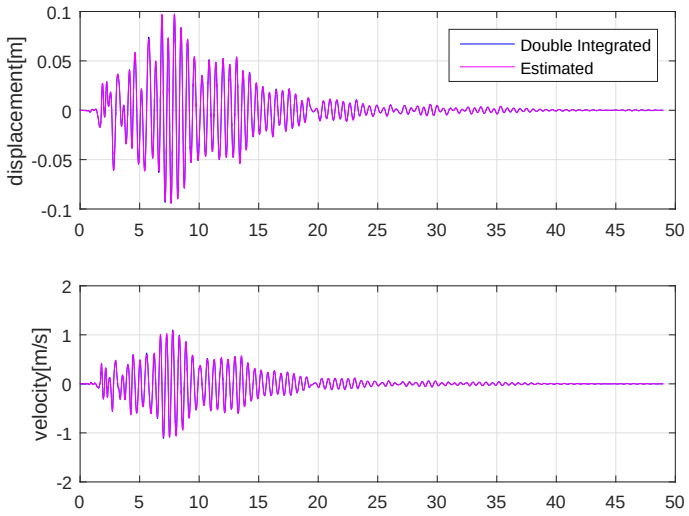

Figure 4-30: State estimation results with UKF-RM - $Q(1,1) = 10^{-17}$ and $\alpha_Q = 1/30$ and $\alpha_R = 1/30$

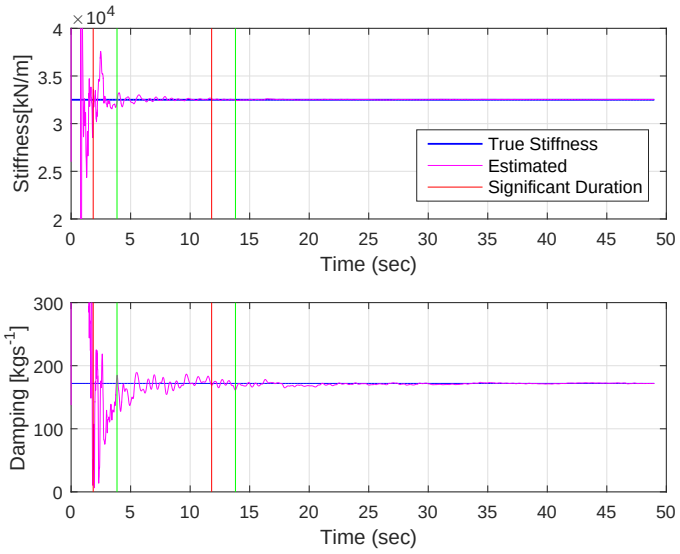

Figure 4-31: Parameter estimation results with UKF-RM - $Q(1,1) = 10^{-17}$ and $\alpha_Q = 1/30$ and $\alpha_R = 1/30$

parameter estimations are given in Figures (4-36) and (4-37) as representative when $Q(2,2) = 10^{-20}$.

For the upper bound, when $Q(2,2) = 10^{24}$ or larger than the velocity estimation starts to get affected adversely, thus divergence occurs in velocity state. Displacement

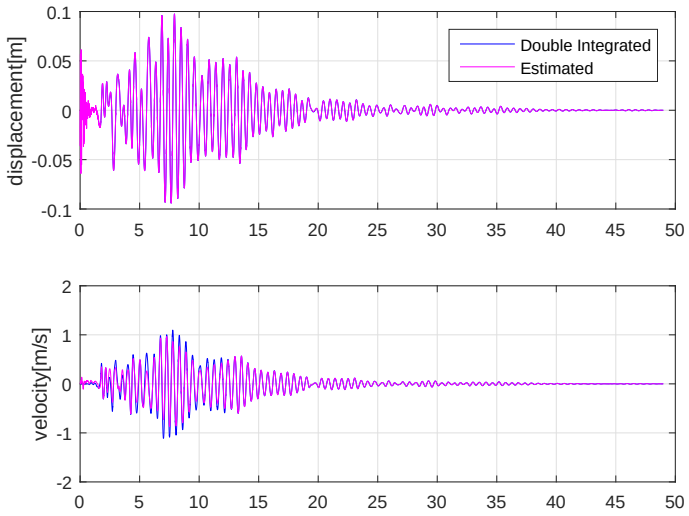

Figure 4-32: State estimation results with UKF-RM - $Q(1,1) = 10^{31}$ and $\alpha_Q = 1/30$ and $\alpha_R = 1/30$

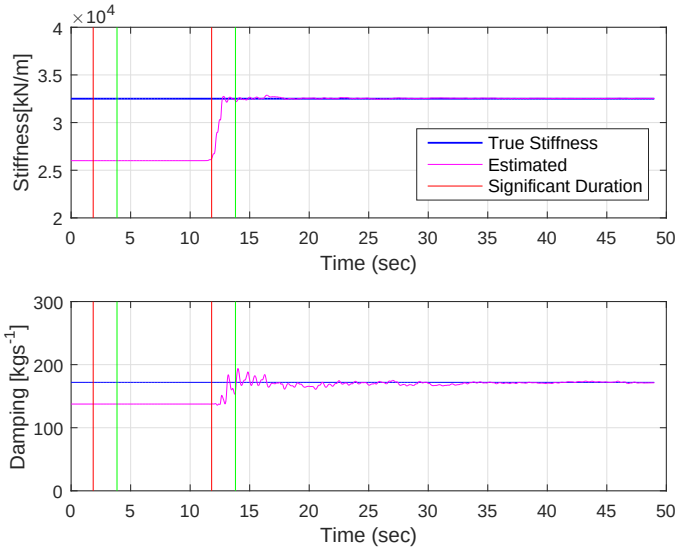

Figure 4-33: Parameter estimation results with UKF-RM - $Q(1,1) = 10^{31}$ and $\alpha_Q = 1/30$ and $\alpha_R = 1/30$

and both parameters can be estimated successfully. When it is set to $Q(2,2) = 10^{23}$ both states (Figure 4-38) and damping are estimated satisfactorily however stiffness estimation was only successful after the significant duration ends (Figure 4-39). The upper bound which can satisfy the stiffness estimation criteria is found as $Q(2,2) =$

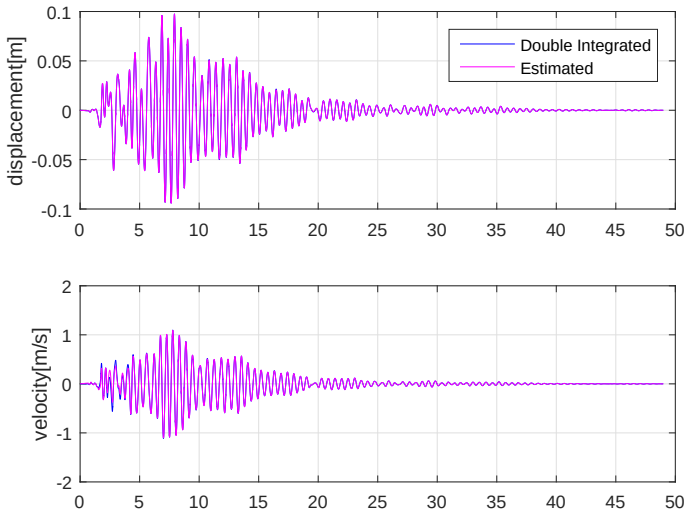

Figure 4-34: State estimation results with UKF-RM - $Q(1,1) = 10^8$ and $\alpha_Q = 1/30$ and $\alpha_R = 1/30$

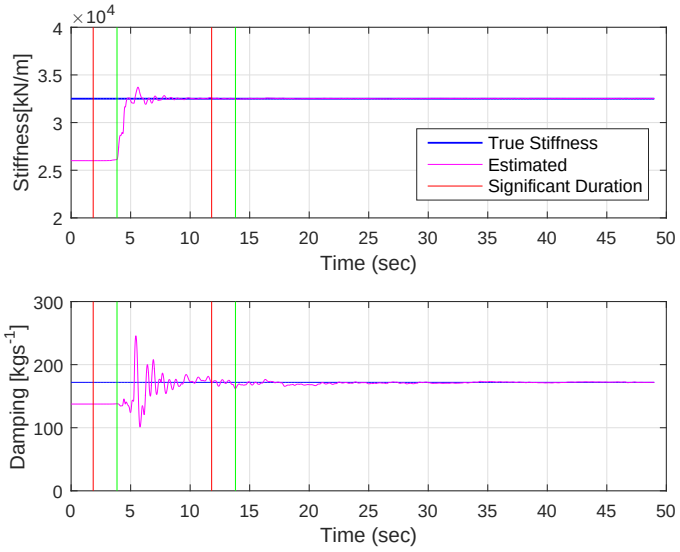

Figure 4-35: Parameter estimation results with UKF-RM - $Q(1,1) = 10^8$ and $\alpha_Q = 1/30$ and $\alpha_R = 1/30$

10^{12}. The proposed method is able to reach stable and consistent successful state and parameter estimation results within the given limits of initial value for $Q(2,2)$. Results of state and parameter estimations are given in Figures (4-40) and (4-41) as representative when $Q(2,2) = 10^{12}$.

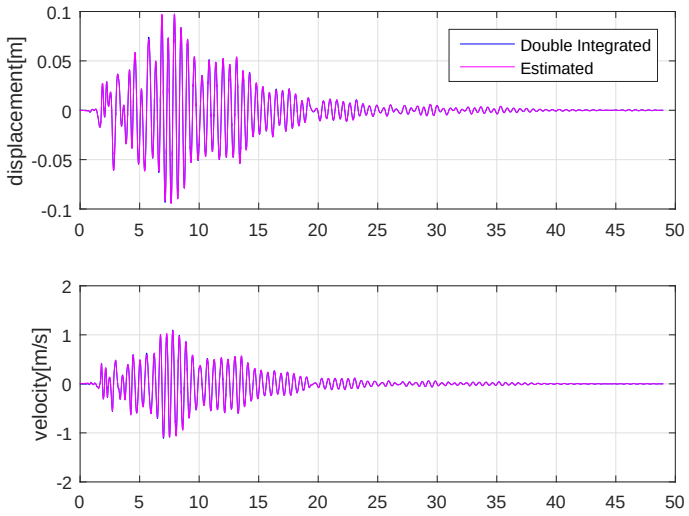

Figure 4-36: State estimation results with UKF-RM - $Q(2,2) = 10^{-20}$ and $\alpha_Q = 1/30$ and $\alpha_R = 1/30$

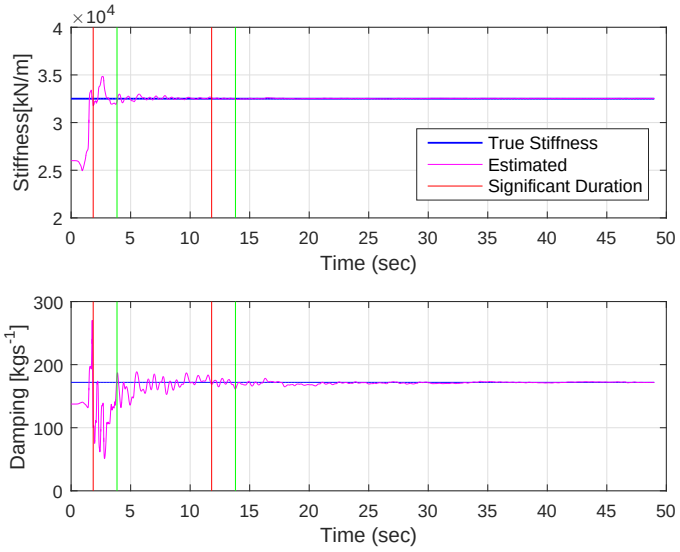

Figure 4-37: Parameter estimation results with UKF-RM - $Q(2,2) = 10^{-20}$ and $\alpha_Q = 1/30$ and $\alpha_R = 1/30$

Although UKF-RM can overcome incorrect initial values as shown with the above investigation for both states, assigning $Q(1,1)$ and $Q(2,2)$ a very large value is not likely. It is recommended to assign initial values of Q for states at the order of the states' maximum value itself or a lower value.

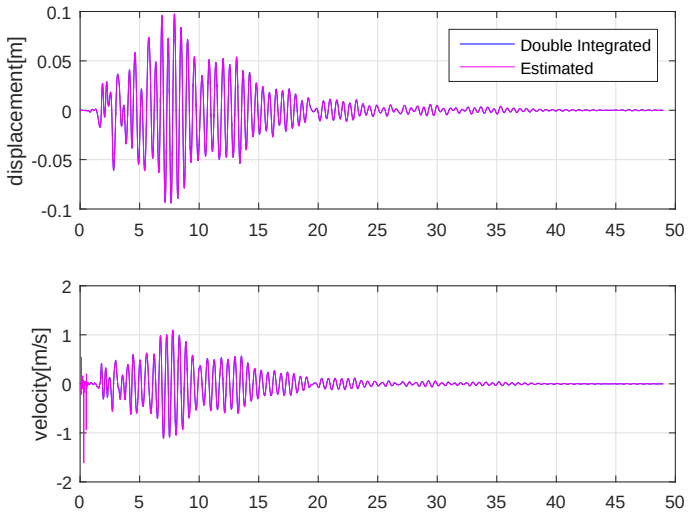

Figure 4-38: State estimation results with UKF-RM - $Q(2,2) = 10^{23}$ and $\alpha_Q = 1/30$ and $\alpha_R = 1/30$

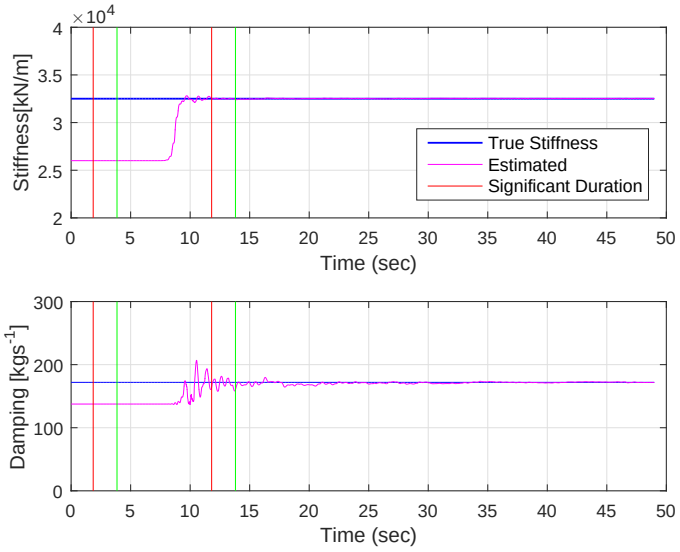

Figure 4-39: Parameter estimation results with UKF-RM - $Q(2,2) = 10^{23}$ and $\alpha_Q = 1/30$ and $\alpha_R = 1/30$

In summary, UKF-RM can achieve successful estimation of states and parameters in a wide range of Q values. On the other hand UKF cannot achieve a good estimation unless the correct Q values are assigned to the filter a-priori by manual fine-tuning. The criteria to judge the performance is that the filter must be able to

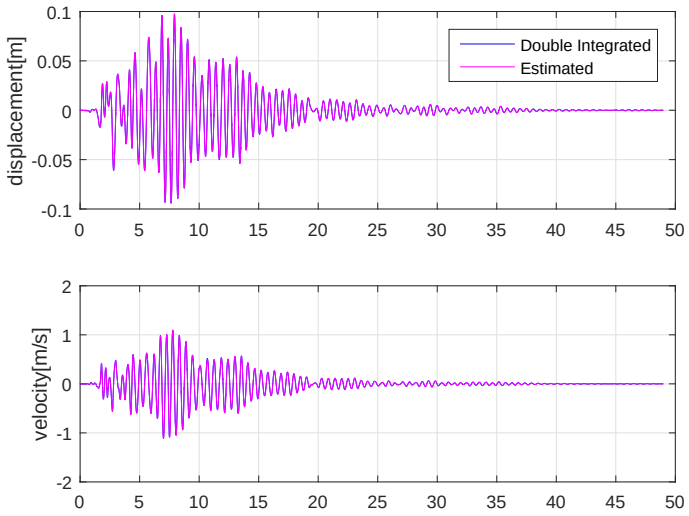

Figure 4-40: State estimation results with UKF-RM - $Q(2,2) = 10^{12}$ and $\alpha_Q = 1/30$ and $\alpha_R = 1/30$

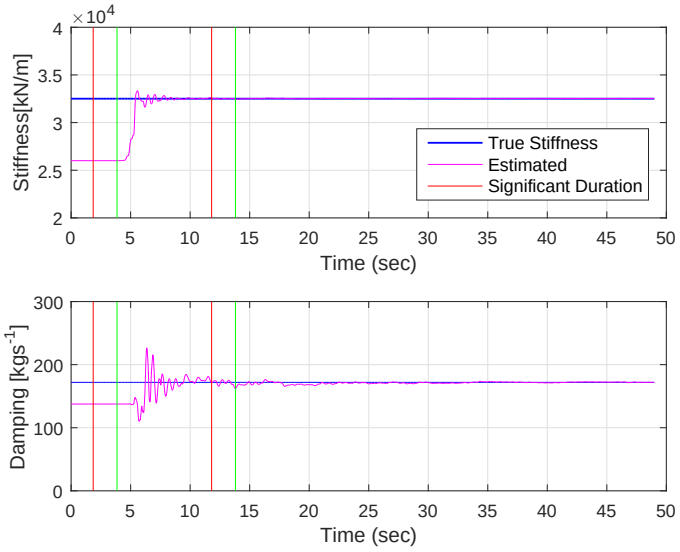

Figure 4-41: Parameter estimation results with UKF-RM - $Q(2,2) = 10^{12}$ and $\alpha_Q = 1/30$ and $\alpha_R = 1/30$

achieve a successful estimate of states from the beginning of the data, stiffness from the beginning of the significant duration and damping from the end of significant duration. Table (4.1) gives the summary of the sensitivity of the UKF-RM results to change in the initial Q, process noise matrix based on this criteria.

Table 4.1: Upper and lower bound suggestions based on the sensitivity analysis for initial Q matrix

	$Q(1,1)$	$Q(2,2)$	$Q(3,3)$	$Q(4,4)$
Lower B.	10^{-17}	10^{-20}	10^{-20}	10^{-20}
Upper B.	10^{8}	10^{12}	10^{13}	10^{8}

4.1.2 Sensitivity to change in elements of R and measurement noise:

R, measurement noise covariance matrix is one dimensional since there is only one observation, namely; displacement. Four cases will be considered to investigate the sensitivity of estimation performance of both algorithms to change in initial R value,R_0, assignment in case of a variety of measurement noise. By assigning initial R value, R_0, different values the table below shows the considered measurement noise cases where measurement noise with a covariance, RR is set to:

- Observation consists no measurement noise, $RR = 0$
- $RR = (0.01 \times RMS_{measurement})^2$
- $RR = (0.05 \times RMS_{measurement})^2$
- $RR = (0.10 \times RMS_{measurement})^2$

where $RMS_{measurement}$ is the root mean squared value of the measurement.

Measurement noise w with a covariance equal to RR, is added to the simulated measurement to obtain observation as follows:

$$w = whitenoise + \sqrt{RR} \tag{4.4}$$

$$observation = measurement + w \tag{4.5}$$

Considered cases are summarized in Table (4.2) as follows:

Table 4.2: Cases considered for sensitivity analysis for initial Q matrix

Case	Measurement Noise	R_0	Result
1	0	20%	UKF-RM:OK UKF:OK
2	1%	20%	UKF-RM:OK UKF:OK
3a	5%	1%	UKF-RM:OK UKF:Diverge
3b	5%	10%	UKF-RM:OK UKF:Diverge
4a	10%	1%	UKF-RM:OK UKF:Diverge
4b	10%	20%	UKF-RM:OK UKF:Diverge

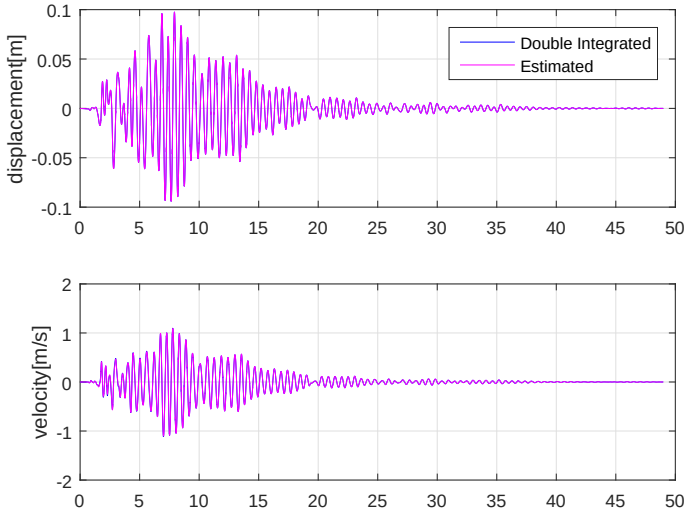

Figure 4-42: State estimation results with UKF - Case 1

Results of state and parameter estimations from UKF and UKF-RM that correspond to cases 1 and 2 are given in Figures (4-42-4-49). Case 1 represents no

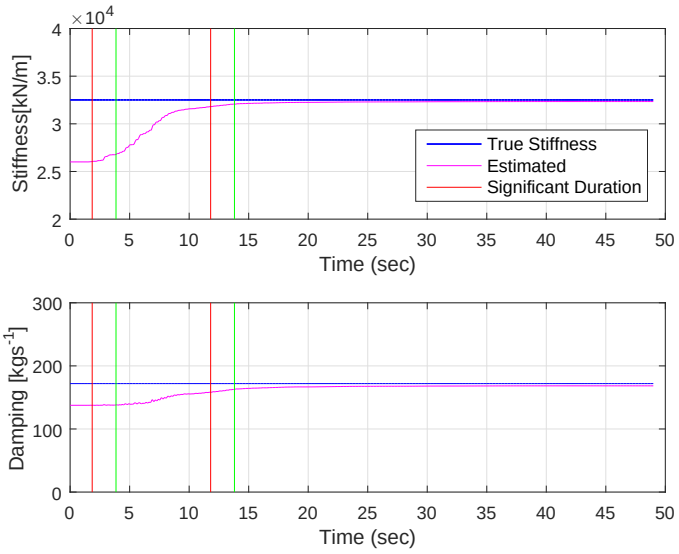

Figure 4-43: Parameter estimation results with UKF - Case 1

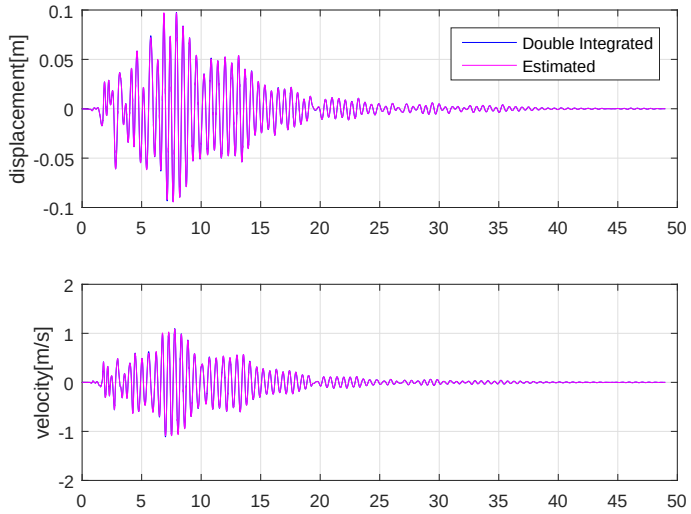

Figure 4-44: State estimation results with UKF-RM - Case 1 and $\alpha_Q = 1/30$ and $\alpha_R = 1/30$

measurement noise and Case 2 represents the case where a low measurement noise is considered. In both UKF and UKF-RM estimations R_0 is set to 20% which is very different from the actual value. As seen from the figures, both algorithms can estimate states successfully. However, stiffness parameter estimations were convergent only

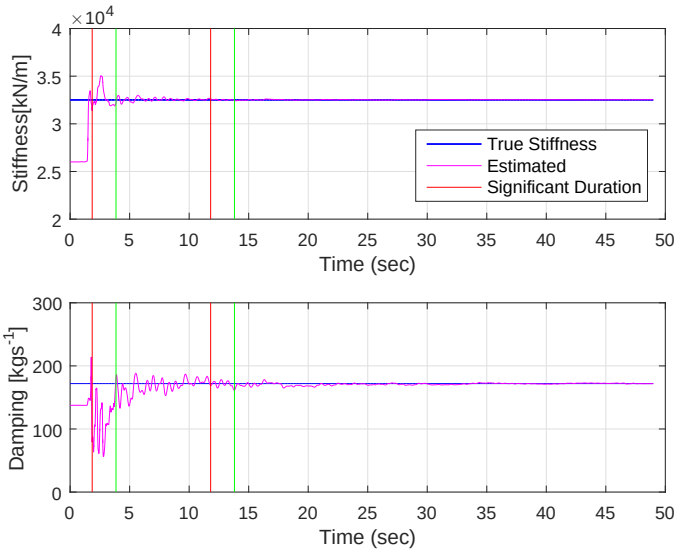

Figure 4-45: Parameter estimation results with UKF-RM - Case 1 and $\alpha_Q = 1/30$ and $\alpha_R = 1/30$

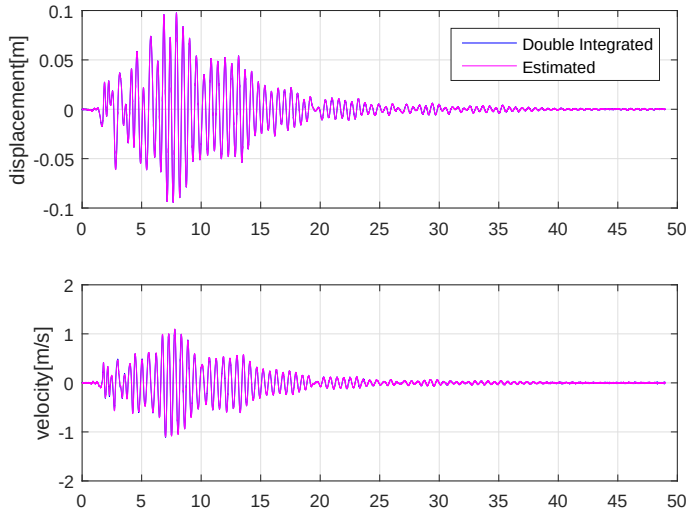

Figure 4-46: State estimation results with UKF - Case 2

after the significant duration in the case of UKF, where UKF-RM was successfully estimated stiffness inside the significant duration with an error less than 1%. In addition, damping parameter was successfully estimated with UKF after the significant duration in both cases. UKF-RM estimates damping parameter inside the significant

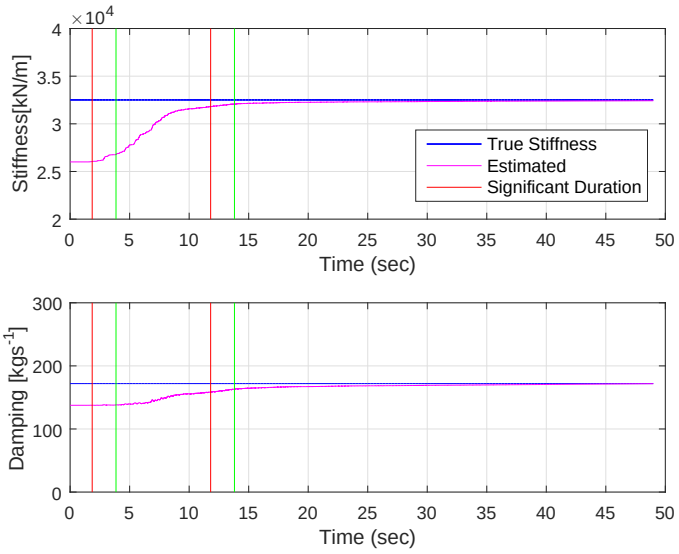

Figure 4-47: Parameter estimation results with UKF - Case 2

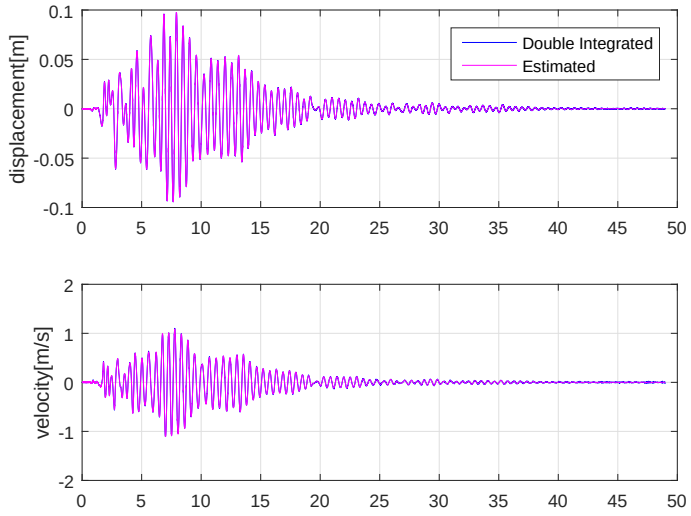

Figure 4-48: State estimation results with UKF-RM - Case 2 and $\alpha_Q = 1/30$ and $\alpha_R = 1/30$

duration with an error less than 1% in no measurement noise case, and with an error less than 3% in Case 2. Thus, it may be concluded that damping parameter estimations are more sensitive to changes in noise statistics and filter characteristics than stiffness parameter estimations. Consecutively, although UKF-RM is more robust

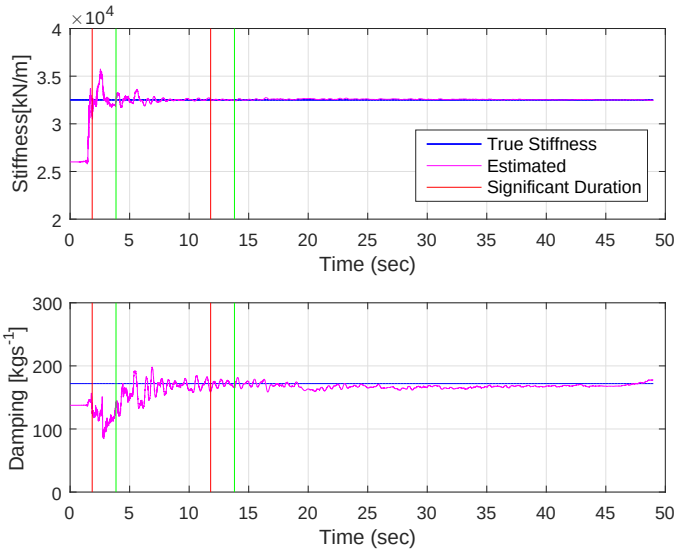

Figure 4-49: Parameter estimation results with UKF-RM - Case 2 and $\alpha_Q = 1/30$ and $\alpha_R = 1/30$

than UKF as the rate of convergence is much faster, UKF can also be considered as robust in the low measurement noise cases.

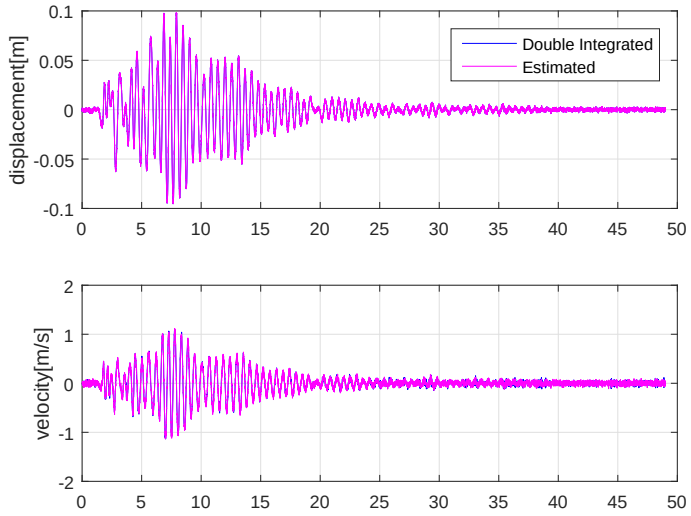

Figure 4-50: State estimation results with UKF - Case 3a

Results of state and parameter estimations from UKF and UKF-RM that correspond to cases 3a and 3b are given in Figures (4-50-4-57). In both cases 5% mea-

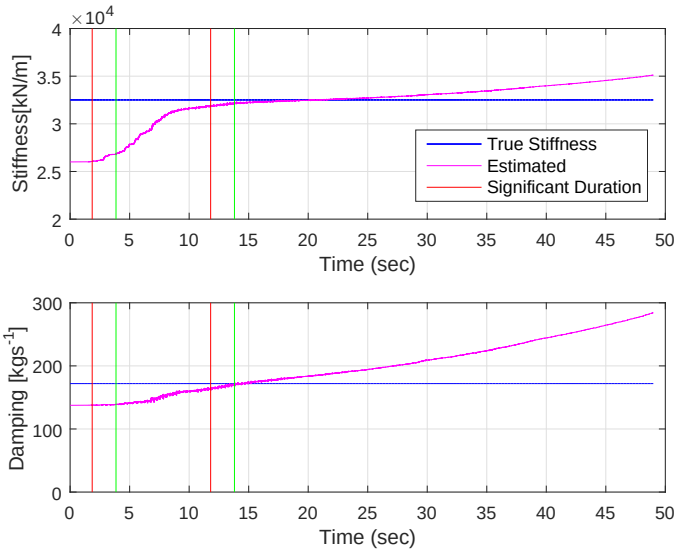

Figure 4-51: Parameter estimation results with UKF - Case 3a

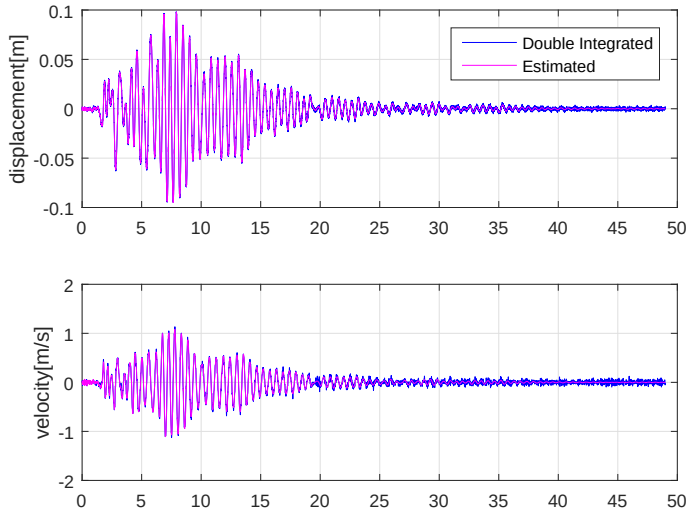

Figure 4-52: State estimation results with UKF-RM - Case 3a and $\alpha_Q = 1/30$ and $\alpha_R = 1/30$

surement noise is added to the observation, which is usually considered as a regular value. Case 3a corresponds to estimations with R_0 is set to 1% and Case 3b corresponds to estimations with R_0 is set to 10% within both algorithms. As seen from the figures, both algorithms can estimate states successfully. However, during param-

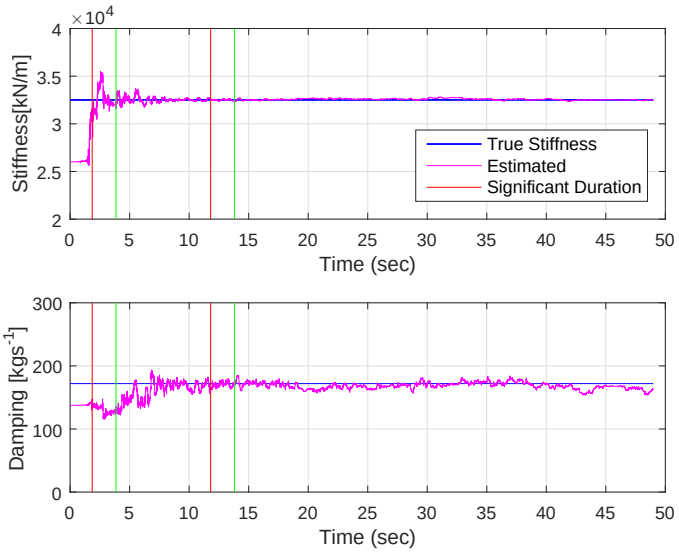

Figure 4-53: Parameter estimation results with UKF-RM - Case 3a and $\alpha_Q = 1/30$ and $\alpha_R = 1/30$

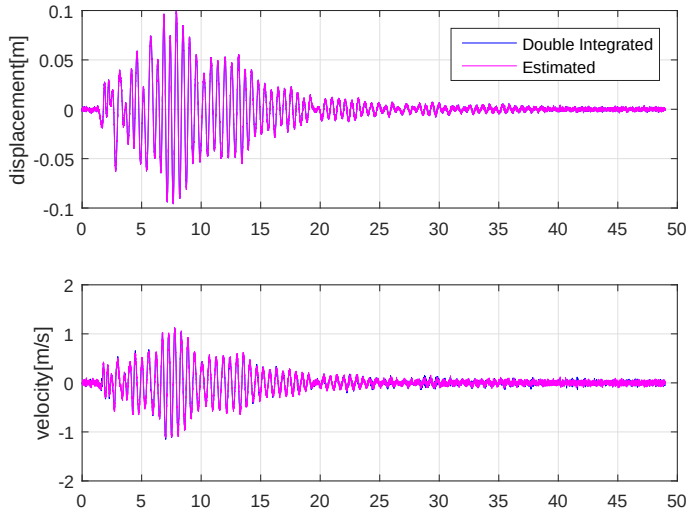

Figure 4-54: State estimation results with UKF - Case 3b

eter estimations divergence occurs with UKF in both cases 3a and 3b. On the other hand, with UKF-RM stiffness parameter was able to be estimated with an error 1% inside the significant duration in both cases. In addition, damping parameter was able to be estimated with an error 3% inside the significant duration in both cases.

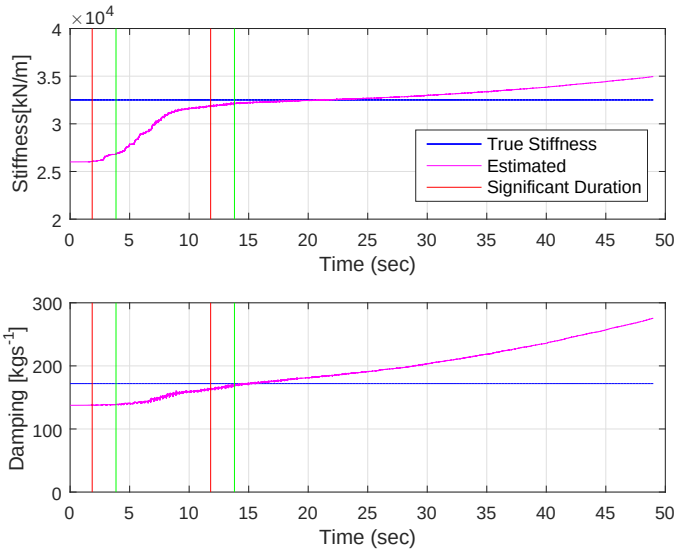

Figure 4-55: Parameter estimation results with UKF - Case 3b

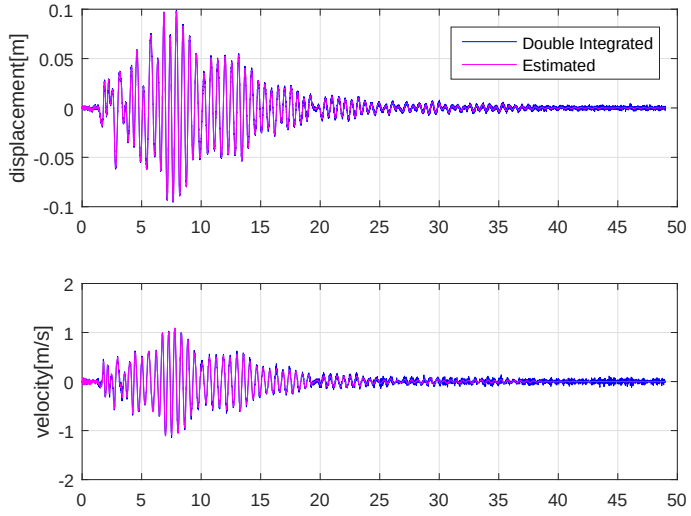

Figure 4-56: State estimation results with UKF-RM - Case 3b and $\alpha_Q = 1/30$ and $\alpha_R = 1/30$

Consecutively, UKF-RM proves to be more robust than UKF even when a regular measurement noise is considered.

Change in R values with UKF-RM considering case 3b is given in Figure (4-58). Change in P values considering case 3b are depicted in Figures (4-59) and (4-60) for

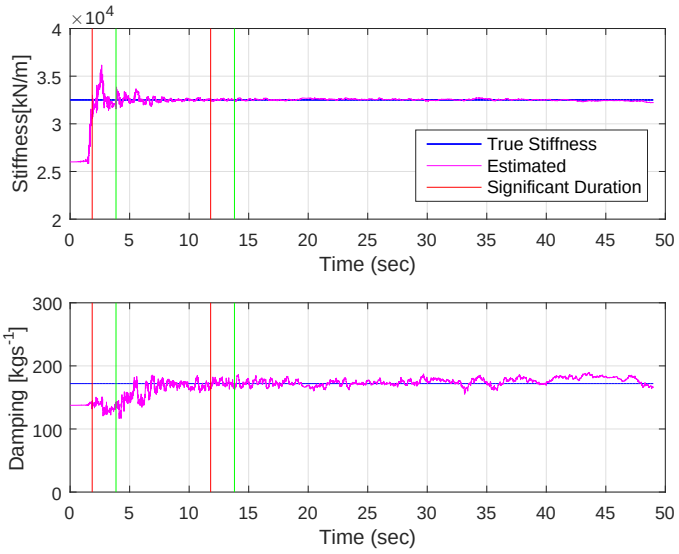

Figure 4-57: Parameter estimation results with UKF-RM - Case 3b and $\alpha_Q = 1/30$ and $\alpha_R = 1/30$

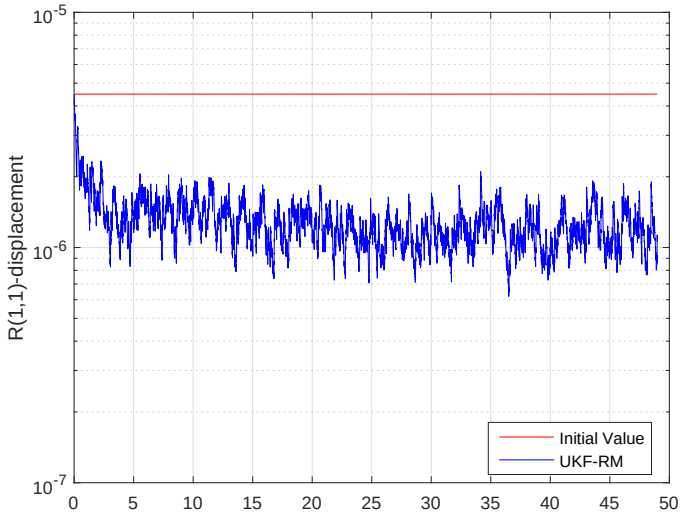

Figure 4-58: Change in R values with UKF-RM - Case 3b and $\alpha_Q = 1/30$ and $\alpha_R = 1/30$

UKF-RM and UKF, respectively.

Considering a large measurement noise (10%), cases 4a and 4b are run with both algortighms. Results of state and parameter estimations from UKF and UKF-RM that correspond to cases 4a and 4b are given in Figures (4-61-4-68). Case 4a corre-

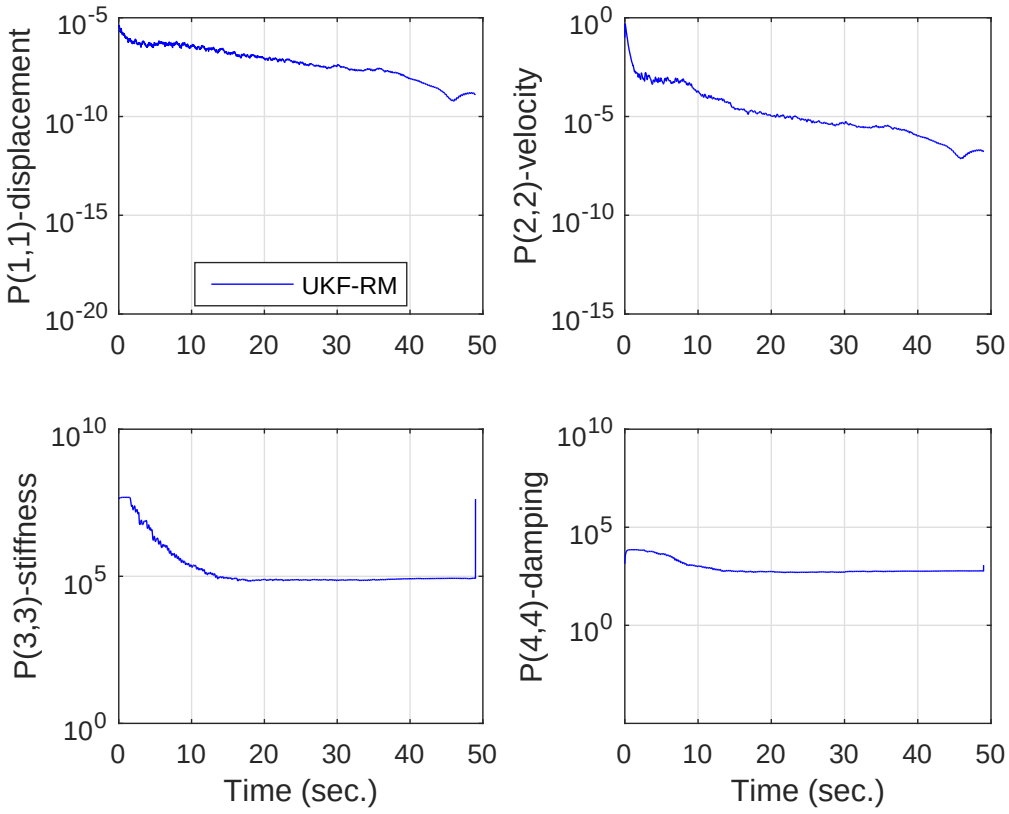

Figure 4-59: Change in P values with UKF-RM - Case 3b and $\alpha_Q = 1/30$ and $\alpha_R = 1/30$

sponds to estimations with R_0 is equal to 1% and Case 4b corresponds to estimations with R_0 is equal to 20% within both algorithms. As seen from the figures, both algorithms can estimate states successfully. However, during parameter estimations divergence occurs with UKF in both cases 4a and 4b. On the other hand, with UKF-RM stiffness parameter was able to be estimated with an error 2% inside the significant duration in both cases. In addition, damping parameter was able to be estimated with an error 6% inside the significant duration in both cases. Consecutively, UKF-RM proves to be more robust than UKF even when a regular measurement noise is considered.

Change in R values with UKF-RM considering Case 4b is given in Figure (4-69). Change in P values considering Case 4b are depicted in Figure (4-70) for UKF-RM.

In conclusion, UKF-RM is robust against erroneous assignment of R_0 in both

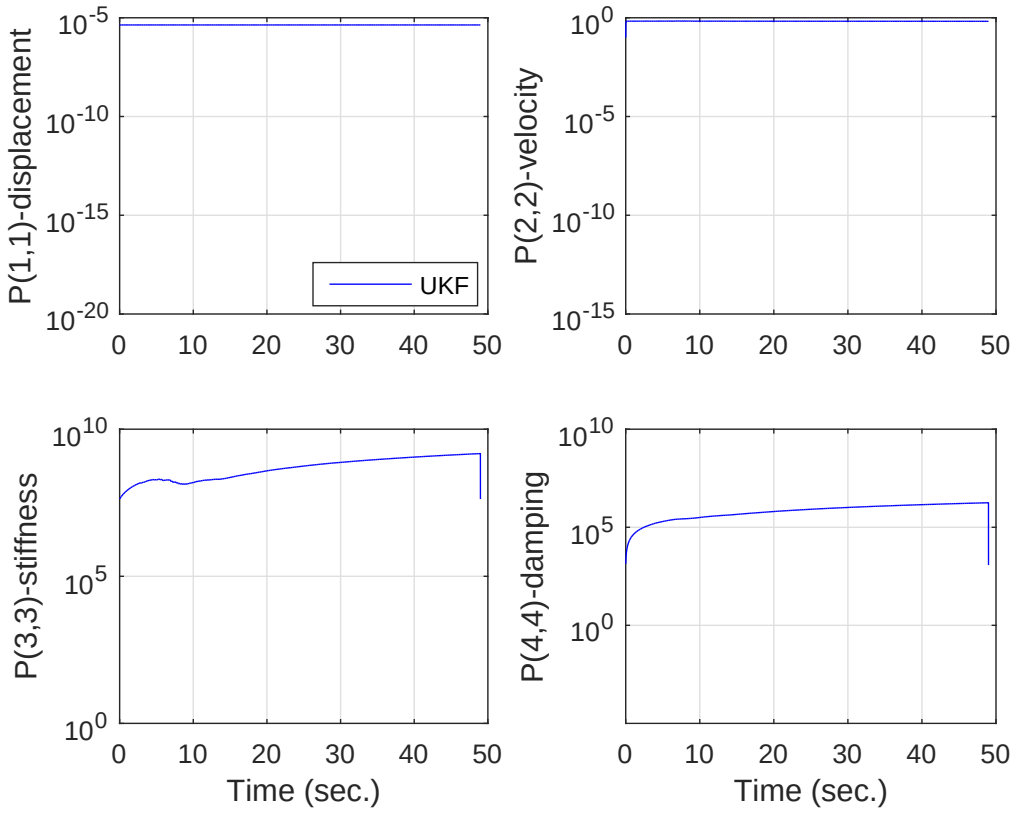

Figure 4-60: Change in P values with UKF - Case 3b

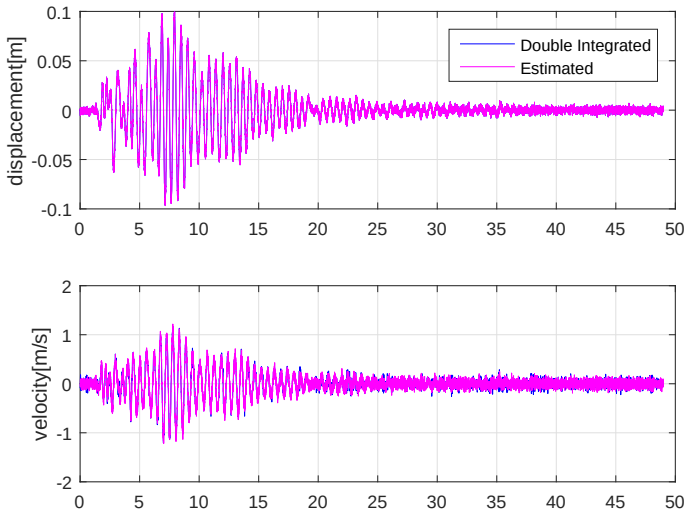

Figure 4-61: State estimation results with UKF - Case 4a

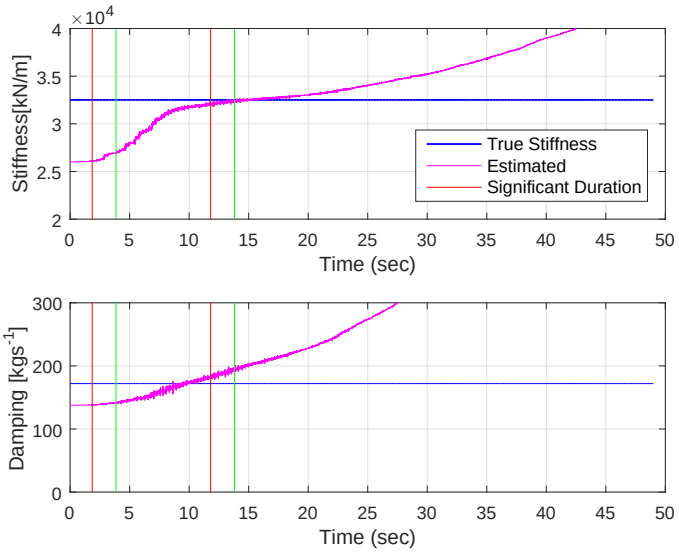

Figure 4-62: Parameter estimation results with UKF - Case 4a

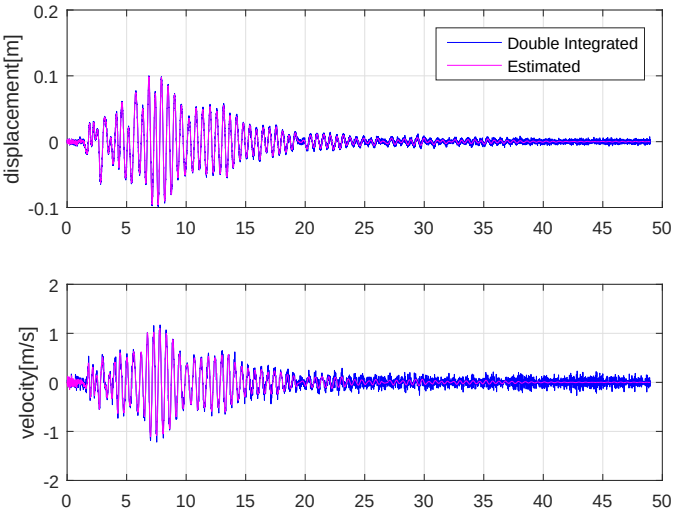

Figure 4-63: State estimation results with UKF-RM - Case 4a and $\alpha_Q = 1/30$ and $\alpha_R = 1/30$

small and large measurement noise conditions, where UKF is only robust when measurement noise is very small (1%) or non-existent. The reason why UKF is not robust is that, actually all filter statistics are related to each other. In order to achieve an optimal estimation all statistics should be defined exactly correct. For example in this

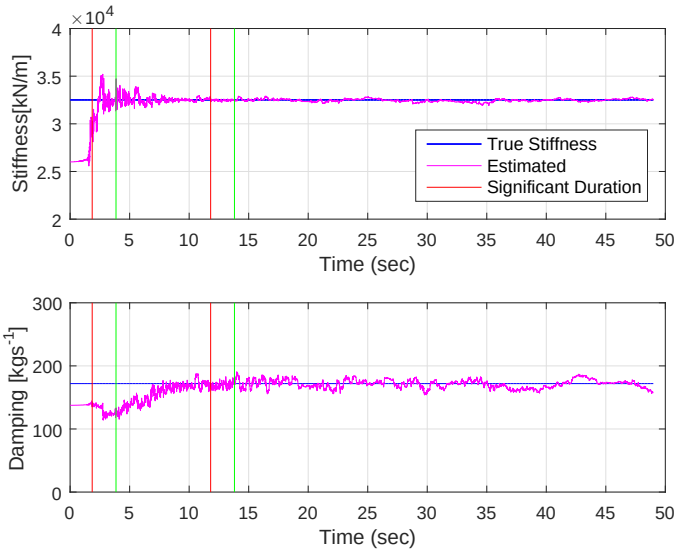

Figure 4-64: Parameter estimation results with UKF-RM - Case 4a and $\alpha_Q = 1/30$ and $\alpha_R = 1/30$

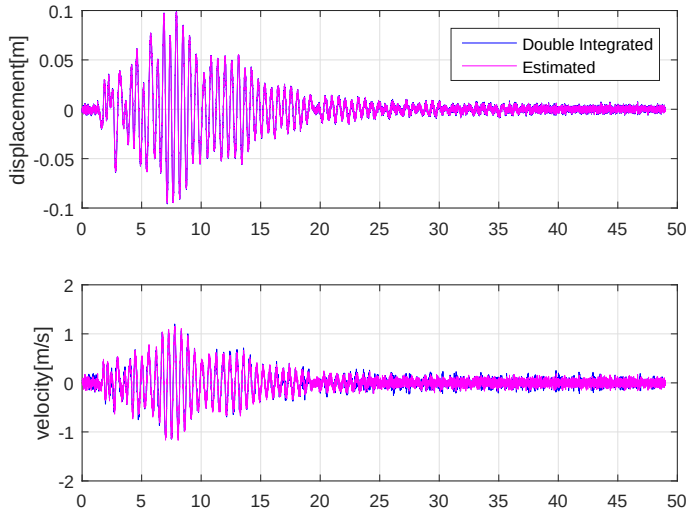

Figure 4-65: State estimation results with UKF - Case 4b

section even though Q and P_0 matrices are kept as the so-called true matrices since R_0, and hence R in UKF is changed. Consecutively, values such as Q/R are changed which had an adverse affect on the estimation performance of UKF. This shows the fact, when one of the filter statistics is changed the remaining must be fine-tuned in

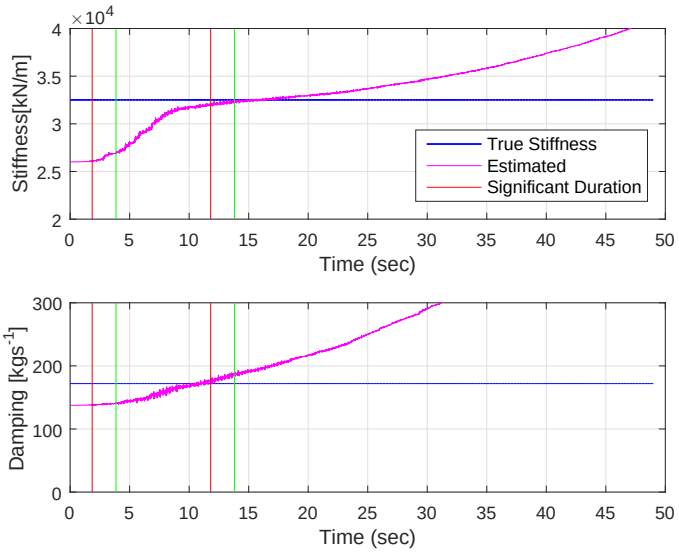

Figure 4-66: Parameter estimation results with UKF - Case 4b

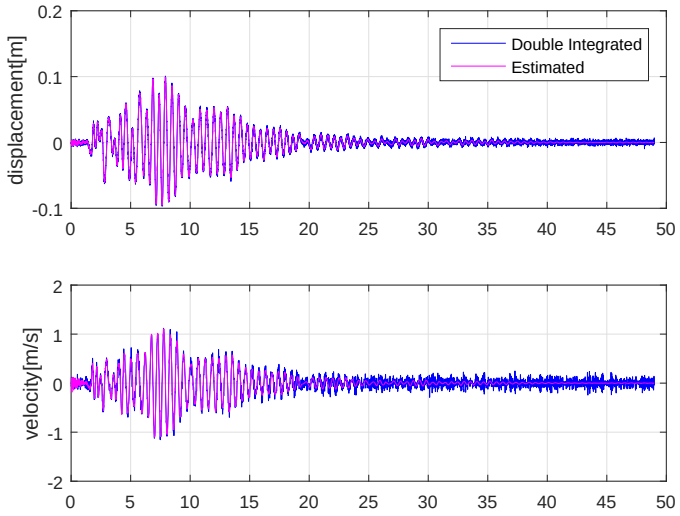

Figure 4-67: State estimation results with UKF-RM - Case 4b and $\alpha_Q = 1/30$ and $\alpha_R = 1/30$

order to be able to achieve a satisfactory estimation which is not a practical way to deal with estimation problems in real world.

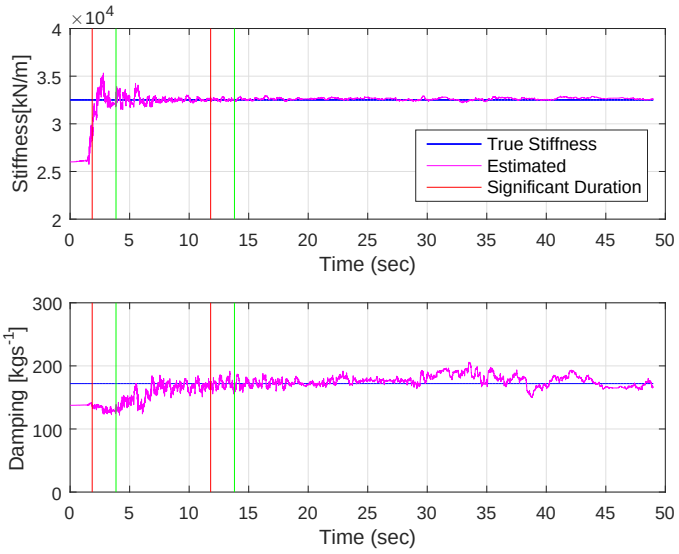

Figure 4-68: Parameter estimation results with UKF-RM - Case 4b and $\alpha_Q = 1/30$ and $\alpha_R = 1/30$

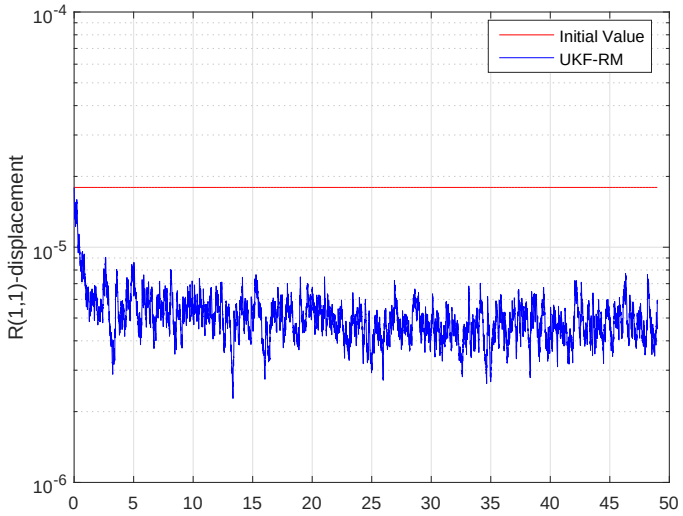

Figure 4-69: Change in R values with UKF-RM - Case 4b and $\alpha_Q = 1/30$ and $\alpha_R = 1/30$

4.1.3 Sensitivity to change in elements of P_0:

P and Q are closely related and P_0 also one of the evolving parameter in the filter. P_0 controls the transition from the initial transient response to the steady state response

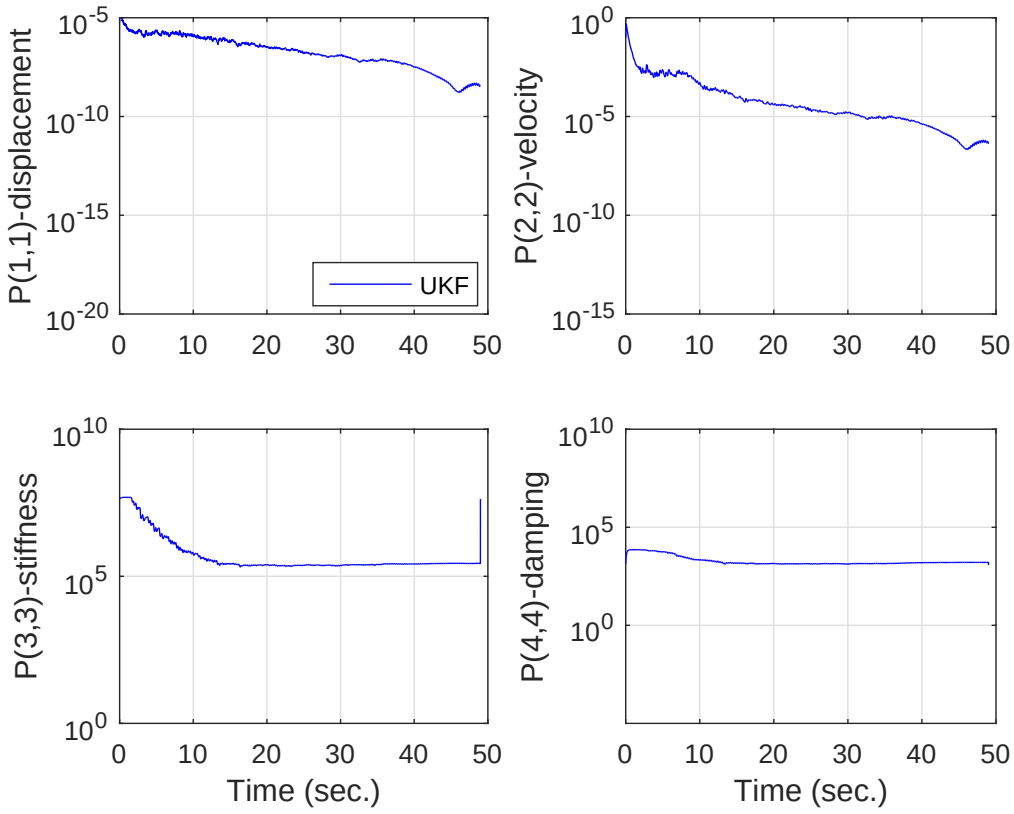

Figure 4-70: Change in P values with UKF-RM - Case 4b and $\alpha_Q = 1/30$ and $\alpha_R = 1/30$

which is controlled by Q. Thus, although effect of P_0 quickly during estimation, if it is not selected correctly the estimations end up sub-optimal. When $P_0 = 0$, it means there is no error in the initial estimates (initial state vector) which in turn the filter ignores and learns nothing from measurements. On the other hand, it is is extremely large then the filter will ignore or provide small weights to the state model and trust in the measurements which would cause large fluctuations in the estimates of parameter and states along with large final uncertainty.

For example, One trick that is applied in the current conventional UKF method is to select the initial P matrix, P_0, rather a large value than it should be so that the filter is enforced to converge more quickly. However it is clear from previous explanations that both P_0 and Q have significant yet separate roles in order to make a filter optimal. Selecting larger P_0 values to enforce convergence may only be a quick

fix, and merely can be a solution for practical applications, in this complex interacting problem at hand.

As given in the beginning, an appropriate definition for P_0 can be given as follows:

$$P_0 = diag[0, 0, (k_{true} - X_0(3))^2, (c_{true} - X_0(4))^2] \tag{4.6}$$

The sensitivity to change in P values will be investigated in this section. Considered cases are summarized in Table (4.3). In the table, P_0^{true} corresponds to the value given in above Eq. (4.6)

Table 4.3: Cases considered for sensitivity analysis for initial P matrix, P_0

Case	P_0	Stiffness	Damping
1	$10^{-6} \times P_0^{true}$	UKF-RM:OK UKF:OK	OK OK
2	$10^{2} \times P_0^{true}$	UKF-RM:OK UKF:1%	OK 10%
3	$10^{6} \times P_0^{true}$	UKF-RM:OK UKF:Diverge	OK Diverge

Figure (4-71) depicts the results of parameter estimation with UKF-RM. In the figure all three cases which correspond to Table (4.3) are shown. First, both stiffness and damping estimations were successfully obtained just 2 seconds after the significant duration begins. Estimation error inside the significant duration is about 1% and 2% for stiffness and damping, respectively. Until the convergence achieved, as the P_0 gets larger (e.g. Case 3 is the largest) fluctuations gets larger too. This is due to the transient response of the filter which depends on P_0. However, it is important to note the convergence rate (which is mostly controlled by Q) does not affected by different P_0 and all three cases reach to convergence almost at the same time and exhibits a stable behavior afterwards. All these observations made from UKF-RM are beneficial in terms of application of system identification in realistic structures.

On the other hand Figure (4-72) presents a different story. Let's first examine stiffness estimation with UKF considering three different P_0 assigned to the filter. The fluctuations in the beginning of the data is very small as expected in Cases 1

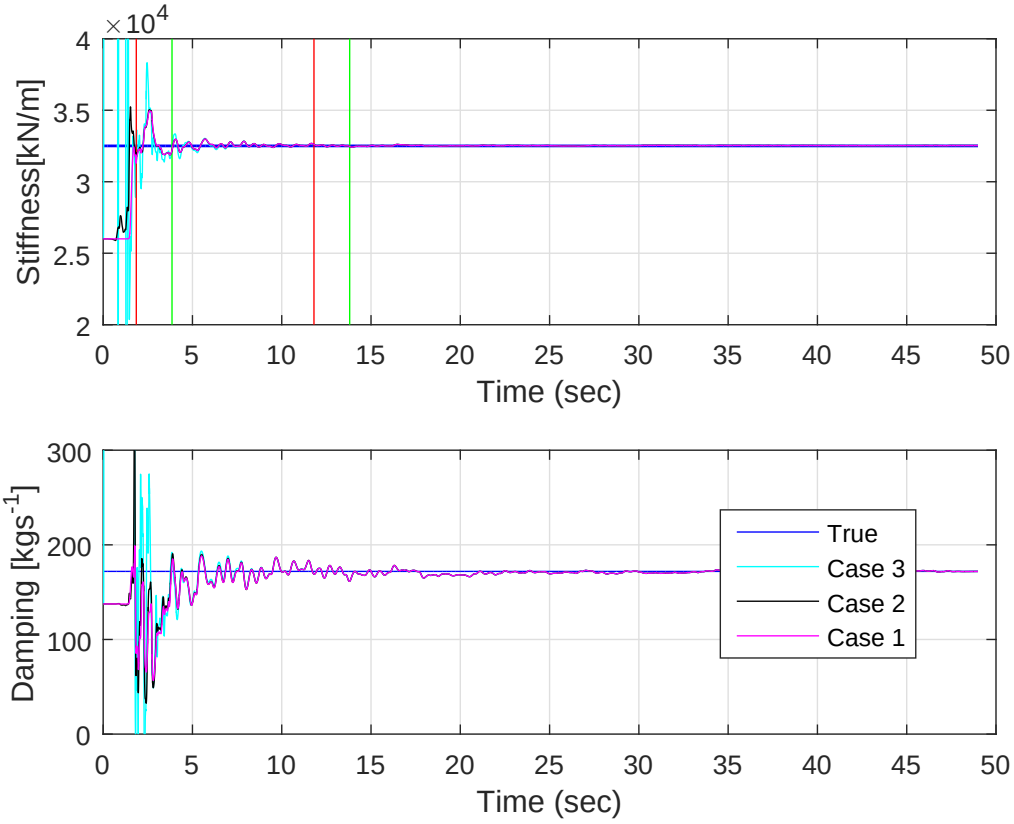

Figure 4-71: Parameter estimations with UKF-RM - Sensitivity to P_0 ($\alpha_Q = 1/30$ and $\alpha_R = 1/30$)

and 2. Case 1 convergence time (at about 10-15 seconds) is almost same as the true value, however, when P_0 is assigned 100 times larger than the true value for the first time the stiffness estimation with 1% error inside the significant duration is achieved by UKF algorithm. However, corresponding damping estimation is overestimated by 10%. When P_0 is increased more as in case 3, then the stiffness estimation starts converging at about 10-15 seconds similar to case 1. In addition damping estimation is also converged, it is overestimated by 180%, which is basically false convergence. Thus, the results of UKF shows that there is a fine line between an optimal solution and sub-optimal solution when the filter is not adapted and noise statistics are kept constant over the estimation. In practice, this would result in many complicated situations and judging the true value would become impossible. Thus, UKF-RM proves itself as a good candidate as it results in fast and stable results with very

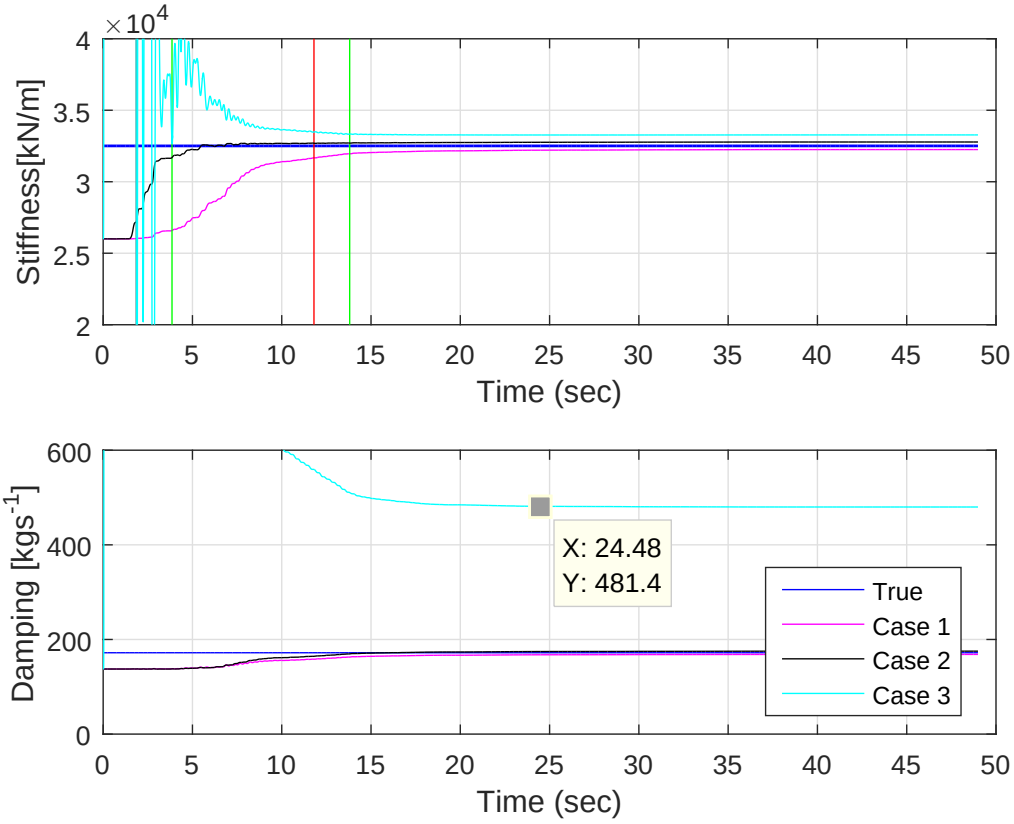

Figure 4-72: Parameter estimations with UKF - Sensitivity to P_0

flexible choices for initial noise covariance.

4.2 Sensitivity to initial state vector, X_0, values

Initial state vector defines the starting value for each state and parameters. As mentioned before we previously assumed a rather small model error and assigned the initial state vector as:

$$X_0 = [0, 0, 0.8k_{true}, 0.8c_{true}]^T \tag{4.7}$$

Now let's consider X_{00} is equal to $[0, 0, k_{true}, c_{true}]^T$. Table (4.4) shows range of initial values considered for the parameters with both UKF and UKF-RM in terms of X_{00}.

Table 4.4: Cases considered for sensitivity analysis for initial state vector, X_0

Case	X_0	residual stiffness	Stiffness (S.D.)	Damping
1	$0.2 * X_{00}$	UKF-RM:OK UKF:OK	OK -	OK Diverge
2	$0.5 * X_{00}$	UKF-RM:OK UKF:OK	OK -	OK Diverge
3	$0.8 * X_{00}$	UKF-RM:OK UKF:OK	OK -	OK OK
4	$1.2 * X_{00}$	UKF-RM:OK UKF:OK	OK -	OK Diverge
5	$1.5 * X_{00}$	UKF-RM:OK UKF:OK	OK -	OK Diverge
6	$1.8 * X_{00}$	UKF-RM:OK UKF:OK	OK -	OK Diverge

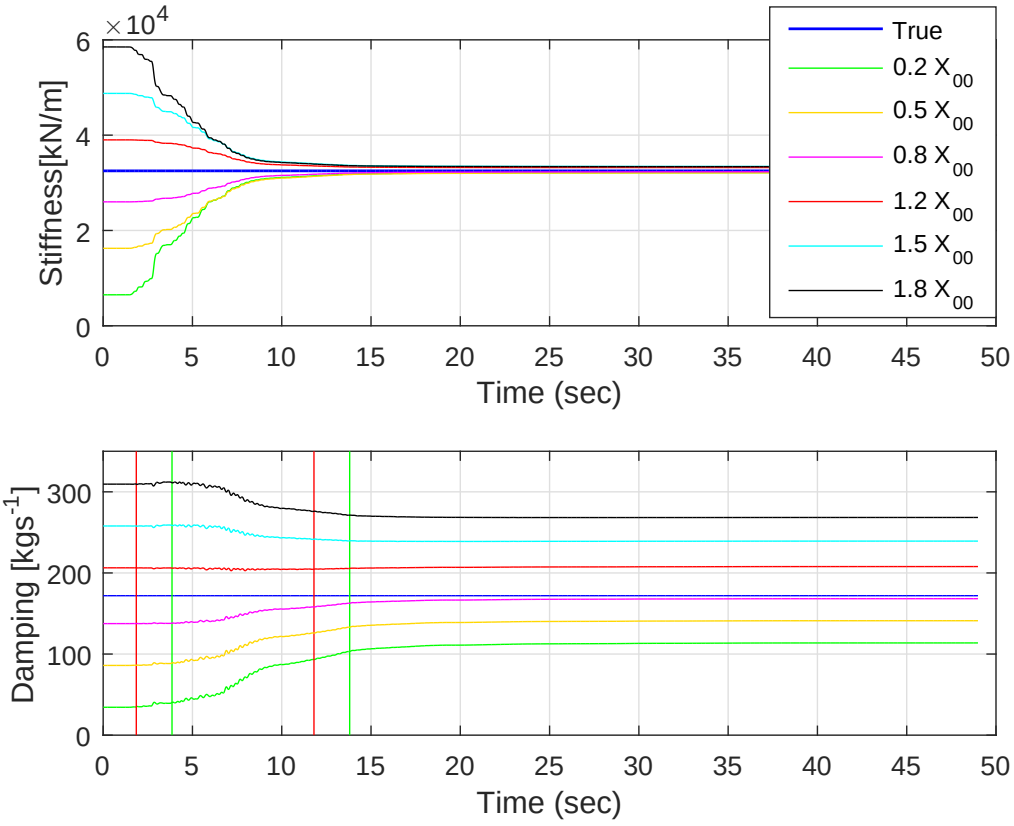

Figure 4-73: Parameter estimations with UKF - Sensitivity to X_0

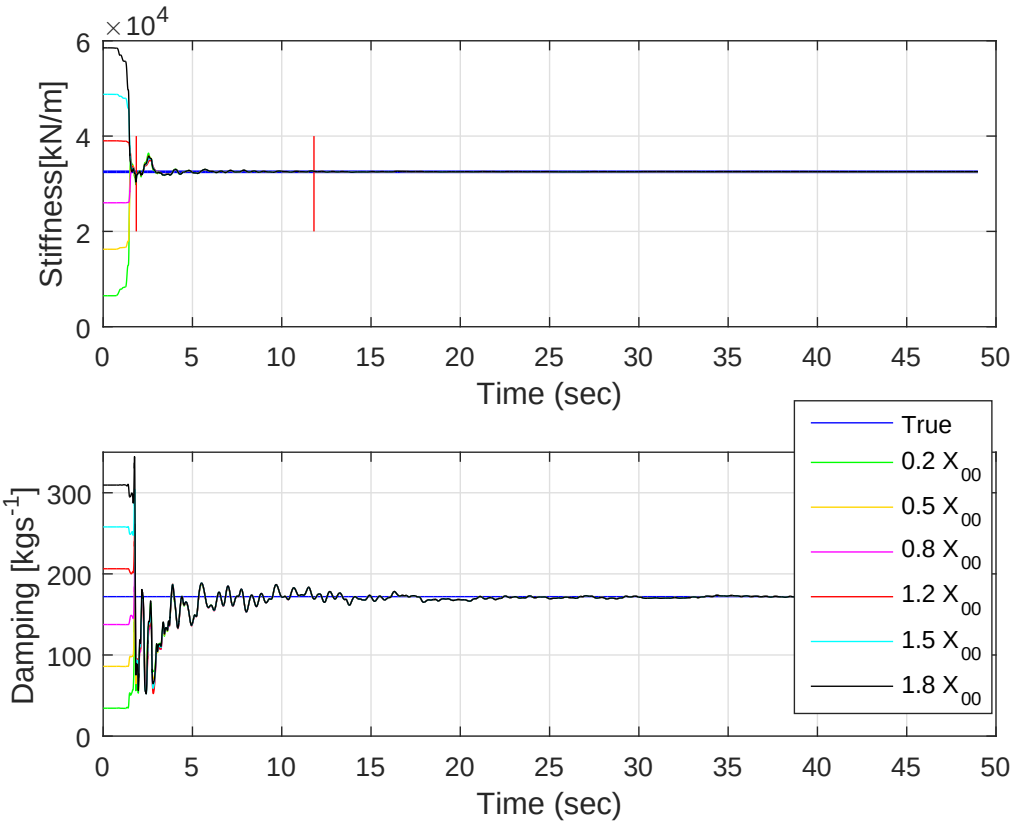

Figure 4-74: Parameter estimations with UKF-RM - Sensitivity to X_0 ($\alpha_Q = 1/30$ and $\alpha_R = 1/30$)

Figure (4-73) shows parameter estimation results with UKF considering a variety of initial state vectors. It is evident from the figure that stiffness estimation converges at around 10 seconds regardless of the initial state vector. When the residual stiffness portion is considered, maximum error in estimation was about 3%. However, damping estimation can only be achieved with Case 3, which was the base case in all earlier analysis. Hence it can be concluded, damping is more sensitive to changes in the initial state vector and hence requires further tuning when ever the initial state vector changes. In practical applications, such requirements are considered as burden. In addition, and more importantly, as the current condition is the target of the problem, a robust estimation algorithm should not be heavily affected by the choice of initial state vector to achieve unbiased and understandable estimations.

On the other hand, UKF-RM (Figure (4-74)) can estimate both stiffness inside sig-

nificant duration and after the significant duration with an error about 1%. Similarly, it can also estimate both stiffness inside significant duration and after the significant duration with an error about 2%.

4.3 Sensitivity to α_Q and α_R selection

In UKF-RM, estimates of the noise covariance Q and R using Robbins-Monro stochastic approximation scheme can be formulated as follows [62],[61],[44].

$$Q_k = (1 - \alpha_Q) * (Q_{k-1}) + \alpha_Q * (K_k) * (z_k - z_k^-) * (z_k - z_k^-)^T * (K_k^T) \tag{4.8}$$

$$R_k = (1 - \alpha_R) * (R_{k-1}) + \alpha_R * (z_k - z_k^-) * (z_k - z_k^-)^T \tag{4.9}$$

where α: a small positive number, which is usually chosen at the order of 10^{-2}. Both α_Q and α_R controls the adaptability of the filter. It can be considered as a forgetting factor, which tells to the filter how quickly it should forget the previous data and learn more from the new information as it becomes available. If it is a rather small value, then the UKF-RM filter becomes more like the conventional one as adaptability is low and evolution ability of the filter is ignores. As it becomes larger, vice versa. However, the sensitivity of the filter to the selection of α should be investigated to find out whether fine-tuning is necessary or not for this filter. This way, a fair comparison between UKF-RM and UKF can be made.

First, let's consider a variety of α_Q values where α_R is kept constant. As mentioned before, the convergence rate depends on Q value and thus α_Q is important in this manner. Figure (4-75) depicts parameter estimation results for a variety of α_Q values when $\alpha_R = 1/30$. When α_Q is too small such as 0.001 then UKF-RM filter basically behaves like the conventional UKF in terms of convergence rate. The estimation of both stiffness and damping is only realized around about 10 seconds. However, as α_Q keeps increasing adaptability of the filter increases. Stiffness estimation is successfully

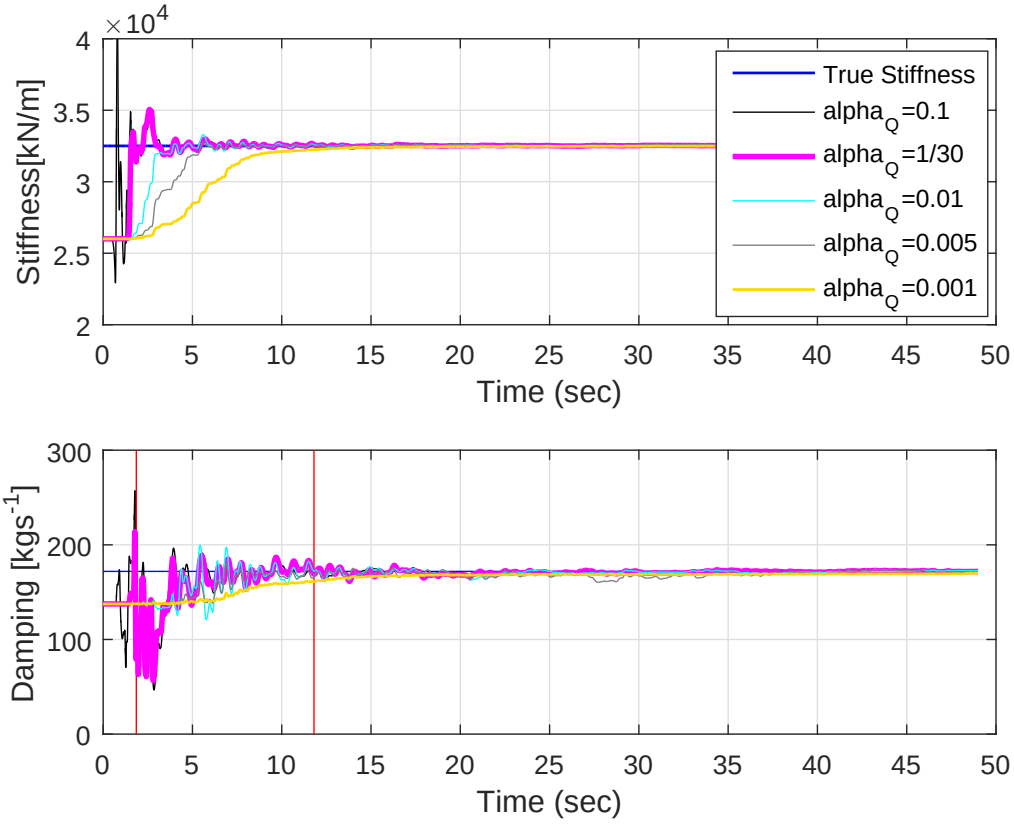

Figure 4-75: Parameter estimations with UKF-RM (Linear model) - Sensitivity to α_Q ($\alpha_R = 1/30$)

achieved inside the significant duration with an error about 1% and then it stays stable until the end of the data. In addition, damping is also achieved successfully after the significant duration ends in all cases with an error less than 2%. Damping is more sensitive than stiffness estimation, inside and outside of the significant duration which is a similar general conclusion drawn before. When damping parameter inside the significant duration is of interest then selecting an α_Q value at about the order of 0.01 or larger is suggested.

Now let's consider a similar sensitivity analysis by assigning the initial Q matrix elements which correspond to stiffness and damping parameters a different value than the so-called true one (Eq. 4.10).

$$Q_0 = diag[1e-4, 1e-1, 2e5, 2e2]^T \tag{4.10}$$

New Q_0 matrix is selected in a random manner as follows:

$$Q_0 = diag[1e-8, 1e3, 1e8, 1e-2]^T \tag{4.11}$$

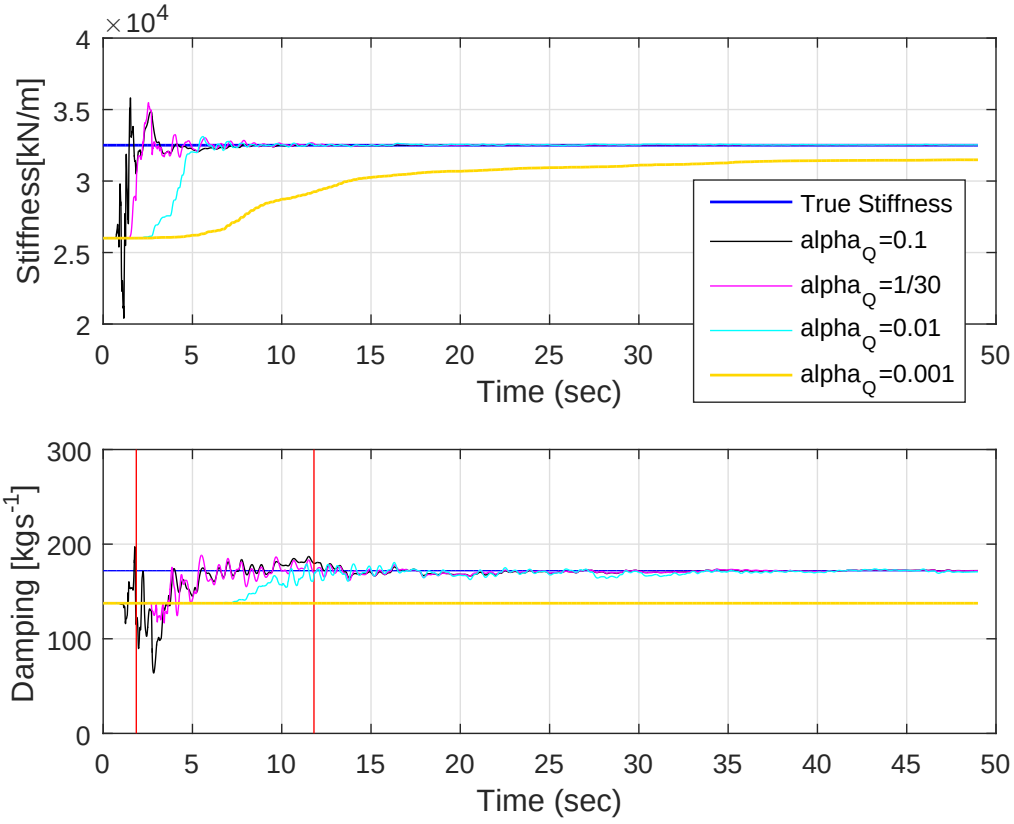

Figure 4-76: Parameter estimations with UKF-RM (Linear model) with Q_0 = Eq. (4.11) - Sensitivity to α_Q ($\alpha_R = 1/30$)

Figure (4-76) shows parameter estimation results for a variety of α_Q values when $\alpha_R = 1/30$ and Q_0 = Eq. (4.11). When α_Q is equal to 0.001 then filter acts similar to conventional UKF since the adaptation is slow and stiffness estimation convergence occurs at around 10-15 seconds. However, damping estimation is not updated at all, which is an evidence of the inference above that the filter acts like conventional non-adaptive UKF. When α_Q is assigned a value larger than 0.001, then filter's ability to adapt gradually increases. Finally when it is assigned 0.01 or a larger value, stiffness estimation is successfully achieved inside the significant duration with an error less

than 1%. In addition, damping is also achieved successfully inside the significant duration with an error less than 2% when $\alpha_Q \geq 1/30$. Thus, when damping parameter inside the significant duration is of interest then selecting an α_Q value at about the order of 1/30 or larger is suggested.

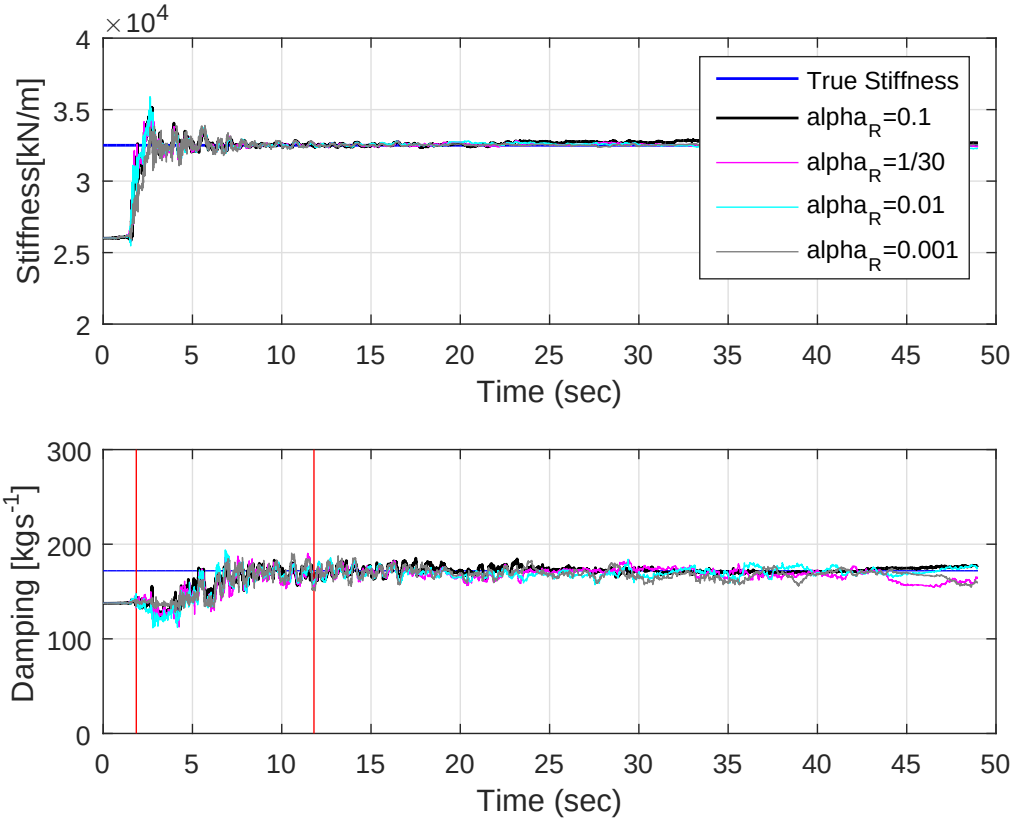

Figure 4-77: Parameter estimations with UKF-RM (Linear model) with Q_0 = Eq. (4.10) - Sensitivity to α_R ($\alpha_Q = 1/30$)

Finally, the performance of UKF-RM based on its sensitivity to α_R, assuming 5% measurement noise, $R_0 = 1\%$ and $Q_0 =$ Eq. (4.10) is investigated. Stiffness estimation is very robust both inside and after the significant duration when α_R is chosen at the order of [0.0010.1] and estimation error is about 2%. Moreover, damping estimations are also successfully achieved for all cases inside the significant duration. damping estimation results in an error of about 9% or less after the significant duration as shown in Figure (4-77). Damping estimation results in an error of about 5% or less during the significant duration as shown in Figure (4-77).

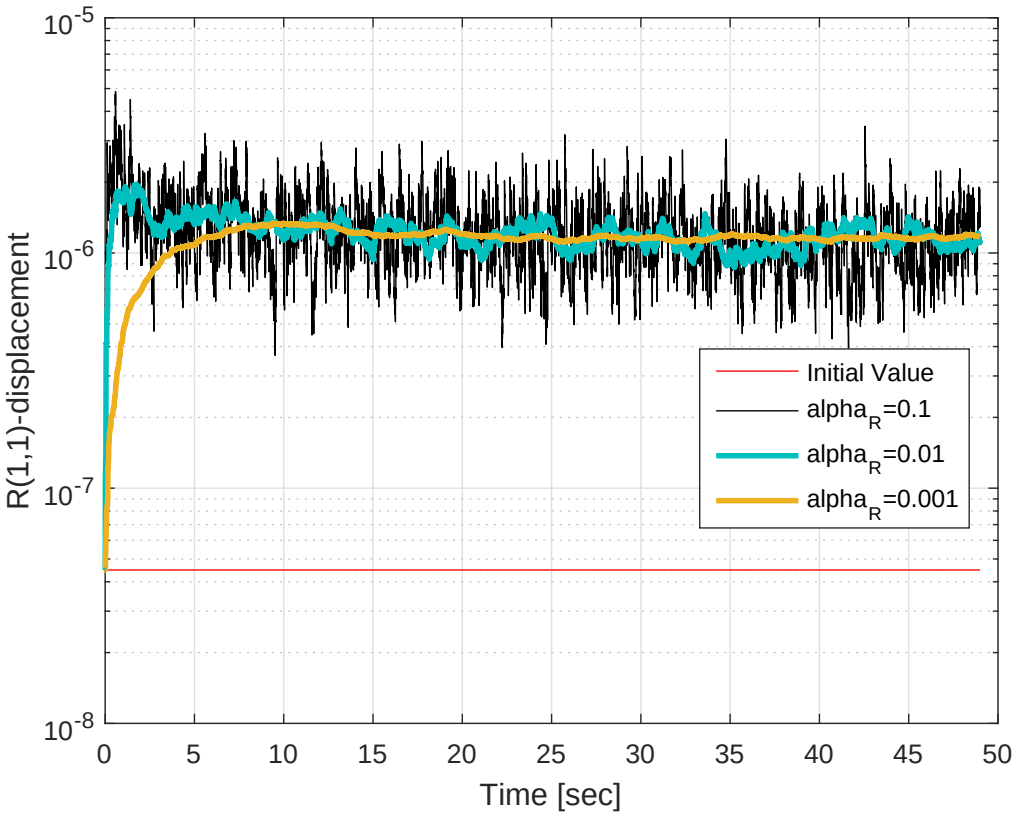

Figure 4-78: Change in R values with UKF-RM with Q_0 = Eq. (4.10) and varying α_R ($\alpha_Q = 1/30$)

Figure (4-78) depicts the change in R values as the filter adaptively estimates the states and parameters. In theory, R value is expected to settle at a constant value after finding the correct one, unless there is measurement faults. From figure, when $\alpha_R = 0.1$, the fluctuations in R value is considerably large when it is compared to other two cases. This means when $\alpha_R = 0.1$, filter searches for a correct R value in a larger range since the adaptivity increases as α increases.

Chapter 5

Stiffness Estimation using Seismic Response Measurements

In this chapter, the proposed method will be first validated through laboratory experiment using only acceleration measurements under small and large seismic excitation. Furthermore, response measurement obtained from a full-scale bridge during aftershocks of Kumamoto Earthquake are used to identify its rubber-bearing stiffness and validate the applicability of the proposed stiffness identification algorithm.

5.1 Bridge Pier Shake Table Experiment

In this section, identification of stiffness will be validated with the proposed method using small and large earthquake response measurements from E-Defense experiment. The system can be considered as SDOF system as the bearings on the bent cap which girder mass rests on is fixed as mentioned in Chapter 2.1.1. Thus for an SDOF system excited at its base with ground acceleration the governing equation of motion becomes:

$$m\ddot{x}(t) + c\dot{x}(t) + kx(t) = -m\ddot{x}_g(t) \tag{5.1}$$

where $x(t)$ is the displacement response and $\ddot{x}_g(t)$ is the ground motion acceleration.

Based on the above given governing equation the augmented state vector becomes

$$X_a = [x, \dot{x}, k, c]^T = [x_1, x_2, x_3, x_4]^T \tag{5.2}$$

with states x, displacement; $\dot{x}$, velocity; k,stiffness and c, damping are to be estimated. Only mass, m is assumed as known in all following structural parameter estimation cases.

Mass is obtained from the E-Defense C1-1 experiment report [1]. The reaction force in the vertical direction measured by the load cells located on the pier cap is given equal to $2080kN$ (Table 2.1) from the dead load of the girder and added mass on top of the girder. In addition, the weight of the pier is given as $794.5kN$. Consequently, the mass is calculated as

$$m = (2080 + 794.5/2)/g = 252.5ton \tag{5.3}$$

where $g = 9.81m/s^2$ is the acceleration of gravity. Thus, half of the pier weight also contributes to the structure mass.

Design value for stiffness was also given as $k = 32506kN/m$ [1]. However, this value was used only to set an initial value for state vector by multiplying it by a factor. In addition, an approximate initial damping constant also calculated by assuming viscous damping $\zeta = 3\%$ because $2 - 5\%$ viscous damping is considered a reasonable range for a single reinforced concrete column. Corresponding damping factor c is calculated based on mass and stiffness as $c = \zeta 2\sqrt{mk}$. However, both k and c are parameters to be identified and unknown as mentioned above.

UKF-RM parameters, α_Q and α_R are both set to 1/30.

Based on Eq. (5.1) the state space equation is formulated as:

$$\dot{X}_a = f(X_a(t), u(t)) \tag{5.4}$$

where

Table 5.1: Selected data sets from the excitations used in C1-1 experiment

ID	Excitation type	Excitation level
2007-1212-006-1M	Takatori(Modified)	30%
2007-1213-004-1M	Takatori(Modified)	100%
2007-1213-014-1M	Takatori(Modified)	100%

$$f(\mathbf{X_a}(t), \mathbf{u}(t)) = \begin{bmatrix} x_2 \\ (-x_3 x_1 - x_4 x_2)/m + \ddot{x_g} \\ 0 \\ 0 \end{bmatrix} \tag{5.5}$$

Among the experiment dataset, three input and response measurements (Tab. 5.1) are selected for experimental validation of the proposed stiffness estimation algorithm because these data are publicly available. The identification procedure is carried out to the undamaged pier in all four cases because the SDOF model is linear in this section. However, during the experiment ground motion was applied to the system in the same order as they appear in the table which is in chronological order.

During ID $\#2007-1212-006-1M$ excitation, the experiment column was undamaged because excitation level is small and system response remains in linear range.

Furthermore, ID $\#2007-1213-004-1M$ excitation is the first input to the system which results in nonlinear response and column bottom experiences some level of stiffness loss as mentioned in 2.1.3. Finally, the last excitation, ID $\#2007-1213-014-1M$ had been exerted to the system which was already damaged. Thus, during the second 100% Takatori excitation, the pier bottom damage kept accumulating, eventually resulting in failure.

Acceleration, velocity, displacement, force and strain response under the above-presented ground motion was measured with dense sensor arrays as mentioned in Chapter 2.1.2. Among these, only acceleration response measurements on top of the pier cap were considered available for the purpose of this study. Displacement and

force measurements on top of the column were used to investigate the accuracy of the estimated stated and performance of the UKF-RM algorithm.

From simulated acceleration response, displacement response of the system is calculated with double-integration as explained in Chapter 2.1.4. Displacement calculated from the acceleration response of the system is the observation in the following parameter estimation cases. With only displacement measurement available on top of the column, the observation equation is as follows:

$$y = \begin{bmatrix} x_1 \end{bmatrix} \tag{5.6}$$

5.1.1 Small Earthquake

The full-scale bridge pier was excited with small and large level earthquakes in a chronological order. In this section, only small level earthquakes will be the focus. First, using acceleration measurements obtained on top of the bridge pier, displacement response is calculated by pre-processing the data and double integration. Then, the calculated displacement is compared with the measured displacement response to verify the accuracy of the estimation. Figure 5-1 shows good match between the measured and estimated displacement responses obtained from the acceleration measurement on top of the column during input $2007 - 1212 - 006 - 1M$. The cut-off frequency for the high-pass filter is set to $0.4Hz$

Fig. (5-2) shows that both estimated displacement and velocity response matches well with the measured displacement and velocity response on top of the pier cap.

Fig. (5-3) shows the stiffness and damping estimation results under excitation $ID : 2007 - 1212 - 006 - 1M$. Estimated stiffness is calculated as the averaged value over the significant duration and equal to $31817kN/m$. The reference stiffness value is calculated as the slope of the force displacement relationship from the measurement data. For example, in Fig. (5-4) gray line is the measured force-displacement relationship during the experiment under excitation $ID : 2007 - 1212 - 006 - 1M$. The input level is small and the RC pier is mostly in linear range. Thus, the linear fit to the measured force-displacement relationship represents the stiffness value of

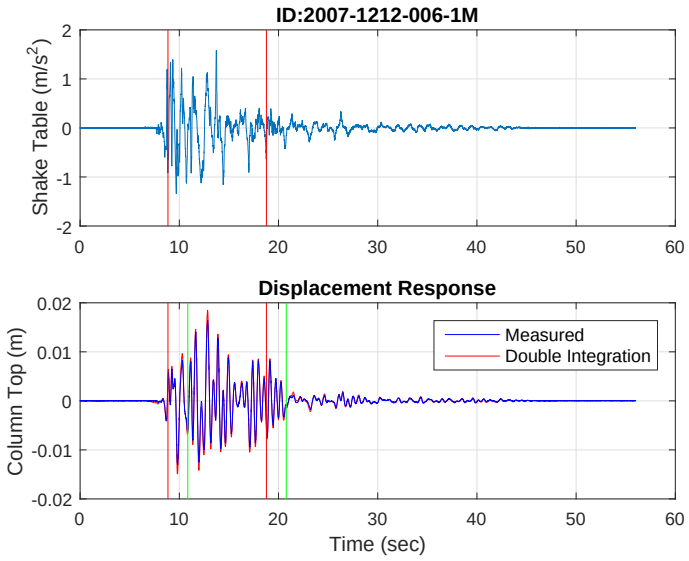

Figure 5-1: Displacement response estimation from acceleration response under excitation $2007-1212-006-1M$

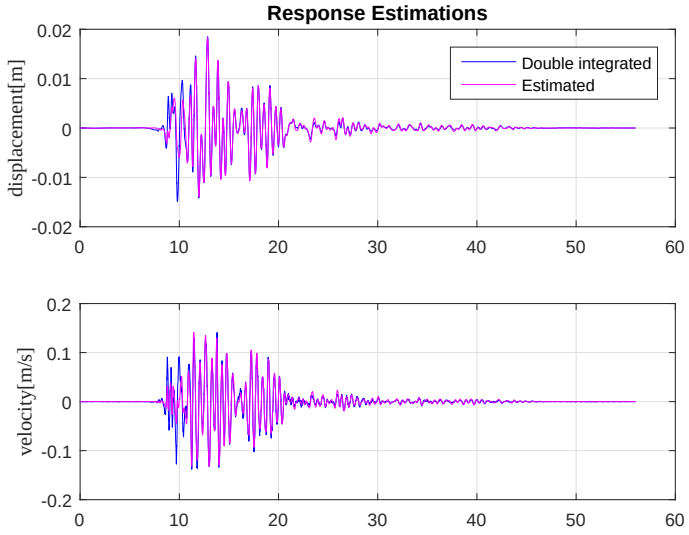

Figure 5-2: State estimation results under $2007-1212-006-1M$ excitation with $\alpha_Q = 1/30$ and $\alpha_R = 1/30$

the column. Accordingly, true stiffness value was calculated as $32506kN/m$ under excitation $ID: 2007-1212-006-1M$. Calculated corresponding damping factor is found as 8%, however, since there is no reference value for damping, it will not be presented here again.

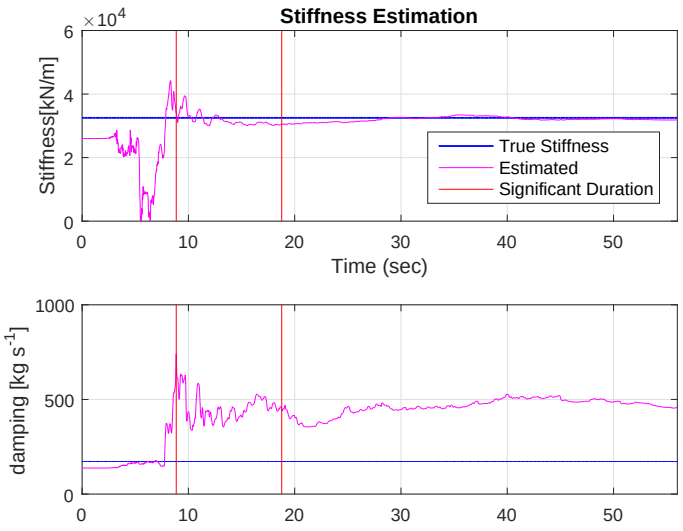

Figure 5-3: Parameter estimation results under $2007-1212-006-1M$ excitation with $\alpha_Q = 1/30$ and $\alpha_R = 1/30$

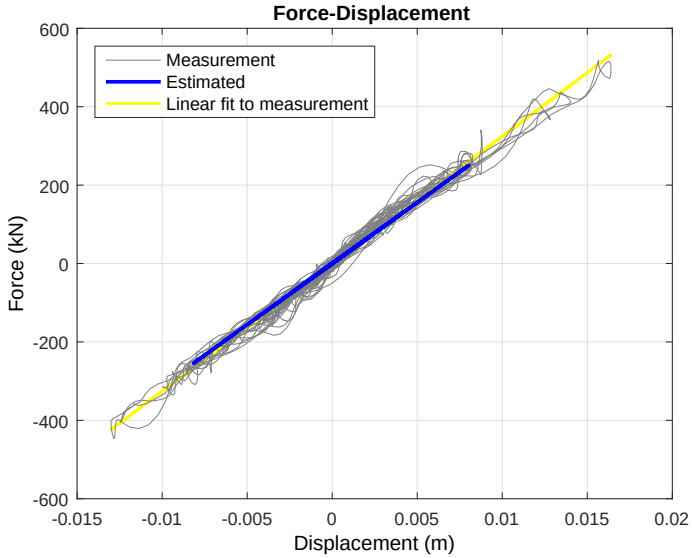

Figure 5-4: Reference stiffness calculation under excitation $2007-1212-006-1M$

Stiffness estimation results obtained with UKF-RM under 30% Takatori excitation is summarized in Table 5.2.

Table 5.2: Parameter estimation results under small earthquake excitation

	True stiffness [kN/m]	Estimated stiffness [kN/m]	Error [%]
$ID: 2007-1212-006-1M$	32506	31817	2.1

5.1.2 Large Earthquake

After small-level earthquakes, two large level earthquake inputs exerted on the bridge column in a sequence which induced damage and hence nonlinearity in the column behavior. In this section, the proposed algorithm's performance of convergence rate and ability to track changes in stiffness are investigated under the effect of large seismic inputs. Data corresponding to the first $7sec$ are deleted for both earthquake inputs because they do not hold information.

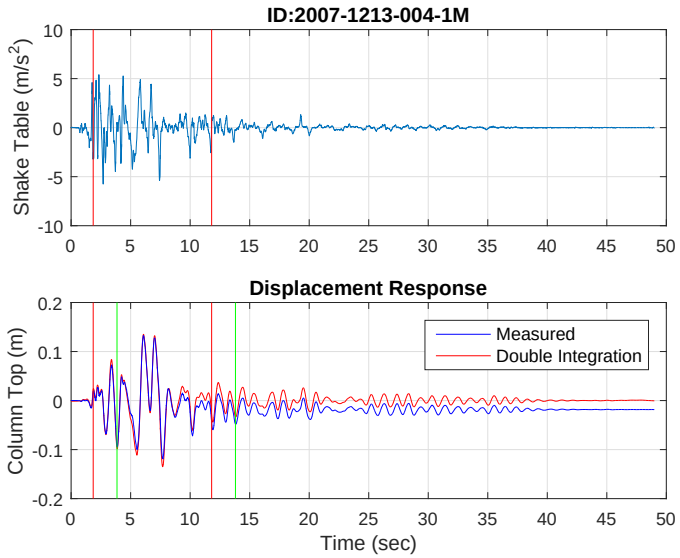

Figure 5-5: Displacement response estimation from acceleration response under excitation 2007-1213-004-1

First, using acceleration measurements obtained on top of the bridge pier, displacement response is calculated by pre-processing the data and double integration. Then the calculated displacement is compared with the measured displacement response to verify the accuracy of the estimation. The cut-off frequency for the high-pass filter for both earthquakes is set to $0.2Hz$. Figures 5-5 and 5-6 show the comparison and

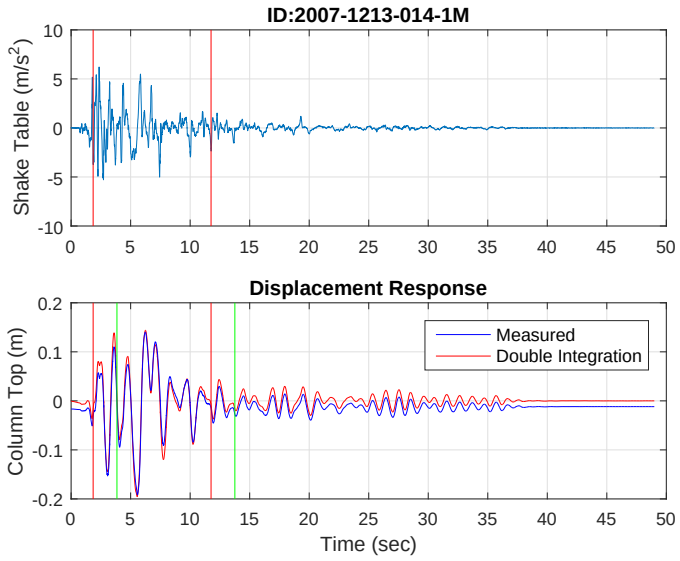

Figure 5-6: Displacement response estimation from acceleration response under excitation 2007-1213-014-1M

good match between the measured and estimated displacement responses for inputs $2007-1213-004-1M$ and $2007-1213-014-1M$. Here, from the displacement-time history figures it can be seen that the displacement which was obtained by double integration of the acceleration lack the pseudo-static displacement due to the applied high-pass filter. Except the residual displacement the remaining information was able to be captured.

In the earlier section it has been shown that the residual stiffness can be estimated with a good accuracy. However, in structural dynamics often large earthquake response is of interest and parameter estimation algorithm's ability to track response during significant duration should be investigated. Because, during significant duration most of the energy from the input is exerted to the structure and thus most of the damage occurs in this region.

UKF-RM extra parameters, α_Q and α_R are both set to 1/30.

(Figs. 5-7,5-8) show the state and parameter estimation results under excitation 2007-1213-004-1M, respectively.

Fig. (5-7) shows that both estimated displacement and velocity response matches well with the measured displacement and velocity response on top of the pier cap

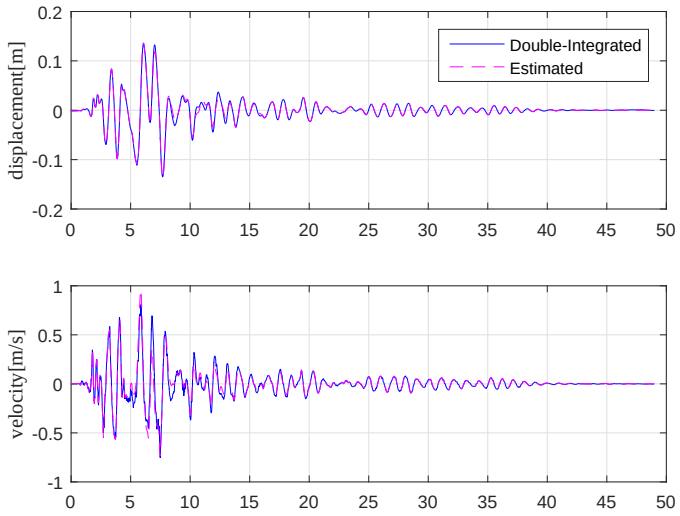

Figure 5-7: State estimation results under excitation 2007-1213-004-1M

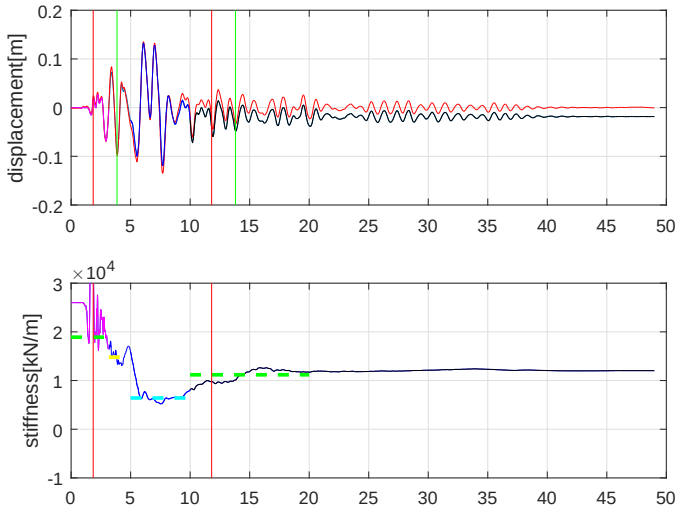

Figure 5-8: Parameter estimation results under excitation 2007-1213-004-1M

except the permanent displacement part which was an expected outcome as the input does not consist this part neither.

Fig. (5-8) shows the stiffness estimation result under excitation $ID : 2007-1213-004-1$. Shortly after start of the significant duration, the stiffness estimation starts converging. During significant duration, where the experiment column bottom

experiences cracks and yielding damage, the stiffness change can be observed from the estimation. After significant duration ends, the estimation stabilizes and stays on the same value which is equal to the residual stiffness of the reinforced concrete bridge column.

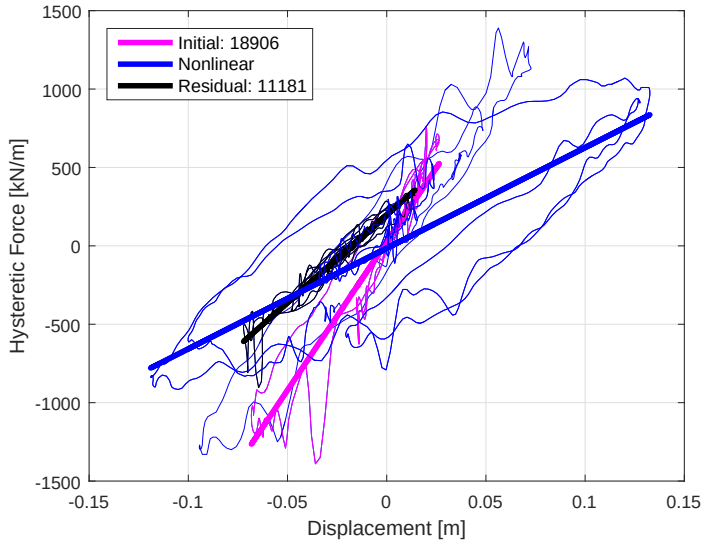

Figure 5-9: Reference stiffness values for three different response regions under excitation 2007-1213-004-1M

The corresponding reference stiffness values is calculated as the slope of the force displacement relationship from the measurement data in three regions: initial response, nonlinear response and residual response, respectively. For example, in Fig. (5-9) force-displacement curve which was constructed from the measured data during experiment is shown under excitation $ID : 2007-1213-004-1$. The above mentioned response regions are presented in the figure in color coded manner. Initial response corresponds to the pink line, the nonlinear response region corresponds to the blue line and lastly the residual response region corresponds to the black line. Linear fit to each particular response is calculated and the slope of the resultant fitted line is taken as the reference value. The residual stiffness is estimated as $12120kN/m$, where the true residual stiffness is $11181kN/m$. Thus, the error is found 7.6%.

Moreover, the nonlinear response range also divided into different regions based on the measured force-displacement relationship (Fig. 5-10). Under earthquake $2007-$

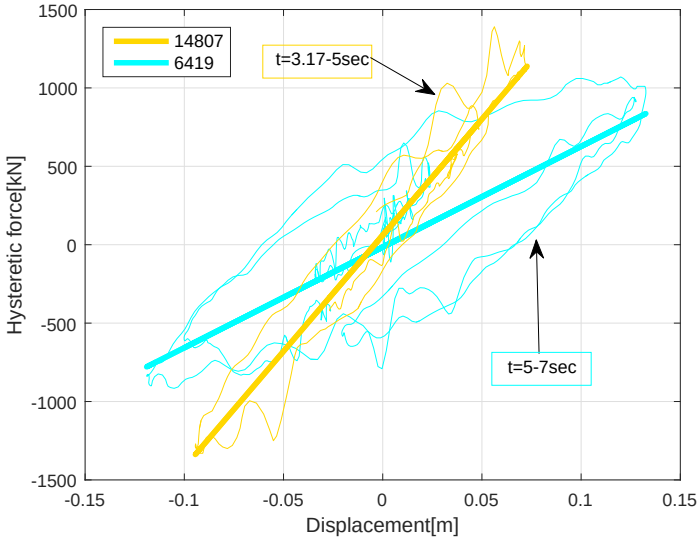

Figure 5-10: Reference stiffness values for various nonlinear response regions under excitation 2007-1213-004-1M

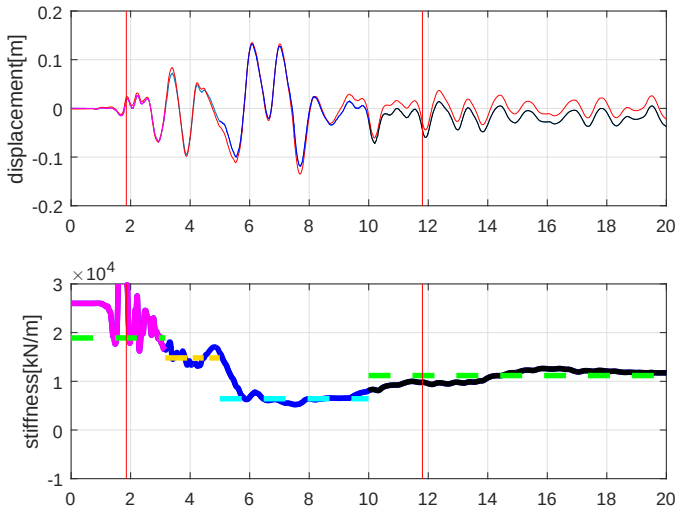

Figure 5-11: Estimated stiffness values for various nonlinear response regions under excitation 2007-1213-004-1M

$1213-004-1M$, there are two different hysteresis curves corresponding to different stiffness levels which represent the nonlinear response. For example, between $3.17-5sec$ the stiffness is $14813kN/m$ and between $5-10sec$ the stiffness is $6417kN/m$. In Fig. (5-11) the dotted orange and cyan lines represent the reference stiffness values

which were shown in (Fig. 5-10). The estimated stiffness is calculated as the mean value of estimation at corresponding times and they are equal to $15281kN/m$ and $7187kN/m$, respectively. Thus, the error percentages based on the reference stiffness values are 3% and 11%, respectively. Actually, 11% error in stiffness estimation may be considered as large. However, this difference may be attributed to the model assumption which is linear. Due to energy dissipation the force-displacement curves are getting a fat loop shape and thus the reference stiffness value cannot be represented as a single linear fitted line's slope. Consecutively, it can be concluded that even though the model is linear, the proposed method is able to track stiffness change even in nonlinear range with an acceptable performance. In the next chapter, stiffness condition change will be investigated considering a nonlinear model.

In fact, damage patterns of the experiment column are tracked during the tests and recorded [1]. Under $ID : 2007 - 1213 - 004 - 1$ excitation, the column bottom experiences hair cracks at around $t = 4sec$, vertical cracks due to compression forces at around $t = 6sec$ and concrete cover spalling at around $t = 7sec$. In the depicted stiffness estimation figure the stiffness change is clearly visible where concrete column experiences damage and dissipates energy.

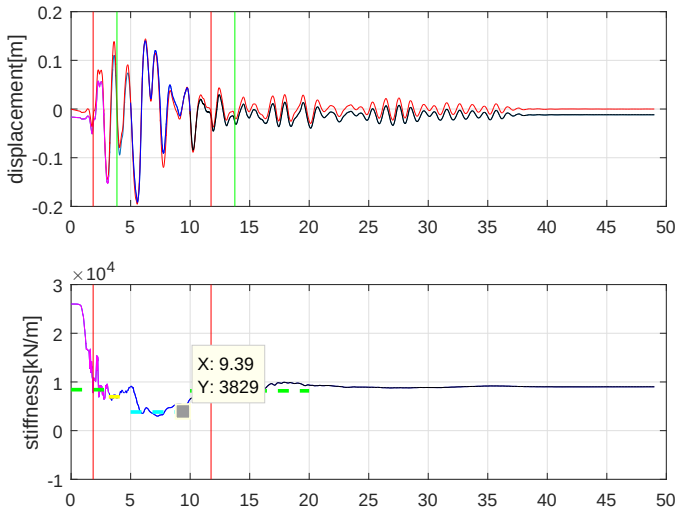

Figure 5-12: Parameter estimation results under excitation 2007-1213-014-1M

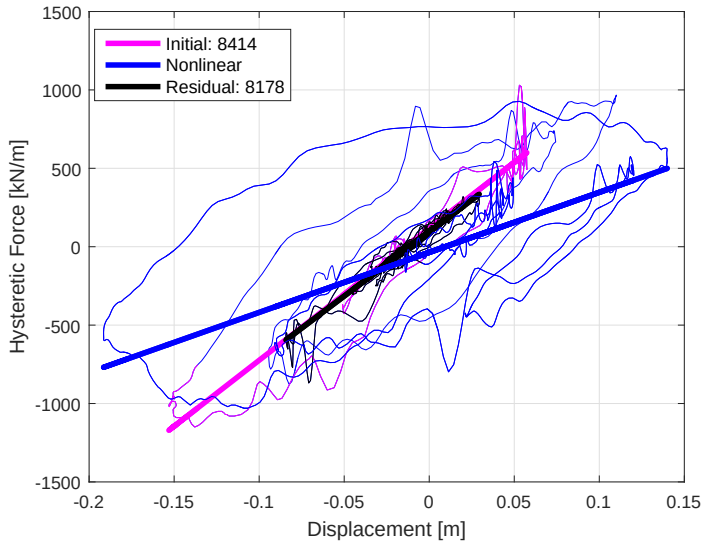

Figure 5-13: Reference stiffness values for three different response regions under excitation 2007-1213-014-1M

Stiffness estimation results (Fig. 5-12) and corresponding reference stiffness (Fig. 5-13) for three response regions are presented below also under excitation $ID : 2007-1213-014-1M$. Again, stiffness condition can be tracked in all three response regions. The residual stiffness is estimated as $8396kN/m$, where the true residual stiffness is $8178kN/m$. Thus, the error is found 3%.

Moreover, the nonlinear response range also divided into different regions based on the measured force-displacement relationship (Fig. 5-14). Under earthquake $2007-1213-014-1M$, there are two different hysteresis curves corresponding to different stiffness levels which represent the nonlinear response. For example, between $3.17-5sec$ the stiffness is $6954kN/m$ and between $5-10sec$ the stiffness is $3829kN/m$. In Fig. (5-15) the dotted orange and cyan lines represent the reference stiffness values which were shown in (Fig. 5-14). The estimated stiffness is calculated as the mean value of estimation at corresponding times and they are equal to $7553kN/m$ and $4841kN/m$, respectively. Thus, the error percentages based on the reference stiffness values are 8% and 21%, respectively. Although the errors may be large, again this difference may be attributed to the model assumption which is linear. Due to increasing energy dissipation and complex reinforced-concrete damage patterns

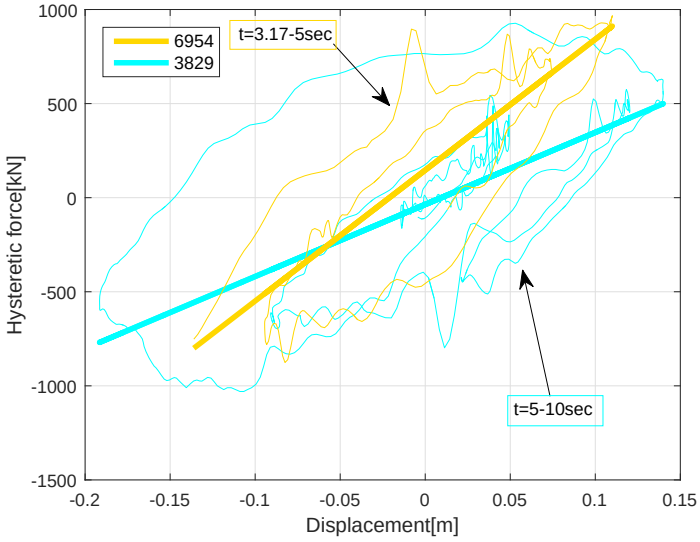

Figure 5-14: Reference stiffness values for various nonlinear response regions under excitation 2007-1213-014-1M

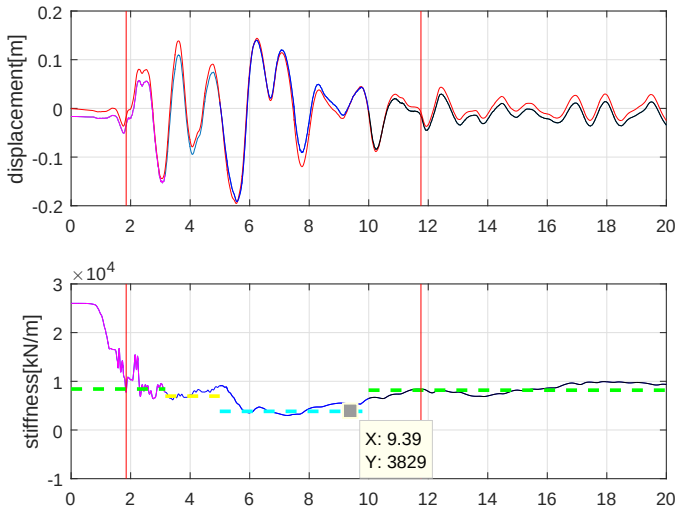

Figure 5-15: Estimated stiffness values for various nonlinear response regions under excitation 2007-1213-014-1M

the reference stiffness value in the nonlinear range cannot be represented as a single slope line. Consecutively, it can be concluded that even though the model is linear, the proposed method is able to track stiffness change even in nonlinear range with an acceptable performance. In the linear range, i.e. residual stiffness is identified

successfully.

Identified residual stiffness values under two large excitations are summarized in Table 5.3. Error percentage in identified stiffness values are both smaller than 8% and thus considered accurate.

Table 5.3: Residual stiffness estimation under large earthquake excitation

	True stiffness [kN/m]	Estimated stiffness [kN/m]	Error [%]
$ID: 2007-1213-014-1M$	11181	12120	7.6
$ID: 2007-1213-014-1M$	8179	8396	3

In conclusion, proposed parameter identification algorithm can successfully identify stiffness condition of bridge lateral resisting systems in the linear range under both small and large seismic input. Furthermore, in nonlinear response range, although the accuracy of the estimation is lower than the linear response range, the algorithm can still track the change in stiffness in a robust manner. To have a complete understanding of the nonlinear behavior and investigate the algorithm's capabilities hysteresis loop identification is necessary which will be presented in Chapter 6.

5.2 Full Scale Bridge In-Situ Seismic Response Measurement

It is a well-known fact that spatially distributed structures, such as long-span bridges, are prone to multi-support excitation (MSE). However, when short-span bridges supported by abutments backfilled with embankments they may also be subjected to MSE. In the target bridge's case, one side is supported by an abutment while the other side is supported by a pier. This results in different input ground motion on both sides. Although the recorded ground motions are considerably small when compared to design level earthquake, it is useful to investigate the feasibility of stiffness estimation on both sides separately for practical applications. For this purpose, first, the capability of the algorithm to estimate different stiffness on pier and abutment

side is investigated with simulations. After that, stiffness estimation of the bearings is performed using acceleration measurements on the real bridge during earthquakes.

5.2.1 Bearing stiffness identification with MSE through simulation

Based on the calculated displacement trajectories from measured acceleration responses during earthquakes the girder can be considered as a rigid body as explained in Chapter 2.2.3. The bridge is modeled as a 3-DOF system where the lumped mass, $m = 180tons$, is located at the center of the span and connected to the four supports with rigid elements. The system scheme is presented in Fig. (5-16).

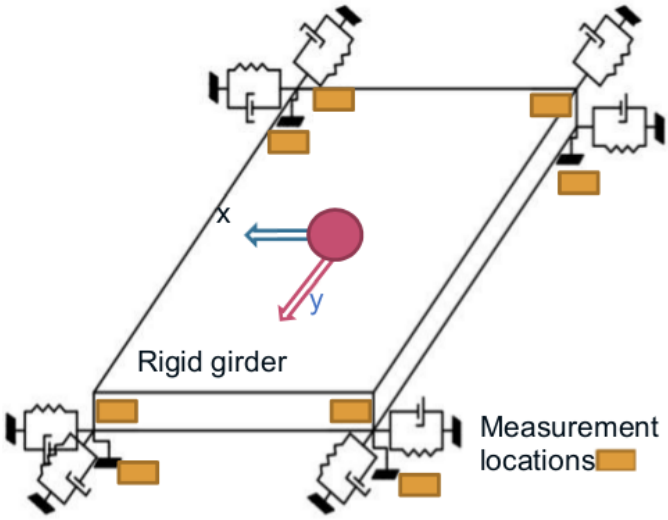

Figure 5-16: Girder and bearing system scheme and measurement locations on the bridge

Abutment and pier side total bearing stiffness are assumed different from each other to replicate a scenario in which bearings on one side are damaged. Thus, the total stiffness of the two bearings on pier side is assumed $k_{pier} = 5200kN/m + 5200kN/m = 10400kN/m$. The total stiffness of the two bearings on abutment side is assumed $k_{abutment} = 6500kN/m + 6500/m = 13000kN/m$. The stiffness values of the bearings in longitudinal (Y) and transverse (X) directions are assumed equal.

$\zeta = 4\%$ viscous damping was given in the design drawings. Corresponding damping factor c is calculated based on mass and stiffness as $c = \zeta 2\sqrt{mk}$.

The displacement and velocity obtained from acceleration measurements (Fig. 5-17) on pier and abutment top at each support node both in longitudinal and transverse directions, 8 in total, are considered as input to the system. Measured accelerations at the support nodes are presented in Fig. (5-18). Observation vector is the displacement and velocity in both directions at the corresponding girder locations which are transformed to the center of the mass in measurement equation.

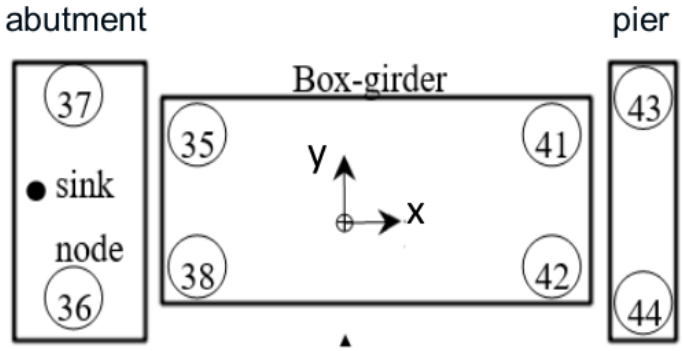

Figure 5-17: Sensor installation plan on the bridge

3DOF system excited at its base (pier top acceleration measurement) with ground acceleration the governing equation of motion in absolute coordinates (EOM-abs) becomes:

$$\begin{bmatrix} M\ \ddot{x_x}(t) + C\ \dot{x_x}(t) + K\ x_x(t) - P_{kx}\ \theta \\ M\ \ddot{x_y}(t) + C\ \dot{x_y}(t) + K\ x_y(t) + P_{ky}\ \theta \\ I\ddot{\theta}(t) + C_\theta\dot{\theta}(t) + K_\theta\theta(t) - P_{kx}x_x(t) + P_{ky}x_y(t) \end{bmatrix} = K_{sg}[x_g] + C_{sg}[\dot{x_g}] \tag{5.7}$$

where $x(t)$ and $\dot{x(t)}$ are the absolute displacement and velocity response on the girder above the bearing.

and $x_g(t)$ and $\dot{x_g}(t)$ are the ground motion displacement and velocity vectors on

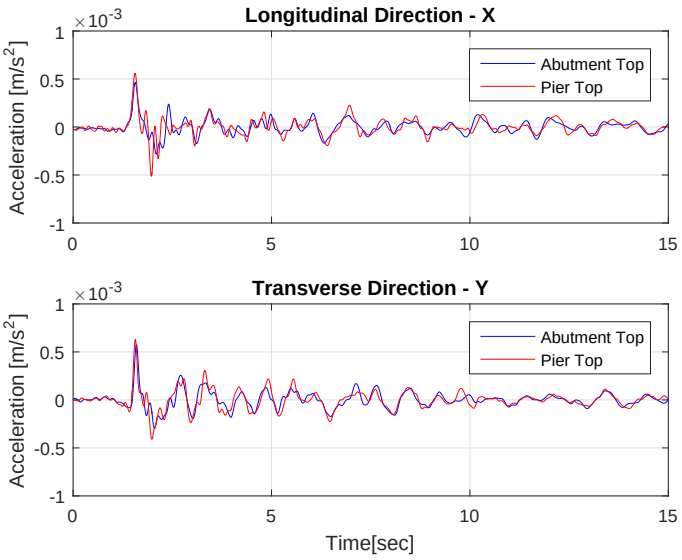

Figure 5-18: Acceleration measurements on the abutment next to the bearings, Nodes 43-44

top of the pier cap at the bottom of the bearing. They are defined as follows.

$$x_g(t) = \begin{bmatrix} x_{gx} \\ x_{gx} \\ x_{g\theta} \end{bmatrix} \tag{5.8}$$

$$\dot{x_g}(t) = \begin{bmatrix} \dot{x_{gx}} \\ \dot{x_{gx}} \\ \dot{x_{g\theta}} \end{bmatrix} \tag{5.9}$$

The subscripts x and y denote the directions x and y (5-17).

In Equations 5.8 and 5.9, $x_{g\theta}$ and $\dot{x_{g\theta}}$ are assumed to be equal to zero.

In Equation 5.7, K_{sg} and C_{sg} are defined as follows:

$$K_{sg} = \begin{bmatrix} -k_{x1} & -k_{x2} & -k_{x3} & -k_{x4} & 0 & 0 & 0 & 0 & 0 \\ 0 & 0 & 0 & 0 & -k_{y1} & -k_{y2} & -k_{y3} & -k_{y4} & 0 \\ k_{x1} \times bh & k_{x2} \times bh & -kx3 \times bh & -k_{x4} \times bh & k_{y1} \times L2 & -k_{y2} \times L1 & k_{y3} \times L1 & -k_{y4} \times L2 & 0 \end{bmatrix} \tag{5.10}$$

$$C_{sg} = \begin{bmatrix} -c_{x1} & -c_{x2} & -c_{x3} & -c_{x4} & 0 & 0 & 0 & 0 & 0 \\ 0 & 0 & 0 & 0 & -c_{y1} & -c_{y2} & -c_{y3} & -c_{y4} & 0 \\ -c_{x1} \times bh & -c_{x2} \times bh & c_{x3} \times bh & c_{x4} \times bh & -c_{y1} \times L2 & c_{y2} \times L1 & -c_{y3} \times L1 & c_{y4} \times L2 & 0 \end{bmatrix} \tag{5.11}$$

where $bh = 2.5m$ which is the half of the width of the bridge, $L1$ and $L2$ are the distance of bearings 1 and 3, and 2 and 4 from the center of mass. In the formulations the numbering of the bearings are as follows. $Bearing\ 1 = Node\ 35-37$, $Bearing\ 2 = Node\ 41-43$, $Bearing\ 3 = Node\ 38-36$, and $Bearing\ 4 = Node\ 42-44$. For example, k_{x1} is the stiffness of $Bearing$ 1 in x direction where c_{y4} is the damping constant of $Bearing$ 4 in the y direction.

The stiffness and damping constant values of each bearing are assumed equal in x and y directions. Thus, $k_{xi} = k_{yi} = k_i$

M is the total mass of the girder, I is the total moment of inertia along the vertical axis of the girder. K_θ is the torsional stiffness and C_θ is the torsional damping. P_{kx} and P_{ky} are defined as:

$$\begin{aligned} P_{kx} &= Ke_y \\ P_{ky} &= Ke_x \end{aligned} \tag{5.12}$$

where e_x and e_y are the eccentricity in both directions. The pier and abutment bearings have different stiffness, thus only eccentricity in x direction (Fig. 5-17) exists. Eccentricity in transverse direction $e_x = 0$.

Eccentricity in longitudinal direction e_y is defined as follows.

$$e_y = L/2 - ((k_{abutment}) * L)/(k_{abutment} + k_{pier}) \tag{5.13}$$

Thus distance of the bearings from the center of mass becomes

$$L1 = L/2 + e_y$$

for bearings on abutment side

$$L2 = L/2 - e_y$$

for bearings on pier side

(5.14)

K, C, K_θ, C_θ are obtained as:

$$\begin{aligned} K &= \sum_{i=1}^{4} k_i = k_1 + k_2 + k_3 + k_4 \\ C &= \sum_{i=1}^{4} c_i = c_1 + c_2 + c_3 + c_4 \\ K_\theta &= \sum_{i=1}^{4} k_i (x_{bi}^2 + y_{bi}^2) \\ C_\theta &= \sum_{i=1}^{4} c_i (x_{bi}^2 + y_{bi}^2) \end{aligned} \tag{5.15}$$

where x_{bi} and y_{bi} are the distance of each bearing from center of mass.

Based on the above given governing equation the augmented state vector becomes

$$X_a = [x_x, x_y, \theta, \dot{x_x}, \dot{x_y}, \dot{\theta}, k_{abutment}, k_{pier}]^T = [x_1, x_2, x_3, x_4, x_5, x_6, x_7, x_8]^T \tag{5.16}$$

with states displecement and velocity in both directions, θ is the rotation about the vertical axis and structural parameters $[k_{abutment}, k_{pier}]$ are to be estimated where

$$k_{abutment} = k_1 + k_3 k_{pier} = k_2 + k_4 \tag{5.17}$$

Mass and damping are assumed as known in all following structural parameter estimation cases.

Based on Eq. (5.7) the state space equation is formulated as:

$$\dot{X}_a = f(X_a(t), u(t)) \tag{5.18}$$

where

$$f(\mathbf{X_a}(t), \mathbf{u}(t)) = \begin{bmatrix} x_4 \\ x_5 \\ x_6 \\ -(x_7 + x_8)\ x_1/M - C\ x_4/M + K_{sg}x_{gi}/M + C_{sg}\dot{x_{gi}} \\ \\ -(x_7 + x_8)\ x_2/M - (x_7\ L1 + x_8\ L2)\ x_3/M \\ -C\ x_5/M + K_{sg}x_{gi}/M + C_{sg}\dot{x_{gi}} \\ \\ -(-x_7 * L1 + x_8 * L2)\ x_2/I_\theta \\ -[bh^2\ (x_7 + x_8) + (L1^2\ x_7) + (L2^2\ x_8)]\ x_3/I_\theta \\ -C_{theta}\ x_6/I_\theta + K_{sg}x_{gi}/I_\theta + C_{sg}\dot{x_{gi}}/I_\theta \\ \\ 0 \\ 0 \end{bmatrix} \tag{5.19}$$

$$e_y\ = L/2 - (x_7 * L)/(x_7 + x_8) \tag{5.20}$$

$$L1 = L/2 + e_y$$

for bearings on abutment side

$$L2 = L/2 - e_y$$

for bearings on pier side

(5.21)

As we know that displacement and velocity starts from zero the corresponding initial state vector values are assigned as zero. However, the current condition of stiffness and damping is not known in practice, thus the selection of initial values is

also an important aspect for a successful estimation. About a 20% difference from the true value is chosen as model error. Initial state vector is shown below.

$$X_0 = [0, 0, 0, 0, 0, 0, 0.8\ k_{abutment}, 0.8\ k_{pier}]^T \tag{5.22}$$

Initial error covariance, by definition, is set to

$$P_0 = diag[0.01, 0.01, 0.01, 0.01, 0.01, 0.01, (k_{abutment})^2, (k_{pier})^2] \tag{5.23}$$

5% of the measurement RMS is assumed as measurement noise. Accordingly, R, measurement noise covariance is set to $R = (measurement\ RMS * 0.05)^2$.

Using the system explained above and initial values, the system simulated with and response obtained by Newmark integration method. Accordingly, parameter estimation with UKF-RM algorithm has been performed. α_Q and α_R, ware both set to 1/7 without any further consideration.

Initial process noise covariance matrix Q is set to:

$$Q = diag[1e-8, 1e-8, 1e-10, 1e-8, 1e-8, 1e-10, 1e-5, 1e-5] \tag{5.24}$$

Figs. (5-19),(5-20) and (5-21) show estimated response comparisons with response obtained by Newmark solutions. As it can be seen from the figures the UKF-RM estimations matching well with the simulation results.

The parameter estimation results are given in Fig. (5-22). As it can be seen, shortly after the start of the significant duration (first vertical red line) the algorithm converges quickly and result in a very stable estimation. After 2 seconds from the significant duration is accepted as the beginning of the correct estimation and the resultant values are averaged over the period of significant duration (between the vertical green lines). The results are summarized in Table (5.4).

By updating both observation and measurement noise covariance matrices the simulation results confirmed that estimation of the stiffness values separately on the

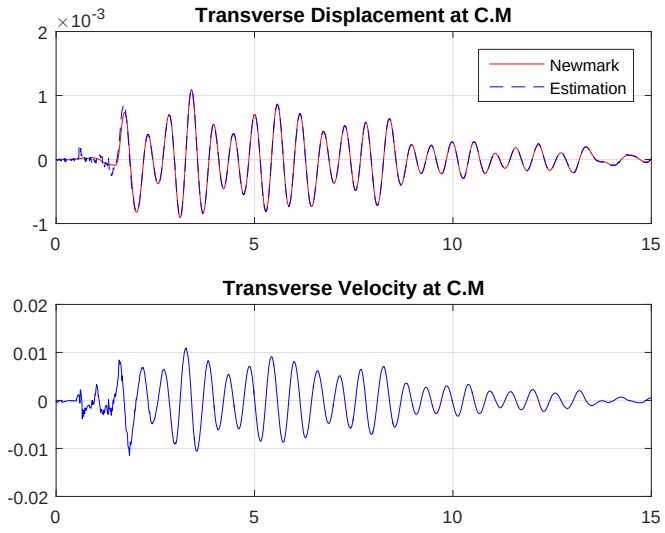

Figure 5-19: Girder response in transverse direction - simulation and estimation comparison

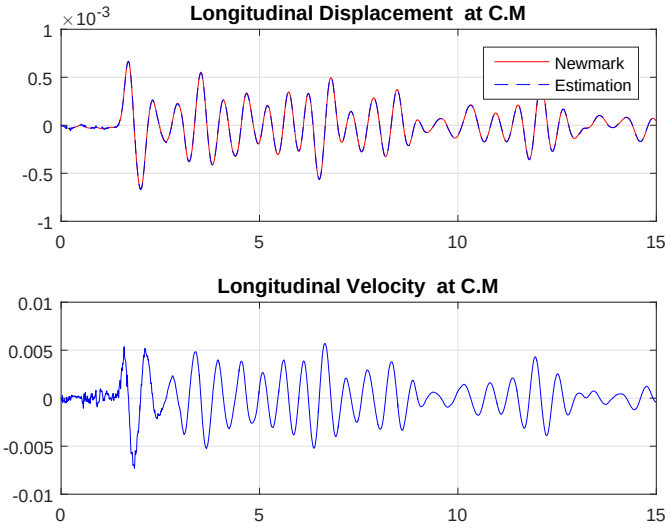

Figure 5-20: Girder response in longitudinal direction - simulation and estimation comparison

Table 5.4: Parameter estimation results

	True stiffness [kN/m]	Estimated stiffness [kN/m]	Error [%]
$k_{abutment}$	13000	12770	1.8
k_{pier}	10400	10460	0.6

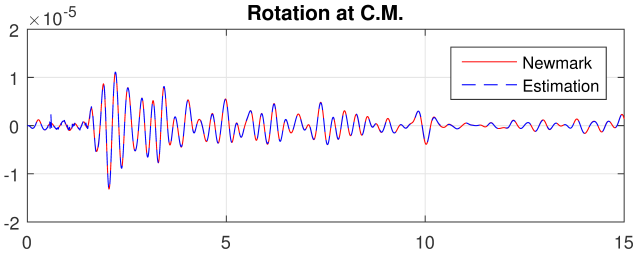

Figure 5-21: Girder response rotation about vertical axis - simulation and estimation comparison

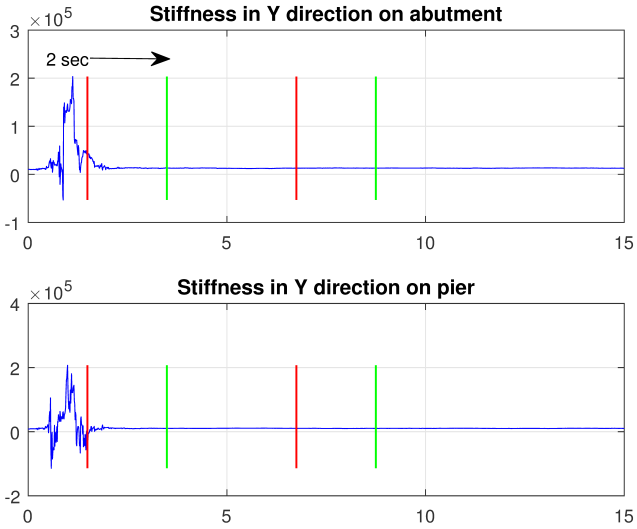

Figure 5-22: Estimated total pier and abutment stiffness

pier and abutment sides is possible. Fig. (5-23) shows the results of the investigation for the dependency of the stiffness estimation to damping value change. The assumed design damping ratio which is 4% has been changed to different values and parameter estimation algorithm has been performed. As shown in Fig. (5-23) changing damping by about 25% does not result in any variation in the stiffness estimation, thus the assumption that the damping is known is confirmed to be a viable approximation.

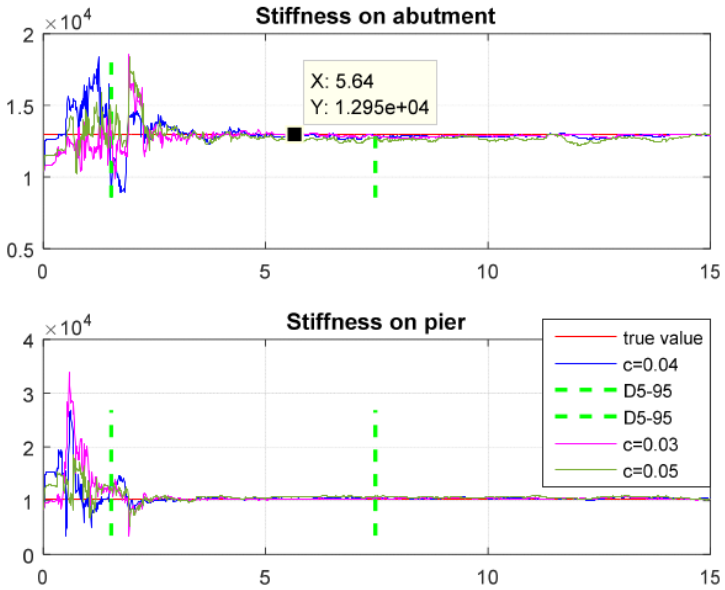

Figure 5-23: Sensitivity of stiffness estimation with respect to different assumed damping ratios

As a result, the capability of the algorithm and validation of assumptions are confirmed based on the above presented results for stiffness identification of rubber bearings on different locations of the a bridge. Consequently, stiffness estimation is performed using the acceleration response data on girders from the experiment conducted in Kumamoto (Chapter 2.2).

5.2.2 Bearing stiffness identification with MSE using measurements

The base isolation system is formed of four elastomeric rubber bearings (Fig. 5-16). Thus initial design value for each bearing is equal to each other, $k_i = 6500kN/m$, in both longitudinal and transverse directions. $\zeta = 4\%$ viscous damping was given in the design drawings. Corresponding damping factor c is calculated based on mass and stiffness as $c = \zeta 2\sqrt{mk}$. 3DOF system description and governing equations are same as presented before.

The displacement and velocity obtained from acceleration measurements (Fig. 5-17) on pier and abutment top at each support node using method explained in Chapter 2. In total, 8 displacement and 8 velocity measurements (in two directions) are considered as input to the system. Measured accelerations at the support nodes are presented in Fig. (5-18). Observation vector is the displacement and velocity in both directions at the corresponding girder locations which are transformed to the center of the mass in measurement equation.

As we know that displacement and velocity starts from zero the corresponding initial state vector values are assigned as zero. However, the current condition of stiffness is not known hence the initial values is not known in practice. Here a 20% difference from the true value is assumed as model error. Initial state vector is shown below.

$$X_0 = [0, 0, 0, 0, 0, 0, 0.8k_{abutment}, 0.8k_{pier}]^T \tag{5.25}$$

Initial error covariance, by definition, is set to

$$P_0 = diag[0.01, 0.01, 0.01, 0.01, 0.01, 0.01, (k_{abutment})^2, (k_{pier})^2] \tag{5.26}$$

because in reality the initial condition of the states are known. Thus by setting P_0 a practical large value model error at the initial stage is considered high.

3% of the measurement RMS is assumed as measurement noise. Accordingly, R,

measurement noise covariance is set to $R = (measurementRMS * 0.03)^2$.

Initial process noise covariance matrix Q is set to:

$$Q = diag[1e-8, 1e-8, 1e-10, 1e-8, 1e-8, 1e-10, 1e-5, 1e-5] \qquad (5.27)$$

Using the same 3-DOF model with MSE (explained above) and initial values, parameter estimation with UKF-RM algorithm has been performed. α_Q and α_R, were both set to 1/7. By updating both observation and measurement noise covariance matrices states and stiffness estimation for abutment and pier side bearings are successfully obtained.

Table (5.5) summarizes some of the estimation results obtained by using seismic response measurements which has $PGAgeq10gal$ both at the ground node (bottom of the pier - Node 49) both in transverse and longitudinal directions (Fig. 2-23).

Table 5.5: Parameter estimation results using Experiment data

	$k_{abutment}$ [kN/m]	Error [%]	k_{pier} [kN/m]	Error [%]
EQ57	3923	-10	4290	-2
EQ9	4003	-8.5	4420	1.1
EQ58	3893	-11	4422	1.1
EQ21	4704	7.5	4390	0.3
EQ20	4924	12.5	4430	1.3
EQ25	4802	9.8	3830	-12.5
EQ26	4458	2	3861	-11.7
EQ47	4455	2	5028	13

By updating both process and measurement noise covariance matrices it was possible to estimate the stiffness parameters as shown. The stiffness estimations converged to similar values during the significant durations of each earthquake with small variations. It is confirmed that separate stiffness identification is viable as the results from different inputs of similar amplitudes resulted in similar estimations.

Some representatives for stiffness identification results from measurements during EQ21, EQ20 and EQ58 are depicted in Figures (5-25), 5-24), and 5-26), respectively.

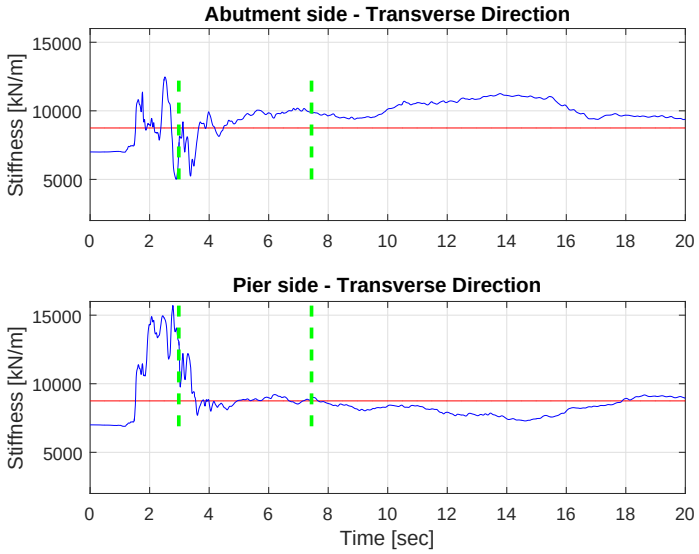

Figure 5-24: Estimated stiffness time-history from on-site measurement - EQ20

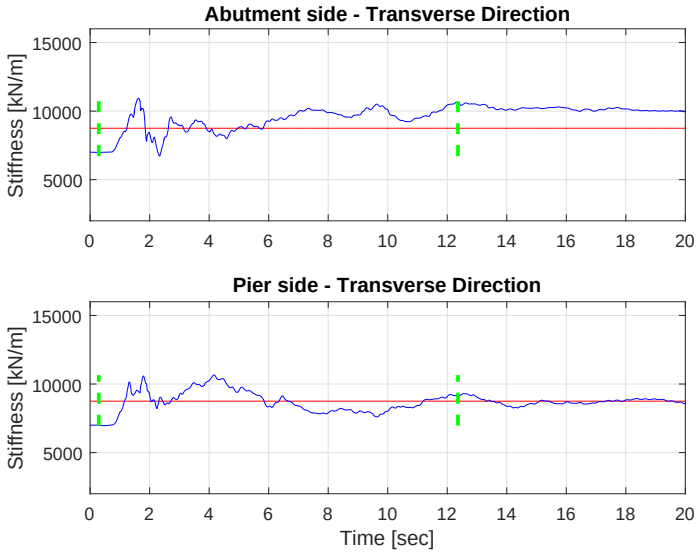

Figure 5-25: Estimated stiffness time-history from on-site measurement - EQ21

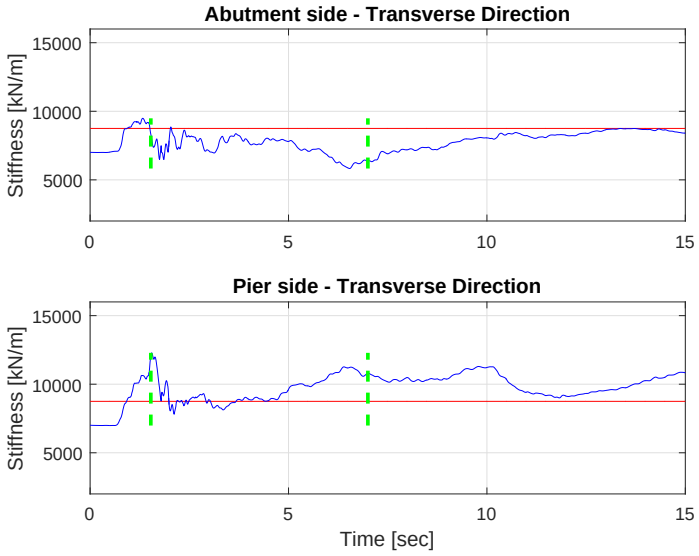

Figure 5-26: Estimated stiffness time-history from on-site measurement - EQ58

In the figures, the green vertical lines represent the beginning and end of the significant duration for each earthquake.

Estimated stiffness values were compared using force-displacement data obtained from tests conducted on the bearings by the manufacturer before installation on the bridge. Bearings on abutment and pier side were both tested four times. Obtained stiffness values were given in Table 5.6.

Table 5.6: Manufacturer's bearing test results

Test no.	$k_{abutment}$ [kN/m]	k_{pier} [kN/m]
1	4673	4816
2	4477	4625
3	4416	4537
4	4370	4503

Ultimately, final design value for the bearing stiffness was provided as $4375kN/m$ in the design drawings. Thus, the reference stiffness value is equal to $4375kN/m$ and estimated stiffness values are compared to this value.

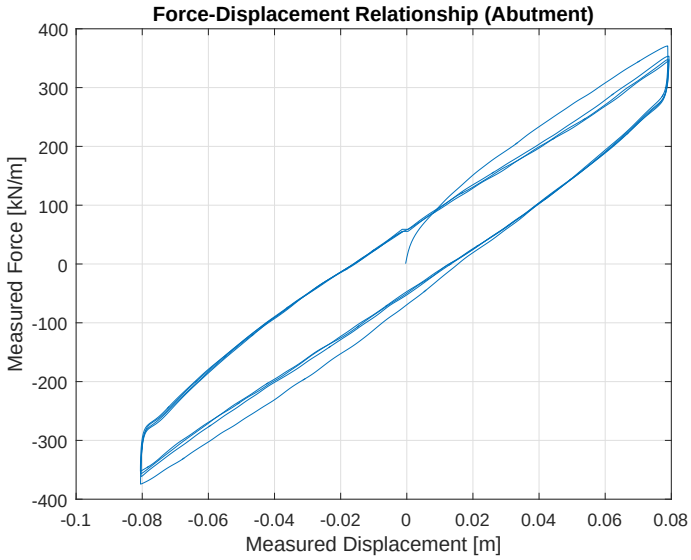

Figure 5-27: Representative force-displacement relationship from the test on a bearing on the abutment side

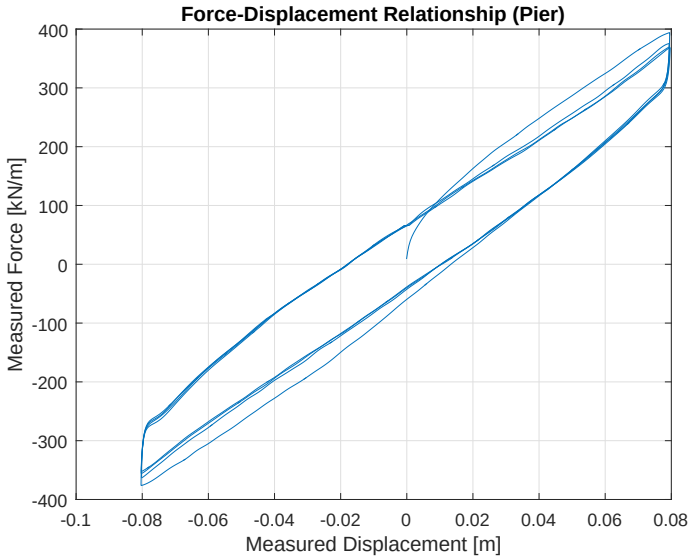

Figure 5-28: Representative force-displacement relationship from the test on a bearing on the pier side

Chapter 6

Hysteresis Response Estimation

Structures exhibit hysteresis response when subjected to cyclic forces such as earthquake excitation. The force-displacement relationship provides important information on quantity of energy dissipation on the element or structure. Thus, in order to have a complete understanding of the structural nonlinear behavior not only residual stiffness but also hysteresis response estimation is necessary.

Structures experience nonlinear response due to enery dissipation in elements such as joints [21], mounted damping devices [24] and reinforced concrete columns [22, 23]. Nonlinear dynamic analysis requires an explicit mathematical expression to represent nonlinear response of the structure. One of the well studied hysteresis models in civil and mechanical engineering is Bouc-Wen model which has been proven to be able to track various damage scenarios in structural dynamics such as hardening and softening.

The model was first proposed by Bouc in [25], and later generalized by Wen in [26], thus the model name is known as Bouc-Wen. The generalized model is a non-degrading hysteresis model and considered as the simplest one among the variety of Bouc-Wen models. Modified types of Bouc-Wen model can account for either only degradation of stiffness and strength which was proposed by [69], or both degradation and pinching behavior which were proposed by [70] and [71]. Recent state-of-the-art review on studies dealing with Bouc-Wen models, from both mathematical derivation to identification of hysteresis parameters perspectives can be found in [72].

Some previous research on Kalman Filter based identification of nonlinear response considering Bouc-Wen model includes but not limited to the following. [73] proposed a recursive least-square based algorithm considering a forgetting factor to adapt the gain matrix using acceleration measurements as observation and presented applications through various simulations. [74] presented identification of a SDOF nonlinear model with Bouc-Wen element considering $n = 1$. Through simulations EKF with weighted global iteration showed satisfactory estimation results when measurement noise is considered and consideration of modeling noise was suggested as an open area of research. [75] identified soil characteristics under earthquake input using EKF with weighted global iteration. A bore hole array is modeled as a 3DOF model considering Bouc-Wen elements at each DOF. Using relative displacement, relative velocity and shear stress as observations from each DOF, they identified the nonlinear response of the soil using only the portions of data where full stress reversals exists.

Furthermore, recently some studies investigated application of data assimilation methods on problems of practical significance. A scaled three-bent bridge was excited by one-directional earthquake input on a shake-table in [17]. First an FEM model was calibrated based on the experiment results which was later used in Extended Kalman Filter as state transition matrix. Elemental residual stiffness values of each bent was estimated using EKF. In another study using simulated response measurements [19] structural parameters of a 3DOF system which consists of a Bouc-Wen element in the first DOF were estimated using GPS displacement for the first DOF measurement and acceleration measurements for the other two. Later in [27], systems including Bouc-Wen elements were further investigated from the observability and identifiablity point of view as Bouc-Wen element consists of many parameters. Recently, [28] proposed a method for online Bayesian model assessment for UKF. However, process noise parameters are assumed as known which is not a realistic condition when practical structures are considered. Verification examples were presented through simulations and then a laboratory experiment on a test apparatus which was designed to simulate a 2DOF non-conservative dissipative joint element as presented in [29].

The main aim of this chapter is to verify parameter estimation algorithm con-

sidering a highly nonlinear hysteresis model with generalized Bouc-Wen model using only acceleration measurements. First, a brief review of the selected hysteresis model is presented. Then, based on the observability analysis model reduction assumptions are reviewed. Furthermore, the parameter estimation algorithm is first verified through simulations using a SDOF system and performance of the algorithm is examined through investigation of sensitivity to change in filter parameters. Lastly, the algorithm is validated using acceleration measurements from E-Defense shake-table laboratory experiment in which hysteresis parameter estimation is performed on a full-scale reinforced concrete bridge pier.

6.1 Observability Analysis and Model Reduction

In this section a SDOF model including a Bouc-Wen element is considered to represent the hysteresis behavior of a nonlinear dynamic system. Considering the classical Bouc-Wen model, the governing equation of motion for a SDOF system is

$$m\ddot{x} + c\dot{x} + \alpha kx + (1-\alpha)kr = -m\ddot{x}_g(t) \tag{6.1}$$

where r is the Bouc-Wen hysteresis component with

$$\dot{r} = A\dot{x} - \beta|\dot{x}||r|^{n-1}\, r - \gamma\dot{x}|r|^n \tag{6.2}$$

β, γ and A are the Bouc-Wen parameters which controls the shape of the hysteresis, n is the Bouc-Wen parameter which controls the sharpness of yield and α is the ratio of the post-yield stiffness to elastic stiffness.

As it can be seen from Eqs. (6.1) and (6.2) the model is highly nonlinear when the exponential term is $n > 1$. Thus, the model is suitable for the performance investigation of the proposed method using only acceleration measurements. For instance, [76] showed through simulations that both EKF and UKF can estimate the generalized Bouc-Wen hysteresis response when nonlinearity is limited in the model, in other words when $n = 1$. However, when n is considered equal to two, then

EKF estimations failed while conventional UKF continued to give satisfactory results estimations.

With the above given governing equation the augmented state vector becomes

$$X_a = [x, \dot{x}, r, k, c, \beta, n, \gamma, \alpha, A]^T = [x_1, x_2, x_3, x_4, x_5, x_6, x_7, x_8, x_9, x_{10}]^T \tag{6.3}$$

For any identification problem, if possible, it is important to limit the number of unknown parameters. Thus, model reduction has been conducted based on the assumptions explained below.

Bouc-Wen parameters are empirical and all of them does not need to be specificed with precision in order to satisfy a good fit to an hysteresis loop. Although a given set of parameters produces a unique hysteresis relationship, its contrary is not valid. When redundant parameters are eliminated by transformations between the Bouc-Wen parameters, [77] showed that same system response can be obtained from two different set of parameters. One of the redundant parameters is A. Consider the Bouc-Wen parameter vector is,

$$\nu = [r, \beta, n, \gamma, \alpha, A]^T \tag{6.4}$$

and Bouc-Wen hysteresis displacement is redefined as

$$\dot{r_A} = \dot{x} - \beta_A |\dot{x}| |r_A|^{n-1} r_A - \gamma_A \dot{x} |r_A|^n \tag{6.5}$$

where

$r_A = r/A$, $\beta_A = \beta |A|^{n-1} A$ and $\gamma_A = \gamma_A |A|^n$

Equations (6.2) and (6.5) are essentially same. Because in this transformation A can be set equal to 1 [77]. Similar parameter transformations can also be done on other parameters also in modified Bouc-Wen models.

Next, the system is assumed purely nonlinear. Thus α, the ratio of the post-yield stiffness to elastic stiffness is set to zero. The basis for this assumption is the fact that

in linear response range structural elements usually dissipate limited amount of energy when compared to nonlinear response range. The target is to achieve estimation of the dissipated energy in the system in the nonlinear response range.

Consequently, the state vector becomes

$$X_a = [x, \dot{x}, r, k, c, \beta, n, \gamma]^T = [x_1, x_2, x_3, x_4, x_5, x_6, x_7, x_8]^T \tag{6.6}$$

and Bouc-Wen hysteretic displacement can be represented as follows.

$$\dot{r} = \dot{x} - \beta|\dot{x}||r|^{n-1} r - \gamma\dot{x}|r|^n \tag{6.7}$$

Using acceleration response measurements as observation and identifying the stiffness condition and hysteretic force of a full-scale bridge lateral resisting system with UKF-RM is one of the main targets of this chapter. In practice, location of sensors in the measurement array holds great importance because an unknown state to be estimated, output measurements must be adequate; not only in terms of quality but also the provided sort of information. The ability of the output measurements of letting unknown states to be estimated is measured by observability. In other words, if a system's states can be estimated by a given set of output measurements in a finite time then the system is observable [27].

To check the algorithms ability to estimate the states given above using only acceleration measurements, nonlinear observability analysis is performed, because even without the presence of Bouc-Wen element, the system is nonlinear due to the augmented state vector. The Observability Rank Condition (ORC) method was first proposed by [78] and recently introduced to structural dynamics are by the work of [27]. ORC method requires measurement and system matrices to be analytic. However, a system which consists of Bouc-Wen element is not analytic because (Eq. 6.7) which is not differentiable due to absolute value functions' presence. Thus ORC method can be applied to the all four branches of Eq.(6.7), evolutionary parameter, and observability condition is checked.

The four branches are given as follows :

$$\left[\begin{array}{c} \dot{r} = \dot{x} - \beta\dot{x}r^n - \gamma\dot{x}r^n, whenr \geq 0, \dot{x} \geq 0 \\ \dot{r} = \dot{x} + \beta\dot{x}r^n - \gamma\dot{x}r^n, whenr \geq 0, \dot{x} < 0 \\ \dot{r} = \dot{x} - \beta\dot{x}{-}r^n - \gamma\dot{x}{-}r^n, whenr < 0, \dot{x} < 0 \\ \dot{r} = \dot{x} + \beta\dot{x}r^n - \gamma\dot{x}r^n, whenr < 0, \dot{x} \geq 0 \end{array}\right] \tag{6.8}$$

Consequently, the system becomes unobservable as the state vector contains 8 unknown parameters and observability rank results in 7.

In order the system to become observable the state vector size should be reduced to 7. This can be achieved by further model reduction based on the Bouc-Wen model properties which are discussed below.

Table 6.1: BIBO stability conditions for Bouc-Wen model (modified from [3])

Case	Condition	Ω	Upper bound on $\lvert r(t)\rvert$	Class
$A > 0$	$\beta+\gamma > 0$ and $\beta-\gamma \geq 0$	R	$\max(\lvert r(0)\rvert, r_0)$	I
	$\beta-\gamma < 0$ and $\beta \geq 0$	$[-r_1, r_1]$	$\max(\lvert r(0)\rvert, r_0)$	II
$A < 0$	$\beta-\gamma > 0$ and $\beta+\gamma \geq 0$	R	$\max(\lvert r(0)\rvert, r_1)$	III
	$\beta+\gamma < 0$ and $\beta \geq 0$	$[-r_0, r_0]$	$\max(\lvert r(0)\rvert, r_1)$	IV
$A = 0$	$\beta+\gamma > 0$ and $\beta-\gamma \geq 0$	R	$\lvert r(0)\rvert$	V
$A = 0$	0			

By separating the unobservable states, either γ or β can be set to a constant value. However, although parameters in Bouc-Wen model does not correspond to a physical identity, the resultant hysteresis has to satisfy dynamic properties of Bouc-Wen model to reproduce physical behavior in mechanical and structural systems which are studied by [3]. First property is the Bouc-Wen model's bounded input-bounded output (BIBO) stability. Physical meaning behind this property is that the mechanical and structural systems are stable in open loop, meaning without a control feedback to the system. Thus, in order to ensure the output hysteresis is bounded for any bounded input five classes of conditions are presented in Table (6.1). The table shows that the output $r(t)$ is independent of input $x(t)$ for classes based on the initial condition of the hysteresis $\lvert r(0)\rvert$ and parameters β and γ. Moreover, $r(t) = 0$ for all

$t \geq 0$ in Class V, thus it corresponds to linear behavior. Furthermore, among the classes I-IV, [3] showed that only Classes I-II are relevant to a physical description of a system, thus the rest of the classes are not relevant from a practical stand point of view. Lastly, only class I is passive which means when a suitable storage function is assumed for the Bouc-Wen model, the system does not generate energy but only dissipates. Furthermore, Class I is also the only one which satisfies the conditions of thermodynamic admissibility for Bouc-Wen model which was investigated by [79]. The following conditions are considered necessary and sufficient for Bouc-Wen model to satisfy thermodynamic admissibility:

$$A > 0 and - \beta \leq \gamma \leq \beta \tag{6.9}$$

However, in the limit case where α is assumed equal to zero (which is the case in this study), [3] states that the system may not always be BIBO stable.

In addition, [80] stated in some cases different β and γ couples results in same hysteresis response and it is considered as the reason why identification results may result in different values than the real ones. In fact the real value is never known.

Considering the above suggestions, and redundancy of the Bouc-Wen model, β and γ must satisfy Class I conditions in which $A > 1$ in order to represent a physical system in engineering applications. Thus, β and γ are chosen as the candidate parameters to set to a constant value. Observability rank is found 7 when either γ or β are assigned as known. Thus, for verification through simulations, γ is set known as $\gamma = 3$. This way, the size of the augmented state vector becomes 7, which is equal to the observability rank, and the system becomes observable with only acceleration or displacement measurement. Consecutively, the reduced augmented state vector is as follows:

$$X_a = [x, \dot{x}, r, k, c, \beta, n]^T = [x_1, x_2, x_3, x_4, x_5, x_6, x_7]^T \tag{6.10}$$

where mass and γ are assumed as known in all following structural parameter estimations.

6.2 Simulation

Mass, m and initial design stiffness, k of the reinforced concrete column that was used in E-Defense experiment are selected as structural parameters. $\zeta = 3\%$ viscous damping is assumed for the column and corresponding damping factor c is calculated based on mass and stiffness. SDOF system nonlinear response is simulated with the above given structural parameters and using fourth order Runge-Kutta integration method to solve the governing equation.

Based on Eq. (6.1) and (6.5) the state space equation is formulated as:

$$\dot{X}_a = f(X_a(t), u(t)) \tag{6.11}$$

where

$$f(\mathbf{X_a}(t), \mathbf{u}(t)) = \begin{bmatrix} x_2 \\ (-x_4 x_3 - x_5 x_2)/m + \ddot{x_g} \\ x_2 - x_6 |x_2||x_3|^{(x_7-1)} x_3 - \gamma x_2 |x_3|^{(x_7)} \\ 0 \\ 0 \\ 0 \\ 0 \end{bmatrix} \tag{6.12}$$

The input acceleration is five times the first 100% Takatori (Modified) excitation. Simulated acceleration response at the column top location has been used to obtain displacement by double-integration which then has been used as the observation in UKF-RM. The input acceleration, simulated displacement and calculated displacement from simulated acceleration response is presented in (Fig. 6-1). Here, from the displacement-time history at the bottom of the figure it can be seen that the displacement which was obtained by double integration of the acceleration lack the pseudo-static displacement due to the applied high-pass filter. The reason why this displacement is used as observation in UKF-RM is actually straight-forward. In a real-world measurement, often measuring velocity and especially displacement or

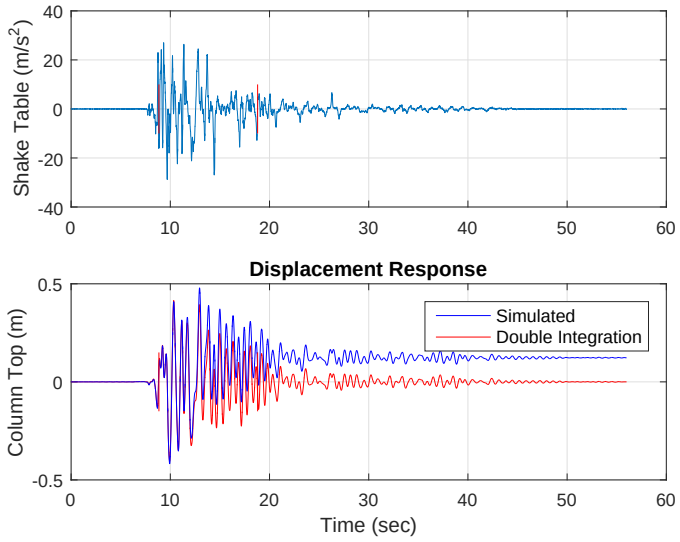

Figure 6-1: Input acceleration at the column bottom and displacement response at the column top

force is not possible during a seismic event. Even acceleration measurements are rare as only a few important bridges have built-in sensor arrays. In addition, the quality of the sensors are also an issue as parameter estimation methods are usually prone to high measurement noise, especially when the dimension of the state vector is large or high nonlinearity exists in the dynamic system. Thus, using only acceleration measurement and obtaining the needed information, in this case displacement time history, is a realistic target in the way of search for a parameter estimation algorithm that can be applied in practice.

Thus, the observation equation becomes:

$$y = \begin{bmatrix} x_1 \end{bmatrix} \tag{6.13}$$

Initial state vector is shown below which consists a realistic model error assumption.

$$X_0 = [0, 0, 0, 0.5k, 0.5c, 0.6\beta, 0.9n]^T \tag{6.14}$$

Initial error covariance is set to:

$$P_0 = diag[0.01, 0.01, 0.1, (k_{true} - x_0(3))^2, (c_{true} - x_0(4))^2, (\beta_{true} - x_0(5))^2, (n - x_0(6))^2] \tag{6.15}$$

Initially it is assumed no measurement noise. However, R, measurement noise covariance is set to $R = (0.05 measurementrms)^2$. Thus, UKF-RM starts with a wrong R value.

α_Q and α_R values are both set to $1/7$.

Using the SDOF system explained above and initial values, parameter estimation with UKF-RM has been performed using the below initial Q matrix.

$$Q_0 = diag[1e-4, 1e-2, 1e-4, 1e-4, 1e-1, 1e-9, 1e-8] \tag{6.16}$$

(Figures 6-2,6-3) show the state and structural parameter estimation results, respectively. Both displacement and velocity and structural parameters; stiffness and damping, are estimated with UKF-RM successfully.

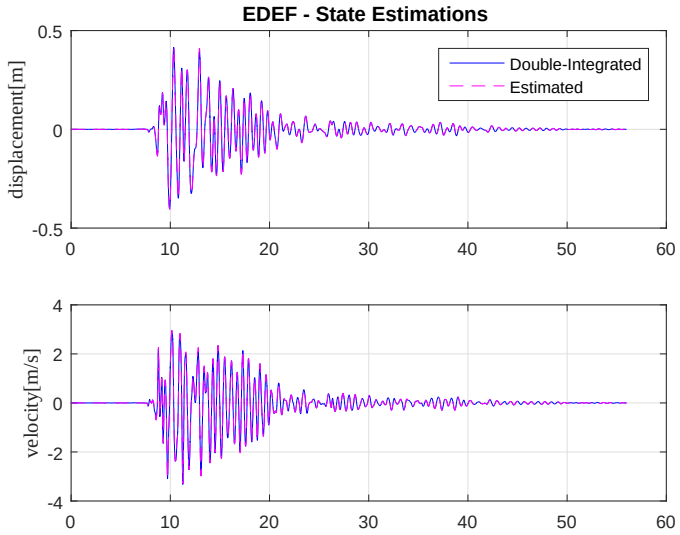

Figure 6-2: State estimation results from UKF-RM with $\alpha_Q = 1/7$ and $\alpha_R = 1/7$

Bouc-Wen parameters which form the hysteresis response are also successfully estimated inside the significant duration with UKF-RM (Fig. 6-4). Bouc-Wen parameter

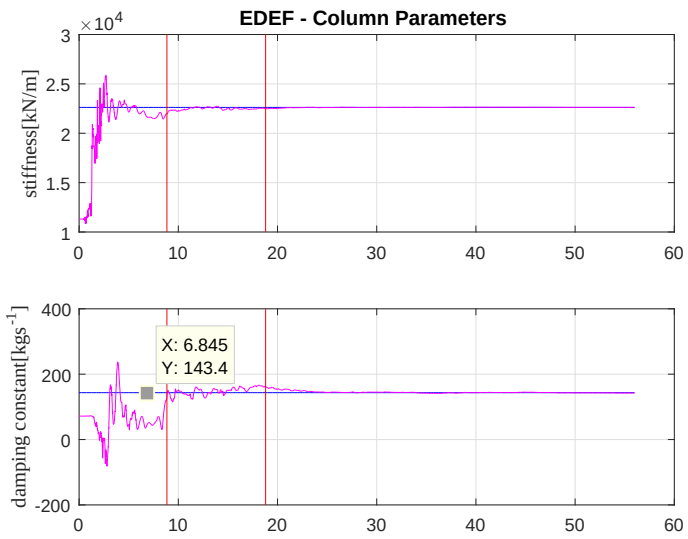

Figure 6-3: Structural parameter estimation results from UKF-RM with $\alpha_Q = 1/7$ and $\alpha_R = 1/7$

Table 6.2: Structural and Bouc-Wen parameter estimation summary with UKF-RM - Simulation

Param.	TRUE	Estimation	error(%)
stiffness (k)	22618	22524	0.4
damping (c)	143.4	151.6	5
beta (β)	3	2.88	-4
(n)	2	2.08	4

estimation convergence seems to be slower when compared to structural parameter estimation. However both achieve convergence inside the significant duration. This may be attributed to the fact that estimation of Bouc-wen parameters need full non-linear response cycles to be identified where the structural parameters do not. Table (6.2) summarizes the error percentage of the estimated mean parameter values between 2 sec after the start and end of the significant duration. All parameters are estimated with an error less than 10% .

Fig. (6-5) shows the comparison between the resultant hysteresis response, force-displacement relationship, between the simulation and UKF-RM estimation. The part until the pseudo-static displacement occurs at about 13 seconds (Fig. 6-1) matches

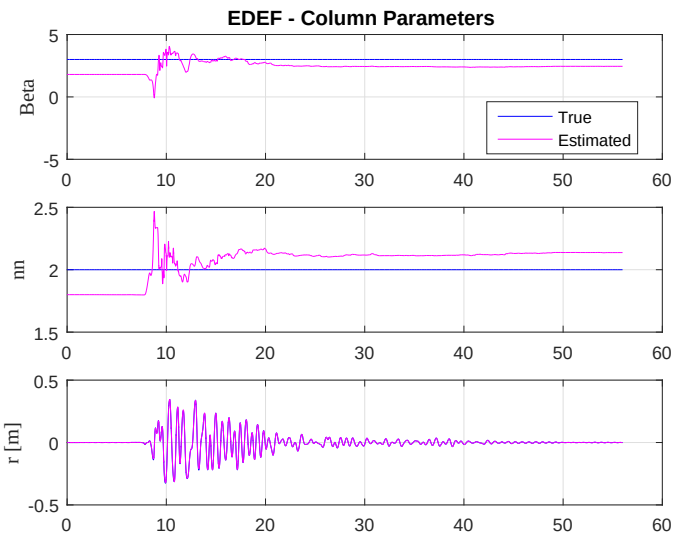

Figure 6-4: Bouc-Wen parameter estimation results from UKF-RM with $\alpha_Q = 1/7$ and $\alpha_R = 1/7$

well with the simulated hysteresis response (Fig. 6-6).

As mentioned before, the displacement obtained from acceleration by double-integration has been used as the observation (Fig. 6-1) and thus pseudo-static displacement is missing information due to the applied high-pass filter. However, the hysteresis response obtained with UKF-RM using double-integrated acceleration as observation contains the cycles after significant duration (Fig. 6-7). The response lacks only the permanent displacement component which corresponds to about 4% of the total energy dissipation. Thus, the difference between the estimated and simulated energy dissipation is considered small.

Simulation with measurement noise

The simulation is repeated in the case of measurement noise which is equal to 5% of the RMS of the observation. RMS of the displacement observation is equal to $0.0764m$. Using same X_0, P_0 and Q_0 in the above simulation, measurement noise is added to the observation. However, initial measurement noise covariance R_0 is set to 0.

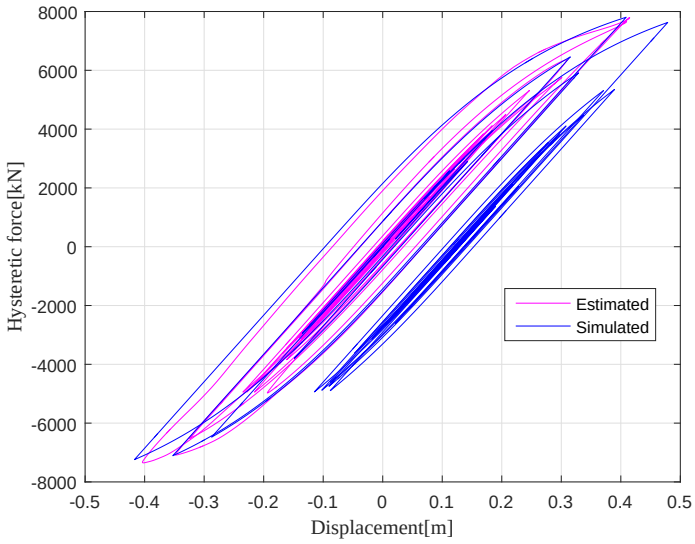

Figure 6-5: Hysteresis loops estimation from UKF-RM with $\alpha_Q = 1/7$ and $\alpha_R = 1/7$

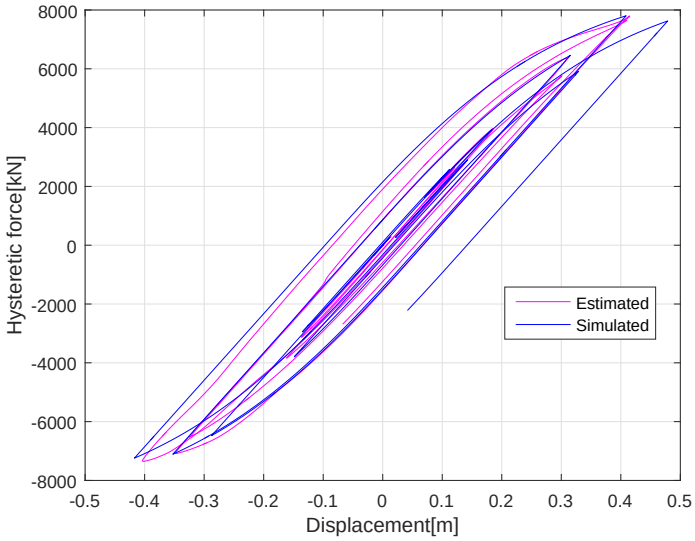

Figure 6-6: Hysteresis loops estimation before residual displacement from UKF-RM with $\alpha_Q = 1/7$ and $\alpha_R = 1/7$

Figures (6-8) and (6-9) show the structural and Bouc-Wen parameter estimation results, respectively. Structural parameters were successfully estimated. On the other hand, while Bouc-Wen parameters could not be estimated, the hysteresis displacement was successfully obtained with UKF-RM. Here, there are two marks

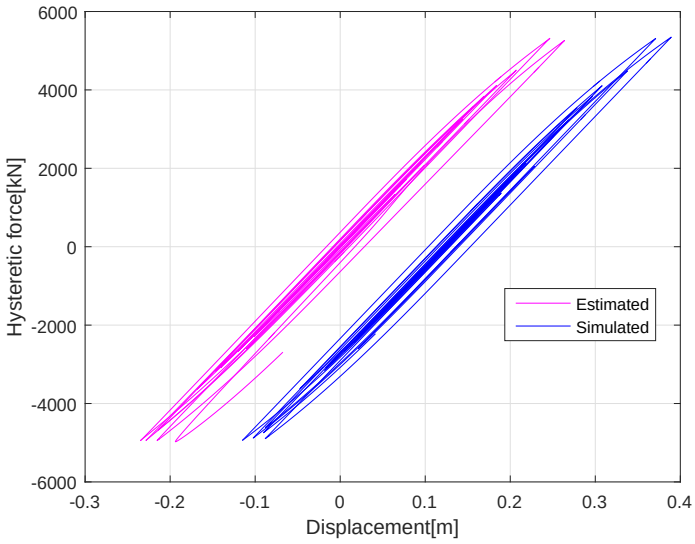

Figure 6-7: Hysteresis loops estimation after residual displacement from UKF-RM with $\alpha_Q = 1/7$ and $\alpha_R = 1/7$

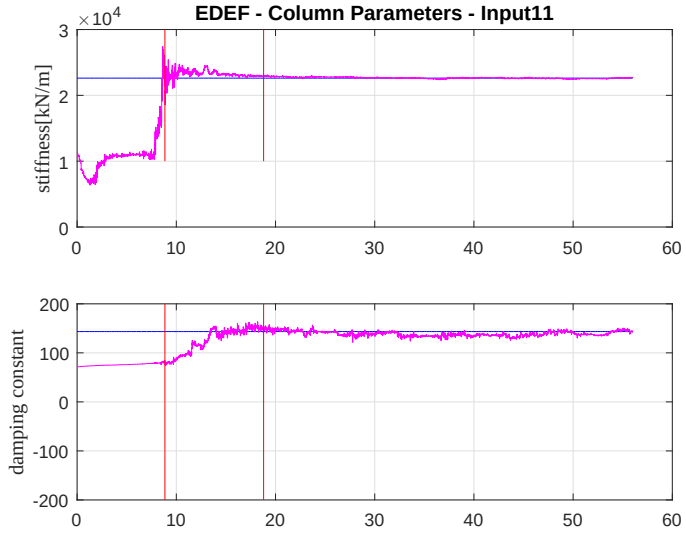

Figure 6-8: Parameter estimation results from UKF-RM with $\alpha_Q = 1/7$ and $\alpha_R = 1/7$

which need to be addressed. First, even though there is high measurement noise in the observation and the initial measurement noise covariance is set to zero, the algorithm was able to estimate structural parameters, namely stiffness and damping. Secondly, although Bouc-Wen parameters were not the real values assigned initially,

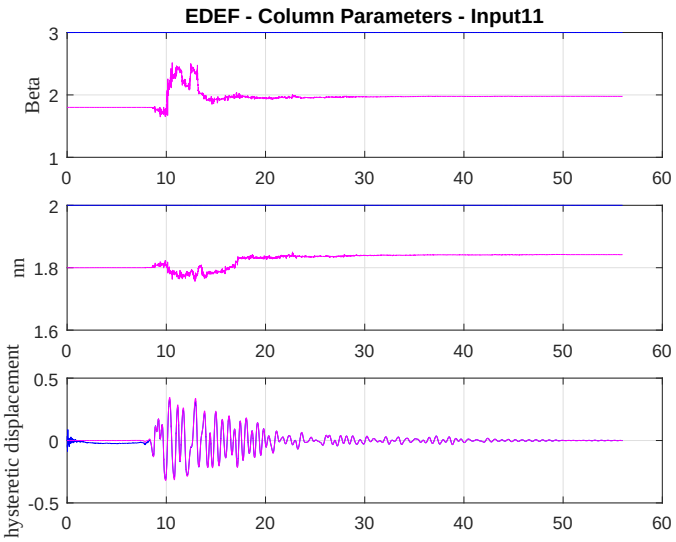

Figure 6-9: Hysteresis parameter estimation results from UKF-RM with $\alpha_Q = 1/7$ and $\alpha_R = 1/7$

the hysteresis displacement estimation was successful which may be attributed to the redundant constitution of the Bouc-Wen model as summarized in the earlier sections of this chapter.

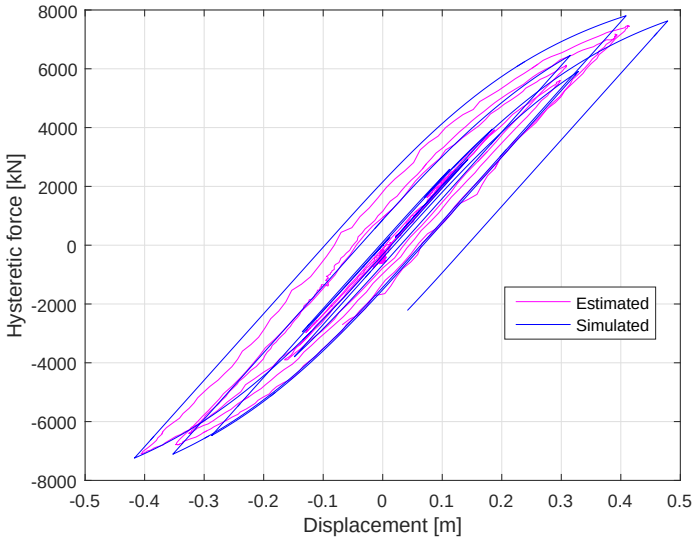

Figure 6-10: Hysteresis response estimation before residual displacement with $\alpha_Q = 1/7$ and $\alpha_R = 1/7$ and 5% measurement noise

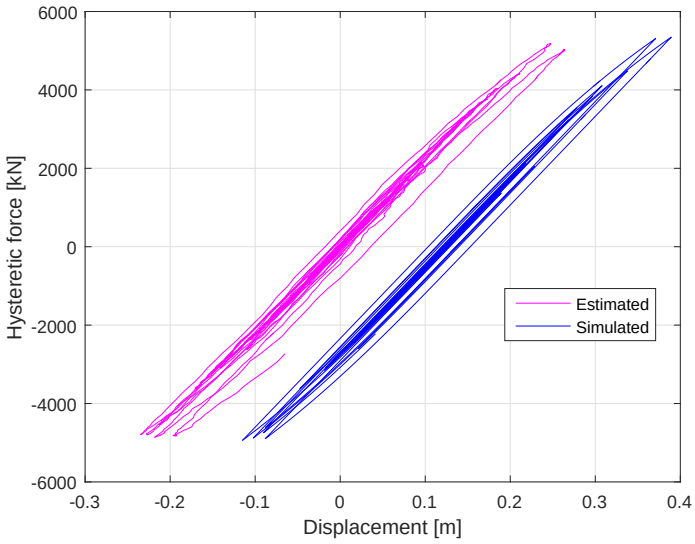

Figure 6-11: Hysteresis response estimation after residual displacement with $\alpha_Q = 1/7$ and $\alpha_R = 1/7$ and 5% measurement noise

Furthermore, Fig. (6-10) shows the comparison between the resultant hysteresis response, force-displacement relationship, between the simulation and UKF-RM estimation before residual displacement occurs and estimation results matches well with the simulated hysteresis response. Fig. (6-11) shows the comparison between the resultant hysteresis response after residual displacement occurs which matches well with the measured force-displacement relationship.

6.3 Simulation Results for Sensitivity Investigation with Nonlinear Model

In this section, sensitivity of UKF-RM to change in initial filter parameters are repeated for nonlinear model in a similar way to Chapter 4. The nonlinear model and initial filter parameters considered in this section is same as in Section 6.2 with no added measurement noise in observation.

Upper and lower bounds for initial Q_0, R_0 and P_0, initial state vector, X_0, and RM parameters α_Q and α_R are summarized. Judging criteria for the performance

is that the filter must be able to achieve a successful estimate of states from the beginning of the data, stiffness and damping from the beginning of the significant duration and hysteretic force inside the significant duration. In this section, representative results will be given only for the cases related to Bouc-Wen parameters, because a detailed explanation on the sensitivity of the states to change in initial filter parameters considering linear model was presented in Chapter 4.

6.3.1 Sensitivity to change in elements of Q_0

Table (6.3) summarizes the results of UKF-RM sensitivity to change in elements of Q_0, initial process noise matrix, considering the nonlinear model. UKF-RM can achieve successful estimation of states and parameters in a wide range of Q_0 values within practical limits.

Table 6.3: Upper and lower bound suggestions based on the sensitivity analysis for initial Q matrix

	$Q(x)$	$Q(\dot{x})$	$Q(r)$	$Q(k)$	$Q(c)$	$Q(\beta)$	$Q(n)$
Lower B.	10^{-20}	10^{-20}	10^{-20}	10^{-20}	10^{-20}	10^{-20}	10^{-20}
Upper B.	10^{9}	10^{4}	10^{1}	10^{7}	10^{9}	10^{5}	10^{-1}

Figures (6-12) and (6-13) present displacement, velocity, stiffness and damping estimations when Q_0 element corresponding to hysteretic displacement r, $Q(r)$, is set to 10^1. Displacement and velocity estimations match well with simulated response from the beginning of the data while stiffness and damping estimations converged to true values from the beginning of the significant duration.

Figure (6-14) presents Bouc-Wen parameter estimations. β and n parameter estimations fluctuates around the true value during significant duration. However, resultant hysteretic displacement, r, estimation matches well with the simulation result.

Resultant hysteretic force and displacement relationship is depicted in Figure (6-15). The part until the pseudo-static displacement, which occurs at about 13 seconds, (Fig. 6-1) matches well with the simulated hysteresis response (Fig. 6-16). As mentioned before, the displacement obtained from acceleration by double-integration has

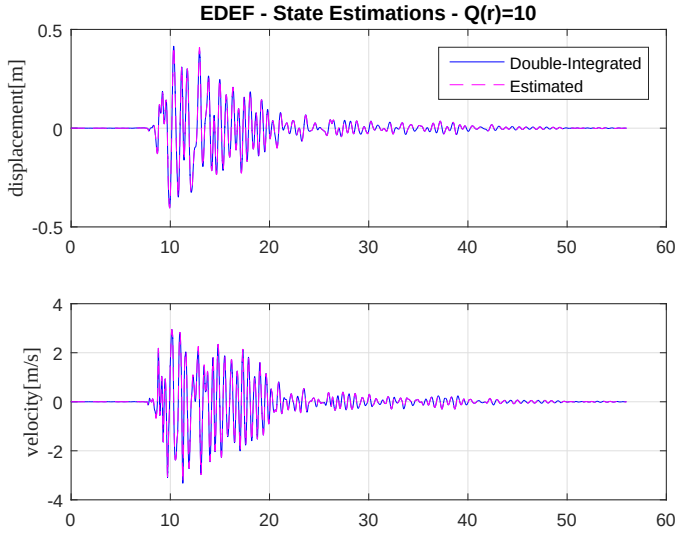

Figure 6-12: Estimated states with $\alpha_Q = 1/7$ and $\alpha_R = 1/7$ and $Q(r) = 10^1$

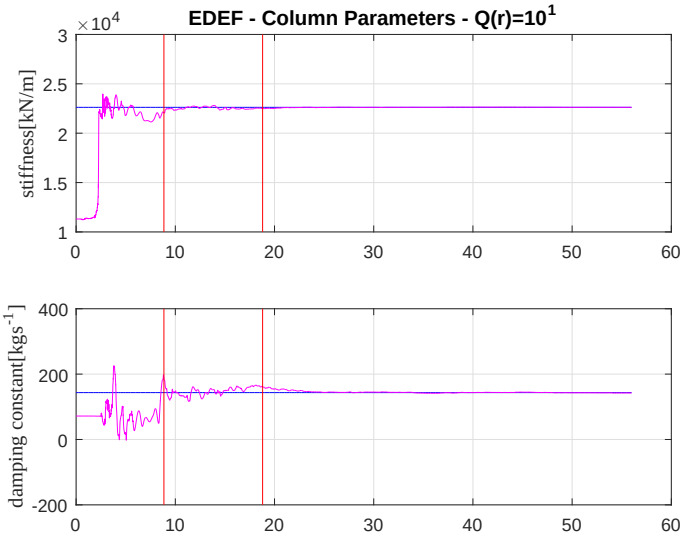

Figure 6-13: Estimated structural parameters with $\alpha_Q = 1/7$ and $\alpha_R = 1/7$ and $Q(r) = 10^1$

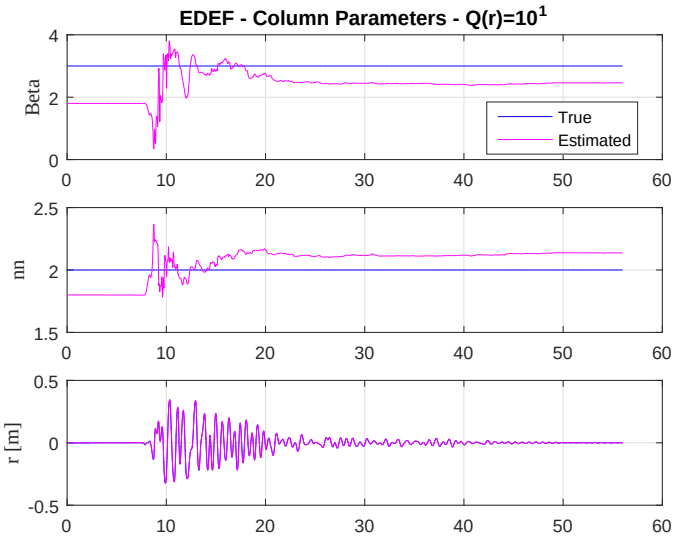

Figure 6-14: Estimated Bouc-Wen parameters with $\alpha_Q = 1/7$ and $\alpha_R = 1/7$ and $Q(r) = 10^1$

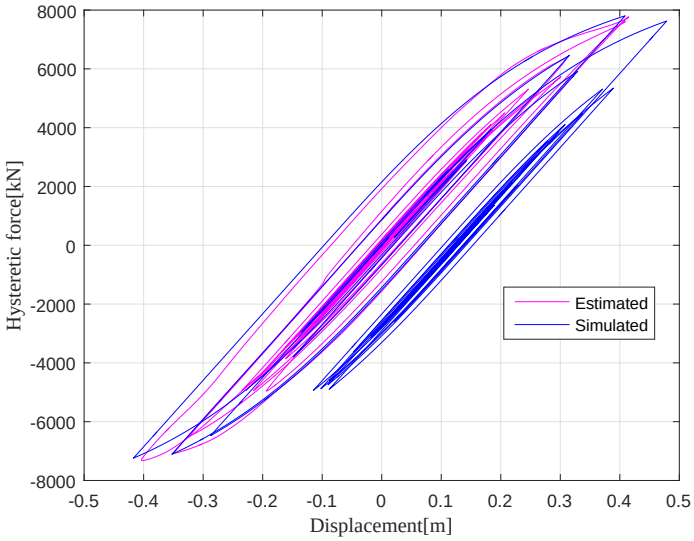

Figure 6-15: Estimated force-displacement relationship with $\alpha_Q = 1/7$ and $\alpha_R = 1/7$ and $Q(r) = 10^1$

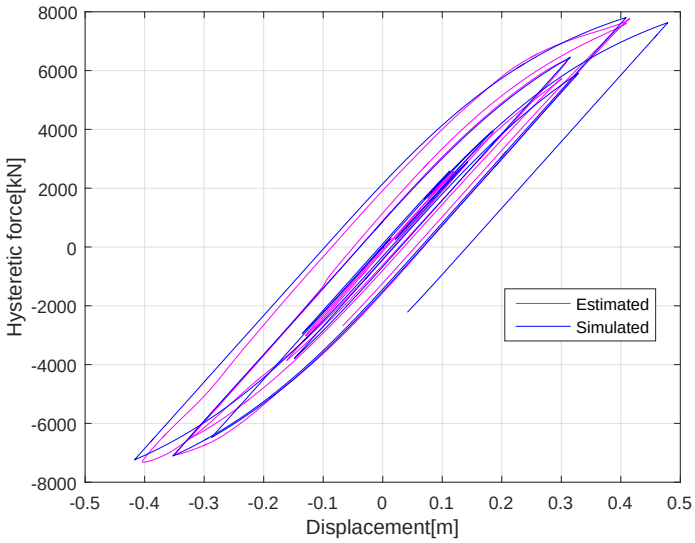

Figure 6-16: Estimated hsyteresis before residual displacement with $\alpha_Q = 1/7$ and $\alpha_R = 1/7$ and $Q(r) = 10^1$

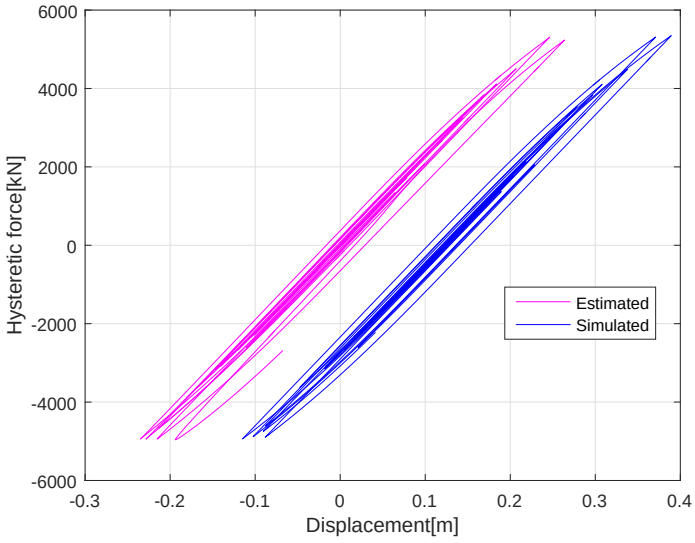

Figure 6-17: Estimated hsyteresis after residual displacement with $\alpha_Q = 1/7$ and $\alpha_R = 1/7$ and $Q(r) = 10^1$

been used as the observation and thus, pseudo-static displacement is missing information due to application of high-pass filter. However, the hysteresis response obtained with UKF-RM using double-integrated acceleration as observation also contains the cycles after significant duration (Fig. 6-17). The response lacks only the permanent displacement component which corresponds to about 4% of the total energy dissipation. Thus, the difference between the estimated and simulated energy dissipation is considered small.

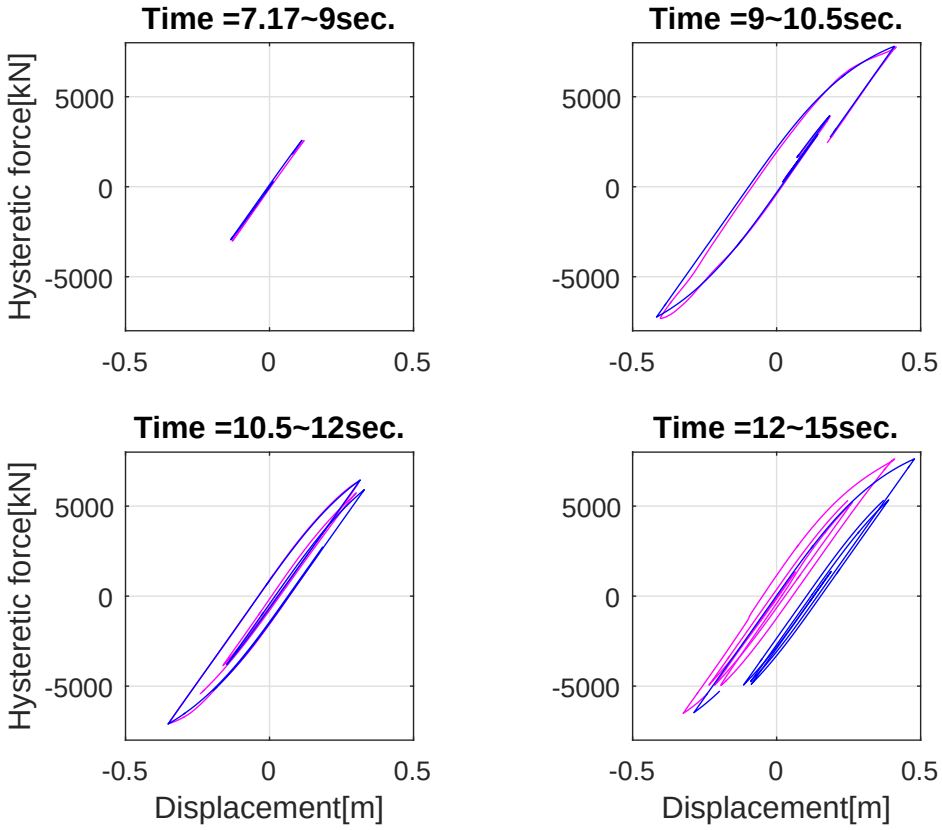

Figure 6-18: Estimated hsyteresis in various time duration with $\alpha_Q = 1/7$ and $\alpha_R = 1/7$ and $Q(r) = 10^1$

Figure (6-18) depicts hysteresis force estimations during various time duration which show good agreement with the simulated force-displacement relationships. Furthermore, to compare the energy dissipation of the system during largest response times, the area inside the selected force-displacement loops are calculated and compared with simulations (Fig. 6-19). The difference between the estimated and simu-

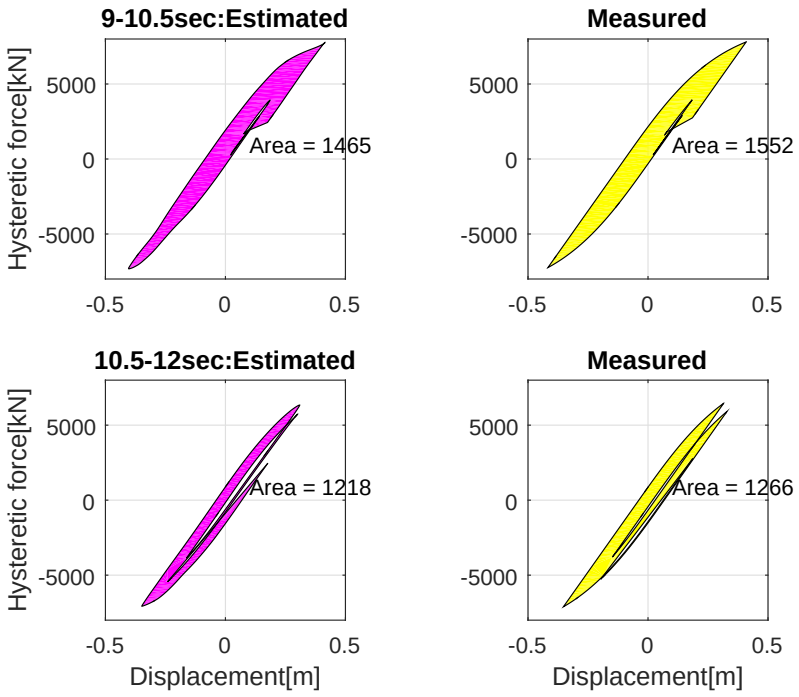

Figure 6-19: Dissipated energy with $\alpha_Q = 1/7$ and $\alpha_R = 1/7$ and $Q(r) = 10^1$

lated energy dissipation between 9-12 sec is about 4.8%.

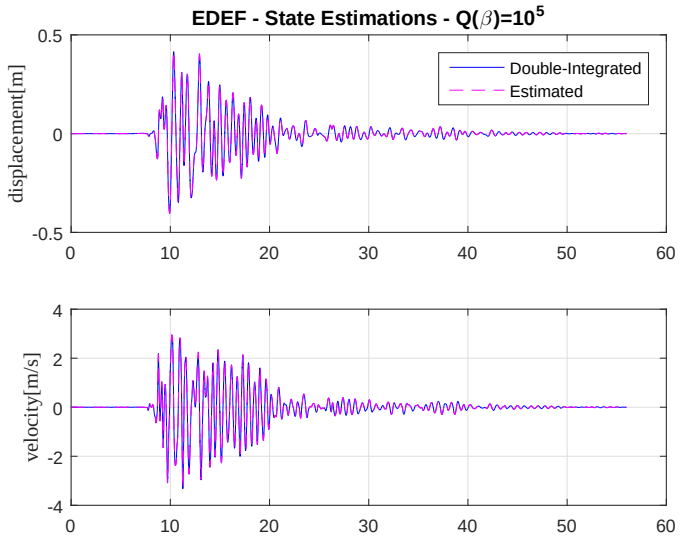

Figure 6-20: Estimated states with $\alpha_Q = 1/7$ and $\alpha_R = 1/7$ and $Q(\beta) = 10^5$

Figures (6-20 to 6-27) show estimation results when Q_0 element corresponding to

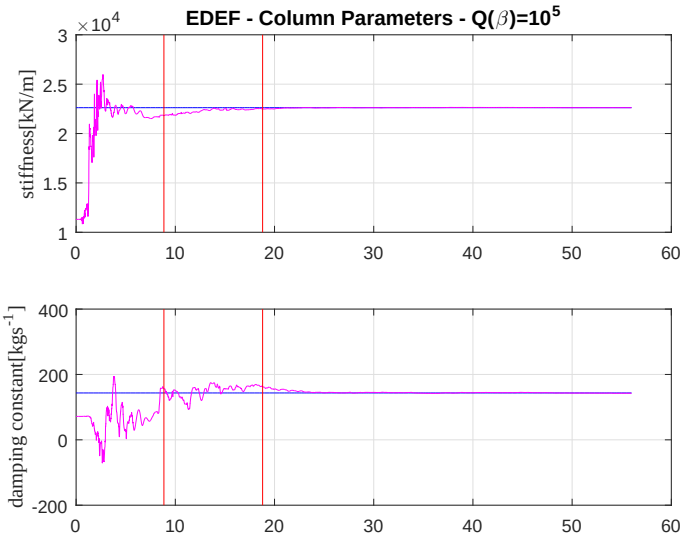

Figure 6-21: Estimated structural parameters with $\alpha_Q = 1/7$ and $\alpha_R = 1/7$ and $Q(\beta) = 10^5$

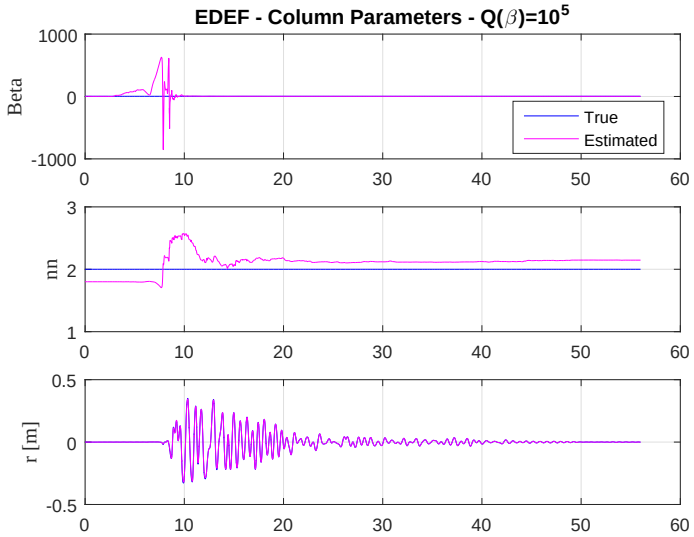

Figure 6-22: Estimated Bouc-Wen parameters with $\alpha_Q = 1/7$ and $\alpha_R = 1/7$ and $Q(\beta) = 10^5$

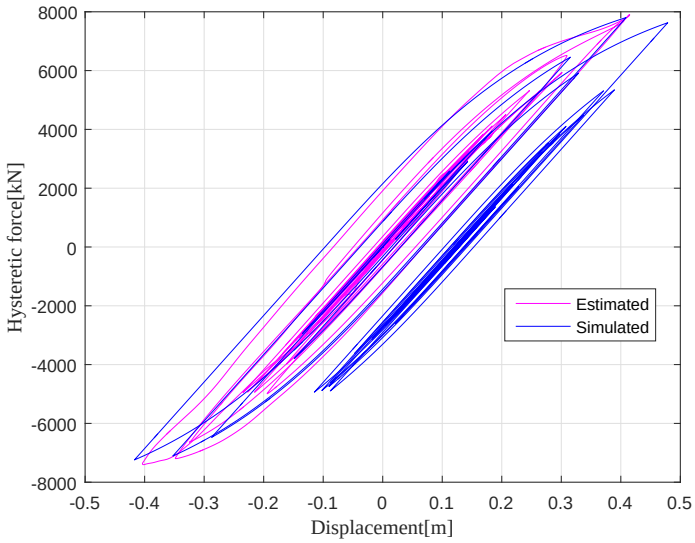

Figure 6-23: Estimated force-displacement relationship with $\alpha_Q = 1/7$ and $\alpha_R = 1/7$ and $Q(\beta) = 10^5$

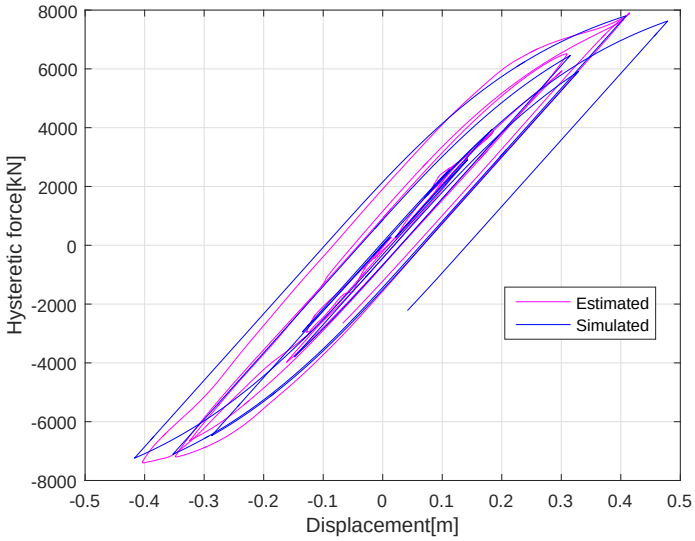

Figure 6-24: Estimated hsyteresis before residual displacement with $\alpha_Q = 1/7$ and $\alpha_R = 1/7$ and $Q(\beta) = 10^5$

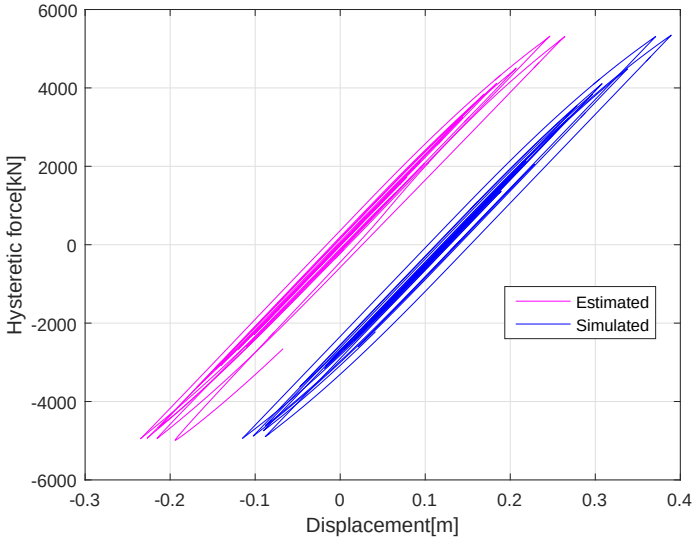

Figure 6-25: Estimated hsyteresis after residual displacement with $\alpha_Q = 1/7$ and $\alpha_R = 1/7$ and $Q(\beta) = 10^5$

Bouc-Wen parameter β, $Q(\beta)$, is set to 10^5. Figures (6-28 to 6-35) shows estimation results when Q_0 element corresponding to Bouc-Wen parameter n, $Q(n)$, is set to 10^{-1}. Similar conclusions which are presented above can be drawn for these two cases, too.

6.3.2 Sensitivity to change in elements of R_0 and measurement noise

In this section, four cases are considered to investigate the sensitivity of estimation algorithm to change in initial R-value,R_0 when various levels of measurement noise present in the observation. R, measurement noise covariance matrix is a scalar since there is only one observation, namely; displacement. Considered cases are summarized in Table (6.4) as follows:

Representative results from Case 4b are presented below. Figure (6-36) and (6-37) depicts structural and Bouc-Wen parameters, respectively. While stiffness and damping estimations are achieved successfully, Bouc-Wen parameter β seems to be sensitive to high measurement noise. Although β cannot converge to its true value,

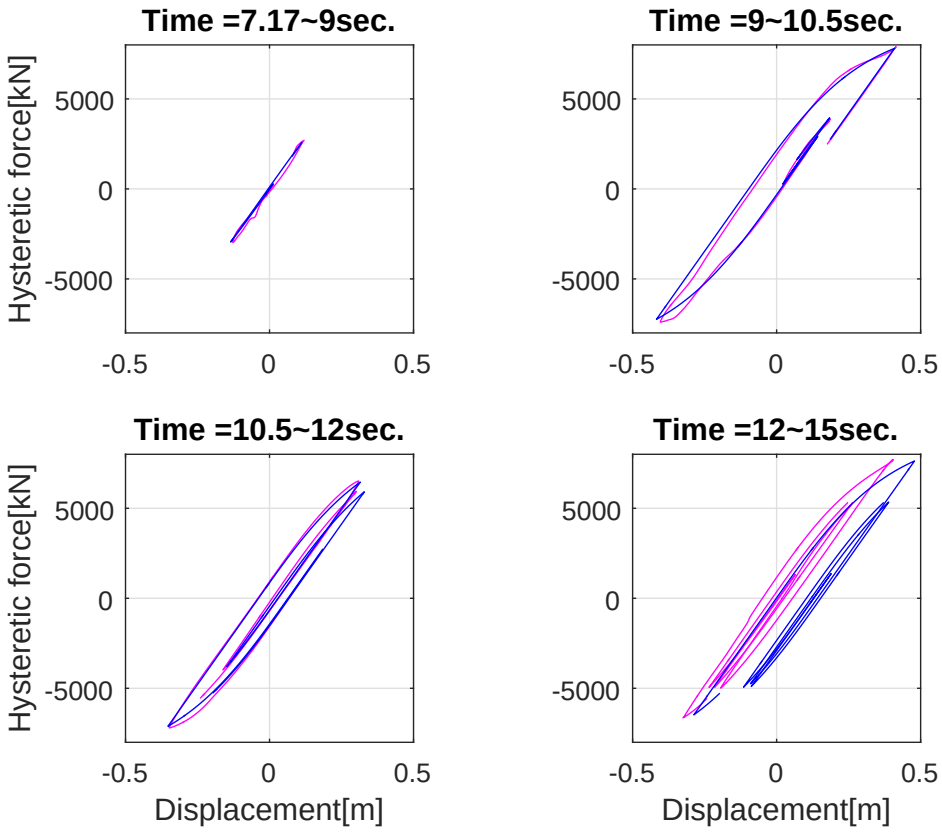

Figure 6-26: Estimated hsyteresis in various time duration with $\alpha_Q = 1/7$ and $\alpha_R = 1/7$ and $Q(\beta) = 10^5$

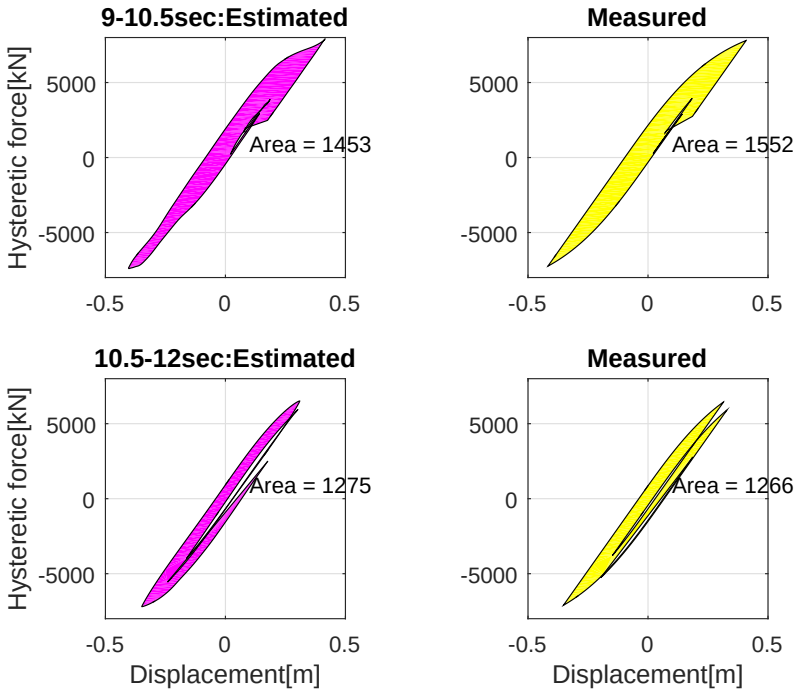

Figure 6-27: Dissipated energy with $\alpha_Q = 1/7$ and $\alpha_R = 1/7$ and $Q(\beta) = 10^5$

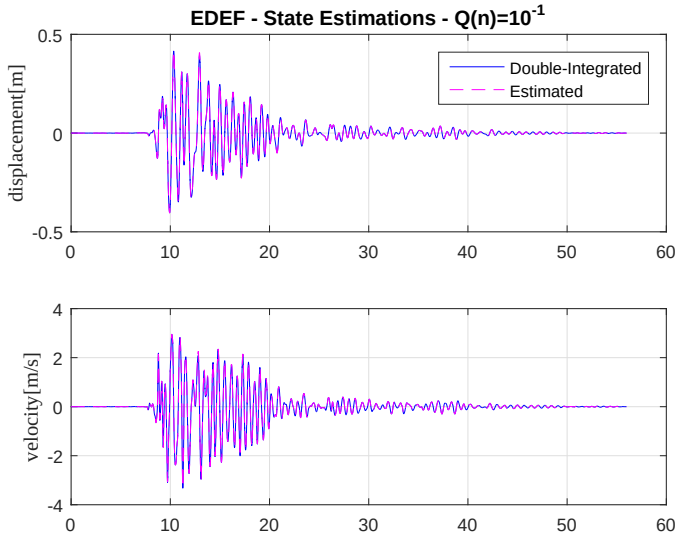

Figure 6-28: Estimated states with $\alpha_Q = 1/7$ and $\alpha_R = 1/7$ and $Q(n) = 10^{-1}$

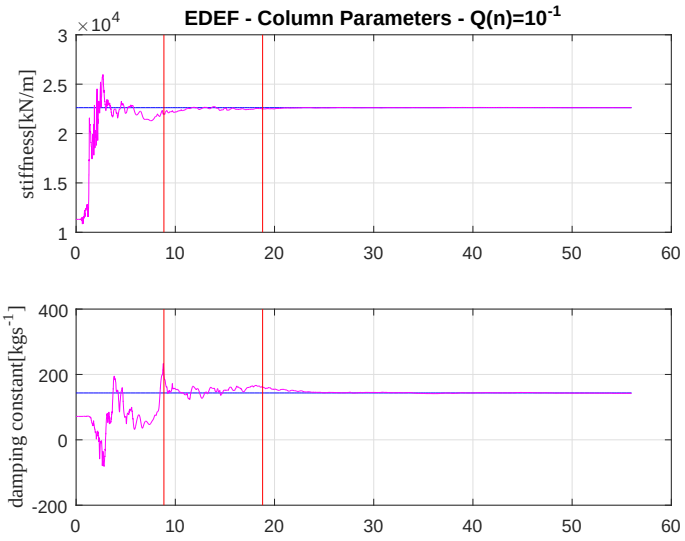

Figure 6-29: Estimated structural parameters with $\alpha_Q = 1/7$ and $\alpha_R = 1/7$ and $Q(n) = 10^{-1}$

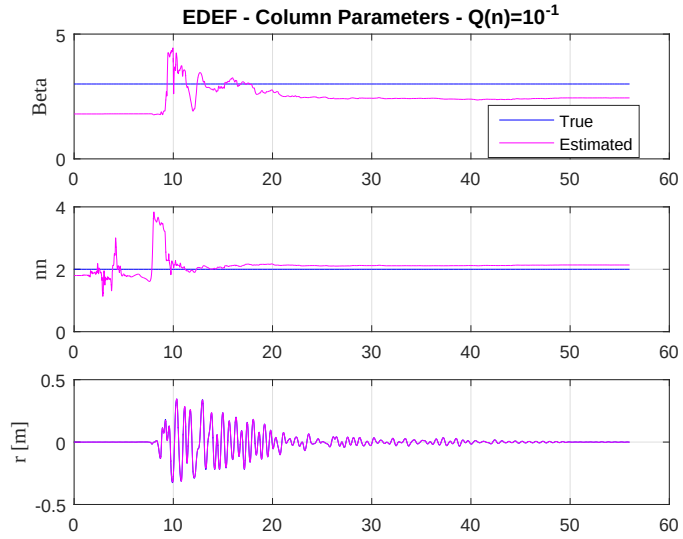

Figure 6-30: Estimated Bouc-Wen parameters with $\alpha_Q = 1/7$ and $\alpha_R = 1/7$ and $Q(n) = 10^{-1}$

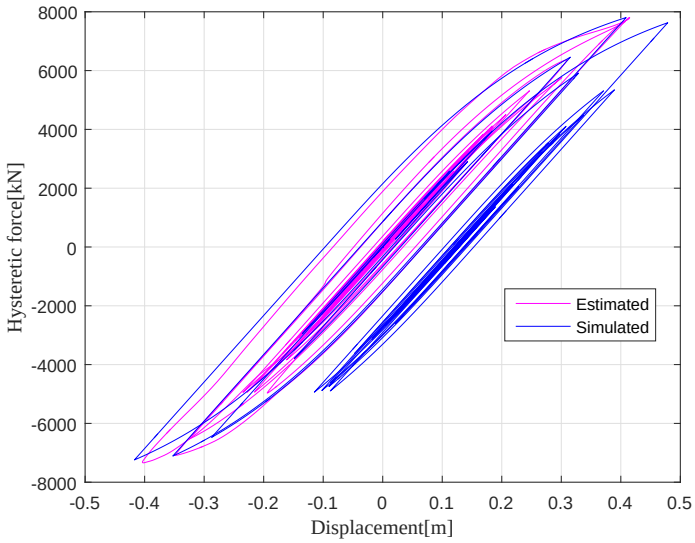

Figure 6-31: Estimated force-displacement relationship with $\alpha_Q = 1/7$ and $\alpha_R = 1/7$ and $Q(n) = 10^{-1}$

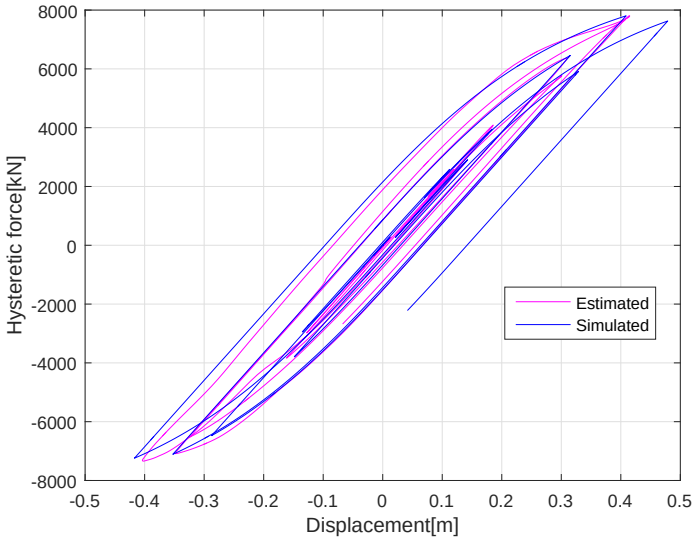

Figure 6-32: Estimated hsyteresis before residual displacement with $\alpha_Q = 1/7$ and $\alpha_R = 1/7$ and $Q(n) = 10^{-1}$

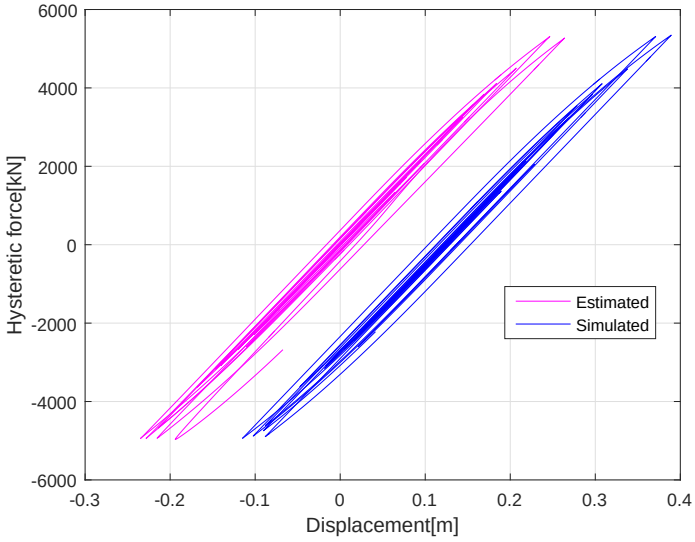

Figure 6-33: Estimated hsyteresis after residual displacement with $\alpha_Q = 1/7$ and $\alpha_R = 1/7$ and $Q(n) = 10^{-1}$

Table 6.4: Cases considered for sensitivity analysis for initial Q matrix

Case	Measurement Noise	R_0	Result
1	0	20%	UKF-RM:OK
2	1%	20%	UKF-RM:OK
3a	5%	1%	UKF-RM:OK
3b	5%	10%	UKF-RM:OK
4a	10%	1%	UKF-RM:OK
4b	10%	20%	UKF-RM:OK

n and r shows satisfactory agreement when compared to simulation results.

Resultant hysteretic force and displacement relationship is depicted in Figure (6-38). Due to high measurement noise, 10% addition to the observation, the estimations become noisy, too. However, when hysteresis force estimations during various time duration (Fig. 6-18) examined, good agreement with the simulated force-displacement relationships can be observed.

Furthermore, to compare the energy dissipation of the system during largest response times, the area inside the selected force-displacement loops are calculated and compared with simulations (Fig. 6-19). The difference between the estimated and simulated energy dissipation between 9-12 sec is considered small.

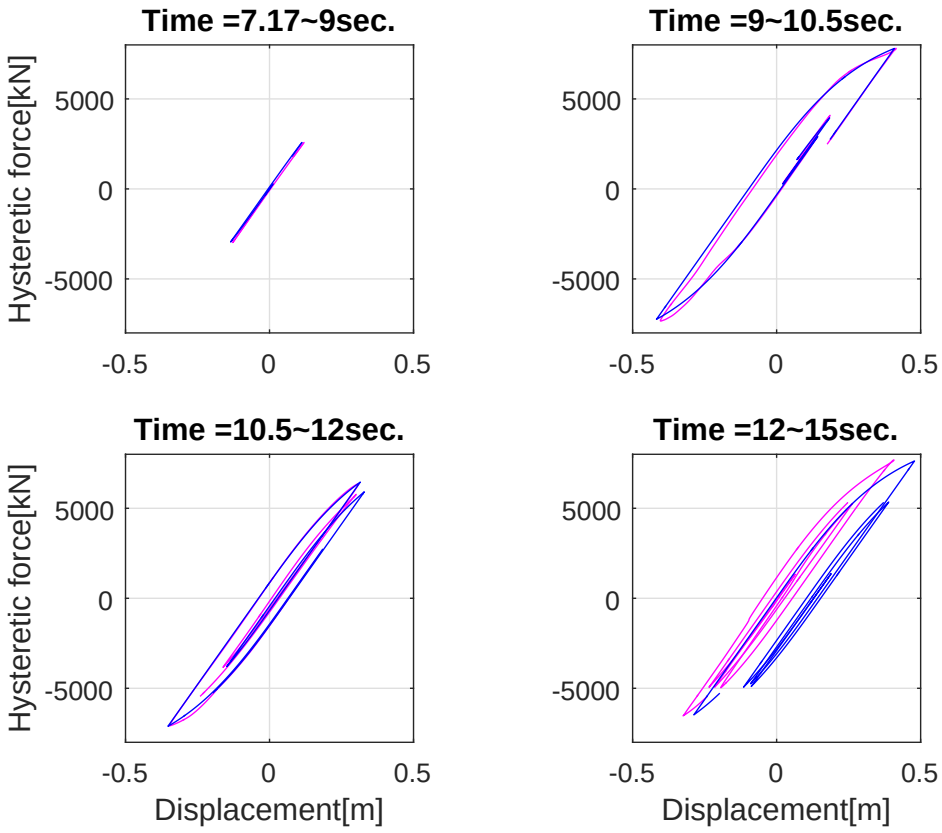

Figure 6-34: Estimated hsyteresis in various time duration with $\alpha_Q = 1/7$ and $\alpha_R = 1/7$ and $Q(n) = 10^{-1}$

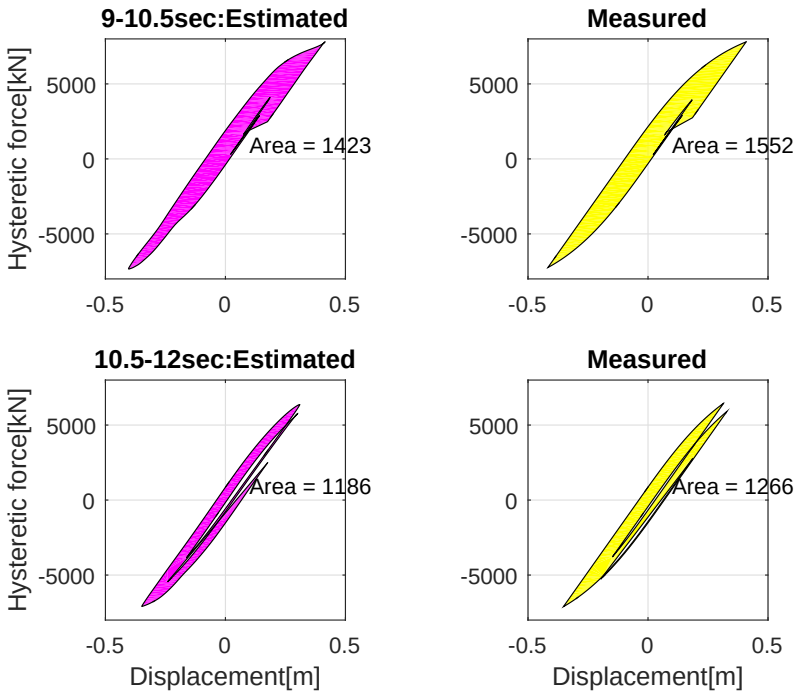

Figure 6-35: Dissipated energy with $\alpha_Q = 1/7$ and $\alpha_R = 1/7$ and $Q(n) = 10^{-1}$

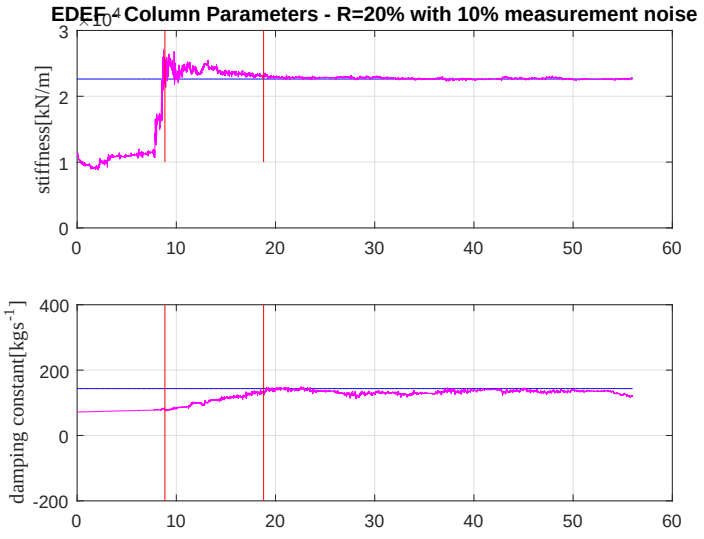

Figure 6-36: Estimated structural parameters with $\alpha_Q = 1/7$ and $\alpha_R = 1/7$ and $R_0 = 20\%$ with 10% measurement noise

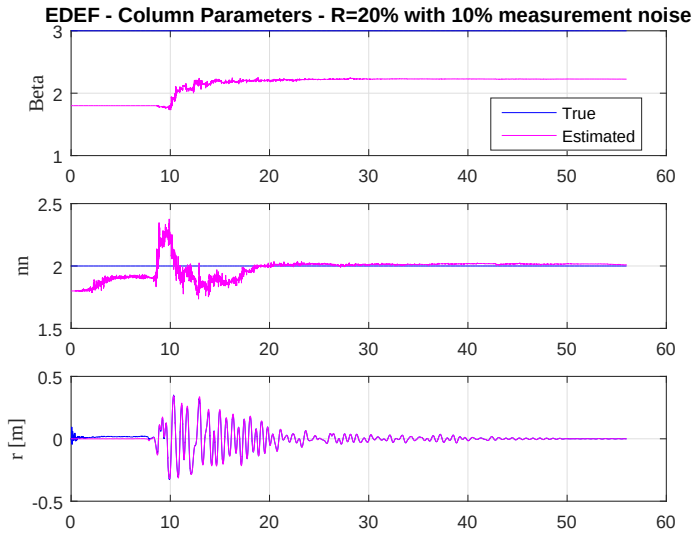

Figure 6-37: Estimated Bouc-Wen parameters with $\alpha_Q = 1/7$ and $\alpha_R = 1/7$ and $R_0 = 20\%$ with 10% measurement noise

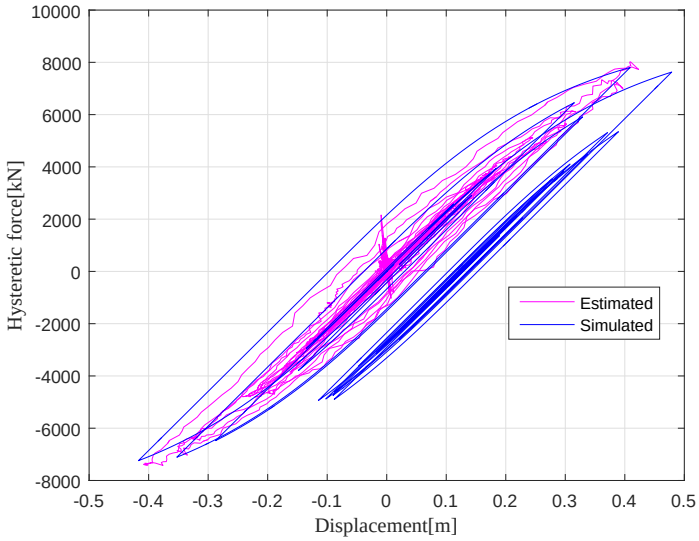

Figure 6-38: Estimated force-displacement relationship with $\alpha_Q = 1/7$ and $\alpha_R = 1/7$ and $R_0 = 20\%$ with 10% measurement noise

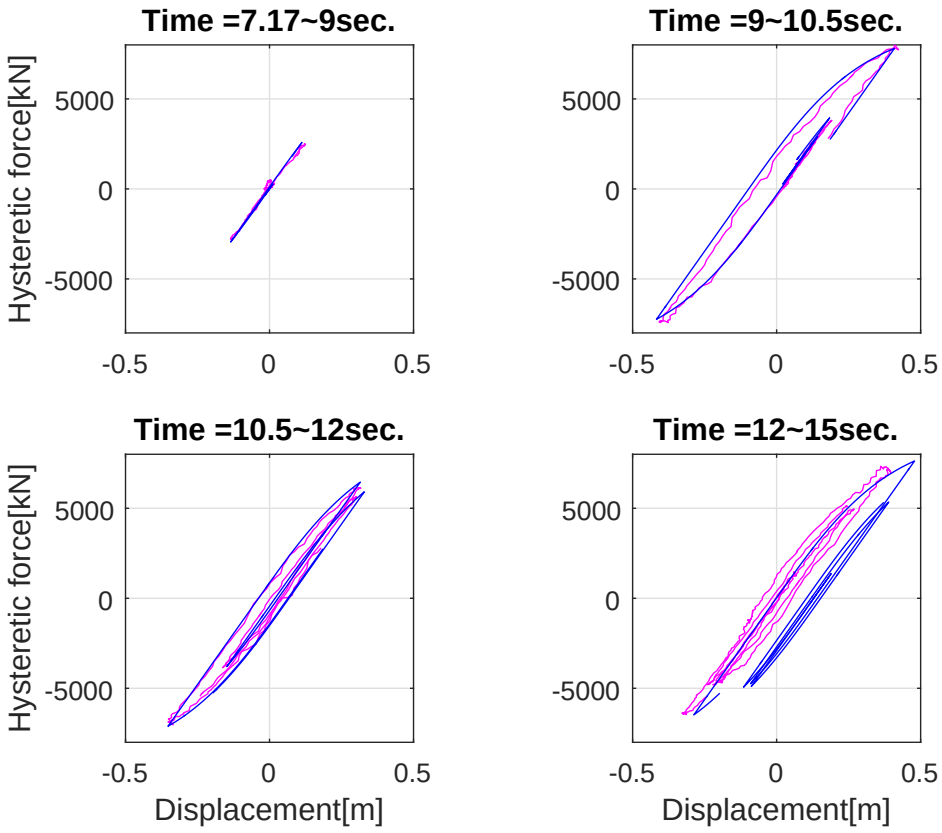

Figure 6-39: Estimated hsyteresis in various time duration with $\alpha_Q = 1/7$ and $\alpha_R = 1/7$ and $R_0 = 20\%$ with 10% measurement noise

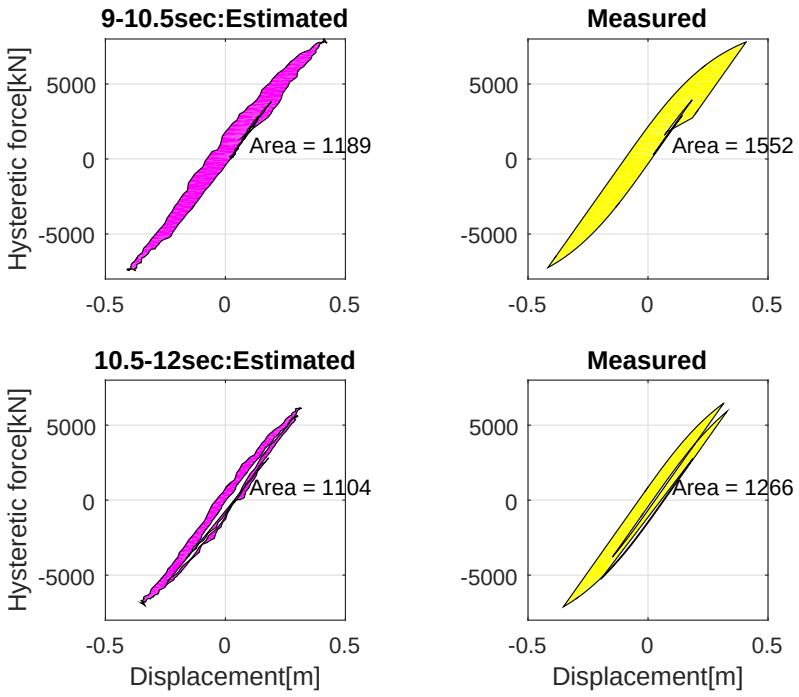

Figure 6-40: Dissipated energy with $\alpha_Q = 1/7$ and $\alpha_R = 1/7$ and $R_0 = 20\%$ with 10% measurement noise

6.3.3 Sensitivity to change in elements of P_0

Considered cases are summarized in Table (6.5). In the table, P_{00} is equal to Eq. 6.15.

Table 6.5: Cases considered for sensitivity analysis for initial P matrix, P_0

Case	P_0	Stiffness	Damping	Hysteresis
1	$10^{-2} * P_{00}$	UKF-RM:OK	OK	OK
2	$1 * P_{00}$	UKF-RM:OK	OK	OK

Representative results from Case 1 are given below.

Representative results from Case 1 are presented below. Figure (6-41) depicts stiffness and damping estimation results which were obtained successfully. However, although Bouc-Wen parameter β estimation was not successful (Fig. 6-42) the n and r shows good agreement with the simulation results.

When hysteresis force estimations during various time duration (Fig. 6-18) ex-

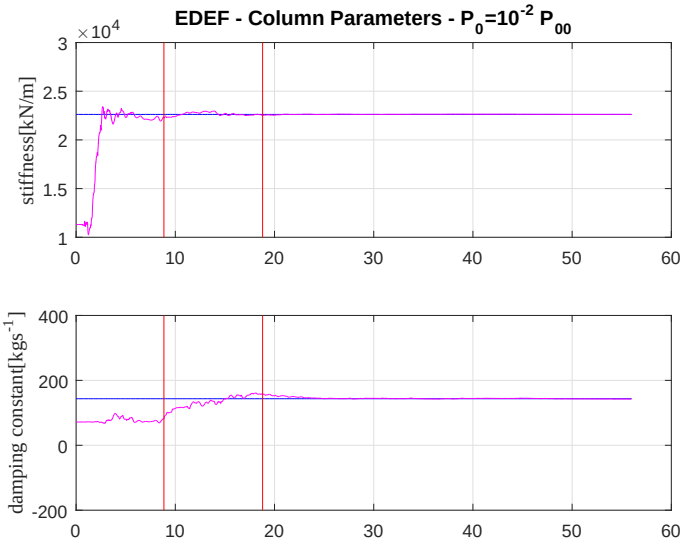

Figure 6-41: Estimated structural parameters with $\alpha_Q = 1/7$ and $\alpha_R = 1/7$ and $P_0 = 10^{-2} * P_{00}$

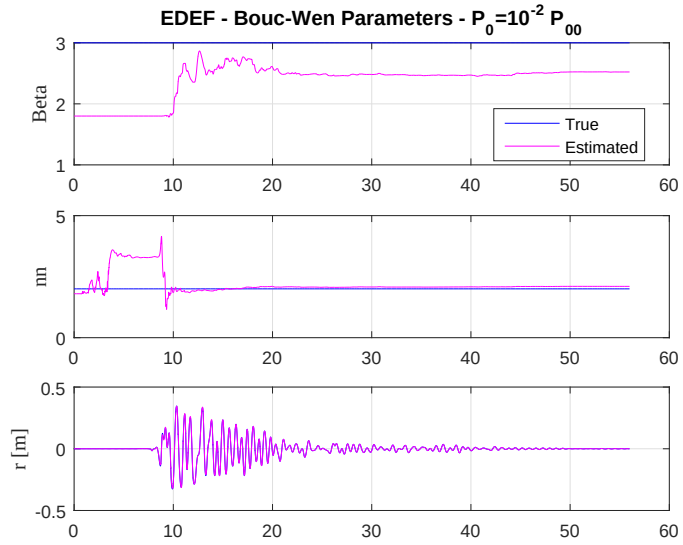

Figure 6-42: Estimated Bouc-Wen parameters with $\alpha_Q = 1/7$ and $\alpha_R = 1/7$ and $P_0 = 10^{-2} * P_{00}$

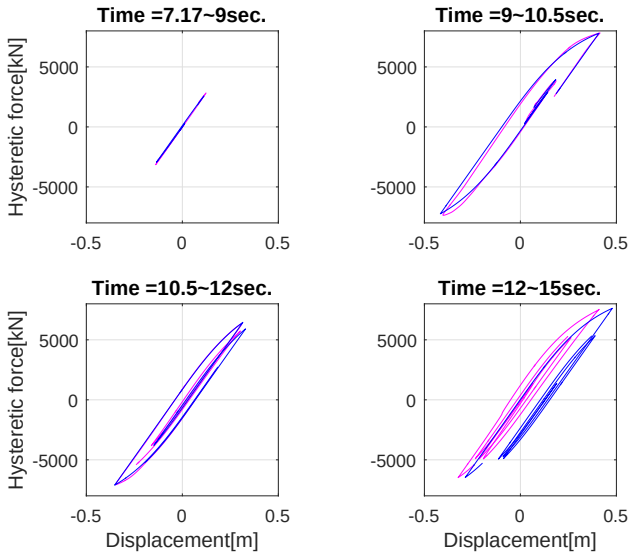

Figure 6-43: Estimated force-displacement relationship with $\alpha_Q = 1/7$ and $\alpha_R = 1/7$ and $P_0 = 10^{-2} * P_{00}$

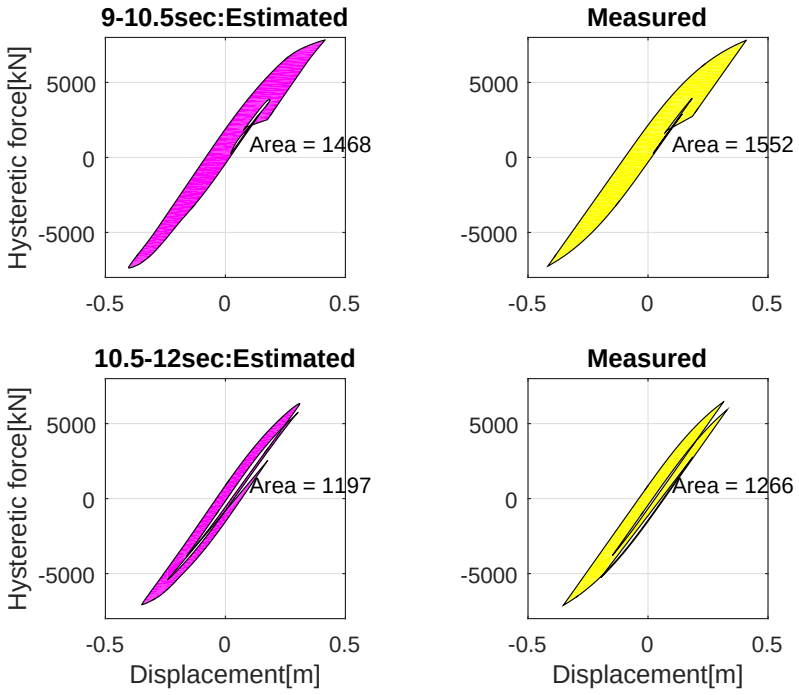

Figure 6-44: Dissipated energy with $\alpha_Q = 1/7$ and $\alpha_R = 1/7$ and $P_0 = 10^{-2} * P_{00}$

amined, good agreement with the simulated force-displacement relationships can be observed. Furthermore, to compare the energy dissipation of the system during largest response times, the area inside the selected force-displacement loops are calculated and compared with simulations (Fig. 6-44). The difference between the estimated and simulated energy dissipation between 9-12 sec is about 10%.

6.3.4 Sensitivity to change in initial state vector X_0

Considered cases are summarized in Table (6.6). X_00 is equal to

$$X_00 = [0, 0, 0, k, c, \beta]^T \tag{6.17}$$

which is an initial state vector but without $X_0(n)$.

Table 6.6: Cases considered for sensitivity analysis for initial state matrix, X_00

Case	X_0	Stiffness	Damping	Hysteresis
1	$0.2 * X_{00}$	UKF-RM:OK	OK	OK
2	$0.5 * X_{00}$	UKF-RM:OK	OK	OK
3	$0.8 * X_{00}$	UKF-RM:OK	OK	OK
4	$1.2 * X_{00}$	UKF-RM:OK	OK	OK
5	$1.5 * X_{00}$	UKF-RM:OK	OK	OK
6	$1.8 * X_{00}$	UKF-RM:OK	OK	OK

The lower and upper bounds for $X_0(n)$ is found equal to $[0.9n, 1.3n]$. To obtain the results presented in the Table 6.6 $X_0(n)$ can be set to either its lower or upper bound value.

Representative results with the initial state vector below are summarized as follows.

$$X_0 = [0, 0, 0, 0.2k, 0.2c, 0.2\beta, 1.3n]^T \tag{6.18}$$

Both stiffness and damping (Fig. 6-45) and Bouc-Wen parameters ((Fig. 6-46)) estimated successfully although initial state vector was assigned far away from the true values. n, Bouc-Wen parameter is the most sensitive state among all states because

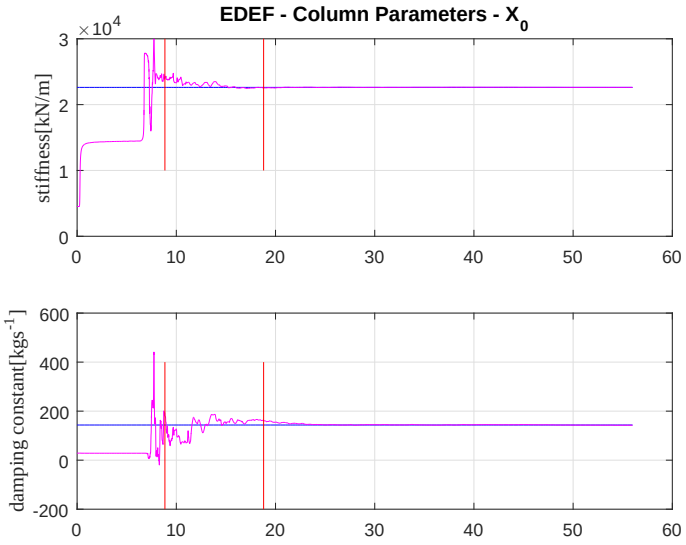

Figure 6-45: Estimated structural parameters with $\alpha_Q = 1/7$ and $\alpha_R = 1/7$ and X_0=Eq. (6.18)

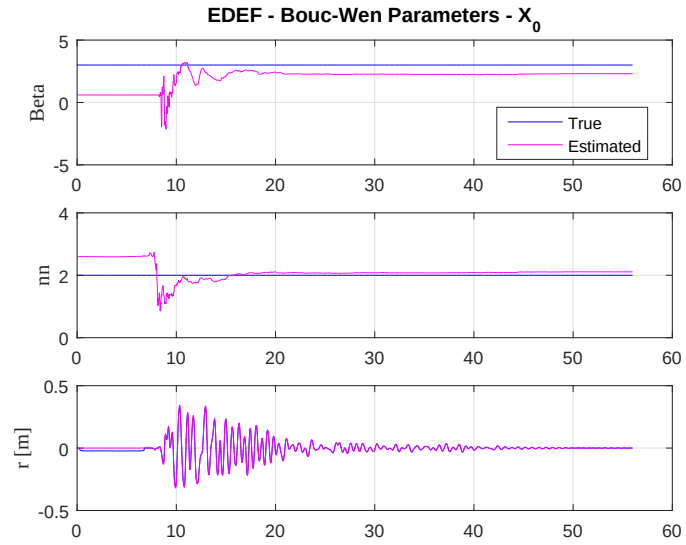

Figure 6-46: Estimated Bouc-Wen parameters with $\alpha_Q = 1/7$ and $\alpha_R = 1/7$ and X_0=Eq. (6.18)

it represent the exponential term in the nonlinear hysteretic displacement equation. Considering this fact the upper and lower bound of n is also in practical limits. Thus, UKF-RM algorithm may be considered as robust against initial condition errors.

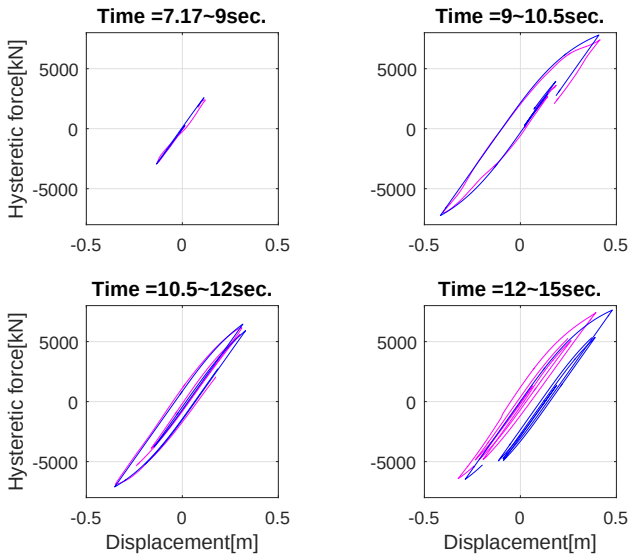

Figure 6-47: Estimated force-displacement relationship with $\alpha_Q = 1/7$ and $\alpha_R = 1/7$ and X_0=Eq. (6.18)

Furthermore, when hysteresis force estimations during various time duration (Fig. 6-47) examined, good agreement with the simulated force-displacement relationships can be observed. Furthermore, to compare the energy dissipation of the system during largest response times, the area inside the selected force-displacement loops are calculated and compared with simulations (Fig. 6-48). The difference between the estimated and simulated energy dissipation between 9-12 sec is about 1.2%.

6.3.5 Sensitivity to change in α_Q and α_R

In UKF-RM, estimates of the noise covariance Q and R using Robbins-Monro stochastic approximation scheme can be formulated as follows [62],[61],[44].

$$Q_k = (1 - \alpha_Q) * (Q_{k-1}) + \alpha_Q * (K_k) * (z_k - z_k^-) * (z_k - z_k^-)^T * (K_k^T) \qquad (6.19)$$

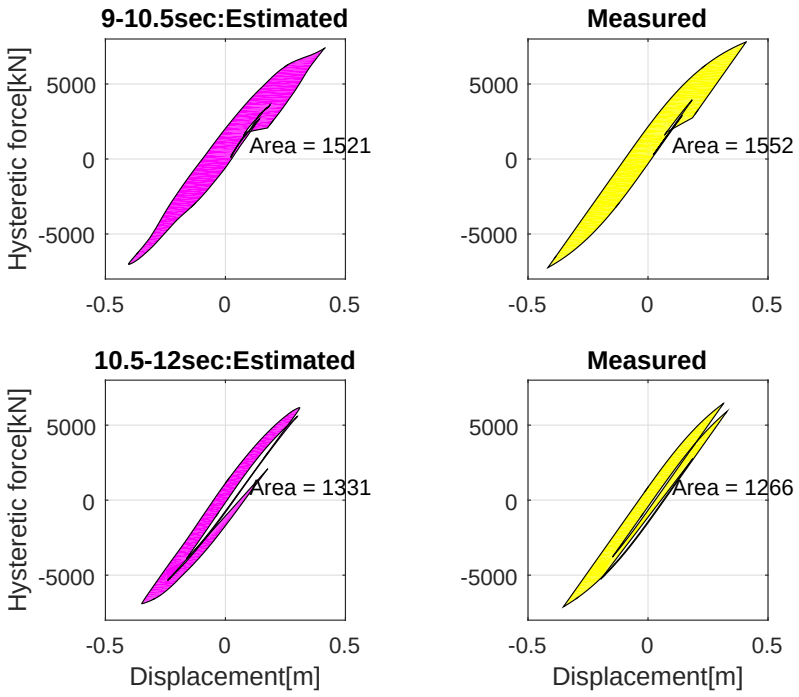

Figure 6-48: Dissipated energy with $\alpha_Q = 1/7$ and $\alpha_R = 1/7$ and X_0=Eq. (6.18)

$$R_k = (1 - \alpha_R) * (R_{k-1}) + \alpha_R * (z_k - z_k^-) * (z_k - z_k^-)^T \tag{6.20}$$

where α: a small positive number, which is usually chosen at the order of 10^{-2}. Both α_Q and α_R controls the adaptability of the filter. It can be considered as a forgetting factor, which tells to the filter how quickly it should forget the previous data and learn more from the new information as it becomes available. In this section, the sensitivity of the filter to the selection of α_Q and α_R is be investigated considering a nonlinear model.

Sensitivity to change in α_Q

First, let's consider the case where α_Q is assigned a variety of values and α_R is kept constant. As mentioned before, the convergence rate depends on Q value and thus α_Q is important in this manner. Figure (6-49) shows parameter estimation results for a variety of α_Q values when $\alpha_R = 1/7$. Stiffness parameter estimation is successfully

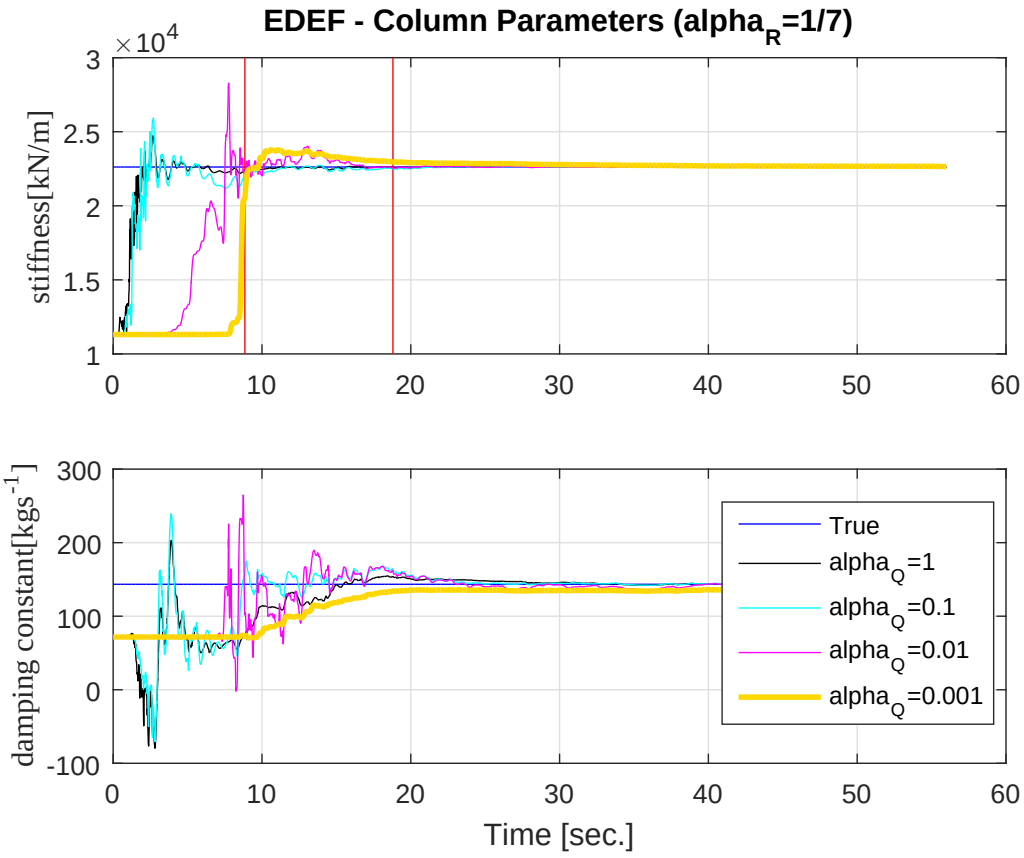

Figure 6-49: Parameter estimations with UKF-RM (Nonlinear model) - Sensitivity to α_Q ($\alpha_R = 1/7$)

achieved inside significant duration for all α_Q values. However, when $\alpha_Q \leq 0.01$ the convergence rate is slower.

Damping parameter estimation is successfully achieved inside significant duration for all $\alpha_Q \geq 0.001$ values. When $\alpha_Q = 0.001$ the the convergence rate of the filter slows down and estimation can be achieved at around the end of the significant duration.

Damping is more sensitive than stiffness estimation inside and outside of the significant duration which is a similar general conclusion drawn before. When damping parameter inside the significant duration is of interest then selecting an α_Q value at about the order of 0.01 or larger is suggested.

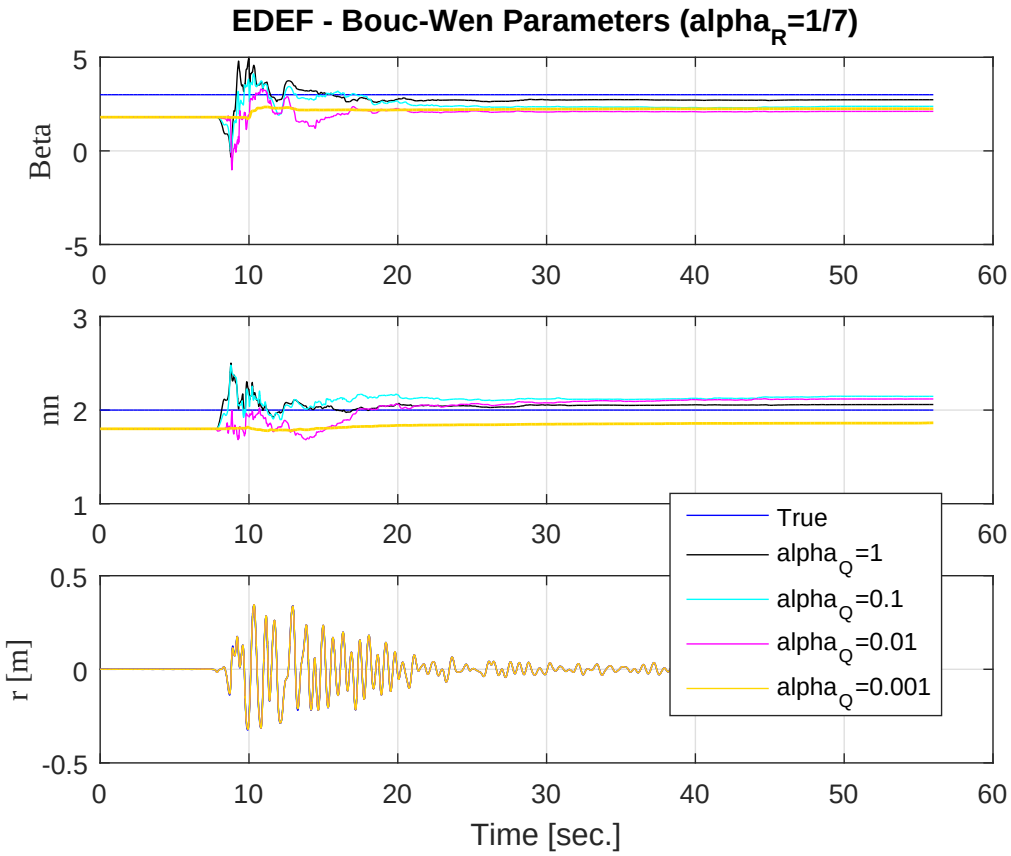

Figure 6-50: Bouc-Wen parameter estimations with UKF-RM (Nonlinear model) - Sensitivity to α_Q ($\alpha_R = 1/7$)

Bouc-Wen parameter estimation results are depicted in Figure (6-50) for a variety of α_Q values when $\alpha_R = 1/7$. Both β and n parameters are successfully estimated when $\alpha_Q geq 0.1$. Thus, it can be concluded that the nonlinear model which includes

Bouc-Wen parameters is more sensitive to the selection of α_Q. To achieve successful parameter estimations, the adaptation of the filter should be fast which can be satisfied with a selection of $\alpha geq 0.1$. Especially when $\alpha = 0.001$, β parameter update slows down and n parameter estimation cannot be updated because the adaptive ability of the filter reduces. On the other hand, due to the redundancy of Bouc-Wen element, hysteretic displacement is successfully estimated with all α values even though the Bouc-Wen parameters cannot be achieved.

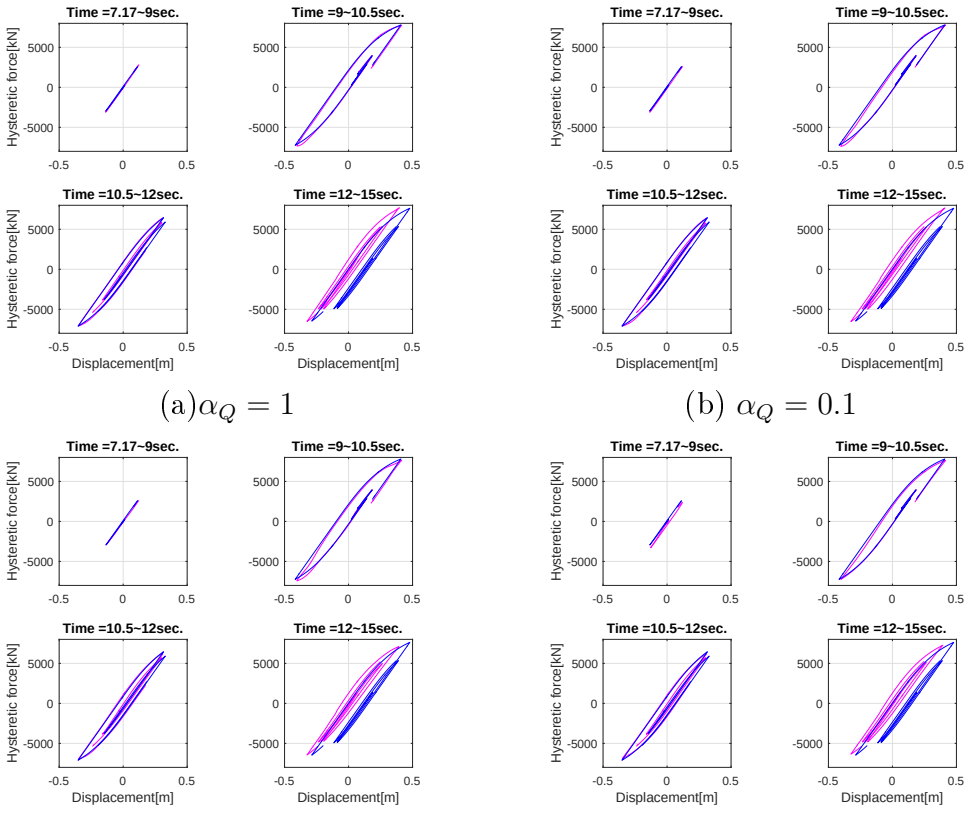

(a)$\alpha_Q = 1$ (b) $\alpha_Q = 0.1$

(c)$\alpha_Q = 0.01$ (d) $\alpha_Q = 0.001$

Figure 6-51: Hysteresis loop estimations with UKF-RM (Nonlinear model) - Sensitivity to α_Q ($\alpha_R = 1/7$)

Figure 6-51 shows the estimated hysteresis loops for different times of the response. For all α_Q value, hysteretic force - displacement relationships are constructed successfully. Thus, hysteresis loop estimations can be considered as insensitive to changes in α_Q value.

Figure 6-52 shows the estimated dissipated energy for the largest hysteresis loops.

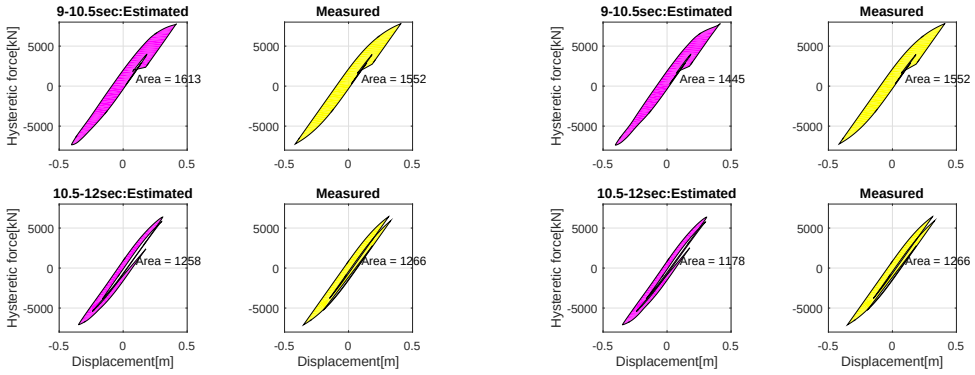

(a)$\alpha_Q = 1$

(b) $\alpha_Q = 0.1$

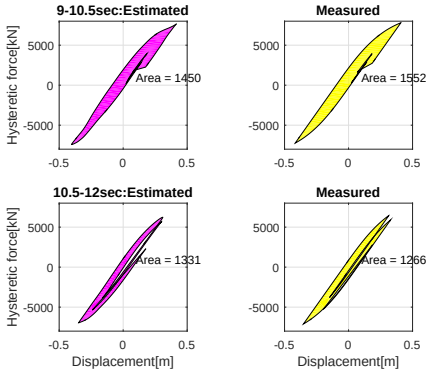

(c)$\alpha_Q = 0.01$

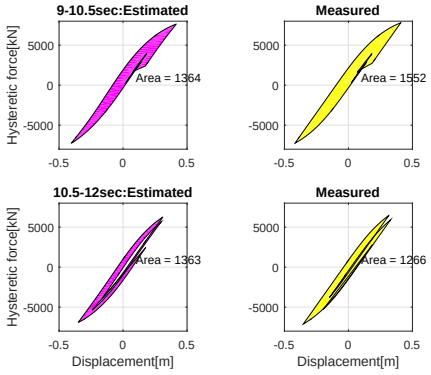

(d) $\alpha_Q = 0.001$

Figure 6-52: Dissipated energy estimations with UKF-RM (Nonlinear model) - Sensitivity to α_Q ($\alpha_R = 1/7$)

Calculated energy dissipation errors are 2%, 7%, 1% and 3% when $\alpha_Q = 1$, $\alpha_Q = 0.1$, $\alpha_Q = 0.01$, and $\alpha_Q = 0.001$, respectively.

Sensitivity to change in α_R

Finally, the performance of UKF-RM based on its sensitivity to α_R, assuming 5% measurement noise, $R_0 = 1\%$ is investigated.

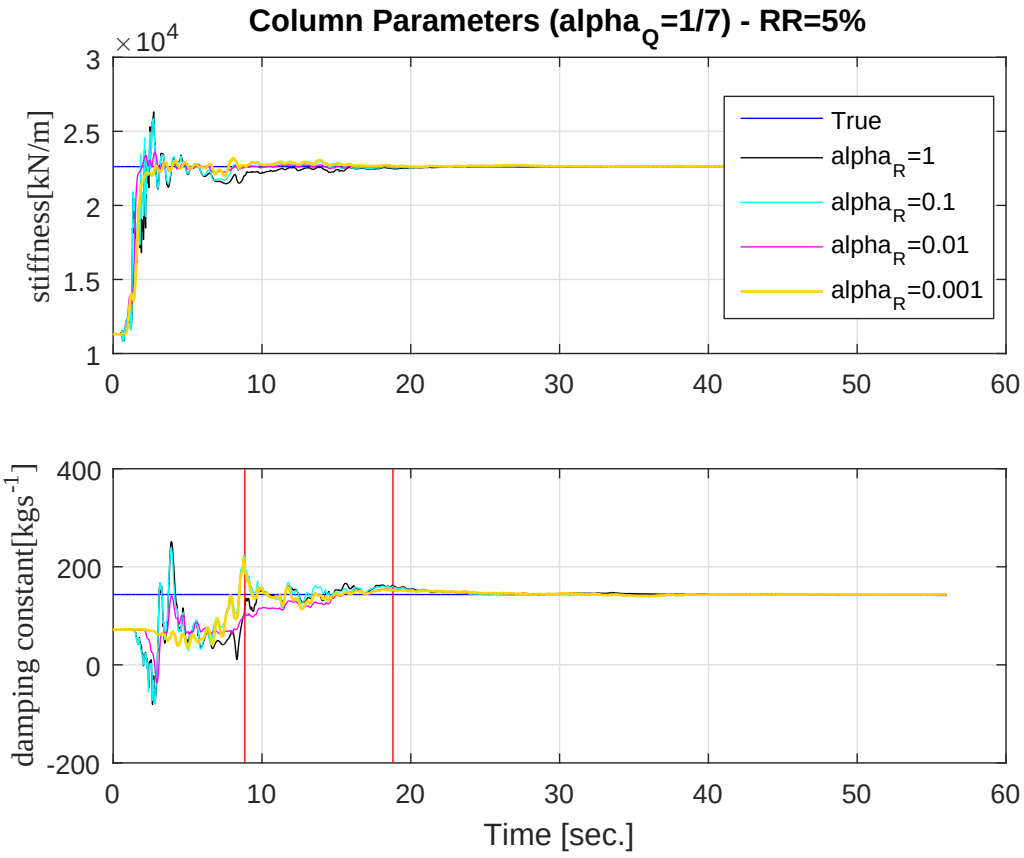

Figure 6-53: Parameter estimations with UKF-RM (Nonlinear model) - Sensitivity to α_R ($\alpha_Q = 1/7$ and 5% measurement noise)

Figure (6-53) shows parameter estimation results for a variety of α_R values when $\alpha_Q = 1/7$ and 5% measurement noise is added to the observation. Both stiffness and damping parameter estimations are successfully achieved inside significant duration for all α_R values when 5% is present in observation. Calculated parameter estimation errors are less than 1%. Thus, structural parameters can be considered as insensitive to changes in α_R value assignments.

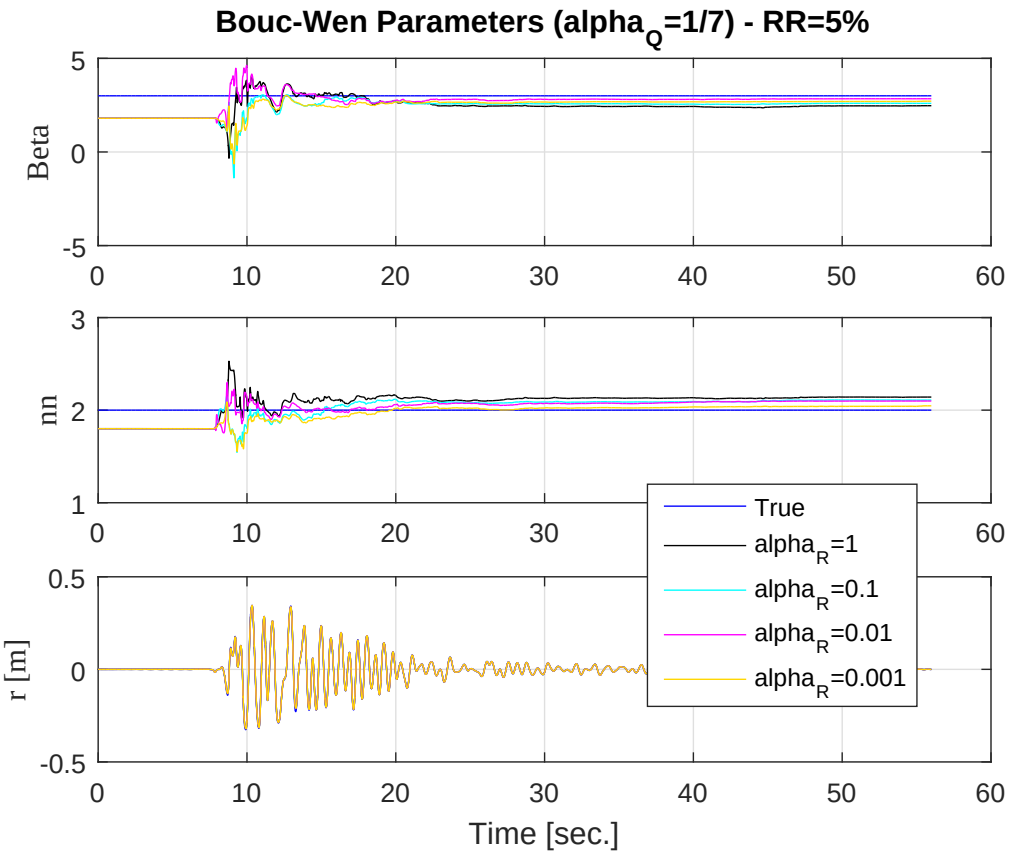

Figure 6-54: Bouc-Wen parameter estimations with UKF-RM (Nonlinear model) - Sensitivity to α_R ($\alpha_Q = 1/7$ and 5% measurement noise)

Bouc-Wen parameter estimation results are depicted in Figure (6-54) for a variety of α_R values when $\alpha_Q = 1/7$ and 5% measurement noise is added to the observation. Both Bouc-Wen parameters β and n, and hysteretic displacement, r are successfully estimated with an error percentage less than 1% regardless of the assigned α_R value.

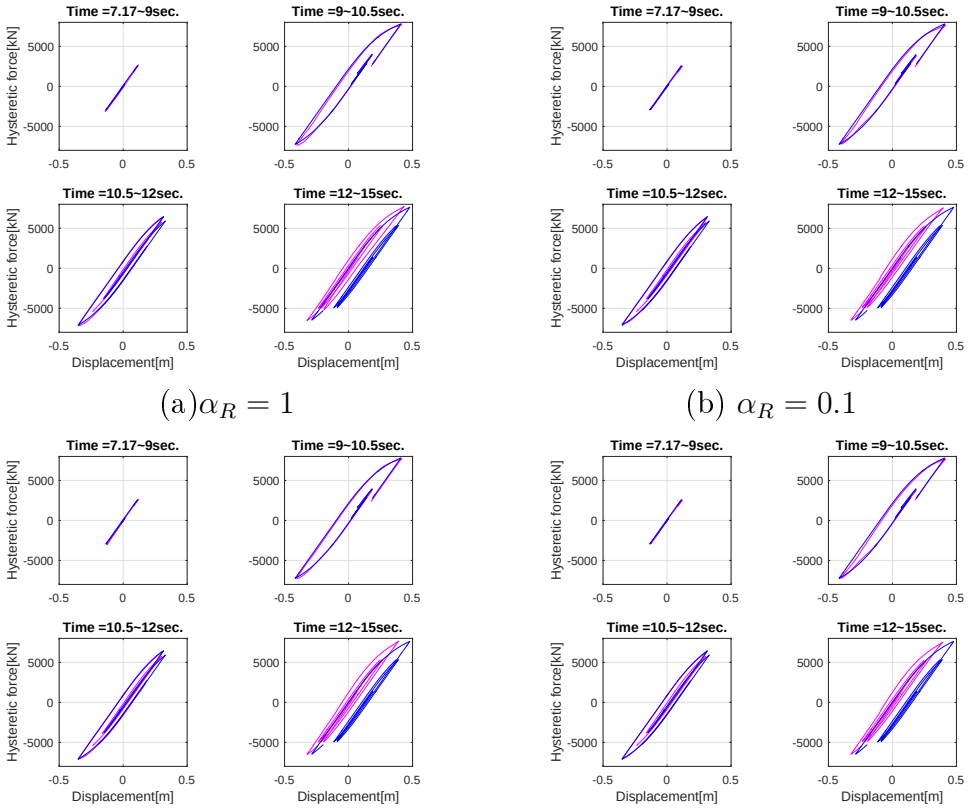

(a)$\alpha_R = 1$ (b) $\alpha_R = 0.1$

(c)$\alpha_R = 0.01$ (d) $\alpha_R = 0.001$

Figure 6-55: Hysteresis loop estimations with UKF-RM (Nonlinear model) - Sensitivity to α_R ($\alpha_Q = 1/7$ and 5% measurement noise)

Figure 6-55 shows the estimated hysteresis loops for different times of the response. For all α_R value, hysteretic force - displacement relationships are constructed successfully. Thus, hysteresis loop estimations can be considered as insensitive to changes in α_R value.

Figure 6-56 shows the estimated dissipated energy for the largest hysteresis loops. Calculated energy dissipation errors are 5%, 8%, 1% and 8% when $\alpha_R = 1$, $\alpha_R = 0.1$, $\alpha_R = 0.01$, and $\alpha_R = 0.001$, respectively.

In conclusion, considering a variety of α_Q and α_R (including measurement noise)

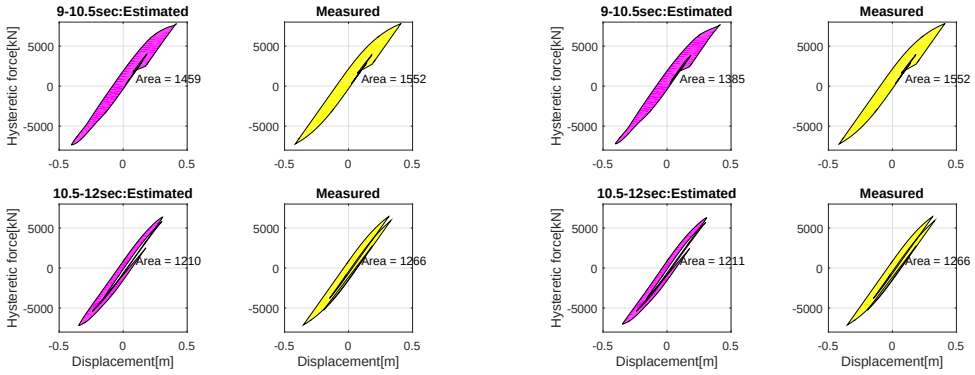

(a)$\alpha_R = 1$ (b) $\alpha_R = 0.1$

(c)$\alpha_R = 0.01$ (d) $\alpha_R = 0.001$

Figure 6-56: Dissipated energy estimations with UKF-RM (Nonlinear model) - Sensitivity to α_R ($\alpha_Q = 1/7$ and 5% measurement noise)

values the sensitivity of the estimations results to change in α values in investigated. In all cases UKF-RM is proven to be robust to achieve successful estimations. When α_Q and α_R are selected in a reasonable range, the estimations can be obtained successfully and consistently. Thus estimations can be considered as insensitive to change in α values. Consequently, UKF-RM is proven to be advantageous in practical applications which eases the interpretation of the obtained parameter due to its consistency in estimations.

6.4 Experiment

In this section, identification of hysteresis response will be validated with the proposed method using large earthquake response measurements from E-Defense experiment. Based on the explanations given in Chapter 6.1, the reduced augmented state vector is as follows:

$$X_a = [x, \dot{x}, r, k, c, \beta, n]^T = [x_1, x_2, x_3, x_4, x_5, x_6, x_7]^T \tag{6.21}$$

where only mass, m and Bouc-Wen parameter γ is assumed as known in all following structural parameter estimations.

Mass is obtained from the E-Defense C1-1 experiment report [1]. The reaction force in vertical direction measured by the load cells located on the pier cap is given equal to $2080kN$ (Table 2.1) from dead load of the girder and added mass on top of the girder. In addition, weight of the pier is given as $794.5kN$. Consequently, the modal mass is calculated as

$$m = (2080 + 794.5/2)/g = 252.5ton \tag{6.22}$$

where $g = 9.81m/s^2$ is the acceleration of gravity. Thus, it is assumed that half of the pier weight also contributes to the structure mass.

γ is assumed as 0.5. In the following sections, sensitivity of the results to change in γ will also be presented. Furthermore, here it should be noted that the estimated

β values should satisfy the Class I conditions presented in Table 6.1.

Based on Eq. (6.1) and (6.5) the state space equation is formulated as:

$$\dot{X}_a = f(X_a(t), u(t)) \tag{6.23}$$

where

$$f(\mathbf{X_a}(t), \mathbf{u}(t)) = \begin{bmatrix} x_2 \\ (-x_4 x_3 - x_5 x_2)/m + \ddot{x_g} \\ x_2 - x_6 |x_2||x_3|^{(x_7-1)} x_3 - \gamma x_2 |x_3|^{(x_7)} \\ 0 \\ 0 \\ 0 \\ 0 \end{bmatrix} \tag{6.24}$$

Observation is double-integrated measured acceleration on top of the pier cap, thus observation equation becomes:

$$y = \begin{bmatrix} x_1 \end{bmatrix} \tag{6.25}$$

Initial state vector is shown below.

$$X_0 = [0, 0, 0, 1.5k, 0.5c, 0.6\beta, 0.9n]^T \tag{6.26}$$

Here, k is equal to the given design value, $32506kN/m$, in the experiment report [1]. $\zeta = 3\%$ viscous damping is assumed for the column and corresponding damping factor c is calculated based on mass and stiffness. β and n are set to one and two, respectively.

Initial error covariance is set to

$$P_0 = diag[0.01, 0.01, 0.01, k^2, c^2, \beta^2, 0.1] \tag{6.27}$$

instead of

$$P_0 = diag[0.01, 0.01, 0.01, (k_{true} - x_0(3))^2, (c_{true} - x_0(4))^2, (\beta_{true} - x_0(5))^2, (n - x_0(6))^2] \tag{6.28}$$

Because in practice, true values and initial values of the states are unknown. Thus, initial error covariance is set in a way such that the given design values are squared. Meaning, the initial state vector is actually zero and the error is equal to the state's design value itself.

Initial measurement noise covariance is set to $R_0 = (0.05RMS_{measurement})^2$.

α_Q and α_R values are both set to $1/7$.

Using the SDOF system explained above and initial values, parameter estimation with UKF-RM has been performed using the below initial Q matrix.

$$Q_0 = diag[10^{-4}, 10^{-2}, 10^{-4}, 10^{-4}, 10^{-1}, 10^{1}, 10^{-8}] \tag{6.29}$$

Among the available dataset, two input and response measurements (Tab. 6.7) are selected for experimental validation of the proposed hysteresis curve estimation algorithm. As mentioned before ground motion presented in the table appear in the same chronological order as they were input to the system. Before input $2007-1213-004-1M$, there were no damage occurs on the pier. Input $2007-1213-014-1M$ was exerted to the system after the pier was damaged due to input $2007-1213-004-1M$.

Table 6.7: Selected data sets from the excitations used in C1-1 experiment

ID	Excitation type	Excitation level
2007-1213-004-1M	Takatori(Modified)	100%
2007-1213-014-1M	Takatori(Modified)	100%

6.4.1 Hysteresis force identification results for input $2007-1213-004-1M$

Input acceleration measured on the shake table is depicted on top of Fig. (6-57). Peak ground acceleration is about $5m/s^2$. In addition, first 7 seconds of the data is disregarded because there is not information during this initial part. The bottom figure shows comparison between the displacement response estimation from acceleration response measurement and measured displacement during the experiment. Maximum displacement response is about $0.13m$. Except the residual displacement, measured and estimated displacements show satisfactory match. Using the estimated displacement with double-integration of acceleration as observation UKF-RM results are obtained and summarized in this section.

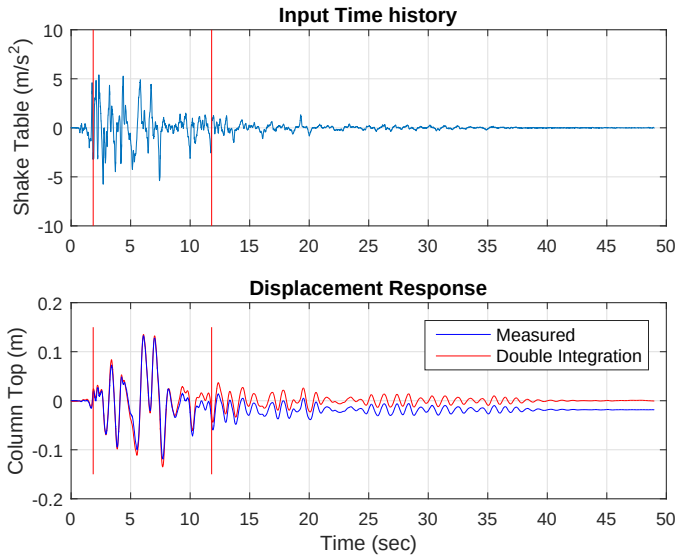

Figure 6-57: Input acceleration and displacement response estimation from acceleration response measurement under excitation 2007-1213-004-1M

Displacement and velocity estimations match well with the measured response which are depicted in Fig (6-58).

To check the accuracy of the stiffness estimation, measured force-displacement relationship is drawn (Figure 6-59). Based on the hysteresis curves, the total duration of response is divided into three regions, namely; initial, nonlinear and residual re-

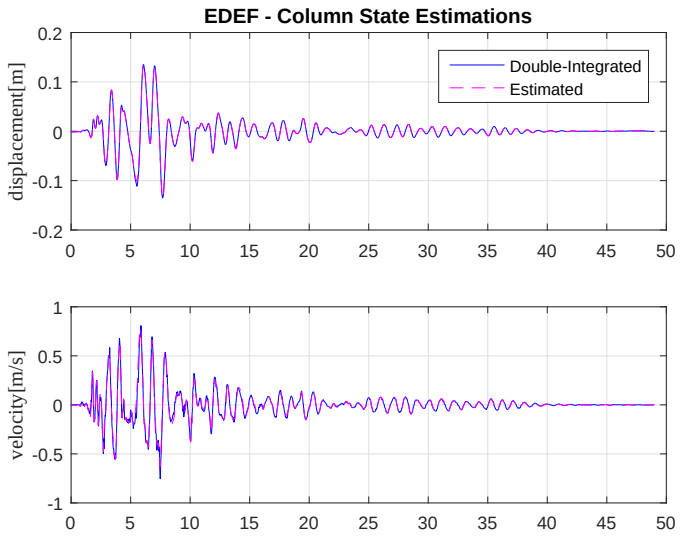

Figure 6-58: State estimation results from UKF-RM with $\alpha_Q = 1/7$ and $\alpha_R = 1/7$ (2007-1213-004-1M)

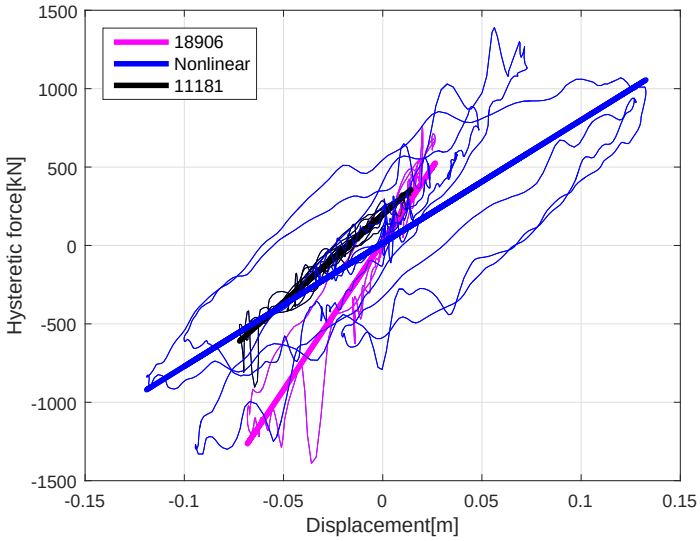

Figure 6-59: Measured force-displacement relationship during experiment (2007-1213-004-1M)

sponses. The legend on the displacement response time history given in Figure (6-60) shows the corresponding response regions and their duration. Two horizontal dotted lines on the stiffness estimation figure represent the measured initial and residual stiffness which are calculated as the slope of the linear fit to the measured hysteresis

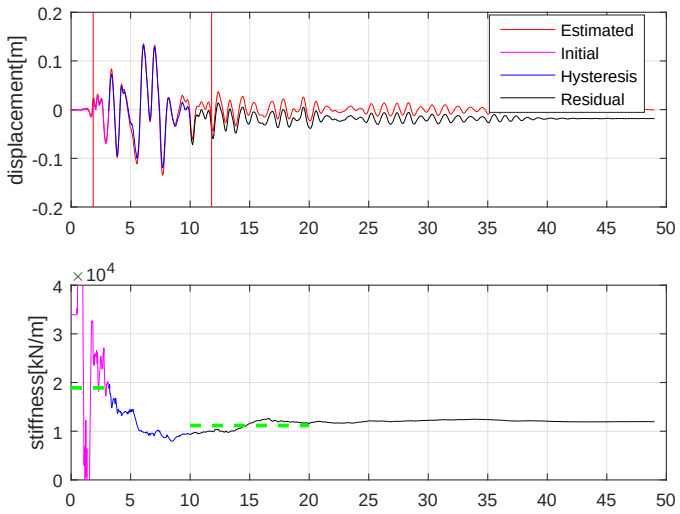

Figure 6-60: Stiffness estimation results from UKF-RM with $\alpha_Q = 1/7$ and $\alpha_R = 1/7$ (2007-1213-004-1M)

curves. Estimated residual stiffness is calculated as the mean value over $10sec.$ duration starting from the end of significant duration, which is equal to $11074kN/m$. The true value of the residual stiffness is $11181kN/m$, hence the estimation error is equal to 1%.

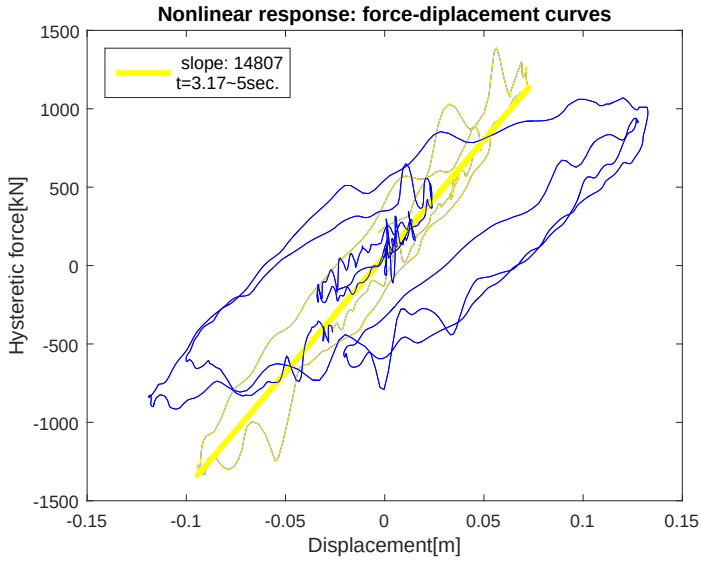

Figure 6-61: Measured force-displacement relationship in nonlinear response region ($3.17sec - 10sec$) (2007-1213-004-1M)

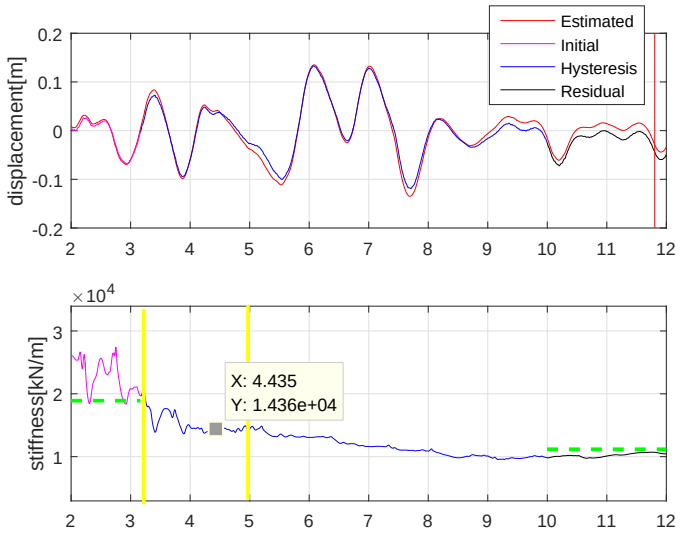

Figure 6-62: Nonlinear response region (zoomed): Stiffness estimation results from UKF-RM with $\alpha_Q = 1/7$ and $\alpha_R = 1/7$

During nonlinear response, there are several hysteresis curves which have various slopes, thus a single value for stiffness cannot be given. For instance, when the response between $(t = 3.17 - 5sec)$ is examined (Figure 6-61), the nonlinearity can be considered as small because because force-displacement relationship generates very thin hysteresis curve, meaning energy dissipation in the system is small. When we zoom in to the nonlinear response region of stiffness estimation results in fact just before $t = 5sec$ stiffness becomes very stable at about $14360kN/m$ (Figure 6-62). When it is compared to the slope of the linear fit of the corresponding measured force-displacement curve ($14807kN/m$) the error is about 3%.

However, when damage occurs to structural components, stiffness cannot be obtained as a single value due to complex cyclic reversals and hence energy dissipation of the system should be known. The area under the force-displacement curves gives an estimate of the energy dissipation of the system. However, hysteresis force cannot directly be estimated using system identification. By estimating nonlinear model parameters, such as Bouc-Wen model, the hysteresis force can be calculated. Figure (6-63) depicts the estimation results for Bouc-Wen parameters. Although all Bouc-Wen parameters converge to a value, the accuracy of the estimation cannot be

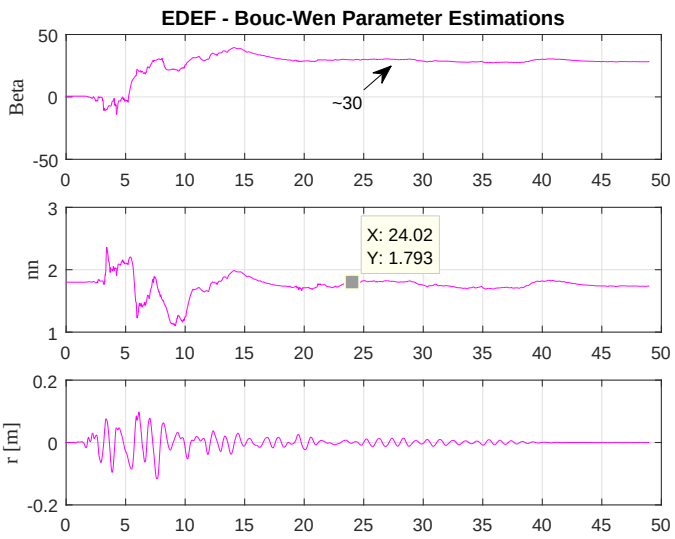

Figure 6-63: Bouc-Wen parameter estimation results from UKF-RM with $\alpha_Q = 1/7$ and $\alpha_R = 1/7$ (2007-1213-004-1M)

validated because true values of the parameters are not known. Thus, a two step check procedure is adopted in this thesis which is discussed below.

First check is that the Class I conditions given in Table 6.1 for β and γ must be satisfied. γ was assumed 0.5 and estimated β changes between 20 to 35 after $t = 5sec$ based on the response reversals. Thus, Class I conditions are satisfied and hence thermodynamic admissibility conditions are met by the identified Bouc-Wen parameters. Consequently, the identified Bouc-Wen model is considered BIBO stable.

Second check is the comparison of estimated and measured force-displacement relationships which are depicted in Figures (6-64) and (6-65) for initial, nonlinear and residual response ranges. Hysteretic force is calculated as follows.

$$Hsytereticforce = k_{residual} r(t) + c_{design} \dot{x}(t) \tag{6.30}$$

where $k_{residual}$ is the estimated residual stiffness, $r(t)$ is the estimated hysteretic displacement, $\dot{x}(t)$ is the estimated velocity in which (t) stands for time step. True damping value is now known, so the estimated damping cannot be validated. Thus, design damping assumption is adopted to calculate the hysteretic force.

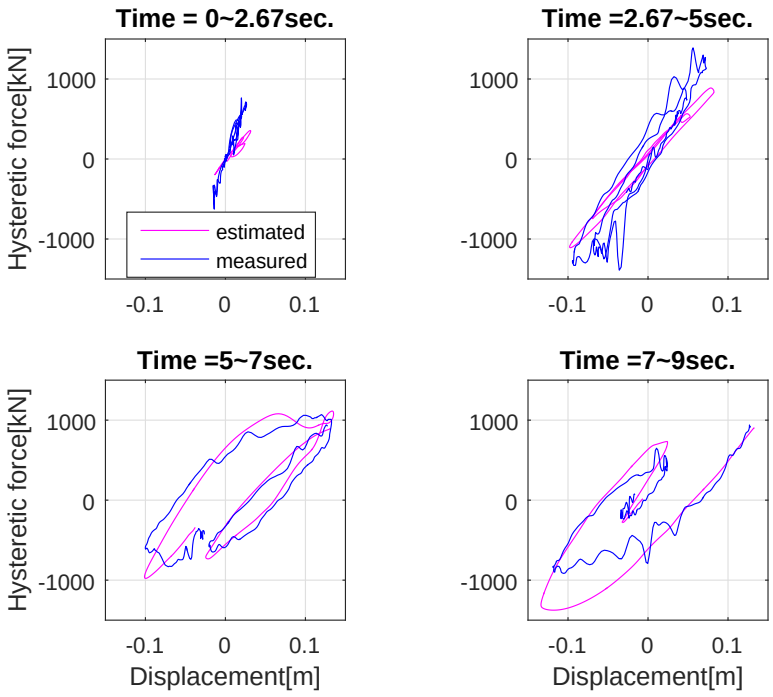

Figure 6-64: Estimated and measured force-displacement curves during initial and nonlinear response ranges (2007-1213-004-1M)

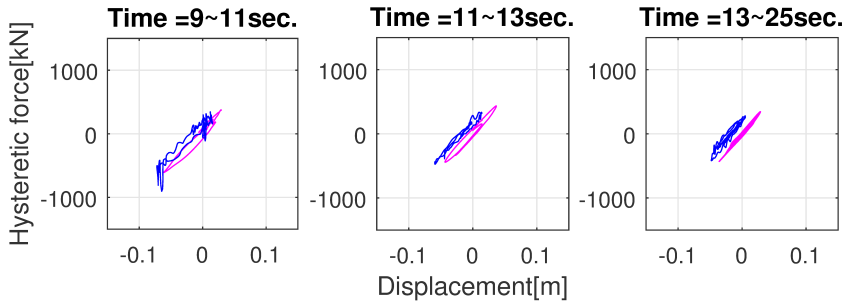

Figure 6-65: Estimated and measured force-displacement curves during residual response ranges (2007-1213-004-1M)

Between $t = 0-5sec$ and $t = 9-25sec$ response, in other words, energy dissipation of the system is considered small. During $t = 5-7sec$ and $t = 7-9sec$ RC pier dissipates more energy which is exerted by earthquake excitation. Damage pattern was also recorded during experiment and can be found in the [1]. According to the experiment report [1], around $t = 4sec$ hair cracks, around $t = 6sec$ vertical cracks

Figure 6-66: Damage to RC pier after 1st 100% Takatori excitation [1] (2007-1213-004-1M)

due to compressive forces and around $t = 7sec$ concrete cover spalling occur at the bottom of the pier (Figure 6-66).

Consequently, dissipated energy due to occurred damage at the pier bottom location is calculated as the enclosed area by the hysteresis curves for $t = 5 - 7sec$ and $t = 7 - 9sec$ (Figure 6-67) from estimated and measured response. Total dissipated energy (area inside the hysteresis curves) is $329kNm$ and $320kNm$ from estimated and measured responses, respectively. Thus, the error of estimation is about 3%.

Sensitivity of parameter identification to change in γ for input $2007-1213-004-1M$

In this section, sensitivity of parameter identification to change in γ is investigated. Based on the information in Chapter 6.1, in Chapter 6.4.1 γ was set to 0.5. By assigning $\gamma = 10$ and keeping all other initial filter parameters same as in 6.4.1, UKF-RM estimation has been performed.

Displacement and velocity estimations match well with the measured response

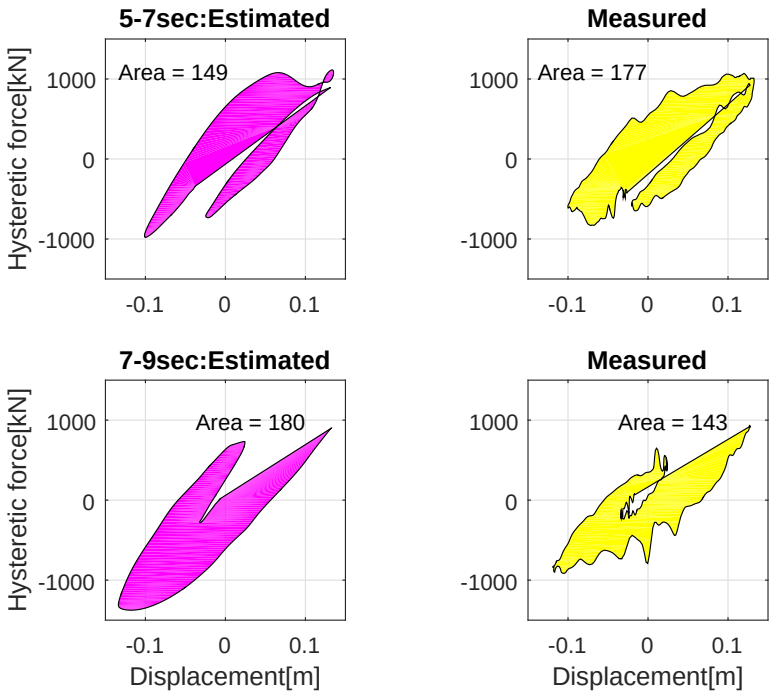

Figure 6-67: Dissipated energy from estimated and measured response at $t = 5-7sec$ and $t = 7-9sec$ for excitation (2007-1213-004-1M)

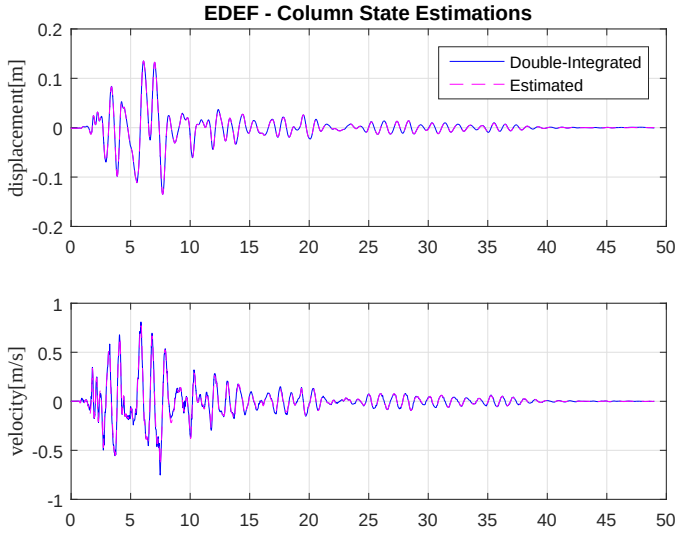

Figure 6-68: State estimation results from UKF-RM with $\alpha_Q = 1/7$, $\alpha_R = 1/7$ and $\gamma = 10$(2007-1213-004-1M)

which are depicted in Fig (6-68).

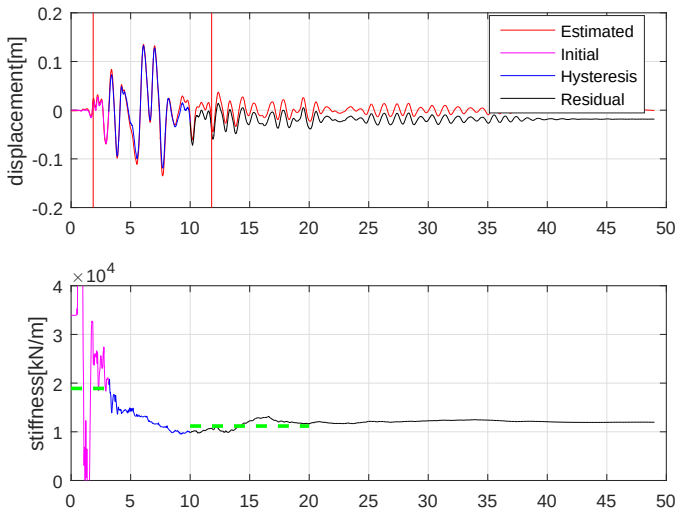

Figure 6-69: Stiffness estimation results from UKF-RM with $\alpha_Q = 1/7$, $\alpha_R = 1/7$ and $\gamma = 10$ (2007-1213-004-1M)

Stiffness estimation result is depicted in Figure (6-69). Estimated residual stiffness is calculated as the mean value over $10sec.$ period starting from the end of significant duration, which is equal to $11352kN/m$. The true value of the residual stiffness is $11181kN/m$, hence the estimation error is equal to 2%.

Figure (6-63) depicts the estimation results for Bouc-Wen parameters. Similar to the previous estimation results, although all Bouc-Wen parameters converge to a value, the accuracy of the estimation cannot be validated because true values of the parameters are not known. Two step check procedure is adopted.

First check is that the Class I conditions given in Table 6.1 for β and γ must be satisfied. γ was assumed 10 and estimated β changes between 16 to 33 after $t = 5sec$ based on the response reversals. Thus, Class I conditions are satisfied and hence thermodynamic admissibility conditions are met by the identified Bouc-Wen parameters. Consequently, the identified Bouc-Wen model is considered BIBO stable.

Second check is the comparison of estimated and measured force-displacement relationships which are depicted in Figures (6-71) and (6-72) for initial, nonlinear and residual response ranges. During $t = 5 - 7sec$ and $t = 7 - 9sec$ RC pier response

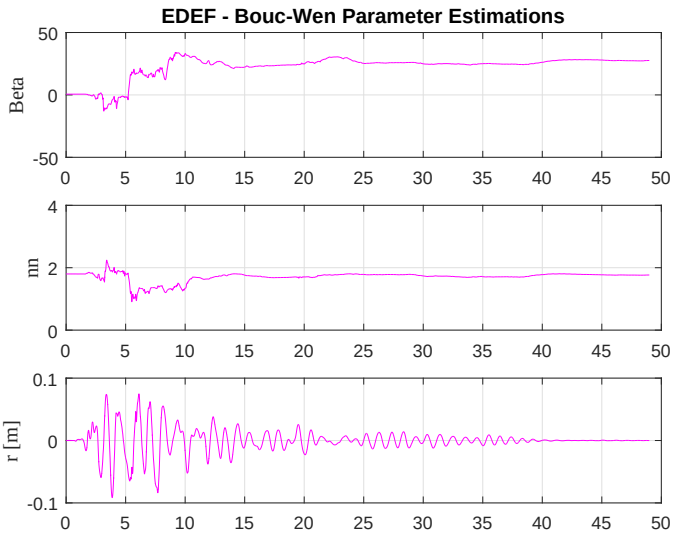

Figure 6-70: Bouc-Wen parameter estimation results from UKF-RM with $\alpha_Q = 1/7$, $\alpha_R = 1/7$ and $\gamma = 10$ (2007-1213-004-1M)

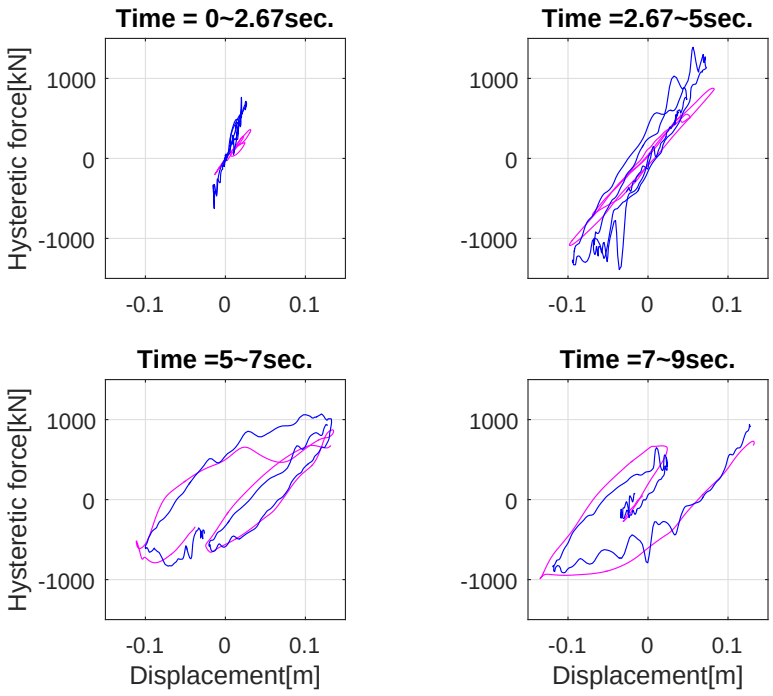

Figure 6-71: Estimated and measured force-displacement curves during initial and nonlinear response ranges with $\gamma = 10$ (2007-1213-004-1M)

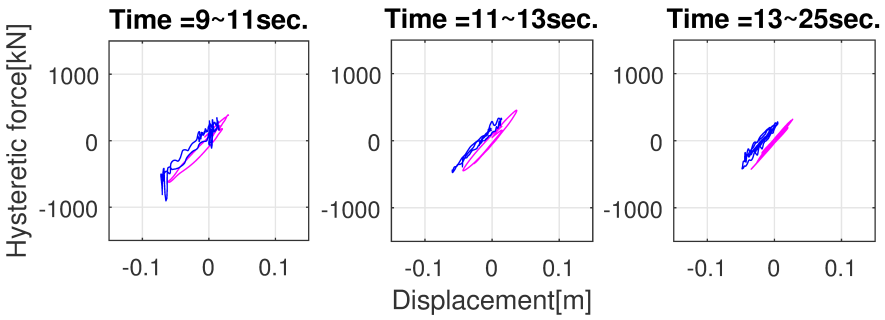

Figure 6-72: Estimated and measured force-displacement curves during residual response ranges with $\gamma = 10$ (2007-1213-004-1M)

is large when compared to other time periods such as in initial and residual response ranges. In addition, estimated and measured force-displacement curves agree well with each other.

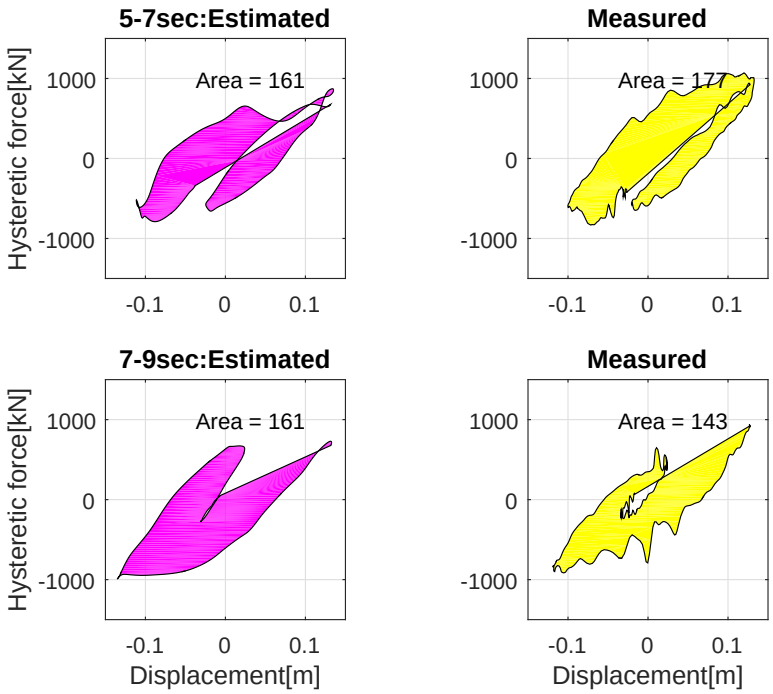

Figure 6-73: Dissipated energy from estimated and measured response at $t = 5-7sec$ and $t = 7-9sec$ for excitation (2007-1213-004-1M)

Consequently, dissipated energy due to occurred damage at the pier bottom location is calculated as the enclosed area by the hysteresis curves for $t = 5-7sec$ and

$t = 7 - 9sec$ (Figure 6-73) from estimated and measured response. Total dissipated energy (area inside the hysteresis curves) is $322kNm$ and $320kNm$ from estimated and measured responses, respectively. Thus, the error of estimation is about 1%. Thus, it can be concluded that for the considered structural system parameter identification methodology sensitivity of the results are small to change in γ in terms of both parameter and hysteretic force. Hence, application of the procedure to practical problems is possible.

6.4.2 Hysteresis force identification results for input $2007 - 1213 - 014 - 1M$

Lastly, the proposed parameter and hysteretic force identification procedure has been validated through a second input and measured response couple. Input acceleration measured on the shake table is depicted on top of Figure (6-74) which is same as input $2007-1213-004-1M$. However, this earthquake input was exerted to the RC pier after it experienced the damage (Figure 6-66) due to input $2007-1213-004-1M$. Thus, the response of the system is different when compared to undamaged state response. The bottom figure (6-74) shows comparison between the displacement response estimation from acceleration response measurement and measured displacement during the experiment. Maximum displacement response is about $0.20m$. Except the residual displacement, measured and estimated displacements show satisfactory match. Using the estimated displacement with double-integration of acceleration as observation UKF-RM results are obtained under input $2007 - 1213 - 014 - 1M$ and summarized in this section.

Displacement and velocity estimations match well with the measured response which are depicted in Fig (6-75).

To check the accuracy of the stiffness estimation, measured force-displacement relationship is drawn (Figure 6-76). Based on the hysteresis curves, the total duration of response is divided into three regions, namely; initial, nonlinear and residual responses. The legend on the displacement response time history given in Figure (6-77)

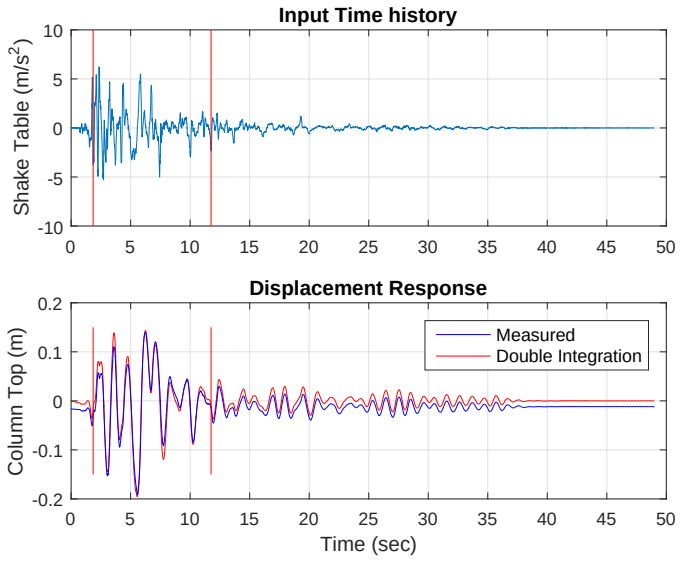

Figure 6-74: Input acceleration and displacement response estimation from acceleration response measurement under excitation 2007-1213-014-1M

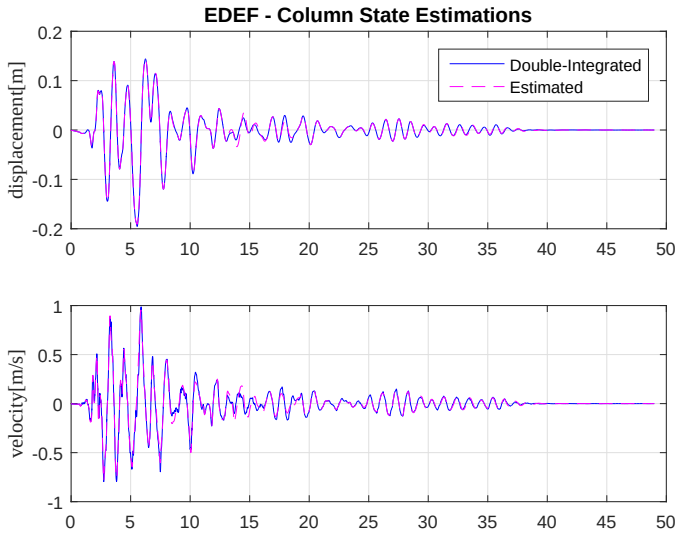

Figure 6-75: State estimation results from UKF-RM with $\alpha_Q = 1/7$ and $\alpha_R = 1/7$ (2007-1213-014-1M)

shows the corresponding response regions and their duration. Two horizontal dotted lines on the stiffness estimation figure represent the measured initial and residual stiffness which are calculated as the slope of the linear fit to the measured hysteresis curves. Estimated residual stiffness is calculated as the mean value over 10*sec*.

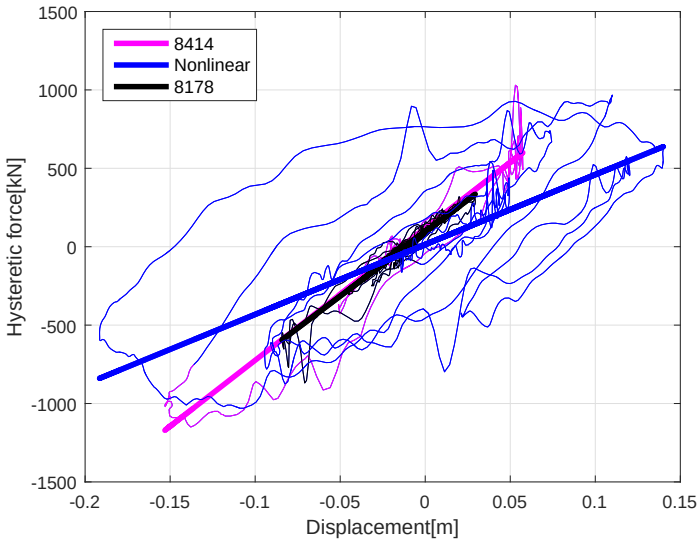

Figure 6-76: Measured force-displacement relationship during experiment (2007-1213-014-1M)

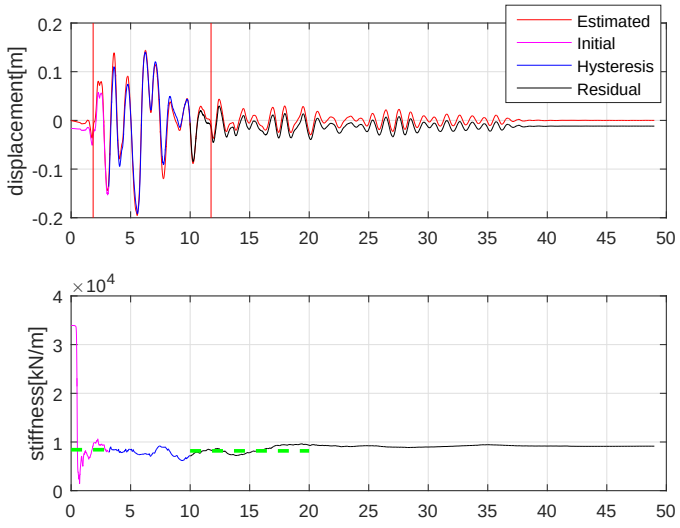

Figure 6-77: Stiffness estimation results from UKF-RM with $\alpha_Q = 1/7$ and $\alpha_R = 1/7$ (2007-1213-014-1M)

duration starting from the end of significant duration, which is equal to $8432kN/m$. The true value of the residual stiffness is $8178kN/m$, hence the estimation error is equal to 3%. The initial and residual stiffness values are very close and due to previous damage, the pier starts nonlinear response immediately when the significant

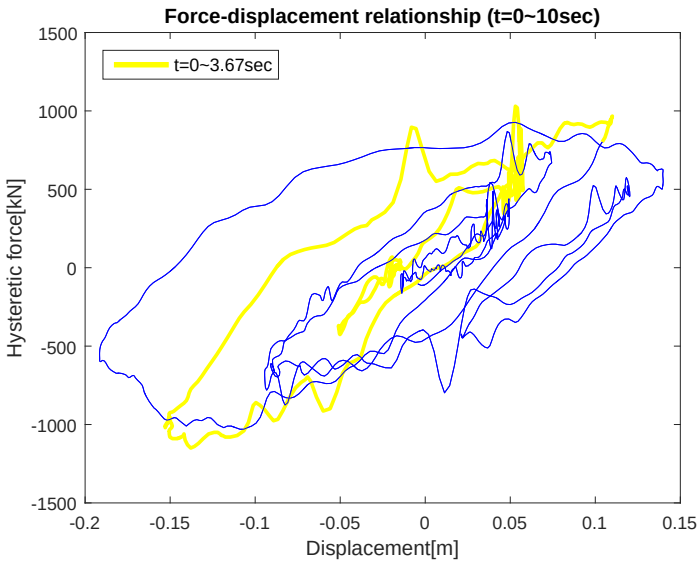

Figure 6-78: Measured force-displacement relationship in nonlinear response region ($0sec - 10sec$) (2007-1213-014-1M)

duration starts (Figure6-78) at about $t = 2sec$. Displacement response at about $t = 3sec$ reaches $-0.14m$ which is larger than the maximum displacement response $0.13m$ under the 1st 100% excitation (Figure 6-57).

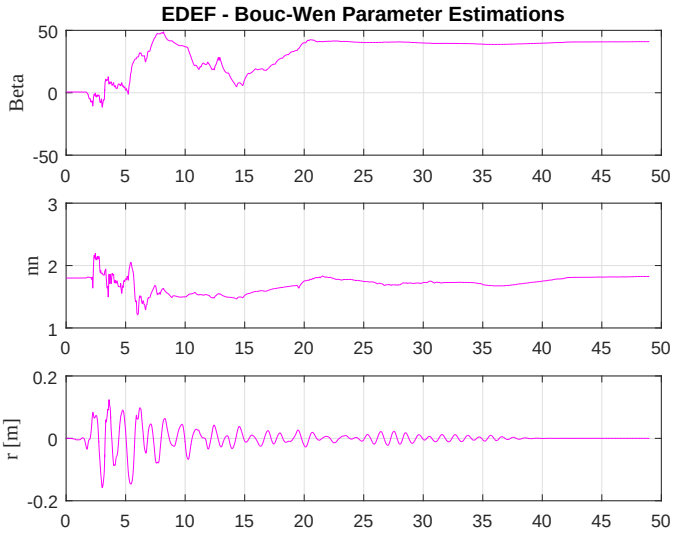

Figure 6-79: Bouc-Wen parameter estimation results from UKF-RM with $\alpha_Q = 1/7$ and $\alpha_R = 1/7$ (2007-1213-014-1M)

Figure (6-79) depicts the estimation results for Bouc-Wen parameters. The accuracy of the Bouc-Wen parameter estimations is again checked based on the two step procedure discussed earlier in section chapter 6.4.1.

First check is that the Class I conditions given in Table 6.1 for β and γ must be satisfied. γ was assumed 0.5 and estimated β changes between 1 to 49 after $t = 5sec$ based on the response reversals. Thus, Class I conditions are satisfied and hence thermodynamic admissibility conditions are met by the identified Bouc-Wen parameters. Consequently, the identified Bouc-Wen model is considered BIBO stable.

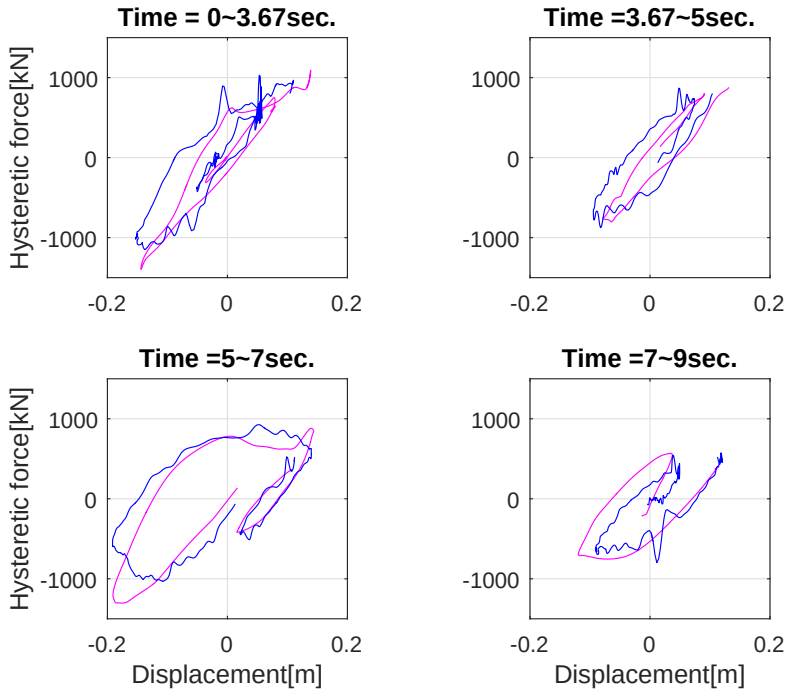

Figure 6-80: Estimated and measured force-displacement curves during initial and nonlinear response ranges (2007-1213-014-1M)

Second check is the comparison of estimated and measured force-displacement relationships which are depicted in Figures (6-80) and (6-81) for initial, nonlinear and residual response ranges. As mentioned earlier due to the damaged initial state of the pier, nonlinear response immediately when the significant duration starts (Figure6-78) at about $t = 2sec$. Thus, the time duration for the initial response range is actually nonlinear and damage to pier continues to grow.

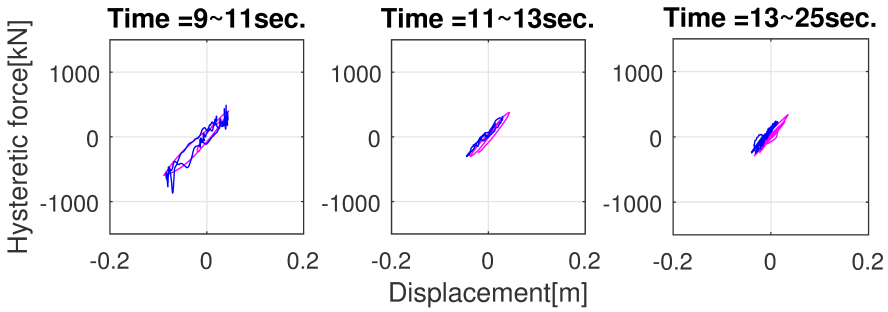

Figure 6-81: Estimated and measured force-displacement curves during residual response ranges (2007-1213-014-1M)

Figure 6-82: Damage to RC pier after 2nd 100% Takatori excitation [1] (2007-1213-014-1M)

After $t = 9sec$ energy dissipation of the system is considered small and response is linear. During $t = 5-7sec$ and $t = 7-9sec$ the estimated and measured hysteretic force matches well. According to the experiment report [1], damage continued to grow until around $t = 7.5sec$ and then concrete core crushed, lateral ties lost their effectiveness and lastly buckling of reinforcing bars were observed (Figure 6-82). However, although estimated maximum force and displacement were matching with the

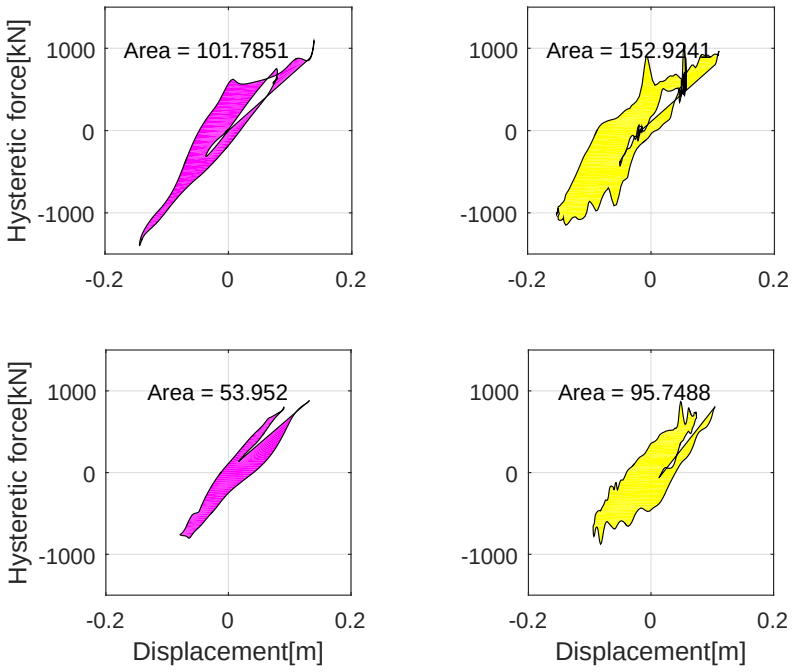

Figure 6-83: Dissipated energy from estimated and measured response at $t = 0 - 3.67sec$ and $t = 3.67 - 5sec$ for excitation (2007-1213-014-1M)

measurements hysteresis loop identification was not successful for the response during $t = 0 - 5sec$. The error between the estimated and measured total energy dissipation between $t = 0sec$ and $t = 5sec$ is about 37%. This may be due to the limitation of non-degrading model assumption in generalized Bouc-Wen model which cannot represent (or track) specific damage patterns especially in the case of reinforced concrete. Selecting a hysteresis model which consists of stiffness and strength degradation and/or pinching effects may improve the identification results in the initial response range.

Dissipated energy due to occurred damage at the pier bottom location is calculated as the enclosed area by the hysteresis curves for $t = 5 - 7sec$ and $t = 7 - 9sec$ (Figure 6-84) from estimated and measured response. Total dissipated energy (area inside the hysteresis curves) is $374kNm$ and $404kNm$ from estimated and measured responses, respectively. Thus, the error of estimation is about 8%.

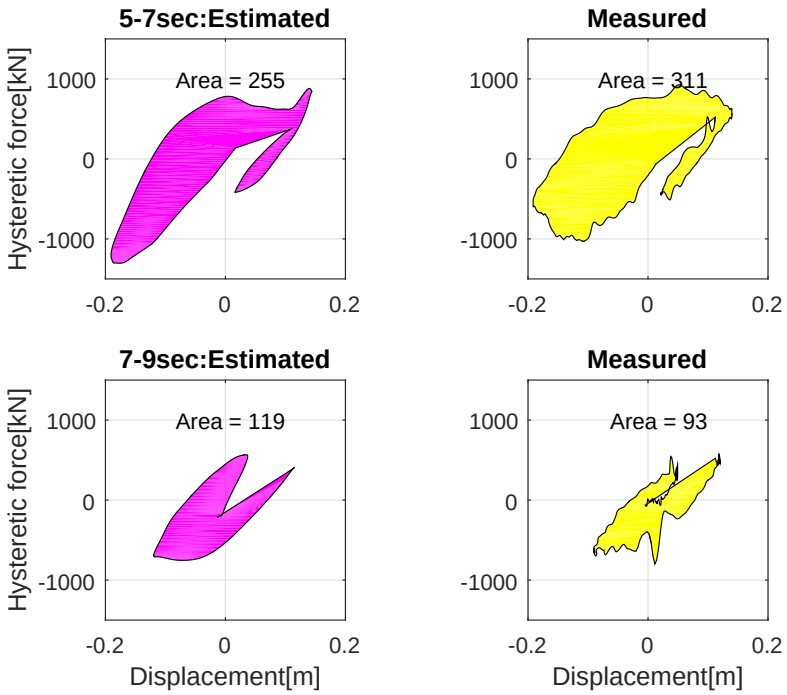

Figure 6-84: Dissipated energy from estimated and measured response at $t = 5-7sec$ and $t = 7-9sec$ for excitation (2007-1213-014-1M)

Chapter 7

Conclusions and Recommendations

The research presented in this thesis has achieved practical application of parameter estimation on full-scale bridge components under seismic excitation. The parameter estimation scheme has been verified via not only numerical simulations but series of laboratory and field measurements, resulting in the first application of Unscented Kalman Filter (UKF) on a problem of practical significance considering seismic response in structural dynamics. The proposed method has essential abilities such as, fast convergence rate, improved traceability and stability. In addition, due to its adaptive nature it is more robust against unknown process and measurement noise covariance, initial error covariance, model errors and high measurement noise in observations when compared to its non-adaptive counterparts.

In the introduction section, background for this research was first provided. Condition assessment of real structures under seismic excitation is the main interest of this study. With the advent of wireless sensor technology, gathering seismic response data from bridges has been made possible as they allow dense, and medium term monitoring with relatively long battery life. Such measurements pave the way for application of system identification methods to practice. System identification methods enables assessment of the condition of structures by detecting changes in the structural parameters. However, either in frequency or time domain, current methods require empirical knowledge at certain levels of the identification steps which makes applications of system identification algorithms to practical problems difficult. Fre-

quency domain methods deal only with linear systems and cannot directly estimate physical parameters. In addition conversion of identified parameters from modal to physical domain is often difficult. Thus, methods which are capable of identifying physical structure parameters considering nonlinear response is preferable. Examples of such methods are Extended Kalman Filter (EKF) and Unscented Kalman Filter (UKF). However, common problem in both methods is that they require initial filter parameters to be known a-priori, which are usually not available in real world applications. Thus, an adaptive system identification method which is also capable of dealing with highly nonlinear systems is necessary. [44, 63] suggested using Robbins-Monro stochastic approximation scheme with UKF and EKF, respectively, to adapt unknown process and measurement noise covariance during parameter estimation as a promising approach that can improve robustness of data assimilation methods which in return increase applicability of condition assessment on real structures. Verification and validation studies of this algorithm was explained in the subsequent chapters.

The availability of seismic response data is essential for realization of direct structural parameter estimation on civil infrastructure. Although, admittedly expensive, open-source large scale shake-table tests on structures allow researchers verify and validate the developed algorithms and their performance comparatively. The input and response measurements from a 1:1 scale reinforced-concrete (RC) bridge pier shake table experiment were obtained from NIED. The gathered data is versatile, consisting small-to-large earthquake response which were applied to test structure in a chronological manner and open to researchers upon request. The test conditions, design of the pier and applied earthquake inputs were explained in Chapter 2. In addition, utilized displacement estimation algorithm was also verified by comparing the measured displacement during test and the obtained displacement. Secondly, a field experiment on a full-scale single span bridge which was conducted by the author was detailed. Especially in the case of earthquakes taking advantage of nature with the help of developing sensors provide a unique test opportunity for real structures. The measurement plan, site conditions and collected seismic response data from aftershocks of a big earthquake were presented in detail. Considering the fact that real-world seis-

mic response measurements had been mostly limited to long-span bridges, gathered quality data is unique. Data from both measurements holds great importance as they allow full-fledged investigation studies for verification of the considered algorithm.

Furthermore, there is large uncertainty involved in the system definition as often the initial condition for structural parameters, e.g. stiffness of the pier or bearing, are not known a-priori. In fact, this is the purpose of the problem at hand. In addition, the stochastic disturbance involved in the system is practically cannot be analytically determined since they arise from a variety of interacting sources, especially in the case of process. Thus, condition assessment of civil infrastructures is often nontrivial. Thus, algorithms that can handle such uncertainties in the initial assumptions of structural parameters and unknowns in the noise parameters are needed for practical applications. For this purpose, in Chapter 3, a conventional nonlinear estimation algorithm UKF is summarized and then the UKF-RM methodology is introduced as its robust counterpart. The difference between two algorithms arise from their treatment to noise covariance matrices. In UKF, the initial Q and R matrices are kept constant as it is initially assigned value during the estimation. However, in reality they are not known a-priori and finding the correct values by trial and error method is impractical, especially when nonlinearity and size of the state vector increases in the system. Furthermore, when earthquake response is considered both process and measurement are time-variant and not stationary, thus not constant. On the other hand, UKF-RM estimates Q and R matrices by employing a stochastic approximation scheme and updates them at each time-step based on the latest information from the auto correlation of innovation, which is the difference between measurement and the estimation. Later in chapter 3, considering a SDOF system which results in nonlinear response under the given excitation, it has been verified that UKF-RM results in more robust and stable parameter estimations than UKF when a wide range of initial Q and R is considered. Furthermore, performance of UKF-RM in terms of accurate and stable estimation capability was found superior than its counterpart based on its lower sensitivity to changes in model error, error covariance, high measurement noise. RM parameters, namely α, for Q and R updates were also found robust. In

addition, since UKF-RM adapts noise covariance during estimation, its convergence rate is faster and traceability of the nonlinear response during significant duration is superior over the conventional UKF.

In Chapter 4, experimental validation of the proposed algorithm is presented using measurements from shake-table laboratory test in linear and nonlinear response levels. In both cases, UKF-RM proved to be faster in convergence and thus capable of better traceability inside the significant duration period where most of the nonlinear response occurs on the structure. This application is the first example of a stiffness condition identification of a 1:1 scale bridge lateral resisting system component, an RC pier, using UKF-RM. Later, using data gathered from the in-situ measurement, experimental validation of the stiffness identification using a 3DOF and multi-support excitation system was performed. First, through simulation the ability of the algorithm to identify bearing stiffness on both sides of the girder separately was verified. After that, using measured response data stiffness of the rubber bearings were identified successfully. This application is the first example of a structural parameters estimation using Unscented Kalman Filter

Finally, hysteresis response identification with UKF-RM was verified and validated through numerical simulations and shake-table test measurements using only acceleration response measurements as observations. Considering a conventional non-degrading Bouc-Wen model first observability analysis was performed. Consequently, based on the observability analysis model reduction has been done to reduce the size of the state matrix and make the system observable in the case where only one observation is available. Then, the algorithm performance considering the nonlinear model was investigated. It has been verified that UKF-RM results in more robust and stable parameter estimations than UKF when a wide range of initial Q and R is considered. Furthermore, performance of UKF-RM in terms of accurate and stable estimation capability was found superior than its counterpart based on its lower sensitivity to changes in model error, error covariance, high measurement noise. RM parameters, namely α, for Q and R updates were also found robust. In numerical simulation, the effect of neglecting residual displacement is investigated by employing an input large

enough that results in 1.3%. The resulting neglected energy dissipation due to residual displacement was found about 4% which was considered small as compared to total energy dissipation. Except the energy dissipated by the residual displacement, the hysteresis response obtained with UKF-RM using double-integrated acceleration as observation contains the cycles before and after inside the significant duration where most of the energy from the input excitation is dissipated by the RC pier. Finally, hysteresis response identification with Bouc-Wen model using only acceleration measurements with UKF-RM algorithm was validated using measurement from the shake table test. Except the first cycle in which the hysteresis response starts, the following two consecutive cycles in which most of the damage and hence energy dissipation occurs were identified with errors 2% and 10% from the acceleration response measurements recorded during 100% Takatori Station input.

This research achieved the first direct physical parameter estimation of lateral resisting systems of real bridge components using only acceleration measurements. The algorithm has good robustness against unknown model and measurement errors which are common to practical applications.

Bibliography

[1] H. Ukon, K. Kajiwara, K. Kawashima, T. Sasaki, S. Unjoh, J. Sakai, Y. Takahashi, K. Kosa, and M. Yabe, "Large-scale shake table experiment on a component model (c1-1model) using e-defense - experiment on a rc column build in 1970s which fails in flexure-," *Technical Note of the National Research Institute for Earth Science and Disaster Prevention*, vol. 331, p. 3, 2009.

[2] K. Kawashima, H. Ukon, and K. Kajiwara, "Bridge seismic response experiment program using e-defense," *Proceedings of 39 th UJNR Panel on Wind and Seismic Effect*, pp. 57–66, 2007.

[3] F. Ikhouane, V. Mañosa, and J. Rodellar, "Dynamic properties of the hysteretic bouc-wen model," *Systems & control letters*, vol. 56, no. 3, pp. 197–205, 2007.

[4] Ministy of Land, Infrastructure, Transport and Tourism, "Road maintenance in japan: Problems and solutions," http://www.mlit.go.jp/road/road_e/pdf/RoadMaintenance.pdf, 2015.

[5] H. Sohn, C. R. Farrar, F. M. Hemez, and J. J. Czarnecki, "A review of structural health review of structural health monitoring literature 1996-2001." Los Alamos National Laboratory, Tech. Rep., 2002.

[6] S. W. Doebling, C. R. Farrar, M. B. Prime *et al.*, "A summary review of vibration-based damage identification methods," *Shock and vibration digest*, vol. 30, no. 2, pp. 91–105, 1998.

[7] E. P. Carden and P. Fanning, "Vibration based condition monitoring: a review," *Structural health monitoring*, vol. 3, no. 4, pp. 355–377, 2004.

[8] M. Friswell and J. Penny, "Is damage location using vibration measurements practical," in *Euromech 365 international workshop: Damas*, vol. 97, 1997, pp. 351–362.

[9] D. M. Siringoringo and Y. Fujino, "System identification applied to long-span cable-supported bridges using seismic records," *Earthquake Engineering & Structural Dynamics*, vol. 37, no. 3, pp. 361–386, 2008.

[10] A. W. Smyth, J.-S. Pei, and S. F. Masri, "System identification of the vincent thomas suspension bridge using earthquake records," *Earthquake engineering & structural dynamics*, vol. 32, no. 3, pp. 339–367, 2003.

[11] R. E. Kalman *et al.*, "A new approach to linear filtering and prediction problems," *Journal of basic Engineering*, vol. 82, no. 1, pp. 35–45, 1960.

[12] C.-B. Yun and M. Shinozuka, "Identification of nonlinear structural dynamic systems," *Journal of Structural Mechanics*, vol. 8, no. 2, pp. 187–203, 1980.

[13] M. Hoshiya and E. Saito, "Structural identification by extended kalman filter," *Journal of Engineering Mechanics*, vol. 110, no. 12, pp. 1757–1770, 1984.

[14] J. N. Yang, S. Lin, H. Huang, and L. Zhou, "An adaptive extended kalman filter for structural damage identification," *Structural Control and Health Monitoring*, vol. 13, no. 4, pp. 849–867, 2006.

[15] C.-H. Loh and S.-T. Chung, "A three-stage identification approach for hysteretic systems," *Earthquake engineering & structural dynamics*, vol. 22, no. 2, pp. 129–150, 1993.

[16] C.-H. Loh and I.-C. Tou, "A system identification approach to the detection of changes in both linear and non-linear structural parameters," *Earthquake engineering & structural dynamics*, vol. 24, no. 1, pp. 85–97, 1995.

[17] S. Soyoz and M. Q. Feng, "Instantaneous damage detection of bridge structures and experimental verification," *Structural Control and Health Monitoring*, vol. 15, no. 7, pp. 958–973, 2008.

[18] S. Mariani and A. Ghisi, "Unscented kalman filtering for nonlinear structural dynamics," *Nonlinear Dynamics*, vol. 49, no. 1, pp. 131–150, 2007.

[19] E. N. Chatzi and A. W. Smyth, "The unscented kalman filter and particle filter methods for nonlinear structural system identification with non-collocated heterogeneous sensing," *Structural control and health monitoring*, vol. 16, no. 1, pp. 99–123, 2009.

[20] R. Omrani, R. Hudson, and E. Taciroglu, "Parametric identification of nondegrading hysteresis in a laterally and torsionally coupled building using an unscented kalman filter," *Journal of Engineering Mechanics*, vol. 139, no. 4, pp. 452–468, 2012.

[21] G. C. Foliente, "Hysteresis modeling of wood joints and structural systems," *Journal of Structural Engineering*, vol. 121, no. 6, pp. 1013–1022, 1995.

[22] S. K. Kunnath, J. B. Mander, and L. Fang, "Parameter identification for degrading and pinched hysteretic structural concrete systems," *Engineering Structures*, vol. 19, no. 3, pp. 224–232, 1997.

[23] Y.-C. Ou, J. Song, P.-H. Wang, L. Adidharma, K.-C. Chang, and G. C. Lee, "Ground motion duration effects on hysteretic behavior of reinforced concrete bridge columns," *Journal of Structural Engineering*, vol. 140, no. 3, p. 04013065, 2013.

[24] B. Spencer Jr, S. Dyke, M. Sain, and J. Carlson, "Phenomenological model for magnetorheological dampers," *Journal of engineering mechanics*, vol. 123, no. 3, pp. 230–238, 1997.

[25] R. Bouc, "Forced vibration of mechanical systems with hysteresis," in *Proceedings of the fourth conference on non-linear oscillation, Prague, Czechoslovakia*, 1967.

[26] Y.-K. Wen, "Method for random vibration of hysteretic systems," *Journal of the engineering mechanics division*, vol. 102, no. 2, pp. 249–263, 1976.

[27] M. N. Chatzis, E. N. Chatzi, and A. W. Smyth, "On the observability and identifiability of nonlinear structural and mechanical systems," *Structural Control and Health Monitoring*, vol. 22, no. 3, pp. 574–593, 2015.

[28] T. Kontoroupi and A. W. Smyth, "Online bayesian model assessment using nonlinear filters," *Structural Control and Health Monitoring*, vol. 24, no. 3, 2017.

[29] E. N. Chatzi, A. W. Smyth, and S. F. Masri, "Experimental application of online parametric identification for nonlinear hysteretic systems with model uncertainty," *Structural Safety*, vol. 32, no. 5, pp. 326–337, 2010.

[30] K. KAWASHIMA, T. SASAKI, K. KAJIWARA, H. UKON, S. UNJOH, J. SAKAI, Y. TAKAHASHI, K. KOSA, and M. YABE, "Seismic performance of a flexural failure type reinforced concrete bridge column based on e-defense excitation," *STRUCTURAL ENGINEERING/EARTHQUAKE ENGINEERING*, vol. 26, no. 1, pp. 28s–46s, 2009.

[31] J. R. Association, *Design specifications for design of steel bridges.* Maruzen, Tokyo, Japan, 1964.

[32] J. J. Bommer and A. Martinez-Pereira, "Strong-motion parameters: definition, usefulness and predictability," in *Proc. of the 12th World Conference on Earthquake Engineering, Auckland, New Zealand*, 2000.

[33] ——, "The prediction of strong-motion duration for engineering design," in *11th World Conference on Earthquake Engineering*, 1996.

[34] A. Arias, "Measure of earthquake intensity." Massachusetts Inst. of Tech., Cambridge. Univ. of Chile, Santiago de Chile, Tech. Rep., 1970.

[35] R. Husid, "Analisis de terremotos: analisis general," *Revista del IDIEM*, vol. 8, no. 1, pp. 21–42, 1969.

[36] P. G. Somerville, N. F. Smith, R. W. Graves, and N. A. Abrahamson, "Modification of empirical strong ground motion attenuation relations to include the amplitude and duration effects of rupture directivity," *Seismological Research Letters*, vol. 68, no. 1, pp. 199–222, 1997.

[37] D. M. Boore and J. J. Bommer, "Processing of strong-motion accelerograms: needs, options and consequences," *Soil Dynamics and Earthquake Engineering*, vol. 25, no. 2, pp. 93–115, 2005.

[38] D. M. Boore, "On pads and filters: Processing strong-motion data," *Bulletin of the Seismological Society of America*, vol. 95, no. 2, pp. 745–750, 2005.

[39] C. W. De Silva, *Vibration: fundamentals and practice*. CRC press, 2006.

[40] A. Converse and A. G. Brady, *BAP: Basic strong-motion accelerogram processing software, version 1.0*. US Department of the Interior, US Geological Survey Virginia, 1992.

[41] SEIKO EPSON Corporation, "Accelerometer m-a351as m-a351au data sheet," https://global.epson.com/products_and_drivers/sensing_system/download_hidden/pdf/m-a351_datasheet_e_rev1_0.pdf, 2016.

[42] M. Suzuki, K. Jinno, Y. Tashiro, Y. Katsumata, C. Liao, T. Nagayama, N. Makihata, M. Takahashi, M. Ieiri, and H. Morikawa, *Development and field experiment of routing-free multi-hop wireless sensor networks for structural monitoring*. Proceedings of the CSIC Conference on International Conference on Smart Infrastructure and Construction (ICSIC 2016), Robinson College, Cambridge, 2016, pp. 179–184. [Online]. Available: http://www.icevirtuallibrary.com/doi/abs/10.1680/tfitsi.61279.179

[43] M. Suzuki, T. Nagayama, S. Ohara, and H. Morikawa, "Structural monitoring using concurrent transmission flooding," The Institute of Electronics, Information and Communication Engineers (in Japanese),J100-B,(12), pp. 952–960, 2017.

[44] R. Van Der Merwe, "Sigma-point kalman filters for probabilistic inference in dynamic state-space models," 2004. [Online]. Available: https://digitalcommons.ohsu.edu/etd/8

[45] S. J. Julier, J. K. Uhlmann, and H. F. Durrant-Whyte, "A new approach for filtering nonlinear systems," in *American Control Conference, Proceedings of the 1995*, vol. 3. IEEE, 1995, pp. 1628–1632.

[46] S. J. Julier and J. K. Uhlmann, "A new extension of the kalman filter to nonlinear systems," in *Int. symp. aerospace/defense sensing, simul. and controls*, vol. 3, no. 26. Orlando, FL, 1997, pp. 182–193.

[47] E. A. Wan and R. Van Der Merwe, "The unscented kalman filter for nonlinear estimation," in *Adaptive Systems for Signal Processing, Communications, and Control Symposium 2000. AS-SPCC. The IEEE 2000.* Ieee, 2000, pp. 153–158.

[48] S. J. Julier, "The scaled unscented transformation," in *American Control Conference, 2002. Proceedings of the 2002*, vol. 6. IEEE, 2002, pp. 4555–4559.

[49] J. Duník, M. Ŝimandl, and O. Straka, "Methods for estimating state and measurement noise covariance matrices: aspects and comparison," *IFAC Proceedings Volumes*, vol. 42, no. 10, pp. 372–377, 2009.

[50] R. Mehra, "On the identification of variances and adaptive kalman filtering," *IEEE Transactions on automatic control*, vol. 15, no. 2, pp. 175–184, 1970.

[51] ——, "Approaches to adaptive filtering," *IEEE Transactions on automatic control*, vol. 17, no. 5, pp. 693–698, 1972.

[52] P. S. Maybeck, *Stochastic models, estimation, and control.* Academic press, 1982, vol. 2.

[53] N. A. White, P. S. Maybeck, and S. L. DeVilbiss, "Detection of interference/jamming and spoofing in a dgps-aided inertial system," *IEEE Transactions on Aerospace and Electronic Systems*, vol. 34, no. 4, pp. 1208–1217, 1998.

[54] P. S. Maybeck, "Multiple model adaptive algorithms for detecting and compensating sensor and actuator/surface failures in aircraft flight control systems," *International Journal of Robust and Nonlinear Control*, vol. 9, no. 14, pp. 1051–1070, 1999.

[55] A. Mohamed and K. Schwarz, "Adaptive kalman filtering for ins/gps," *Journal of geodesy*, vol. 73, no. 4, pp. 193–203, 1999.

[56] N. Naik, R. Gemson, M. Ananthasayanam *et al.*, "Introduction to the kalman filter and tuning its statistics for near optimal estimates and cramer rao bound," *arXiv preprint arXiv:1503.04313*, 2015.

[57] H. E. Soken and S.-i. Sakai, "Adaptive tuning of the unscented kalman filter for satellite attitude estimation," *Journal of Aerospace Engineering*, vol. 28, no. 3, p. 04014088, 2014.

[58] S. O. Haykin, *Adaptive filter theory*. Pearson Higher Ed, 2013.

[59] A. T. Nelson, "Nonlinear estimation and modeling of noisy time-series by dual kalman filtering methods," 2000. [Online]. Available: https://digitalcommons.ohsu.edu/etd/106

[60] H. Robbins and S. Monro, "A stochastic approximation method," *The annals of mathematical statistics*, pp. 400–407, 1951.

[61] L. Ljung and T. Söderström, *Theory and practice of recursive identification*. JSTOR, 1983, vol. 5.

[62] J. P. Sum, C. Leung, and L. Chan, "Extended kalman filter in recurrent neural network training and pruning," Tech. Rep., Department of Computer Science and Engineering, Chinese University of Hong Kong, CS-TR-96-05, Tech. Rep., 1996.

[63] J. P.-f. Sum, "Extended kalman filter based pruning algorithms and several aspects of neural network learning," Ph.D. dissertation, Chinese University of Hong Kong, 1998.

[64] S. S. Haykin *et al.*, *Kalman filtering and neural networks*. Wiley Online Library, 2001.

[65] S. Ramadurai, S. N. Kosari, H. H. King, H. J. Chizeck, and B. Hannaford, "Application of unscented kalman filter to a cable driven surgical robot: A simulation study," in *Robotics and Automation (ICRA), 2012 IEEE International Conference on*. IEEE, 2012, pp. 1495–1500.

[66] M. Havlicek, K. J. Friston, J. Jan, M. Brazdil, and V. D. Calhoun, "Dynamic modeling of neuronal responses in fmri using cubature kalman filtering," *NeuroImage*, vol. 56, no. 4, pp. 2109–2128, 2011.

[67] D. Sierociuk and A. Dzieliński, "Fractional kalman filter algorithm for the states, parameters and order of fractional system estimation," *International Journal of Applied Mathematics and Computer Science*, vol. 16, pp. 129–140, 2006.

[68] M. Grewal and A. Andrews, *Kalman Filtering: Theory and Practice Using MATLAB*. Wiley, 2008. [Online]. Available: https://books.google.co.jp/books?id=zDHncuewKsQC

[69] T. T. Baber and Y.-K. Wen, "Random vibration hysteretic, degrading systems," *Journal of the Engineering Mechanics Division*, vol. 107, no. 6, pp. 1069–1087, 1981.

[70] T. T. Baber and M. N. Noori, "Random vibration of degrading, pinching systems," *Journal of Engineering Mechanics*, vol. 111, no. 8, pp. 1010–1026, 1985.

[71] ——, "Modeling general hysteresis behavior and random vibration application," *Journal of Vibration, Acoustics, Stress, and Reliability in Design*, vol. 108, no. 4, pp. 411–420, 1986.

[72] M. Ismail, F. Ikhouane, and J. Rodellar, "The hysteresis bouc-wen model, a survey," *Archives of Computational Methods in Engineering*, vol. 16, no. 2, pp. 161–188, 2009.

[73] J.-W. Lin and R. Betti, "On-line identification and damage detection in non-linear structural systems using a variable forgetting factor approach," *Earthquake engineering & structural dynamics*, vol. 33, no. 4, pp. 419–444, 2004.

[74] L. Jeen-Shang and Z. Yigong, "Nonlinear structural identification using extended kalman filter," *Computers & structures*, vol. 52, no. 4, pp. 757–764, 1994.

[75] J.-S. Lin, "Extraction of dynamic soil properties using extended kalman filter," *Journal of geotechnical engineering*, vol. 120, no. 12, pp. 2100–2117, 1994.

[76] W. Song, "Dynamic model updating with applications in structural and damping systems: From linear to nonlinear, from off-line to real-time," Ph.D. dissertation, Purdue University, 2011.

[77] F. Ma, H. Zhang, A. Bockstedte, G. C. Foliente, and P. Paevere, "Parameter analysis of the differential model of hysteresis," *Journal of Applied Mechanics*, vol. 71, no. 3, pp. 342–349, 2004.

[78] R. Hermann and A. Krener, "Nonlinear controllability and observability," *IEEE Transactions on automatic control*, vol. 22, no. 5, pp. 728–740, 1977.

[79] S. Erlicher and N. Point, "Thermodynamic admissibility of bouc–wen type hysteresis models," *Comptes rendus mecanique*, vol. 332, no. 1, pp. 51–57, 2004.

[80] Y. Ni, J. Ko, and C. Wong, "Identification of non-linear hysteretic isolators from periodic vibration tests," *Journal of sound and vibration*, vol. 217, no. 4, pp. 737–756, 1998.